After the 2010 Mw 8.8 Maule earthquake: Tectonics in central Chile derived by an automated analysis of aftershocks from an amphibious seismic network

Dissertation
zur Erlangung des Doktorgrades
der Mathematisch-Naturwissenschaftlichen Fakultät
der Christian-Albrechts-Universität zu Kiel
vorgelegt von

Kathrin Lieser

Kiel, 2015

Erster Gutachter:	Prof. Dr. Ingo Grevemeyer
Zweiter Gutachter:	Prof. Dr. Wolfgang Rabbel
Tag der mündlichen Prüfung:	21.05.2015
Zum Druck genehmigt:	21.05.2015

gez. Prof. Dr. Wolfgang J. Duschl, Dekan

Abstract

The Chilean subduction zone is among the seismically most active plate boundaries in the world and coastal ranges suffer from a magnitude 8 or larger megathrust earthquake about every ten years. The Constitución-Concepción or Maule segment in central Chile between about 35.5°S and 37°S was considered to be a mature seismic gap, rupturing last in 1835 and being seismically quiet without any magnitude 4.5 or larger earthquakes reported in global catalogues. It is located to the north of the nucleation area of the 1960 magnitude 9.5 Valdivia earthquake and to the south of the 1928 magnitude 8 earthquake near Talca. On 27 February 2010 this segment ruptured in a Mw 8.8 earthquake, nucleating near 36°S and affecting a 500 km long segment of the margin between 34°S and 38.5°S. Most of the aftershocks occurred offshore. Therefore, a network of 30 ocean-bottom seismometers (OBS) was deployed in the northern part of the rupture area for a three month period, recording local offshore aftershocks between 20 September 2010 and 25 December 2010. In addition, data of a network consisting of 33 land stations of the GeoForschungsZentrum Potsdam were included into the network, providing an ideal coverage of both the rupture plane and areas affected by post-seismic slip as deduced from geodetic data. Two years prior to the Maule event the Collaborative Research Center SFB 574 "Volatiles and Fluids in Subduction Zones" operated an amphibious seismic network in the same area. Both data sets gave a great opportunity to compare seismicity and stress distributions before and after a megathrust event and to study the evolution of a subduction zone within the seismic cycle of a megathrust event.

In this study the aftershocks of the Mw 8.8 Maule earthquake are analysed in order to gain information about the rupture zone, stress distributions, and faulting in the forearc after a megathrust event. As most of the temporary and permanent seismic networks are located on land, automatic picking routines have been developed with land station data and there are few studies with automatically determined phase arrivals from OBSs in the literature. The analysis of aftershocks in this study is performed in an automated approach to show that an automated determination of phase arrivals and polarisation, focal mechanisms and magnitudes can be accomplished with OBS data as well.

Aftershock seismicity analysis in the northern part of the survey area reveals a well resolved seismically active splay fault in the accretionary prism of the Chilean forearc. Splay faults, large thrust faults emerging from the plate boundary to the sea

floor in subduction zones, are considered to enhance tsunami generation by transferring slip from the very shallow dip of the megathrust onto steeper faults, thus increasing vertical displacement of the sea floor. These structures are predominantly found offshore, and therefore, hard to detect in seismicity studies as most seismometer stations are located onshore. Application of critical taper theory analysis suggests that in the northernmost part of the rupture zone, co-seismic slip likely propagated along the splay fault and not the subduction thrust fault while in the southern part it propagated along the subduction thrust fault and not the splay fault.

The most profound features of a comparison of aftershocks to data collected in 2008 before the Maule event are: (1) a sharp reduction in intraslab seismic activity after the Maule earthquake, (2) an increase in seismic activity at the slab interface above 50 km depth, where large parts of the rupture zone were mainly aseismic prior to the Maule earthquake. Further, the aftershock seismicity shows a broader depth distribution above 50 km depth, shifting the updip limit of the seismogenic zone about 30 km closer to the trench, and (3) an active seismic cluster in the 2008 data while in 2010 there is a seismic gap in about 40 to 50 km depth along the plate boundary probably related to a relic mantle body.

Zusammenfassung

Die Subduktionszone vor Chile gehört zu den seismisch aktivsten Plattengrenzen weltweit. Die angrenzenden Küstengebiete werden im Durchschnitt alle 10 Jahre von Erdbeben mit einer Stärke von 8 oder mehr heimgesucht. Vom Constitutión-Concepción-Plattensegment in Zentralchile, oder Maule-Segment, wurde angenommen, dass es eine ausgeprägte seismische Ruhezone ist, da es letztmalig im Jahr 1835 zu einem größeren Beben kam. Das Maule-Segment liegt nördlich der Bruchzone des Mw 9.5 Valdivia-Bebens aus dem Jahr 1960 und südlich des Erdbebenzentrums des 1928 Talca-Beben (Mw 8.0). Am 27. Februar 2010 brach dieses Plattensegment bei 36°S auf. Das dadurch entstandene Beben der Stärke 8.8 beeinträchtigte ein Gebiet von ca. 500 km Länge zwischen 34°S und 38,5°S. Da die meisten Nachbeben vor der Küste registriert wurden, wurde ein aus 30 Ozeanboden-Seismometern (OBS) bestehendes Netzwerk in der nördlichen Gegend der Bruchzone installiert. Dieses Netzwerk wurde für ca. 3 Monate, zwischen September und Dezember 2010, betrieben und zeichnete die lokal vorkommenden Nachbeben auf. Zusätzliche Daten von 33 Landstationen des GeoForschungszentrums Potsdam wurden mit in das Netzwerk integriert, um eine nahezu lückenlose Abdeckung der nördlichen Bruchzone sowohl land- als auch seewärtig zu erreichen. Zudem hatte der Sonderforschungsbereich 574 "Volatile und Fluide in Subduktionszonen" zwei Jahre vor dem Maule-Beben ein seismisches Netzwerk, bestehend aus Ozeanboden-Seismometern und Landstationen, ausgebracht. Beide Datensätze erlaubten einen einmaligen Einblick in die vom Beben beeinträchtigte Subduktionszone und ermöglichen einen Vergleich der Seismizität und Stressverteilung vor und nach einem großen Subduktionserdbeben.

In dieser Dissertation werden die Nachbeben des Maule-Bebens analysiert, um Informationen über die Bruchzone, Stressverteilung und Verwerfungen im submarinen Forearc-Bereich nach dem großen Beben zu erlangen. Da sich die meisten der temporären sowie permanenten seismischen Netzwerke an Land befinden, wurden automatisierte Routinen zum Bestimmen der seismischen Phaseneinsätze anhand von Landstationsdaten entwickelt, und es gibt nur sehr wenige Studien über diese Routinen für Daten von Ozeanboden-Seismometern. Bei der Analyse der Maule-Nachbeben wurden die Phasenankunft und Polarisierung der Erdbebenwellen sowie Herdmechanismen und Magnituden automatisch bestimmt um zu zeigen, dass dieses auch für OBS-Daten möglich ist.

Die Analyse der Nachbebenseismizität im nördlichen Teil des Untersuchungsgebiets zeigt deutlich eine seismisch aktive Splayfault im Akkretionskeil des chilenischen

Forearc. Von Splayfaults, die in Subduktionszonen von der Plattengrenze hinauf bis zum Meeresboden reichen, wird angenommen, dass sie die Entstehung von Tsunamis begünstigen, indem sie die vertikale Verschiebung des Meeresbodens verstärken. Da diese Splayfaults überwiegend im Seebereich auftreten, sind sie auf Landstationen nur sehr schwer deutlich zu erkennen. Auswertungen legen nahe, dass sich der Bruch im nördlichen Teil des Untersuchungsgebietes koseismisch entlang der Splayfault, und nicht entlang der Plattengrenze, ausgebreitet hat. Im Süden des Arbeitsgebiets hingegen scheint sich der Bruch jedoch entlang der Subduktionsverwerfung ausgebreitet zu haben.

Die größten Auffälligkeiten zwischen den Nachbeben und der Seismizität von 2008 vor dem Maule-Beben sind: (1) eine starke Reduzierung der Intraplatten-Seismizität nach dem Maule-Beben, (2) ein Anstieg der seismischen Aktivität entlang der Plattengrenze oberhalb von 50 km Tiefe, wo große Teile der Bruchzone vor dem Beben aseismisches Verhalten aufwiesen, wodurch die seewärtige Grenze der seismogenen Zone ca. 30 km näher an den Tiefseegraben heran gebracht wurde, (3) eine Gruppe von Erdbeben im 2008 Datensatz, die in einem Bereich in 40 bis 50 km Tiefe entlang der Plattengrenze liegt, der nach dem Maule-Beben aseismisches Verhalten aufweist.

Contents

List of Figures

List of Tables

[...] because once you have been in an earthquake you know, even if you survive without a scratch, that like a stroke in the heart, it remains in the earth's breast, [...], always promising to return, to hit you again, with an even more devastating force.

(Salman Rushdie – The ground beneath her feet)

1. Introduction

Western South America has continually been struck by large earthquakes in the past. The earliest report about a magnitude 8 earthquake in Chile dates back to the 16th century (*National Geophysical Data Center, NOAA*, 2015) and the largest earthquake ever recorded (Mw 9.5) ruptured the margin in south-central Chile in 1960 near the city of Valdivia (*National Geophysical Data Center, NOAA*, 2015). About every ten years on average an earthquake with a magnitude larger than 8 occurs (*Campos et al.*, 2002). However, in the past five years two magnitude 8.2 and 8.8 events hit Chile; the last in northern Chile near Iquique in April 2014 and the Maule region in central Chile was struck by a Mw 8.8 megathrust event in February 2010 (*National Geophysical Data Center, NOAA*, 2015).

The cause for the high seismic activity in Chile, and western South America, is the subduction of the Nazca Plate under the South American Plate. When both plates slide along each other, stress is accumulated that will be released in earthquakes. Other effects of subduction zones are volcanism and mountain building. In this study the aftershocks of the 2010 Maule event are analysed on ocean-bottom seismometers (OBS) and land stations to gain information about the rupture zone, stress distributions, and faulting in the forearc after a megathrust event.

This chapter gives an overview about the general structure of subduction zones and more specific information about the continental margin in central Chile and the rupture area of the 2010 earthquake. After explaining the seismic network configuration, the objectives of this study and a thesis outline are pointed out.

1.1. Subduction zones

A subduction zone is a convergent plate boundary where one of the colliding plates descends under the other into the mantle. The lithosphere of the subducted plate, or slab, consists of oceanic crust and upper mantle while the lithosphere of the overriding plate can comprise both, oceanic or continental crust. Because continental

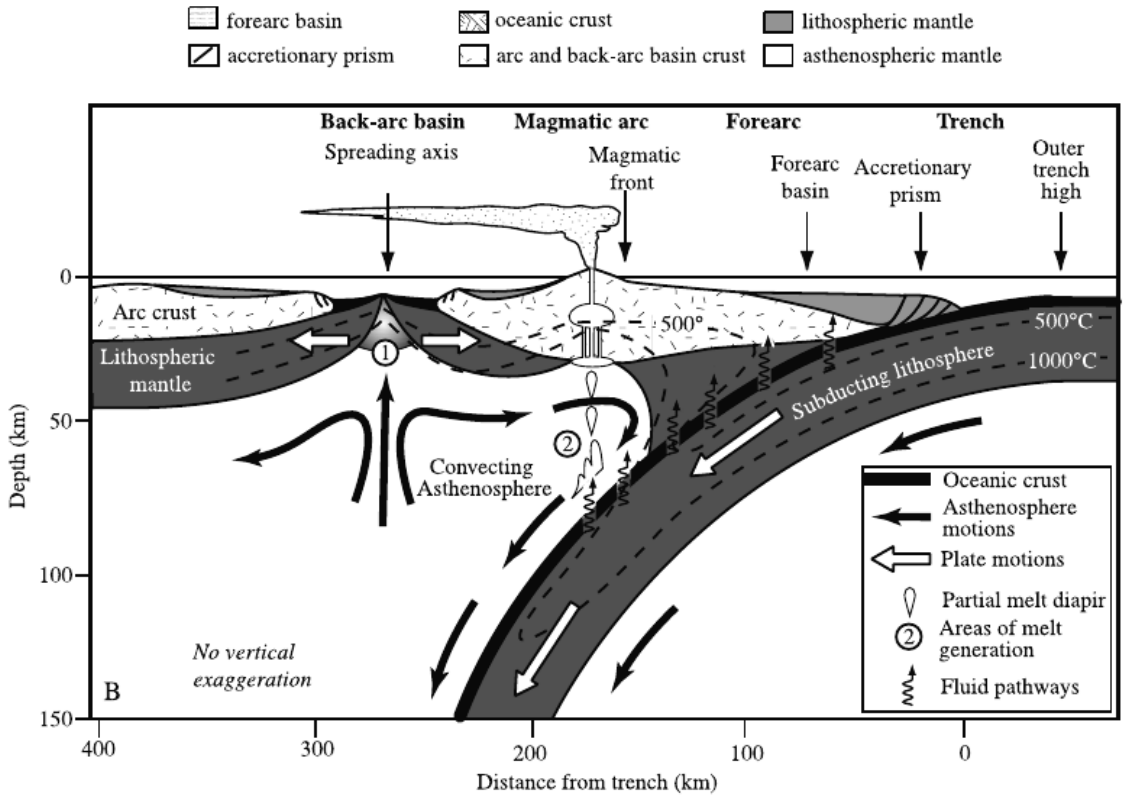

Figure 1.1.: Schematic section through a subduction zone (*Stern*, 2002). Copyright 2002 by the American Geophysical Union.

crust does not have enough buoyancy to sink deep into the mantle, the collision of two continental plates does not result in a subduction zone (*Stern*, 2002). The major structures of a subduction zone are presented in Figure 1.1. A good general overview of subduction zones is given by *Stern* (2002) in his review article that provides the base of this section. The overriding plate can be divided into three regions: the forearc, the magmatic arc and the backarc. The forearc is about 166±60 km wide (*Gill*, 1981) and reaches from the trench, where the subducting slab starts to descend into the mantle, to the magmatic front. Depending on sediment supply and thickness of subducted sediments, an accretionary or a non-accretionary forearc may form (e.g. *Stern*, 2002; *Ranero et al.*, 2006). A thick layer of sediments will be scraped off the subducting plate forming an highly deformed accretionary prism or wedge and adding material to the over-riding plate. Deformation of an accretionary prism will be discussed in Section 1.1.1, in more detail. Non-accretionary forearcs form where the sediment supply is low. Here, the subducting plate can scrape off parts of the crust and mantle of the over-riding plate and carry them down into the mantle. This process is called subduction erosion or tectonic erosion and can occur in different intensities depending among other things on the roughness of the sea

floor topography of the downgoing plate (*Clift and Vannucchi*, 2004). The magmatic arc is about 100 km wide (*Bremond d'Ars et al.*, 1995) and is characterized by high magmatic activity that sets in at the magmatic front located about 105 km (*Syracuse and Abers*, 2006) above the slab. Here, the water that is subducted within the slab is pushed out of the plate and lowers the melting temperature of the asthenosperic mantle material above and melting occurs. The melts rise up and feed volcanoes and thicken the crust by underplating. The backarc is characterised by orogenesis or by backarc-basins where even sea floor spreading might occur in highly extensional environments (*Stern*, 2002).

Oceanic crust originates at mid ocean ridges where new magma constantly emerges to the sea floor and spreads away from the ridge. With increasing age the plate gets colder and thicker, and therefore, more dense and sinks deeper into the mantle underneath until the negative buoyancy of the plate causes it to descend at a convergent margin. The slab pull resulting from excess density is considered to be the major force that drives plate motion (*Stern*, 2002). By descending in to the mantle, the downgoing plate is bent and forms a topographic high, the outer trench high or outer rise (see Fig. 1.1). Here, seismic activity can occur along trench parallel normal faults that are caused by the bending of the plate. *Ranero et al.* (2003) proposed that those faults, that can reach down into the mantle, support the hydration of the downgoing slab.

The greatest earthquakes within a subduction zone occur in the seismogenic zone, that mainly consists of the part of the downgoing slab sliding along the overriding plate at depths of about 35 to 55 km (*Stern*, 2002) resulting in the locking of the plate interface and the accumulation of elastic strain. The updip and downdip limit of the seismogenic zone is mainly depended on the surrounding temperatures. Downdip of the seismogenic zone the rocks are too weak to build up strain energy that would be released in an earthquake, usually where the surrounding temperatures are higher than about 350°C (*Oleskevich et al.*, 1999) or where the rocks themselves are weak, e.g. serpentinite (*Hyndman et al.*, 1997). *Oleskevich et al.* (1999) found that the location of the continental Moho, or crust-mantle boundary, the 350°C isotherm and the downdip limit of the seismogenic zone defined by aftershocks are in a good agreement. However, in Sumatra, the downdip limit of the seismogenic zone is located below the downdip extend of the continental moho (*Simoes et al.*, 2004; *Dessa et al.*, 2009; *Collings et al.*, 2012). Updip of the seismogenic zone the shear strength of the rocks and sediments is not sufficient enough to cause rupture and slip is generally aseismic. However, the rupture of the 2011 Tohoku-Oki earthquake, off Japan, reached the trench-axis (*Fujiwara et al.*, 2011; *Lay et al.*, 2011). With progressing suduction the material gets stronger and seismic activity sets in. A change in pore pressure fluid, dehydration and the transition from stable sliding clays to stronger clays at about 100–150°C at depth of 5–15 km (*Hyndman et al.*,

1997; *Grevemeyer et al.*, 2005; *Tilmann et al.*, 2010) are considered to be reasons for the strengthening of rocks at the updip limit. The downdip limit of the seismogenic zone is better constrained than the updip limit because it is in general located under land, or close to the land, where the coverage of seismic stations is considerably higher. The updip limit plays an important role in tsunami generation because the location of the seaward rupture limit and the sea floor displacement strongly affects the severity of a tsunami. Intermediate-depth events, earthquakes that nucleate in the slab deeper than the seismogenic zone and above about 300 km, are likely caused by metamorphic dehydration reactions, e.g. of serpentinite (*Hacker et al.*, 2003). Deep events, below about 300 km are usually caused by an increase in relative slab density due to phase transitions of minerals (olivine to spinel). The whole extend where earthquakes occur along the subducting slab is called Wadati-Benioff zone and can reach down to 700 km depth (*Stern*, 2002).

The distribution of aftershocks that are triggered by a megathrust event gives a good estimation about the main shock fault area (*Richter*, 1955; *Das and Henry*, 2003). Further, *Das and Henry* (2003) concluded that aftershocks occur in regions of increased stress induced by the main shock and only few, and usually the smaller, aftershocks originate in high-slip regions of the main shock.

1.1.1. Splay faults

Thrust faults rising from plate interfaces to the sea floor in subduction zones are referred to as splay faults or megasplay faults (*Moore et al.*, 2007; *Melnick et al.*, 2012a). Splay faults can dip in both directions, landwards or seawards and depending on the depth of the megathrust slip and a critical depth they can be triggered as reverse or normal faults (*Li et al.*, 2014). Figure 1.2 shows a sketch of a landward dipping splay fault in the submarine forearc at the transition from frontal accretionary prism (outer wedge) to continental crust (inner wedge) where splay faulting often occurs (*Collot et al.*, 2008). At the transition the updip limit of the seismogenic zone is expected because here the behaviour of the subduction thrust fault switches from velocity-strengthening below the outer wedge to velocity-weakening below the inner wedge (*Wang and Hu*, 2006). Splay faults are considered to play a significant role in tsunami generation by enhancing vertical surface displacement and bringing it closer to the coast (e.g. *Wendt et al.*, 2009), and may limit rupture propagation of great earthquakes (e.g. *Melnick et al.*, 2012a). Splay faults have been detected several times on reflection seismic profiles, e.g., in Chile and Japan (*Geersen et al.*, 2011; *Moore et al.*, 2007). In Sumatra, ocean-bottom seismometer deployments in the aftermath of the 2004 Sumatra-Andaman megathrust earthquake have shown shallow forearc seismic activity, which has been associated with splay faults. How-

ever, seismicity distribution was diffuse and did not define a clear fault plane (*Araki et al.*, 2006; *Sibuet et al.*, 2007). Also in Sumatra, a deep-rooted master splay fault branching off at 50 km depth was postulated based on relocated global earthquakes (*Waldhauser et al.*, 2012), and extrapolation of seismic reflection data. However, the inferred fault is not outlined directly by the seismicity. Observing seismicity associated with splay faults is challenging because they are located offshore, usually at the landward edges of accretionary prisms. Most of the local networks are installed onshore, so offshore seismicity and its relation to splay faulting are not well constrained and little is known about along strike variation of splay fault activity.

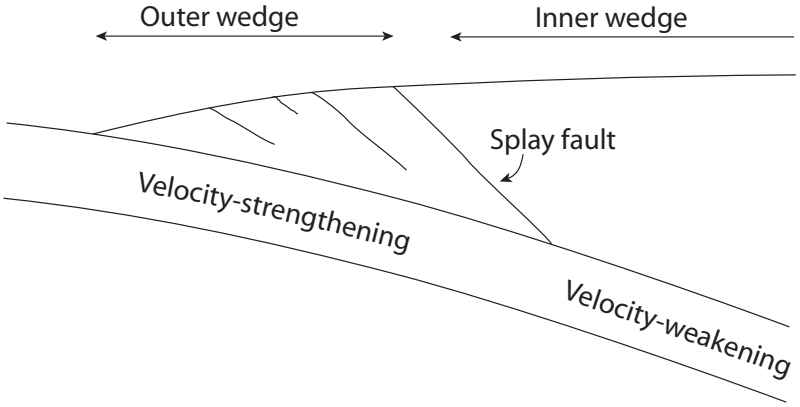

Figure 1.2.: Sketch of a landward dipping splay fault at the transition from outer wedge to inner wedge (after *Wang and Hu* (2006)).

1.1.2. Stress state in subduction earthquake cycles

When the downgoing plate bends under the overriding plate existing faults in the incoming plate can be reactivated and new faults may be created parallel to the trench axis. *Christensen and Ruff* (1988) proposed that the bending related stresses in the outer rise are superimposed by stresses in the subducted slab and therefore, outer rise faulting may give indications if a subduction zone segment is locked. If the subduction zone is locked the outer rise would be under compression and shallow compressional events occur. After a megathrust event slab pull is transferred to the outer rise inducing shallow extensional events. *Mueller et al.* (1996) suggests as well that stress variations in the outer rise may support thrust faulting in the outer rise prior to a subduction earthquake and normal faulting after. However, they also conclude that it is unlikely that both types of outer rise seismicity will occur for the same subduction event but that the absence of large outer rise events

either before or after a subduction event is likely. Compression-dominated stress distributions are likely to occur only in response to specific tectonic situations, like buoyant bathymetric features or interplate asperities, while bending related normal faulting describes the predominant state of stress in the outer rise. This is also in accordance with the observation that normal faulting events occur about six times as often as thrust events in the outer rise (*Christensen and Ruff*, 1988).

Astiz and Kanamori (1986) studied events down dip of the 1960 Chile earthquake and observed that events after the main shock were down-dip compressional while before they were down-dip tensional. They suggest that before a major thrust event the plate boundary is strongly coupled and the slab is under tension at intermediate depths whereas after the event displacement on the thrust boundary induces compressional stresses.

The forearc of the over-riding plate is also affected by stress changes in great earthquake cycles. *Wang and Hu* (2006) studied accretionary prisms in subduction earthquake cycles by considering temporal variations of stresses along the megathrust fault and within the wedge. For the end-member scenario in which the seismogenic zone alternates between interseismic locking and coseismic slip the outer wedge switches between stable and critical states. During great subduction earthquakes the outer wedge can be pushed into a compressively critical state, i.e. prone to failure, while in between earthquakes the stresses in the outer wedge relax. In contrast, the stronger inner wedge remains mostly stable throughout the earthquake cycles.

1.2. Tectonics in central Chile and the Maule event

The western margin of South America is characterised by the subduction of the Nazca plate that descends under the South American Plate with a velocity of about 65 mm/a (*Angermann et al.*, 1999). North of 28°S and south of 33°S the Nazca plates sinks with an angle of about 30° into the mantle. In the segment in between, the slab does not descend any deeper into the mantle in a depth of about 100 km but forms a flat plateau. This flat slab plateau extends over several 100 km until the subduction continues (*Wagner et al.*, 2005). The transition from flat slab to normal slab takes place gradually at the northern segment while it is rather abrupt in the South. In some studies it was suggested that this may be due to a tear in the slab or to strong bending of the slab (*Cahill and Isacks*, 1992; *Wagner et al.*, 2005). However, *Pesicek et al.* (2012) tried to resolve the slab tear from aftershock data of the Maule event but their results suggest that slab bending rather than tearing accommodates the transition from flat slab to normal subduction. The flat slab may be caused by

the subduction of the Juan-Fernandez-Ridge because its thickened crust may have sufficient positive buoyancy to prevent the slab from sinking any deeper into the mantle (*Anderson et al.*, 2007). The ridge acts as a barrier for along strike sediment transport as well. North of the ridge the sediments are about 0.5 to 1 km thick and the margin is affected by tectonic erosion while further south they are about 2.5 km thick and the margin is in an accretionary mode (*Ranero et al.*, 2006; *Vietor and Echtler*, 2006). The Nazca Plate is made of relatively young lithosphere with about 40 Ma in the area where the Juan-Fernandez-Ridge is subducted (Fig. 1.3). The age decreases in the southern direction until 46°S where the Chile Rise, an active spreading centre and the southern border of the Nazca Plate, is subducted. The young age leads to a high amount of accumulated strain that was released in large events rupturing the Chilean margin in the past. The worldwide biggest recorded earthquake with a magnitude of Mw 9.5 nucleated near Valdivia in 1960 and events with magnitudes larger than 8 occur about every ten years (*Campos et al.*, 2002).

In February 2010, the south-central Chilean margin near Maule was struck by a megathrust event (moment magnitude Mw 8.8) followed by a destructive tsunami. The affected Constitutión-Concepción segment in central Chile was considered to be a mature seismic gap showing little seismic activity on the megathrust since the last great earthquake in the area in 1835. On 27 February 2010, this segment ruptured in the Mw 8.8 Maule earthquake, nucleating near 36°S and affecting a 500 km-long area of the margin (*Vigny et al.*, 2011; *Moreno et al.*, 2012). Coseismic slip, with as much as 16 m slip in the main patch north of the hypocentre, released most of the accumulated strain since the 1835 Darwin earthquake, therefore closing a known seismic gap (*Melnick et al.*, 2012b; *Moreno et al.*, 2012). The rupture propagated bilaterally to the north and to the south (e.g. *Delouis et al.*, 2010; *Lay et al.*, 2010; *Moreno et al.*, 2012). The northern boundary of the 2010 rupture zone coincides with the rupture area of the 1985 event while the southern border overlaps for about 100 km with the rupture area of the large 1960 event. After the Maule main shock, a tsunami as high as 14 m hit the coast and caused enormous destruction (*Vargas et al.*, 2011). Aftershocks of the Mw 8.8 Maule earthquake occurred along a portion of the central Chilean margin, almost 500 km in length; most of them offshore (*Lange et al.*, 2012a; *Rietbrock et al.*, 2012). The Maule event triggered intense activity in the upper plate, particularly near Pichilemu, at about 34.5°S north of the main shock along a northwest-striking fault (e.g. *Ryder et al.*, 2012; *Farías et al.*, 2011); the two largest events (approx. Mw 7) occurred on 11 March 2010 and showed normal faulting focal mechanisms. Splay faulting along the Chilean margin is a known process (e.g. *Geersen et al.*, 2011; *Moreno et al.*, 2012) and splay faults may have limited rupture propagation along-strike at the northern boundary of the 2010 rupture zone (*Moreno et al.*, 2012). A prominent thrust ridge that is considered to be related to splay faulting in the survey area coincides with

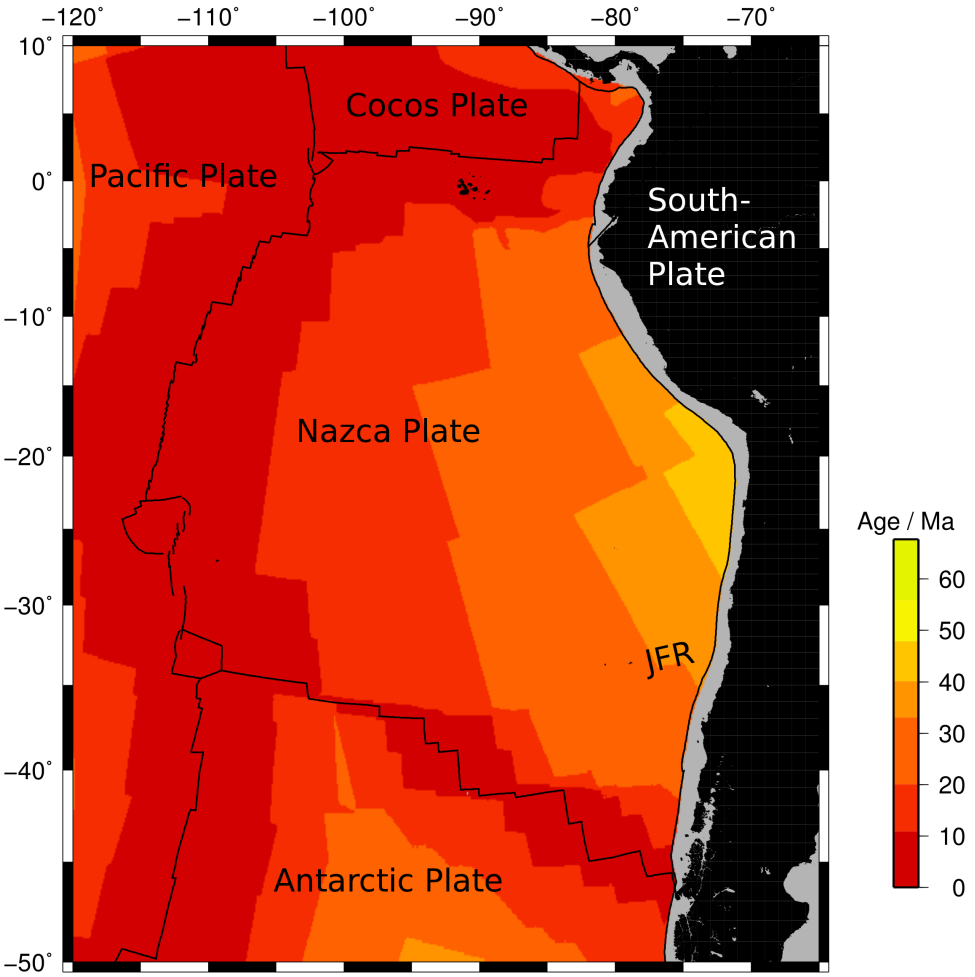

Figure 1.3.: Age of lithospheric plates in South America after *Müller et al.* (1997). JFR = approximate location of the Juan-Fernandez-Ridge.

the transition from frontal accretionary prism to continental framework rock. The frontal accretionary prism near the trench (outer wedge) in the Maule region is about 40 km wide and is made of poorly consolidated sediments (*Moscoso et al.*, 2011; *Contreras-Reyes et al.*, 2010). It is limited by a backstop from an inner wedge, which consists of continental framework rock or continental crust made of paleo-accretionary complexes (*Contreras-Reyes et al.*, 2010). Seismological constraints show that the updip limit of aftershock seismicity of the Maule event corresponds to the transition between the frontal accretionary prism (outer wedge) and continental crust (inner wedge) (*Moscoso et al.*, 2011; *Lange et al.*, 2012a), where splay faulting can occur (*Collot et al.*, 2008).

1.3. OBS and land station network

A local seismic network consisting of 30 OBS was deployed for a three month period between 20 September and 25 December 2010 in the northern part of the rupture zone, where the highest slip rates occurred, to record the aftershocks of the Maule event offshore (Fig. 1.4). The station spacing averages about 40 km. Five of the deployed instruments were equipped with broadband seismometers with corner frequencies of 0.03 Hz while the remaining 25 stations were equipped with 4.5 Hz seismometers. In addition to the seismometer a hydrophone was attached to all instruments. Almost all stations recorded continuously during the whole deployment time span (Fig. 1.5). Only OB18 did not record any data and OB07 stopped recording in mid November (see Figure A.1 in Appendix A for station names). For 24 instruments all four channels showed good data quality while for two stations (OB03 and OB15) the horizontal components and for OB30 the vertical and hydrophone components showed poor data quality and were not used for processing. The remaining three instruments showed good data at least on one horizontal and one vertical component.

In addition, a total of 33 temporary land stations from the late phase of the International Maule Aftershock Deployment IMAD (Beck et al., 2014) were included in the analysis. The corner frequency of all instruments was 1 Hz. As some stations were moved further south at the end of October 2010 (Fig. 1.6) the coverage onshore varies. The combination of the OBS and land stations lead to an amphibious seismic network which provides an excellent coverage of the northern part of the rupture plane offshore as well as onshore.

Two years prior to the Maule event the Collaborative Research Center SFB 574 "Volatiles and Fluids in Subduction Zones" (www.sfb574.geomar.de) operated a seis-

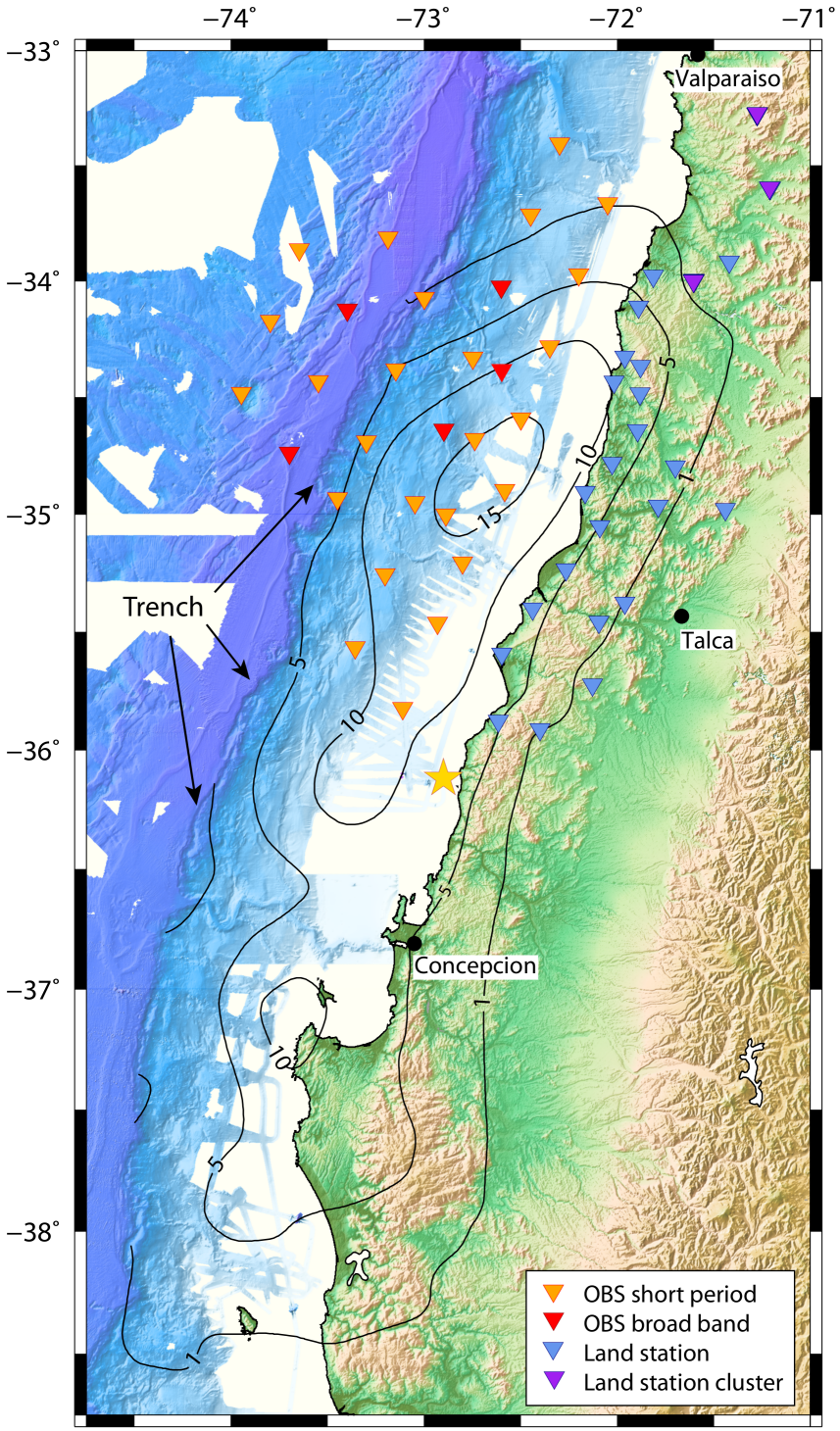

Figure 1.4.: Map of station configuration and coseismic slip distribution from *Moreno et al.* (2012). The land station cluster consist of 3-5 stations each.

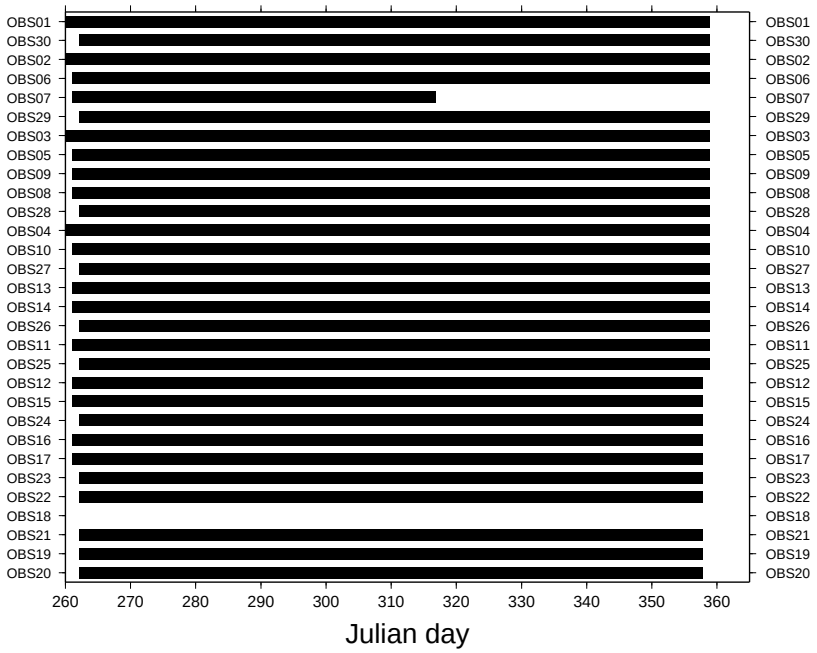

Figure 1.5.: Recording time of OBS stations. The stations are sorted by latitude with the northernmost station plotted at the top. See Figure A.1 for station names.

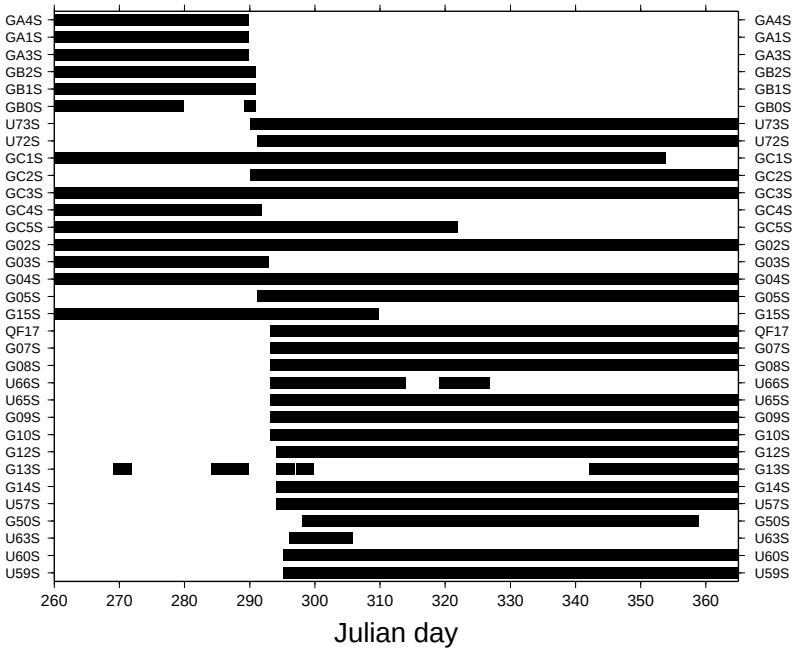

Figure 1.6.: Recording time of land stations. The stations are sorted by latitude with the northernmost station plotted at the top. See Figure A.1 for station names.

mic network consisting of OBS and land stations in the same area for six month during 2008. The network consisted of 27 land stations (19 broadband and 8 short period stations) and 15 ocean-bottom seismometers. In addition, eleven permanent stations from the Chilean Seismological Service were included into the data set. P and S phase arrivals as well as amplitudes were picked manually by Ivonne Aden-Arroyo and Helene Kraft at GEOMAR. Both data sets provide a great opportunity to compare seismicity and stress distributions and study the evolution of a subduction zone within the seismic cycle of a megathrust event.

1.4. Automatic determination of seismic phase arrivals

Because *Lange et al.* (2012a) automatically determined phase arrivals for over 20,000 aftershock events of the Maule event from 15 March to 30 September 2010, it was worth considering to detect the seismic phase arrivals from the combined OBS and land station network with an automatic picker as well. With increasing computer processing capabilities, several automatic picking routines have been developed over the last decades. Automatic picking engines have the advantage that they are faster and generally more consistent than human analysts because a computer does not get tired or bored. There are several established P phase picking algorithms, for example those from *Allen* (1978, 1982) and *Baer and Kradolfer* (1987), or picking based on higher order statistics (*Küperkoch et al.*, 2010) or the Autoregressive-Akaike-Information-Criterion-picker (AR-AIC). The New Manual of Seismological Observatory Practice, NMSNOP, (*Küperkoch et al.*, 2012) gives a good summary and estimation of applicability for those automatic picking routines. This section gives a brief summary based on the NMSOP. The Allen picker is a fast and robust algorithm that is based on a characteristic function of the seismic trace that increases abruptly when a seismic wave arrives at the receiver. It also includes a quality assessment of the picked phases. The picker of *Baer and Kradolfer* (1987) is a modification of the Allen picker and uses a different characteristic function. The algorithm is fast and robust as well but lacks a quality assessment. Higher Order Statistics exploit the fact that the statistical properties of the seismogram change abruptly with an incoming seismic wave. Based on those statistical properties a characteristic function is determined as well. Higher Order Statistics lead to high quality results but the application of the picker is difficult and needs some experience. In the AR-AIC picker, based on information theory, a time series is modelled as a autoregressive process on that the Akaike Information Criterion is applied. The processing times are longer but more powerful. There are also different picking engines that use com-

binations or expand the picking algorithms, e.g. MPX by *Aldersons* (2004) that uses the picker by *Baer and Kradolfer* (1987) including a quality assessment or a picker of *Diehl et al.* (2009) who use a combination of three algorithms in order to pick S phase arrivals including a quality measure.

However, because the majority of seismological networks, temporary and permanent, are located on land, automatic picking routines have been developed with land station data and there are sparse studies with automatically determined phase arrivals from OBSs in the literature. In a study with data collected onshore and offshore Taiwan (*Kuo-Chen et al.*, 2012) P wave onsets have been picked with an AIC picker on OBSs. However, the determined picks were controlled manually after the picking procedure and adapted where necessary and the above study does not compare the data quality of the picked onsets from OBSs and land stations. *Baillard et al.* (2014) developed a P and S phase picker based on a characteristic function derived from kurtosis and applied it to both, land stations as well as OBSs. They accomplished good results but they do not offer a comparison of qualities of OBS picks to land station picks. However, the studies show that it is possible to detect seismic phase arrivals on OBS stations despite their usually lower data quality than land station data (*Collins et al.*, 2001).

1.5. Objectives and thesis outline

With most of the local and permanent seismic networks located on land, observing seismic activity related to faulting in the submarine forearc, the outer rise, or the updip limit of the seismogenic zone is challenging as they are usually located offshore. The deployment of a local OBS network increases the resolution of such features significantly. In this study the aftershocks of the Mw 8.8 Maule from amphibious seismic networks are analysed in order to gain information about the rupture zone, stress distributions, and faulting in the forearc after a megathrust event. Another effect of the location of most of the seismic networks onshore is that automatic picking engines have been mainly applied to land station data. The analysis of aftershocks in this study is performed in an automated approach to test if an automated determination of phase arrivals and polarisation, focal mechanisms and magnitudes can be accomplished with OBS data as well.

The aims and objectives of this study are to answer the following questions:

- Is it possible to automatically detect P and S phase arrivals of the Maule aftershocks on ocean-bottom seismometers and accomplish reliable hypocentre

locations from those automatic picks? How is the quality of the determined phase arrivals compared to the automatically picked onsets from land station data? Is the quality of the automatically determined picks from the OBS data sufficient to extend the automated approach in such way that also magnitudes and focal mechanisms can be obtained automatically as well?

- Are there any hints whether active splay faulting occurred in the wake of the Maule event, and if so, what triggered or promoted the splay fault reactivation?

- How did the seismicity and magnitude distributions change after the Maule megathrust event? Did the stress field change within the seismic cycle?

Chapter 2 of this thesis discusses the choice of the automatic phase picker used in this study and its application to the data set. In **Chapter 3** the hypocentre determination and quality classification of the event locations are explained. On the base of the best classified hypocentres determined in Chapter 3 the automated picking of S phase arrivals will be discussed in **Chapter 4**. **Chapter 5** provides theoretical background of the moment magnitude and focal mechanism determination. **Chapter 6** consist of a stand alone paper that was published in Geology in September 2014 where the discovery of a seismically active splay fault in the submarine forearc and the implications are presented. In **Chapter 7** the seismicity and magnitude distributions as well as focal mechanisms and stress directions are presented. The results are discussed in **Chapter 8** and compared to the results of the data set that was deployed two years prior to the Maule event in order to detect any changes in seismicity distribution and changes in the stress field. The results of this thesis and answers to the questions raised above are summarised in **Chapter 9**.

2. Automated picking of P wave onsets

Over the last decades several methods and approaches to automatically detect phase onsets on seismic traces have been developed (see Section 1.4). However, only few picking engines include a quality and uncertainty assessment of the picked phase arrivals. Estimation of picking uncertainties are important as they will have an influence on the quality of event locations because onsets with less qualities will be weighted down in the process. In the picking engine MannekenPix (MPX) by *Aldersons* (2004) a weighting scheme is implemented; and MPX has been successfully applied to several data sets (*Di Stefano et al.*, 2006; *Valoroso et al.*, 2009; *Aldersons*, 2004; *Diehl et al.*, 2009) including central Chile (*Lange et al.*, 2012a). The latter include land stations that will be added to the OBS data set of this study. The data analysis performed by *Lange et al.* (2012a) ends on 30. September 2010, therefore, there is only a short overlap in time of ten days with this study. A reliable picking engine is important to test if OBS data is also qualified for an automated picking process to be certain that complications are caused by the data set and not the picking engine itself. Because of its successful application to several data sets and the implemented quality assessment (*Küperkoch et al.*, 2012) the P wave onsets will be determined by MannekenPix (version 1.7.9) in this work.

2.1. How MannekenPix works

This section briefly describes the main steps of MannekenPix and follows the user guides for MannekenPix by *Aldersons* (2005) and *Diehl and Kissling* (2008). A deeper mathematical background offers *Aldersons* PhD thesis (*Aldersons*, 2004). The full MPX processing sequence consists of three stages:

(1) Pre-picking → application of Wiener filter
(2) Picking → algorithm by *Baer and Kradolfer* (1987)
(3) Post-picking → delay correction and application of a weighting scheme

2.1.1. Wiener filter

The aims of the application of the Wiener filter are (a) to increase the signal-to-noise ratio to improve the detection of P wave onsets, (b) to derive thresholds for the picking algorithm, and (c) to determine waveform characteristics for the weighting scheme. Removing noise with a simple frequency filter, e.g. bandpass, would affect the signal content too much since noise and signal frequency spectra usually overlap. The Wiener operator accomplishes that only those frequencies where the signal content is low, compared to the noise content, is attenuated by comparing a time window consisting only of noise to a time window containing signal and noise. Therefore, MPX requires at first an initial pick time near the P wave onset, usually an existing manual pick or a calculated onset based on catalogue locations and a chosen velocity model. Then the signal is estimated by evaluating the noise spectral density inside the window before the initial pick and subtracting it from the signal+noise spectral density inside the window after the initial pick. To prevent overfitting and attraction to the initial pick MPX introduces safety gaps between the time windows and the initial pick (Fig. 2.1).

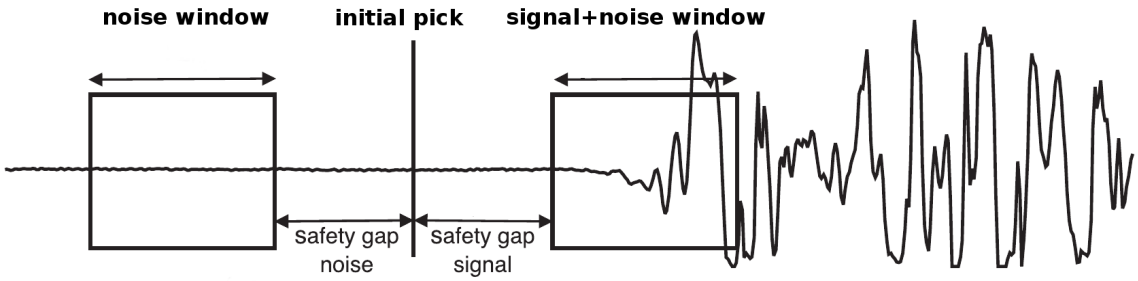

Figure 2.1.: Safety gaps and search windows for Wiener filter (modified after *Diehl and Kissling* (2008))

2.1.2. Picking algorithm

The P wave onset is determined with the picking algorithm by *Baer and Kradolfer* (1987) which is derived from a picker by *Allen* (1978, 1982). It defines an approximate squared envelope function of the seismogram of which a characteristic function (CF) is calculated. If the value of this CF increases above a certain threshold, evaluated in step (1), a picking flag is set. If the CF decreases in a certain amount of time below the threshold the flag will be removed and the algorithm continues in detecting an onset. With a manually picked reference data set the parameters for

the picking engine, and later the weighting scheme, are tested and adopted until the performance is sufficient. This is described for the Maule data set in Chapter 2.2, in detail.

2.1.3. Delay correction & weighting scheme

A deficiency of the Baer-Kradolfer algorithm is that it detects onsets up to a few samples later compared to manual picks. *Aldersons* (2004) accounted for that by applying two delay corrections based on the steepness of the characteristic function, and deviation bands from a moving average.The pick flag moves backwards for up to three samples as long as the CF decreases significantly, i.e. if the difference between the CF at one sample to the CF at the sample before is greater than 0.01. However, if the CF is not monotonically decreasing, the delay correction is insufficient.

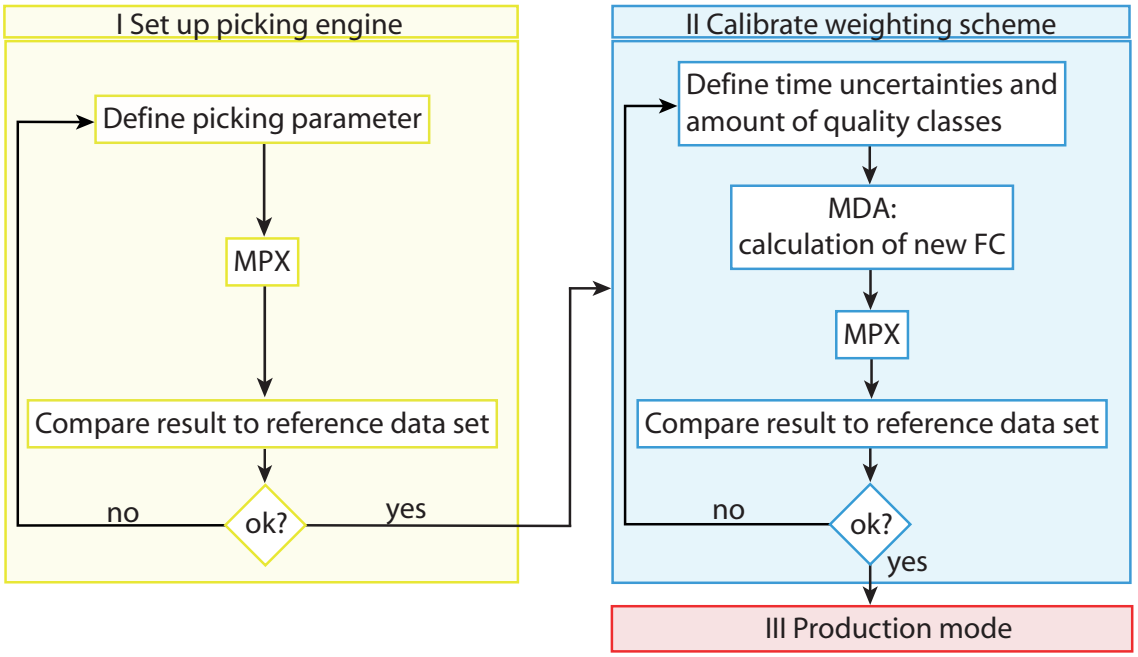

Figure 2.2.: Flow chart of MPX parameter and weighting scheme calibration (after *Diehl and Kissling* (2008))

The determined onsets will be the basis on which a localisation software determines the hypocentre locations of the events. These programs weight the onsets according to their time uncertainty, usually defined by a seismologist while manually picking the data set. Those onsets with lower qualities will be weighted down and will

have less influence on the hypocentre determination to increase the accuracy of the hypocentre locations. Therefore, it is important that the quality of an automatically picked onset will be evaluated as well. With MPX it is possible to define several quality classes through statistical tests and calibrations with a manually picked reference data set. In stage (1) of the MPX processing sequence, the Wiener filter determines nine wave form characteristics such as signal-to-noise ratios in time and frequency domain, as well as characteristics of the CF. Those wave form characteristics will serve as discriminating variables, or so called "predictors", to distinguish between quality classes. With a multiple discriminant analysis (MDA) relationships between criterion groups and predictors can be identified by weighting and linearly combining the predictors with the aim of maximizing differences of the predictors between groups while minimizing differences of them within groups (*Fischer*, 1936, 1938). The result of the MDA are weighting coefficients, called "Fisher coefficients". Because MPX cannot perform a MDA internally, fisher coefficients have to be calculated with a statistical software package, such as SPSS. After the successful calibration with the reference dataset, MPX can run in production mode. A flow chart of the MPX calibration procedure is presented in Figure 2.2.

2.2. Adaption of MPX to ocean-bottom seismometer data

The differences in data quality such as noise content and noise variability between OBS and land station data are significant due to their different deployment methods (e.g. *Collins et al.*, 2001). While land stations are usually carefully placed in a quiet area, in a hole in the subsurface to improve coupling to the ground and reduce noise, with horizontal components aligned to North and East, ocean-bottom seismometers are deployed off a ship, travel through a up to several kilometre high water column and settle somehow unaligned on the sea floor. Here, sea floor roughness, sedimentary cover, and strong currents influence data quality considerably. Therefore, the adaption of picking parameters were optimised for both OBS and land station network separately.

Before setting up of the automated picking engine, event detection was carried out with the *reftrig* STA/LTA trigger by PASSCAL (*Aster et al.*, 2005) and a coincidence criterion leading to 3024 events for the OBS network.

In order to optimise picking parameters such as window length and security gaps between time windows and initial pick as well as to calibrate the weighting scheme, a

reference data set consisting of 60 events with 2670 manually picked P phase arrivals on both hydrophone and vertical seismometer components was generated. In the user guides of *Aldersons* (2004) and *Aldersons* (2005), at least 500-1000 manually picked P phase arrivals for the reference data set are recommended.

2.2.1. Initial pick

The Wiener filter in stage (1) requires an initial pick time near the P wave onset because MPX was was originally developed to repick large data sets. Usually this is an existing manual pick, a routine pick from routine analysis of an agency, or a predicted pick based on catalogue locations and a chosen velocity model. The aim was to ensure consistency when several human analysts with usually different picking experiences were working on the same data set, or when data from several networks is merged (*Aldersons*, 2004). Since neither manual picks nor any locations exist for the data in this study, the traces of each station per event were analysed a second time with *reftrig* with adapted parameters in order to get the initial pick. Trigger parameters were optimised to obtain as many P wave onsets as possible but also as little noise, spikes, and S wave onsets as possible. The application of a bandpass filter with the corner frequencies of 2 and 10 Hz before triggering improved the hit rate of P wave onsets considerably. A bandpass with 1 and 10 Hz corner frequencies was also applied and resulted in fewer mispicks but also in less P phase detections. However, some spikes and noise etc. was triggered as well. To reduce the amount of mistriggered initial picks they are statistically analysed and outliers are removed on the basis of interquartile range (IQR). For every event the first and third quartiles ($Q_{1,3}$) of the trigger times distribution as well as the interquartile range is calculated. Outliers (O) are defined as follows (*Mittag*, 2011):

$$O \leq Q_1 - 1.5 \cdot IQR \qquad \text{and}$$
$$O \geq Q_3 + 1.5 \cdot IQR.$$

Figure 2.3 gives an example of this scheme and shows some traces with several triggered initial picks that are caused by spikes and were identified as outliers (e.g. OB17 and the vertical component of OB03). For the reference data set about 3% of all triggers were eliminated. The remaining initial picks will be processed with MPX that should be capable of discriminating between noise, spikes and phase onsets in most cases. Those picks that were recognized by MPX, but do not represent the correct onset, will be evaluated in later processes.

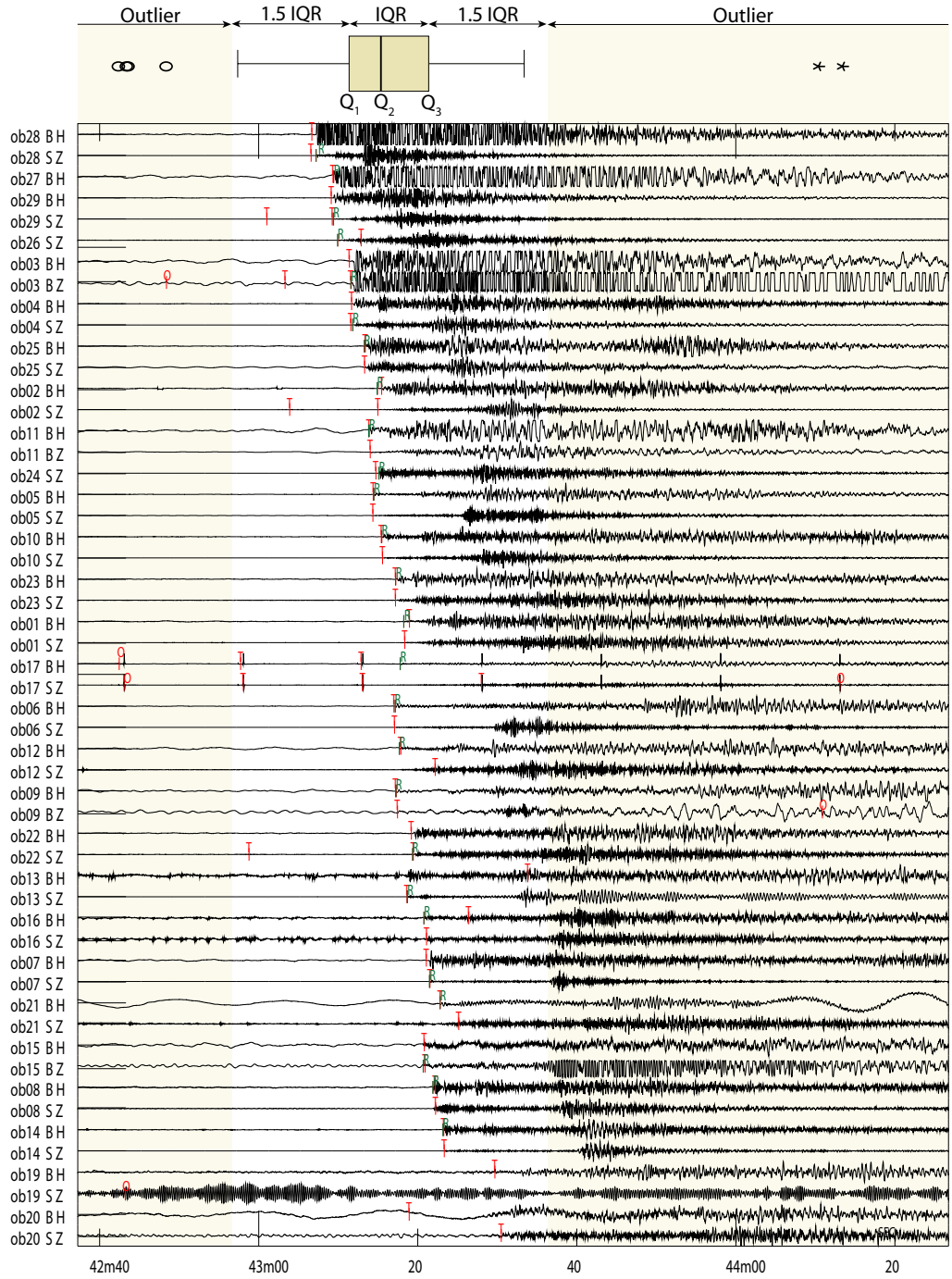

Figure 2.3.: Example of an event with initial picks (T) determined by *reftek* and the classification of outliers on the base of inter quartile range (IQR). Further abbreviations are: Q=Quartile, O=outlier, R=manual reference pick. Starting time of the traces is 10/10/2010 8:42:37.244 UTC.

2.2.2. Parameter set up

The MPX user manual (*Aldersons*, 2005) offers guide lines on how to set up the picking parameters such as window lengths and security gaps between initial pick and time windows. However, as mentioned above, ocean-bottom seismometer data show a considerably higher amount and variability of noise than land station data and MPX was only applied to land stations before. Therefore, MPX picking parameters were tested in broader ranges and combinations than the manuals suggest. The following paragraphs describe the different picking parameters MPX uses.

Window lengths

The estimation window lengths for the Wiener filter depend on the frequency content of noise and signal. And therefore dependent on epicentral distances because of the attenuation of higher frequencies over distance. The smaller the estimation windows for the Wiener filter, the better the localisation of an onset will become. Small windows may be too short to estimate the lower frequencies correctly, hence there is a trade off between localisation and reliability. The MPX user guides (*Aldersons*, 2005; *Diehl and Kissling*, 2008) recommend window lengths for local events of about 1 s for epicentral distances smaller than 150 km and about 2.0 to 2.5 s for epicentral distances between 150 and 500 km. The combined amphibious network is about 200 times 300 km wide and window lengths of 1 and 2 s are tested. The lengths of the Wiener filter itself should be twice the estimation window length and will be set to 2 s and 4 s.

Security gaps

The security gaps safely separate the noise estimation window from the signal+noise estimation window (see Fig. 2.1). Narrow gaps result in higher accuracies but if the difference between initial pick and actual onset is much larger than the gaps, MPX might not be able to detect the onset at all. On the other hand, if the gaps are too wide later phases after the onset might be detected. *Diehl and Kissling* (2008) showed a good example of this trade-off (see Fig. 2.4). MPX reduces the gap sizes iteratively if the difference between first automatic pick and initial pick is too large until a stable final value is obtained. Therefore, four security gaps with decreasing lengths have to be set in the command file (see Appendix B.1). The first and largest gap should be about the size of the largest expected error between initial pick and phase arrival. The standard deviation between initial pick and manual reference pick

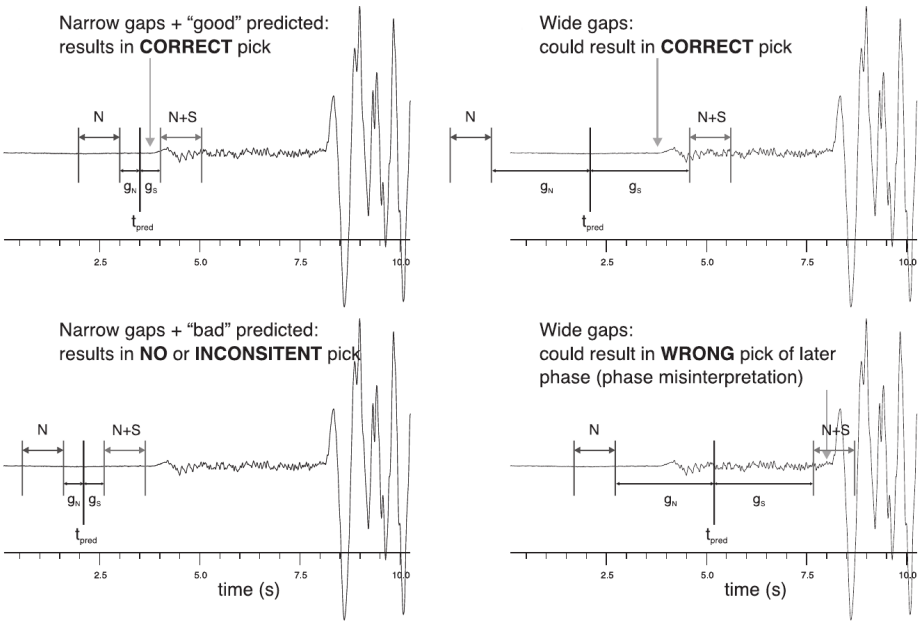

Figure 2.4.: The adjustment of the safety gaps is a trade off between hit rate and accuracy. Narrow gaps increase inaccuracy but could be too short to detect the phase arrival at all while large gaps may result in the picking of later phases (*Diehl and Kissling*, 2008).

for the OBS data set is 0.71 s with a mean difference of -0.35 s. Differences larger than 3 s were considered to be related to an incorrectly triggered initial pick and neglected in the calculations. The parameter test was carried out with the first gap set to the standard deviation of 0.7 s, the standard deviation + mean $\approx$ 1 s as well as values randomly set larger and smaller, ranging from 0.55 s to 2.5 s. The second gap can be set as half the value of the first gap whereas the third and fourth gaps depend on the frequency content with small windows for higher frequencies. Again, the setting of this gap is a compromise between frequency content and accuracy. The user guide suggests about 40 to 80 ms for the last gap and about 60 to 120 ms for the third. Generally, the first and last gaps are set and the second and third are equally distributed in between. To generate different sets of parameters several approaches were applied which are shown in Table 2.1

Frequency threshold

The lower threshold for the maximum of the signal amplitude spectrum constrains the lowest frequency included in the calculation of the signal to noise ratio. It is recommended to be about half the lowest frequency expected for the first arrivals,

Table 2.1.: Different approaches to define security gaps between initial pick and Wiener filter estimation windows.

	Gap 1 (a)	**Gap 2 (b)**	**Gap 3 (c)**	**Gap 4 (d)**
(1)	fixed	a/2	← equal distribution (b) to (d)→	fixed
(2)	fixed	←— equal distribution (a) to (d)—→		fixed
(3)	fixed	a/2	b/2	c/2

which is about 1 Hz for the OBS data set. Thus, the best value for the threshold is expected to be about 0.5 Hz. For the parameter test this parameter ranges from 0.5 to 1.5 Hz.

Results

This leads to 93 different parameter sets (Table B.1). Standard deviation and mean of the difference between manual reference pick, and the amount of picked phase onsets were determined for each set of parameters. As the aim is to determine the parameter set with the least deviation between automatic pick to reference pick, absolute differences are calculated as well. This distribution is highly asymmetric, as can be seen by comparing median and mean. For parameter 1, for example, the mean of the absolute deviation is 0.1158 s while the median is 0.04 s. In a symmetric distribution both values would be about the same. In asymmetric distributions the mean would be strongly influenced by high and for the distribution atypical values (*Mittag*, 2011). Therefore, quartiles are the better statistical parameters. To better compare the deviation distributions of the 93 parameters they were displayed as box plots that combine five characteristics of a distribution: minimum, maximum, first and third quartiles, and median (second quartile). Again, only those automatic picks were taken into account for the calculations that show a maximum deviation between reference and initial pick of 3 s. This is to ensure that only automatically picked phase onsets and no spikes or other noise will have an influence on the analysis. Mispicked onsets will be evaluated in a later step. Parameter sets 2, 5, 17, 18, 91, 92 and 93 show the best box plots (see appendix Fig. B.3) because their quartiles and maxima show the lowest values with 0.1 s for the third quartile, 0.01 s for the first quartile and 0.21 s for the maximum. All other parameter sets have at least one statistical parameter with a higher value. The median for all parameters is 0.04 s. To finaly decide which parameter is best for production mode, hit rates and standard deviations are considered in addition. Of the remaining seven parameter sets, number 93 shows the highest hit rate with about 2128 automatically picked phase arrivals of 2670 manually picked P wave onsets which results in a hit rate of about

80% (Table B.2). The standard deviations for the remaining seven parameter sets lie very close together with values between 0.21 s and 0.24 s. Parameter set 17 shows the best standard deviation but also the lowest hit rate with 74 %. As parameter set 93 shows the highest hit rate and the difference to the best standard deviation is only 0.02 s, it is considered to be the best and will be applied in production mode. The final picking parameters are:

Security gaps:	0.7 s / 0.35 s / 0.18 s / 0.09 s
Estimation window lengths:	2 s
Wiener filter lengths:	4 s
Frequency threshold:	0.5 s

The parameter setting for the OBS data set behaves almost according to the manual. Frequency threshold, window lengths and security gaps are set in the ranges as suggested. But as the distribution of the second to fourth gaps followed scheme (3), the fourth gap ended up at a slightly higher value than suggested.

2.2.3. Calibration of weighting scheme

To calibrate the weighting scheme to the quality classes of a manually picked reference data set, the predictors determined by the Wiener filter in stage (1) (see Section 2.1.1) are connected with the manually set quality classes via a MDA. In order to train the weighting scheme correctly it is necessary to take only those automatic picks into account that actually hit the correct phase arrival. The maximum difference between automatic and initial pick for the OBS data set is 0.84 s. This means, that if the difference between initial and reference pick is larger than this difference, MPX is not able to determine the correct phase onset but will pick whatever triggered the initial pick. This can clearly be seen in Figure 2.5 where the absolute deviations of the automatic to the manual reference picks are plotted over the absolute deviation of initial to reference pick. A linear dependency with a gradient of 1 is obvious. The cut-out shows that for differences between initial to reference pick below about 0.8 s most of the differences between the corresponding automatic pick to reference pick lie below the gradient and the correct phase arrival could be detected. Thus, only picks where the difference between automatic and reference pick was smaller than 0.8 s were considered in the calibration of the weighting scheme in order to avoid biasing the calibration.The manually picked reference data set consisted of 44 events and 1220 P wave onsets with quality classes ranging from 0 to 2 with 0 being the best class. In order to calibrate the weighting scheme to group picked noise, spikes etc into a class consisting of lowest quality picks, automatic picks on traces with no reference pick were set to class 3 in the reference data set. Unfortunately, this

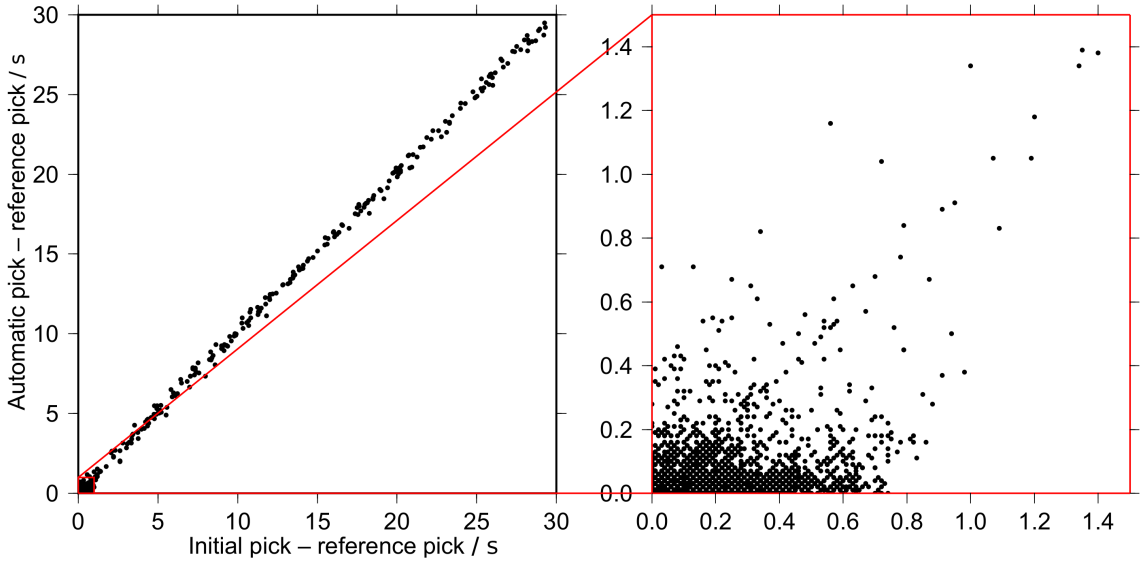

Figure 2.5.: Difference between automatic pick and manual reference pick over difference of initial pick to reference pick to determine automatic picks suitable for calibrating the weighting machine. The cut-out (right) shows that below a distance of about 0.8 s between initial and reference pick, MPX was able to detect correct phase arrivals. If the initial pick was set more than about 0.8 s from the reference pick, MPX detected whatever caused the trigger algorithm to set a flag. Therefore, only those automatic picks where the difference of initial to reference pick was below 0.8 s were considered in the weighting scheme.

did not work properly and automatic picks on a traces without reference picks were visually evaluated and deleted or set to class 3 if it was in the vicinity of a phase arrival. The reason probably is that the range of predictors for spikes, noise and low quality picks are too wide for the MDA to differentiate properly between the classes.

In order to take the absolute picking error ε_{pick} between automatic and reference pick into account, different classification targets *"TrueWeight"* for the MDA instead of the reference weights are defined (*Di Stefano et al.*, 2006; *Diehl et al.*, 2009). They are based on reference weights W_{ref} and absolute picking error boundaries ε_{1-3}:

(1) *"TrueWeight1"*: Based only on picking error boundaries ε_{1-3}.
(2) *"TrueWeight2"*: Based on reference weights W_{ref}, if ε_{pick} is inside error boundaries. Otherwise: $TrueWeight2 = W_{ref} + 1$.
(3) *"TrueWeight3"*: Best class of *TrueWeight1*. Otherwise: $TrueWeight3 = TrueWeight2 + 1$.

TrueWeight2 is recommended by *Diehl and Kissling* (2008) and will be used to find the ideal weighting scheme. The MDA was performed with IBM's statistics package SPSS according to the manual of *Diehl and Kissling* (2008). With the resulting Fisher coefficients another MPX run was carried out to compare manual reference weights to automatic weights in a classification matrix (cross tabulation). If the weighting configuration is not able to resolve the classes properly merging unresolved classes or different error boundaries may be tested. Lower quality classes should not be upgraded to the highest class and picking errors ε_{pick} should fall into the picking error boundaries of the corresponding classes. A variety of error boundaries and amounts of classes were tested. Some examples are shown in Table 2.2. The best solutions were achieved with schemes R and U (see cross tabulations in Figures 2.6 and 2.7), because they show the least amount of upgraded qualities and the picking errors fall well inside the picking error boundaries (see Table 2.2). Because the upgrading of qualities is more critical than the downgrading and correct classification scheme, O2 was considered to be less suitable although more qualities were assigned correctly than in scheme R and U. Here, the higher amount of correctly assigned picks are due to less downgraded picks but higher upgraded picks at the same time. According to *Diehl et al.* (2009) moderate upgrading of classes is tolerable but upgrading of very low to very high quality classes (i. e. from 3 to 0) should be completely avoided for tomographic studies because the resolution of velocity perturbations is strongly dependent on the quality and consistency of phase arrivals. However, for hypocentre determination the upgrading of about 1 % of the picks from very low to very high quality classes is less critical. In order to decide

Table 2.2.: Tested weighting schemes with picking error boundaries ε (see *"TrueWeights"* on page 26), amount of quality classes and upgraded, downgraded and correctly classified qualities. Cl. = amount of Classes; A: Picking error within the boundaries, where o = inside the boundaries and X = outside the boundaries.

Scheme	ε_1 **s**	ε_2 **s**	ε_3 **s**	**Cl.**	**Correct** %	**Downgraded** %	**Upgraded** %	**A**
O	0.05	0.15	–	3	61.8	23.4	14.8	X
O1	0.05	0.13	–	3	61.4	23.2	15.3	X
O2	0.06	0.12	–	3	62.1	23.6	14.3	o
P	0.05	0.1	0.15	4	53.6	30.0	16.5	X
P1	0.05	0.07	0.15	4	53.4	30.1	16.6	X
R	0.06	0.12	0.18	4	57.1	30.4	12.5	o
U	0.07	0.12	0.25	4	58.5	29.8	12.0	o

what calibration scheme will give the best results, i. e. the least hypocentre deviations, the events of the reference data set inside the network were located with *HYPOCENTER 3.2* (*Lienert and Havskov*, 1995) and a 1D velocity model for this area (*Arroyo et al.*, 2010) and compared to the hypocentres determined from automatic picks. Absolute differences of latitude, longitude, depth and total deviation between reference and automatic data sets were calculated and plotted as box plots (Fig. 2.8 and Fig. B.9). Figure B.9 shows the absolute total location errors of all tested schemes. Schemes O, O1, P and P1 are plotted only for comparison but are no candidates for final weighting schemes because their picking errors do not match the picking error boundaries. Compared to R and U, considered to be the most suitable schemes, the box plots do not differ very much. P and P1 give the best results for all located events (see Fig. B.9a) while for those events located by all of the schemes, P1 give the result with the highest error (see Fig. B.9b). O2 does match the boundaries but as it shows the highest error for all located events (Fig. B.9a) and with 26 located events with gaps smaller than 180 °one event less than R and U (see Table B.3), R and U turn out to be the best schemes again. Figure 2.8 shows the absolute differences of latitude, longitude, depth and total deviation between for schemes U and R. The 75th percentiles for both schemes are in the range of 2.3 - 5 km for deviations in longitude, latitude and depth (see Table 2.3). The median was even below 1 km deviation what is a very good result. Scheme R gave the best results in all categories and was chosen to be applied in the production mode. The final MPX command file is presented in Appendix B.1.

			MPX				
			0	1	2	3	Total
TW2	0	Count	464	148	37	35	684
		% within TW2	67,8%	21,6%	5,4%	5,1%	100,0%
		% of Total	38,0%	12,1%	3,0%	2,9%	56,1%
	1	Count	57	121	59	56	293
		% within TW2	19,5%	41,3%	20,1%	19,1%	100,0%
		% of Total	4,7%	9,9%	4,8%	4,6%	24,0%
	2	Count	12	25	45	36	118
		% within TW2	10,2%	21,2%	38,1%	30,5%	100,0%
		% of Total	1,0%	2,0%	3,7%	3,0%	9,7%
	3	Count	16	29	13	67	125
		% within TW2	12,8%	23,2%	10,4%	53,6%	100,0%
		% of Total	1,3%	2,4%	1,1%	5,5%	10,2%
Total		Count	549	323	154	194	1220
		% within TW2	45,0%	26,5%	12,6%	15,9%	100,0%
		% of Total	45,0%	26,5%	12,6%	15,9%	100,0%

(a) Cross tabulation of MPX weights and *TrueWeight2*

MPX	Mean / s	Std. Deviation / s
0	-.0259	.05536
1	-.0171	.10016
2	-.0812	.10863
3	.0039	.20385

(b) Standard deviations

Figure 2.6.: Weighting scheme R: (a) Cross tabulation of automatically assigned MPX weights and *TrueWeight2*. Ideally, the entries on the diagonal would be 100 %. Grey: upgraded qualities, blue: downgraded qualities. (b) Standard deviations between automatically and manually picked phases within every MPX assigned weight. The standard deviations should fall within the error boundaries (see Table 2.2). In this case, the standard deviations lie inside the boundaries.

Table 2.3.: Absolute differences (ABS) of latitude, longitude, depth and total deviation in km between reference and automatic data sets. The reference data set consisted of 33 events inside the network.

Weighting scheme			ABS_Lat / km	ABS_Long / km	ABS_Depth / km	ABS_total / km
R	Events		27	27	27	27
	Percentiles	25	,1776	,4017	,0000	1,1634
		50	,3552	,7478	,6250	2,3815
		75	2,2755	4,8885	3,0859	10,9408
U	Events		27	27	27	27
	Percentiles	25	,1776	,4150	,0391	1,3952
		50	,6993	,9223	,8984	3,6475
		75	2,4531	4,8885	3,5547	10,7341

			MPX				Total
			0	1	2	3	
TW2	0	Count	496	158	35	29	718
		% within TW2	69,1%	22,0%	4,9%	4,0%	100,0%
		% of Total	40,7%	13,0%	2,9%	2,4%	58,9%
	1	Count	42	123	48	46	259
		% within TW2	16,2%	47,5%	18,5%	17,8%	100,0%
		% of Total	3,4%	10,1%	3,9%	3,8%	21,2%
	2	Count	18	47	46	46	157
		% within TW2	11,5%	29,9%	29,3%	29,3%	100,0%
		% of Total	1,5%	3,9%	3,8%	3,8%	12,9%
	3	Count	8	22	9	47	86
		% within TW2	9,3%	25,6%	10,5%	54,7%	100,0%
		% of Total	,7%	1,8%	,7%	3,9%	7,0%
Total		Count	564	350	138	168	1220
		% within TW2	46,2%	28,7%	11,3%	13,8%	100,0%
		% of Total	46,2%	28,7%	11,3%	13,8%	100,0%

(a) Cross tabulation of MPX weights and *TrueWeight2*

MPX	Mean / s	Std. Deviation / s
0	-,0269	,05463
1	-,0177	,10574
2	-,0759	,11855
3	,0019	,21151

(b) Standard deviations

Figure 2.7.: Weighting scheme U: (a) Cross tabulation of automatically assigned MPX weights and *TrueWeight2*. Ideally, the entries on the diagonal would be 100 %. Grey: upgraded qualities, blue: downgraded qualities. (b) Standard deviations between automatically and manually picked phases within every MPX assigned weight. The standard deviations should fall within the error boundaries (see Table 2.2). In this case, the standard deviations lie inside the boundaries.

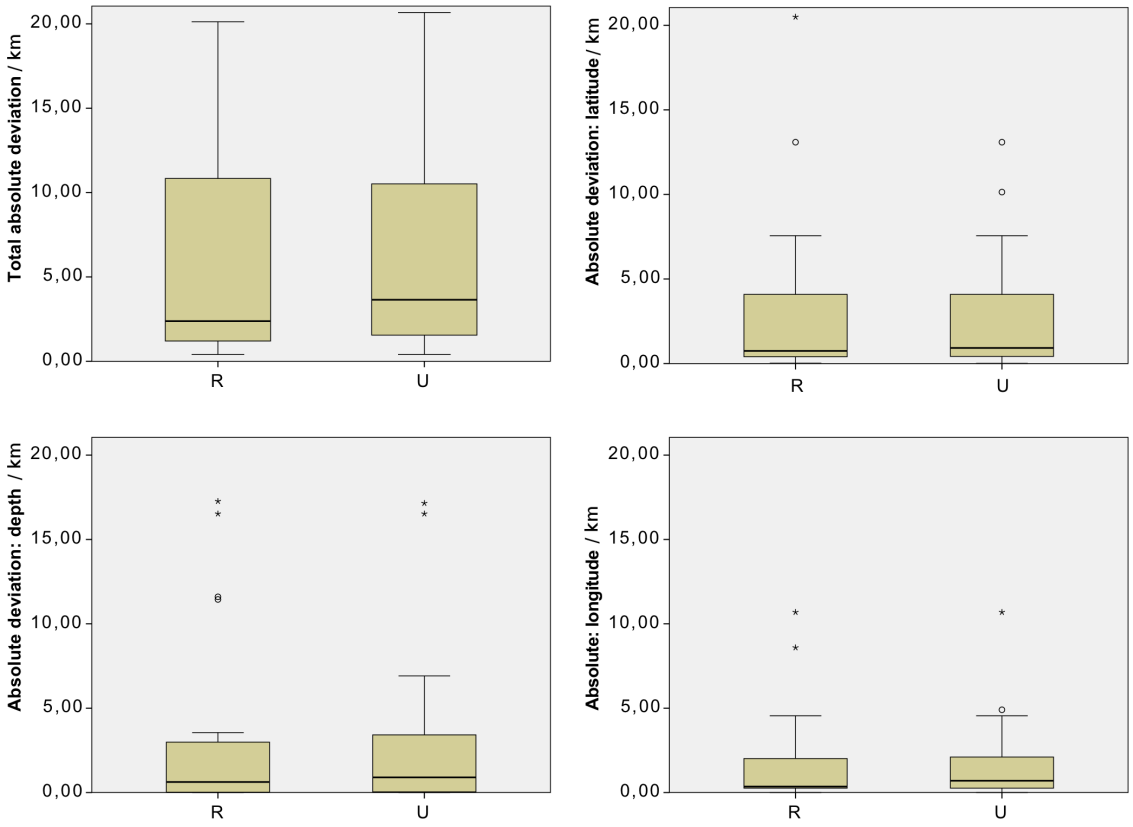

Figure 2.8.: Box plots showing absolute differences of latitude, longitude, depth and total deviation between reference and automatic data sets. In order to scale the y-axis to the same value some outliers were cut off.

2.2.4. Preparation for localisation

The automatic picks were set on both the vertical component of the seismometer as well as the hydrophone. In cases where the phase arrival was detected on each trace, the one with the best weight was selected. If weights on both traces were equal, the vertical component of the seismometer was selected. Multiple picked onsets on a single trace have been evaluated before event location as follows: the event is located with a 1D model of *Arroyo et al.* (2010) in *HYPOCENTER 3.2* (*Lienert and Havskov*, 1995) which calculates the residual for every onset. The one with the least residual is considered to be the correct pick. Stations where only a single pick was made but did not detect the correct onset will be automatically weighted down in the final event location (see Chapter 3). In this process about 400 events could not be determined by HYPOCENTER. After manually evaluating about 200 of those events only one showed good data quality while the remaining were mainly mispicks, spikes or very noisy onsets. Therefore, further investigations of those events were not considered.

Because OB17 and the vertical component of OB03 were disturbed by spikes every few second, almost over the whole deployment time, they were neglected for the hypocentre determination procedure.

2.3. Adaption of MPX to land station data

The set up of picking parameters and weighting scheme to the land station data set was principally carried out the same way as for the OBS data set. The traces were analysed with the STA/LTA trigger to determine an initial pick. Other than with the OBS data a Bessel filter with one pole gave better results than a bandpass filter. However, the corner frequency remained the same, i.e. 2 and 10 Hz. Again, every pick with a larger difference than 3 s between initial and manual reference pick was considered to be a mispick and was not used in the parameter set up.

2.3.1. Parameter set up

The reference data set for the land station data consisted of 939 manual reference picks. The value for the first security gap was defined by the standard deviation of the differences between reference to initial pick, in this case 0.4 s and the same scheme as for the OBSs was applied to find the remaining three security gaps (Tab. 2.1).

All gaps lay inside the suggested values of the guide books (see *Aldersons* (2005); *Diehl and Kissling* (2008) and Section 2.2.2). Wiener filter lengths were kept the same as for the OBS data as they are mainly dependent on the epicentral distance from events to station, which is basically the same for both data sets. Frequency thresholds were tested in a range between 0.5 and 2.5 Hz. In order to test and compare if greater gaps would improve the results, the land station data set was also processed with the OBS parameters with a frequency threshold of 1 and 2.5 Hz. In total, 7 different parameter sets were tested (see Table 2.4). The absolute difference

Table 2.4.: Picking parameter sets tested for the P wave picking on the land station data.

Parameter	**Estimation windows**	**Wiener filter**	**Gaps**				**Threshold**
	s	**s**	**s**				**Hz**
1	2.0	4.0	0.4	0.20	0.10	0.05	0.5
2	2.0	4.0	0.4	0.20	0.10	0.05	1.0
3	2.0	4.0	0.4	0.20	0.10	0.05	1.5
4	2.0	4.0	0.4	0.20	0.10	0.05	2.0
5	2.0	4.0	0.4	0.20	0.10	0.05	2.5
6	2.0	4.0	0.7	0.35	0.18	0.09	1.0
7	2.0	4.0	0.7	0.35	0.18	0.09	2.5

between reference and automatic pick was calculated and displayed as box plots (Fig. 2.9). Parameters 1 to 5 almost show the same results, while parameters 6 and 7 show higher deviations. That was expected since those are the OBS parameters. The median for both parameter sets 4 and 5 are, with 0.025 s, slightly lower than for parameters 1 to 3 (0.0275 s) and the 75th percentile for parameter 5 is the lowest with 0.0775 s of the first five parameters. The 25th percentile is 0.01 s for parameter sets 1-5. However, the differences may scatter less for parameters 4 and 5 but they also show a lower hit rate (see Table 2.5). Therefore, parameters 1 to 3 are considered to be the most suitable for picking the onsets. As they all show the same results regarding hit rate, percentiles and standard deviations, it makes no difference which one will be applied and parameter 2 was chosen.

2.3.2. Calibration of weighting scheme

In order to evaluate only those automatic picks that refer to an actual phase onset, the maximum distance between initial and automatic pick where MPX is able to

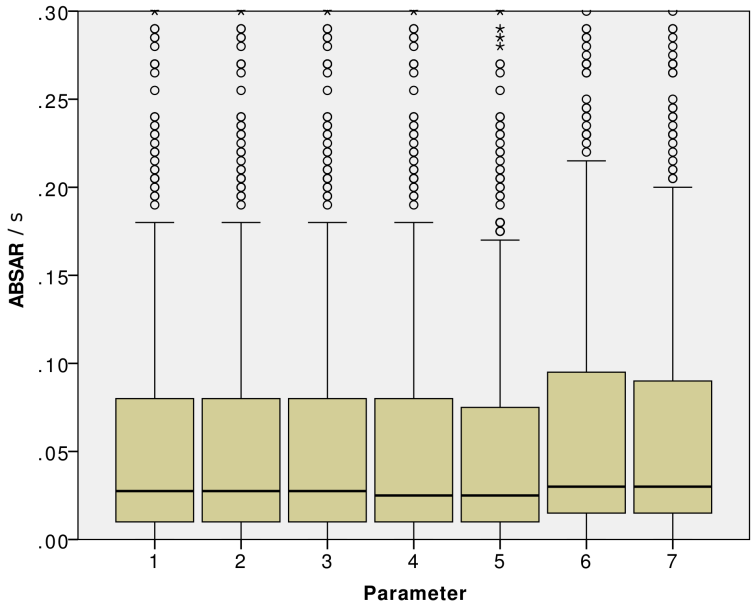

Figure 2.9.: Box plots showing the scattering of absolute difference between manual reference picks and automatic picks (ABSAR). Outliers were calculated as described in Chapter 2.2.1, and plotted as small circles.

Table 2.5.: Statistical parameters of the difference between reference and automatic picks sorted by standard deviation. N = Amount of automatically picked phases.

Parameter	Mean	Standard deviation	Picked phases	
	s	s	N	%
1	-0,0003	0,1864	754	80
2	-0,0003	0,1864	754	80
3	-0,0003	0,1864	754	80
4	-0,0002	0,1866	752	80
5	-0,0003	0,1869	745	79
7	0,0036	0,2049	784	83
6	0,0015	0,2052	797	85

detect a phase onset was determined. For distances larger than 0.4 s, between the automatically determined pick by MPX and the initial pick, MPX is not able to detect the correct phase arrivals but will pick whatever caused the trigger to set a flag (Fig. 2.10). Thus, all automatic picks with differences between initial pick and

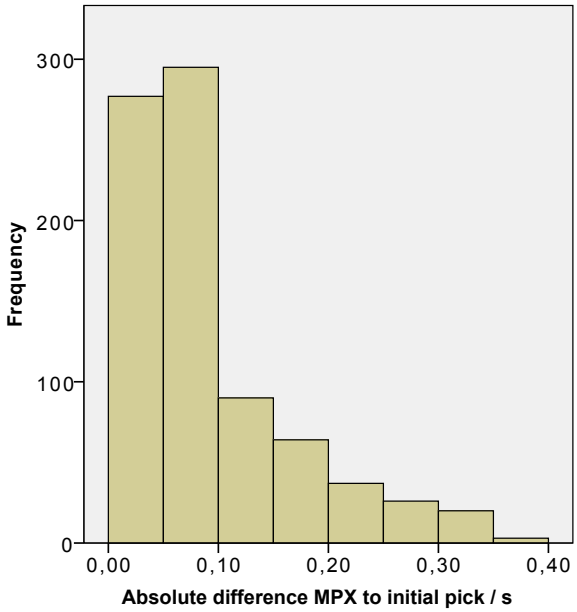

Figure 2.10.: Histogram of absolute differences between automatic pick and initial pick. For distances bigger than 0.4 s between initial to reference pick MPX is not able to detect correct phase arrivals.

corresponding reference pick larger than 0.4 s were not considered in the weighting scheme. The reference data set for the calibration consists of 777 manual picks with quality classes between 0 and 2, with 0 being the best class. For the weighting schemes the same as for the OBS were tested and cross tabulations were calculated to compare manual weights to automatic weights (see Fig. 2.11 and Figs. B.10 – B.15). Schemes R, O and O1 show the lowest amount of upgraded qualities and their picking errors fall well inside the defined picking error boundaries (see Table 2.6). Again, events of a reference data set consisting of 36 events inside the network were located with manually as well as automatically determined picks, and absolute deviations in latitude, longitude, depths as well as total deviations were calculated and plotted as box plots (Fig. 2.12 and B.16). With all schemes all reference events could be located. Scheme R was found to be most suitable to be used in the production mode for the OBS data set. Because it shows the lowest amount of scattering of the absolute total deviations, latitude and depth values (Figs.2.12, B.16a and B.16c) it will be applied to the production mode for the land station data set too. It also is an advantage to use the same picking error boundaries for both data sets, OBS and land stations, because then they can be easily implemented in the event

			MPX				Total
			0	1	2	3	
TW2	0	Count	263	77	28	14	382
		% within TW2	68,8%	20,2%	7,3%	3,7%	100,0%
		% of Total	33,8%	9,9%	3,6%	1,8%	49,2%
	1	Count	24	100	43	44	211
		% within TW2	11,4%	47,4%	20,4%	20,9%	100,0%
		% of Total	3,1%	12,9%	5,5%	5,7%	27,2%
	2	Count	9	24	35	28	96
		% within TW2	9,4%	25,0%	36,5%	29,2%	100,0%
		% of Total	1,2%	3,1%	4,5%	3,6%	12,4%
	3	Count	10	20	19	39	88
		% within TW2	11,4%	22,7%	21,6%	44,3%	100,0%
		% of Total	1,3%	2,6%	2,4%	5,0%	11,3%
Total		Count	306	221	125	125	777
		% within TW2	39,4%	28,4%	16,1%	16,1%	100,0%
		% of Total	39,4%	28,4%	16,1%	16,1%	100,0%

(a) Cross tabulation of MPX weights and *TrueWeight2*

MPX	Mean / s	Std. Deviation / s
0	-,0278	,02893
1	-,0105	,08767
2	-,0128	,11927
3	,0857	,12663

(b) Standard deviations

Figure 2.11.: Weighting scheme P1: (a) Cross tabulation of automatically assigned MPX weights and *TrueWeight2*. Ideally, the entries on the diagonal would be 100 %. (b) Standard deviations between automatically and manually picked phases within every MPX assigned weight. The standard deviations should fall within the error boundaries (see Table 2.6). In this case, the standard deviations lie inside the boundaries.

Table 2.6.: Tested weighting schemes with picking error boundaries (ε), amount of quality classes and upgraded, downgraded and correctly classified qualities. Cl. = Classes; A: Picking error within the boundaries, with o: inside the boundaries, and X: outside the boundaries.

Scheme	ε_1 **s**	ε_2 **s**	ε_3 **s**	**Cl.**	**Correct %**	**Downgraded %**	**Upgraded %**	**A**
O	0.05	0.15	–	3	63.7	23.8	12.5	o
O1	0.05	0.13	–	3	63.7	23.3	13.0	o
O2	0.06	0.12	–	3	63.1	22.7	14.3	o
P	0.05	0.1	0.15	4	55.1	29.5	15.4	o
P1	0.05	0.07	0.15	4	53.5	29.1	17.5	X
R	0.06	0.12	0.18	4	56.2	30.1	13.7	o
U	0.07	0.12	0.25	4	55.1	26.5	18.3	o

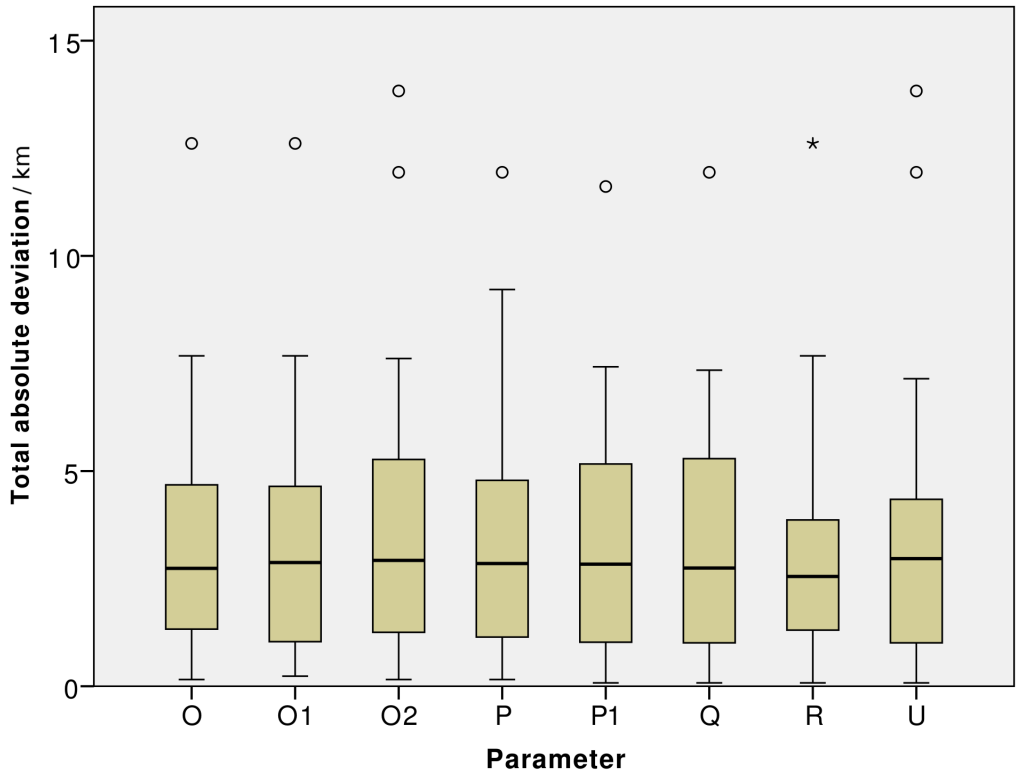

Figure 2.12.: Box plots showing absolute total deviation between reference and automatic data sets.

location procedure. Absolute differences between locations showed 75th percentiles with values in the range of about 0.5 - 2 km in all three directions. These results are better than those of the OBS data set (Tab. 2.7), what was expected because land station data are generally less noisy and, therefore, show higher qualities.

2.3.3. Preparation for localisation

The generation of input data for the localisation software was simpler for the land station data than for the OBS data because the land stations only had one vertical component and no best picks on seismometer and hydrophone traces had to be selected. However, multiple picked onsets on a single seismogram occur here as well and are evaluated in the same way as for the OBS. The event is located in HYPOCENTER 3.2 (*Lienert and Havskov*, 1995) with a 1D model determined in a local earthquake study between 34°S and 36°S for the onshore domain (*Kraft*, 2011; *Dannowski et al.*, 2013) and the pick with the least residual is considered to be the

Table 2.7.: Deviations between manually and automatically picked data sets for OBS and land station (LS) data sets.

Percentiles	**Picking time**	**Hypocenter location**		
		Latitude	**Longitude**	**Depth**
%	**s**	**km**	**km**	**km**
OBS				
25	0.01	0.18	0.40	0.00
50	0.04	0.36	0.75	0.63
75	0.09	2.28	4.89	3.09
LS				
25	0.01	0.00	0.28	0.58
50	0.03	0.42	0.69	1.29
75	0.08	0.85	1.51	2.03

correct phase arrival. Land station data and OBS data were then merged into a single file.

2.4. Event detection for the combined amphibian data set

Because the main idea was to attempt the application of an automatic picker to an OBS data set, the focus lay, in the beginning, on the OBS network and the land station data was merged in at a later stage. Therefore, event detection was only applied to the OBS network at first. In order to trigger events inside the land station network as well as the coastal area, the event detection with the STA/LTA trigger and a coincidence criterion was extended onto the whole amphibious network with both, OBS and land stations. About 1500 local events could be added to the data base. In total, 4592 potential events are located with 83,610 picked P wave onsets (46,397 on OBS and 37,213 on land stations) in Chapter 3.

3. Hypocentre determination

The event localisation was performed by NonLinLoc (NLL) (*Lomax et al.*, 2000), a probabilistic, global-search earthquake location software that is based on the probabilistic formulation of nonlinear inverse problems by *Tarantola and Valette* (1982). NLL calculates travel-times between each station and all nodes of a x,y,z-spacial grid. Afterwards, an estimate of the posterior probability density function (PDF) is constructed that gives a measure of how good any hypocentre solution within the grid explains the observed data, i.e. phase onsets. There are two choices of likelihood functions in NLL to build the PDF, one of them is the equal-differential-time (EDT) formulation that is very robust to outliers. The likelihood function is given by Equation 3.1

$$L(x) = \left[\sum_{a,b} \frac{1}{\sqrt{\sigma_a^2 + \sigma_b^2}} \cdot \exp\left(- \frac{\left(\left(T_a^{obs} - T_b^{obs} \right) - \left(T_a^{calc} - T_b^{calc} \right) \right)^2}{\sigma_a^2 + \sigma_b^2} \right) \right]^N , \quad (3.1)$$

where x is the x,y,z coordinate in the grid, $T_{a,b}^{obs}$ are the observed arrival times and $T_{a,b}^{calc}$ are the calculated travel times for two observations, N is the total number of observations, and $\sigma_{a,b}$ are standard deviations which summarize assigned uncertainties (*Lomax et al.*, 2009). In the two brackets in the exponent the differences between arrival and travel times of two observations are determined and subtracted from each other. Thus, the exponential has a maximum value 1 at point x, where the two differences are equal. Other than a PDF calculated with the more common L2-norm (see Eq. 3.2),

$$L(x) = \exp\left(-\frac{1}{2} \sum_i \frac{\left(T_i^{obs} - T_i^{calc}(x) \right)^2}{\sigma_i^2} \right) \quad (3.2)$$

the summation over observations takes place outside the exponent and the EDT PDF is largest for those points x where most pairs of observations are satisfied. Thus, it is much more robust to outliers than L2 norms where all of the observations are tried to be satisfied simultaneously. This is important since the location procedure is supposed to eliminate the remaining mispicks. In addition, for the EDT likelihood function no origin time calculation is required and the hypocentre search is reduced to a 3-parameter problem which contributes to the robustness of

the EDT method (*Lomax et al.*, 2009). However, an origin time corresponding to the maximum likelihood hypocentre can be calculated.

To obtain the maximum likelihood hypocentre (i.e. maximum of the PDF) the PDF has to be evaluated with a global-sampling algorithm. In NLL one can chose between three different methods. Here, the Oct-tree importance sampling algorithm is used as it converges rapidly and robustly and also produces stable results for PDFs with a complex topography as may be the case in the presence of outlier data (*Lomax et al.*, 2009). The Oct-tree method subdivides the 3D-grid into a coarse grid of cells and calculates the probabilities for each cell that the hypocentre is located within it. The probabilities are ordered and listed and the cell with the highest probability is divided into 8 smaller cells for which the hypocentre location probabilities are calculated again. The values of the sampled cells are added to the list and the cell with the highest probability is subdivided again. This is repeated until a termination criterion is reached, for example a predefined number of iterations. This process leads to a high density of cells in areas with high probabilities (low misfit) and the PDF is approximately sampled (Fig. 3.1).

3.1. 1D vs. 2.5D velocity model

Besides the robustness towards outlier data another advantage of NLL is that it is capable of processing 3D velocity models. For the Maule aftershock data set 1D velocity models provided either good results for the onshore or the offshore domain but only poor results for the whole survey area because the velocity models for both domains differ substantially. Figure 3.2a shows the events located with a 1D P wave velocity model from an OBS and land station data study from 2008 in the Maule area (for velocities see Table C.1). It is clear that the model does not fit the offshore domain well. Outer rise events scatter a lot in depth and slab seismicity in the coastal region does not match the plate boundary very well and appears to be too deep. In addition, the layer boundaries in 45 km and 60 km depth produce artefacts almost over the length of the entire profile.

As a consequence, a 2.5-D model was generated. Results from a seismic refraction and wide-angle profile crossing the network by *Moscoso et al.* (2011) (Fig. 3.3) defined the offshore domain and coastal region while constraints from a local earthquake study between 34°S and 36°S (*Kraft*, 2011; *Dannowski et al.*, 2013) defined the domain onshore. The upper part of the subducting slab, until about 20 km depth, was constrained by the results of the seismic refraction and wide-angle profile. Due to decreasing depth resolution of the refraction seismic data below 20 km depth the

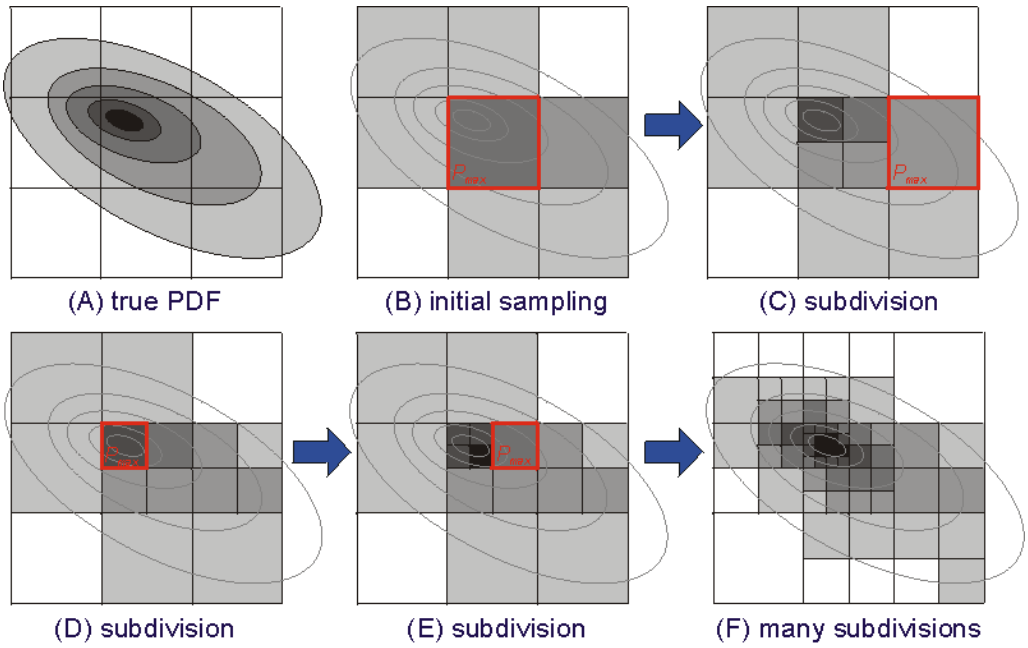

(a) The true PDF (A) is subdivided into several cells and the probabilities in the centre of the cells is calculated. The cell with the highest probability P_{max} (red square in (B)) is subdivided into smaller cells and the probabilities are evaluated again ((C)–(E)). After the termination criterion is reached the structure will have a higher number of cells in areas with higher values of the PDF (F).

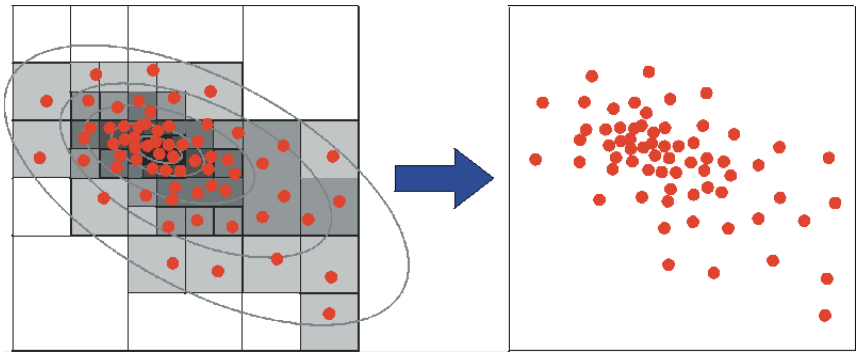

(b) Approximation of the PDF. The red dots mark the sampled cells in 3D projected onto a 2D plane. Where the probability is highest, the cloud of red dots is more dense.

Figure 3.1.: Principle of the Oct-tree importance sampling algorithm. Figure (a) shows the iteration process leading to a high density of cells in areas with high probabilities (low misfit). Figure (b) illustrates how the PDF is finally sampled in 3D. By Anthony Lomax (http://alomax.free.fr/nlloc/octtree/OctTree.html)

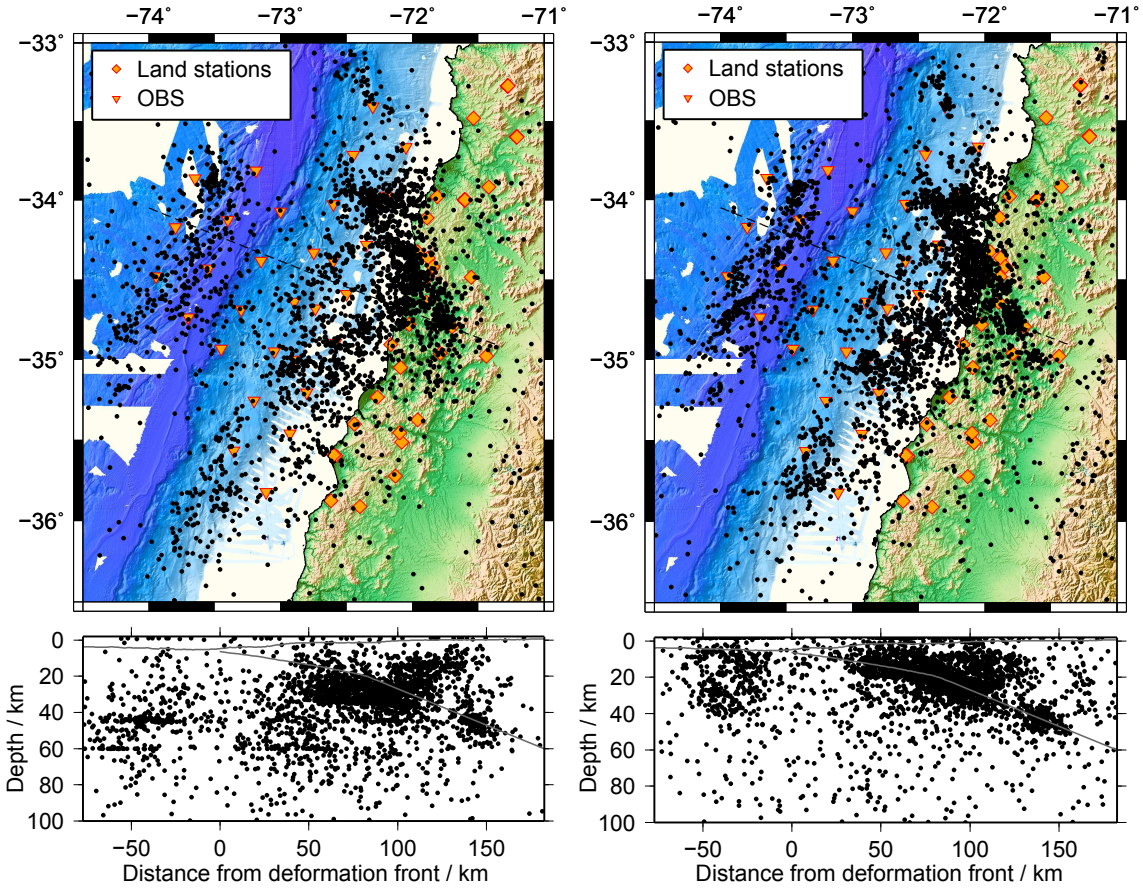

(a) Event location with a 1D P wave velocity model.

(b) Event location with the 2.5D P wave velocity model.

Figure 3.2.: Event locations determined with (a) a 1D model and (b) with the generated 2.5D model after one location run, i.e. without any station corrections. It is obvious that the 2.5D model represents the velocity structure better, especially offshore. The outer rise events scatter less in depth and also better fit the bathymetric features. Slab derived as described in Section 3.1.

slab was linearly approximated to the Slab1.0 model of *Hayes et al.* (2012) for larger depths (Fig. 3.4). By stretching this 2D model along the geometry of the trench, a 2.5D model was generated with a Matlab script written by Frederik Tilmann (GFZ Potsdam). The script considers the bathymetry and topography of the entire area and sets velocities to water and air velocities above. Because the 2D line consist only of information of a local profile water and air velocities were set to sediment and rock velocities in the offshore and onshore domains in order to prevent stations to be placed in the water column or in air. The final velocity grid was 700 km wide in both horizontal directions and 102 km long in the vertical direction with 2 km height above sea level and 100 km below. Distance between grid nodes was 1 km (Fig. 3.5). Travel times and take of angles to each station were calculated with NLL for each grid node. The initial number of cells for the Oct-tree algorithm was set to a value of 10 for each direction. The termination criterion for the search was either a cell width of 0.01 (about 0.7 km for the grid of this study) or 125000 iterations. In addition, a topographic surface grid was put in NLL to mask the search volume to the half-space below the topography in order to prevent NLL to locate events in water or air.

After location runs with phase arrivals weighted as class 0 to 2 as well as with all detected phase arrivals including the lowest quality class 3, it was decided to use all phase qualities because this leads to a higher amount of located events. The several good phase arrivals weighted down by MPX to the lowest quality class 3 provided more information on the hypocentre location of the events while actual low quality picks in quality class 3 were weighted down by NLL during the location process. Of the 4592 triggered potential events, 3,751 events could be located.

3.2. Station corrections

Because the Earth is usually more complicated than assumed in velocity models, predicted travel times may be affected by inaccuracies of the velocity model (*Lay and Wallace*, 1995). The velocity model used in this study does come from actual measured data cutting through the network. However, the velocity model varies along the trench and if a station is, for example, located on top of a thick layer of sediment, the actual travel times may differ from the predicted ones. To account for those velocity inaccuracies NLL calculates station corrections, i.e. the average residuals of phase arrival times for each station, during a location run. Ten sequential location runs were performed with station corrections of the previous run until the standard deviations of the total station corrections converged (Fig. 3.6b). The station corrections are plotted in Figure 3.6a. They varied between -0.7 to 1 s

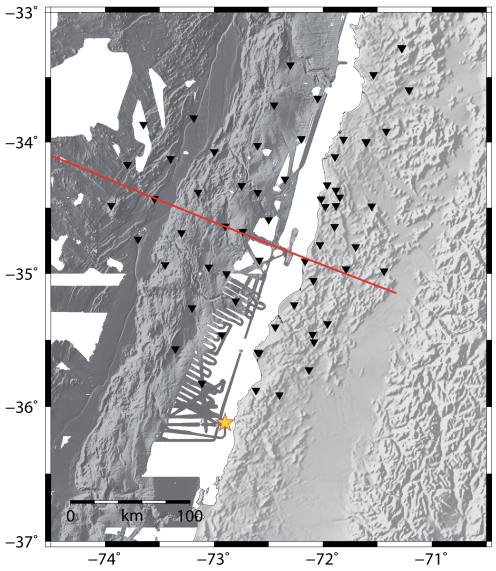

Figure 3.3.: Position of the seismic refraction and wide-angle profile from *Moscoso et al.* (2011) crossing the network defining the coastal region and offshore domain. Black triangles represent station locations. The yellow star marks the epicentre of the Maule main shock.

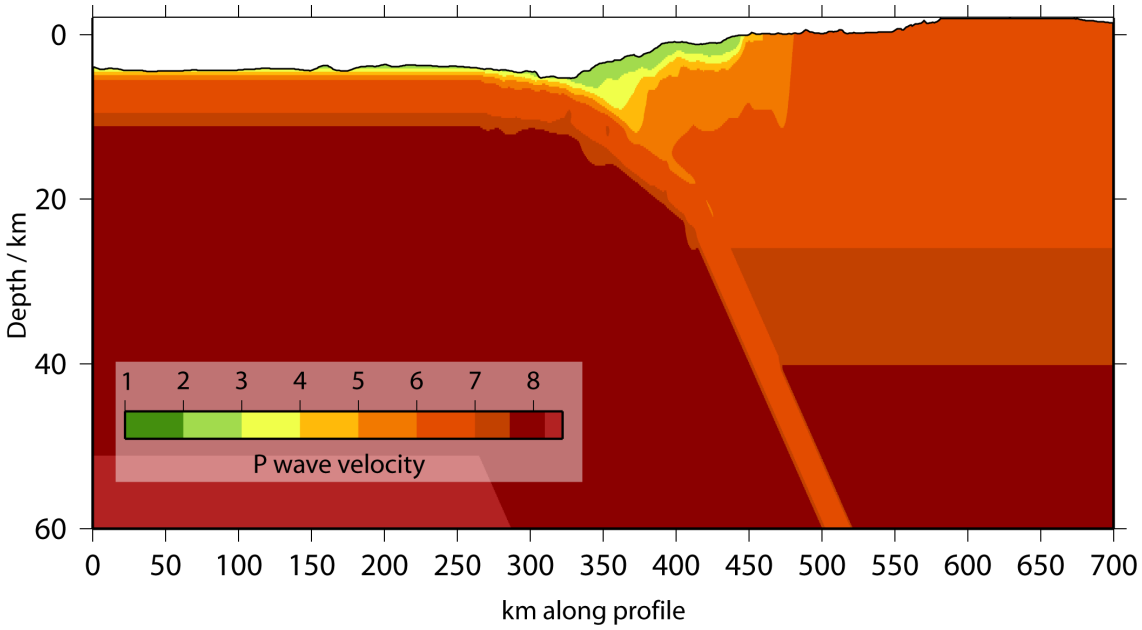

Figure 3.4.: Final 2D P wave velocity model which was extruded along the margin using the curved path of the trench.

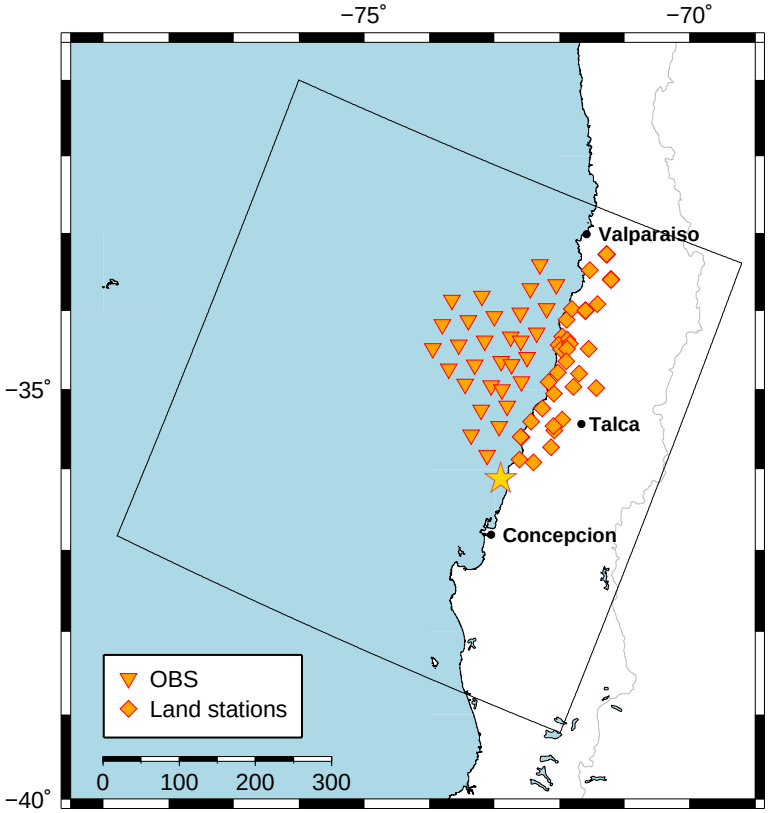

Figure 3.5.: Map of location of the 700x700 km wide search grid (black box) for NNL. The yellow star marks the epicentre of the Maule main shock.

(mean: 0.03 s) with standard deviations between 0.12 to 0.43 s (mean: 0.26 s). NLL determines the gap between event and surrounding stations based on all stations in the input file, also those which P phase arrivals were weighted down as 0. Therefore, a final 11th run was performed without the phase arrivals that were weighted down completely by NLL in order to get the correct gap value in the NLL output files.

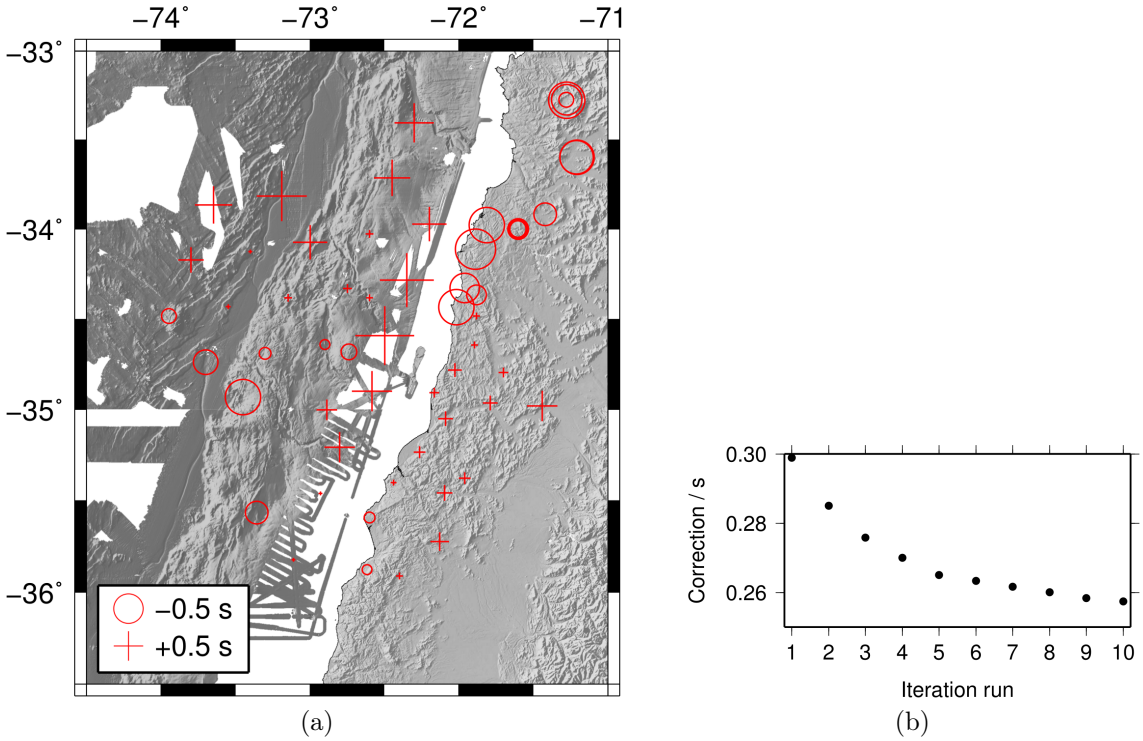

Figure 3.6.: Station corrections for the network. (a) Cumulative station corrections for each station after 10 iterations. (b) Mean standard deviations over all stations per iteration.

3.3. Quality classification

From the PDF scatter sample distributions a 3D 68% confidence error ellipsoid and an expected hypocentre, located in the centre of the ellipsoid, is calculated. Those parameters give a good indication of uncertainties in cases where the PDF has a single maximum and an ellipsoidal form (*Lomax et al.*, 2009). Based on the distances between maximum likelihood and expected location, the average length of the three axes of the confidence ellipsoid, and RMS-error of origin times the located events were classified into five quality categories (see Table 3.1, after *Husen and Smith*

(2004)). A map of all located and classified events is shown in Figure 3.7. In general, events within the network are better constrained and show a better classification as events located outside the network. An interpretation of the seismicity distribution will be discussed in more detail in Chapters 6 and 7.1.

Table 3.1.: Quality classes for earthquake locations (after *Husen and Smith* (2004)). "Distance" is the difference between the maximum likelihood and the expectation hypocentre location. "Average error" is the mean of the three axes of the 68 % error ellipsoid determined by NLL.

Class	**RMS** s	**Distance** km	**Average error** km	**Number of events**
A – excellent	< 0.5	< 0.5	< 2	145
B – very good	< 0.5	< 0.5	≥ 2	370
C – good	< 0.5	0.5 - 2	< 5	528
D – ambiguous	< 0.5	≥ 0.5*	–	1689
E – poor	> 0.5	–	–	1019
* Except class C				

The events in class D (ambiguous) may be poorly located or may be the result of a complex PDF with a broader scattering. An example for a possible cause for this scenario is shown in Figure 3.8. Because of a sharp interface in the velocity model the PDF sample cloud scatters broadly in space and consists of two maxima, one above and one below the interface. However, this does not mean that the maximum likelihood hypocentre is poorly constrained. In this example the probabilistic direct search procedure did find the correct hypocentre but the PDF is too complex to be linearly approximated with confidence ellipsoids. Figure 3.9 shows this example in the data set. The maximum likelihood hypocentre of this class D event is located in a region where also well defined events are located in the slab seismicity (see Fig. 3.7) and the location is probably correct. But because of the complex PDF with three maxima, probably caused by the velocity change in the slab, it is poorly constrained. Outlier data may produce complex PDFs as well resulting in larger confidence ellipsoids and a lower classification. In Figure 3.10b an event in a lower qualification class is plotted while the event in Figure 3.10a shows an event with the highest quality A. Here, the PDF sample cloud converges into one narrow minimum and the ellipsoids approximate the uncertainty correctly. For the ambiguous event on the other hand most of the PDF sample cloud does converge as well and, therefore, probably represents a correct hypocentre. But because the scatter samples distribute over a large extent of the search grid, the error ellipsoid is large and the expected hypocentre is located far away from the maximum likelihood hypocentre. Generally, with this quality classification procedure well located events can be detected reliably.

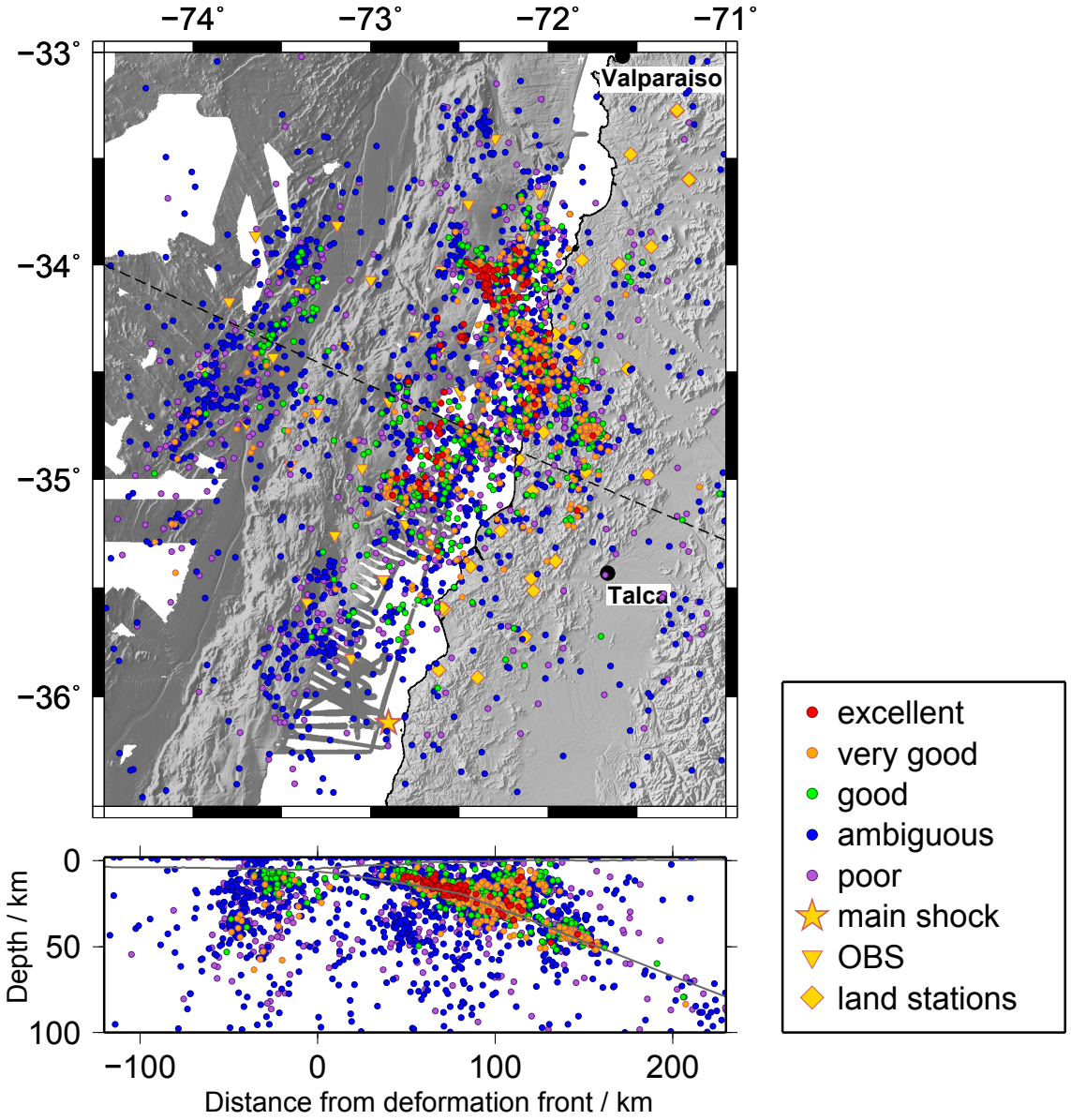

Figure 3.7.: Map and cross sections with aftershock locations colour coded by quality class (see Table 3.1). Slab derived as described in Section 3.1.

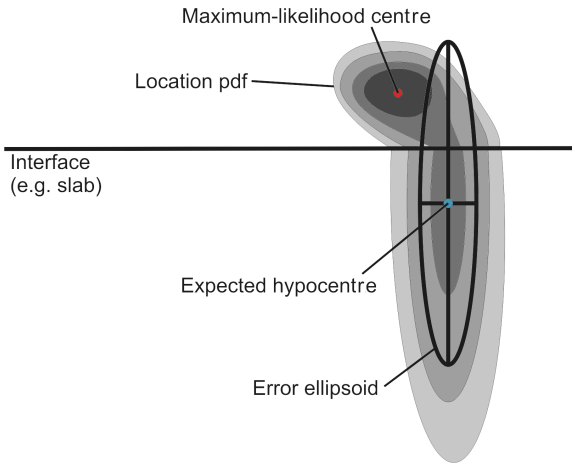

Figure 3.8.: Schematic diagram comparing linearised and direct-search locations for the case where the complete location is moderately complicated because of a sharp, horizontal interface in the velocity model. The linearised error ellipsoid and expected/optimal hypocentre are based on the second maximum of the location PDF below the interface while the probabilistic, direct, global-search algorithm determines the complete location PDF and identifies the maximum likelihood hypocentre above the interface (after *Lomax et al.* (2009)).

Events in a lower quality class, however, do not necessarily represent a poor location but a well located event with a complex PDF.

In total 3,751 of the triggered events could be located and 1,043 events were classified as good or better. A lot of the events were categorised into lower quality classes but that was expected, and desired, as NLL was supposed to evaluate mistriggered noise, spikes etc.

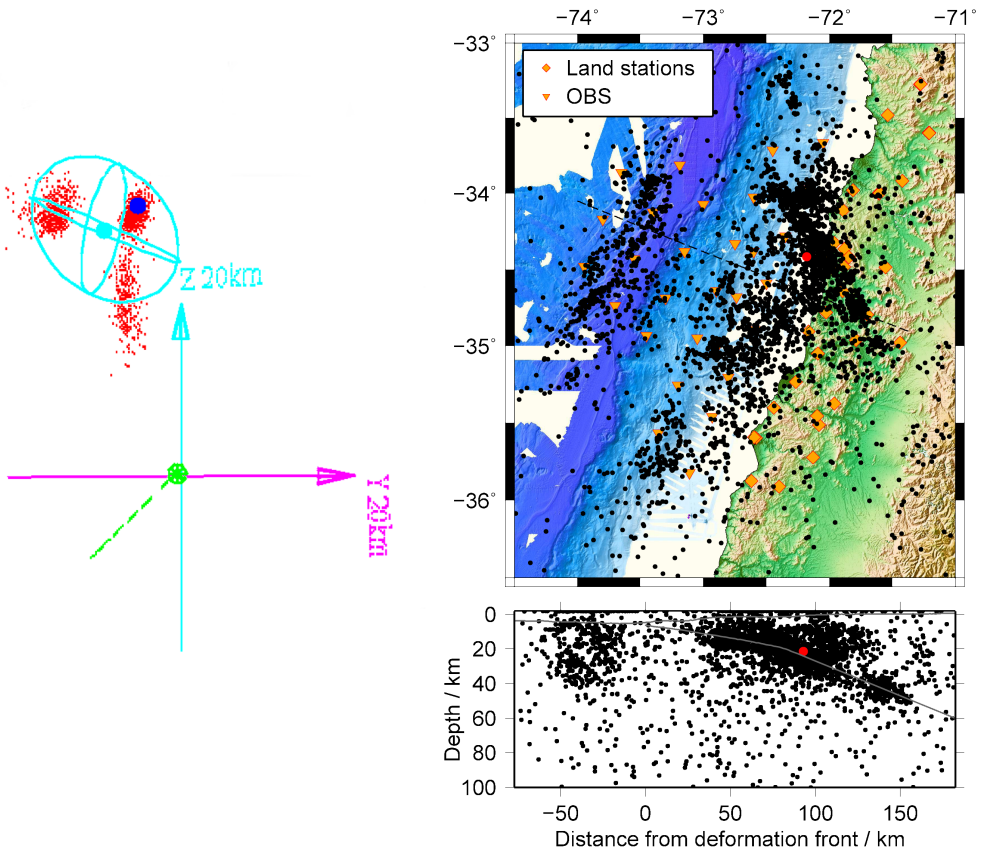

Figure 3.9.: Example of an event in the slab with a complex PDF. The red dot in the map and cross section marks the location of the maximum likelihood hypocentre. The left figure is a cut-out of a 3D visualisation of the 3D search grid. Red: PDF scatter samples, blue: maximum likelihood hypocentre, cyan: error ellipsoids and expected hypocentre. The y-axis is perpendicular to the trench. Slab in cross section derived as described in Section 3.1

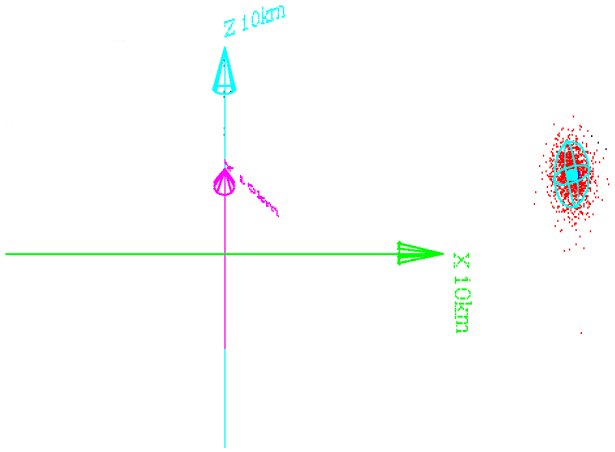

(a) Example of an excellent event (class A).

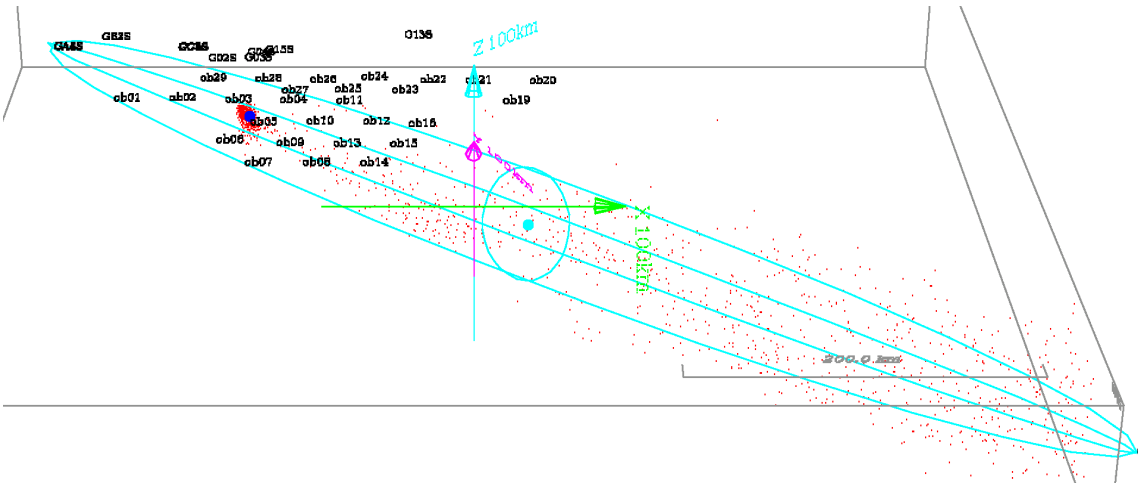

(b) Example of an ambiguous event (class D)

Figure 3.10.: Examples of PDF scatter clouds for two quality classes in a cut-out of a 3D visualisation of the 3D search grid. Red: PDF scatter samples, blue: maximum likelihood hypocentre, cyan: error ellipsoids and expected hypocentre. The x-axes are parallel to the trench.

4. Automated picking of S wave onsets

The automatic detection of S wave arrivals is more complex than of P wave arrivals. One reason is that it can be difficult to distinguish between P and S phase arrivals or other phases that overlap and interfere with the S phase arrivals. There are several successful approaches to automatically determine S phase arrivals on land station data. *Diehl et al.* (2009) combines three commonly used phase detection and picking methods that require the rotation of the components into the direction of the incoming wave in order to maximise the amplitude of the incoming S phase. As mentioned in Chapter 2, OBSs settle on the sea floor without any specific alignment along the North and East directions. Therefore, the application of this picker cannot easily be transferred to an OBS network. However, while manually evaluating the automatically detected P phase arrivals in the parameter setup process, it turned out that MPX detected some S phase arrivals accurately in those cases where the initial pick was set near a S wave arrival by mistake. When considering the P wave signal as "noise" and the S phase as signal, MPX should be capable of detecting the correct S phase arrival as well. By now, a newer version of MPX apparently includes a S phase picker. However, this version is at the moment not available on Aldersons homepage and up to now no studies were published. To test if MPX is capable of detecting the S phase arrivals for the OBS data set, a small set of earthquakes were evaluated in a preliminary test to see if it is reasonable to continue any further with this approach before preparing a complete calibration and reference data set.

4.1. Preliminary test

In the preliminary test theoretical S phase arrival times were calculated with *onset* (*Schweitzer*, 2004) with the 1D velocity model of *Arroyo et al.* (2010) and a constant vp/vs ratio of 1.75 in order to estimate a predicted S arrival time for the initial pick. The S wave spectra showed frequencies between 4 and 8 Hz, thus, the minimum frequency threshold in MPX is expected to be between 2 and 4 Hz and will be tested

in 0.5 Hz steps; in addition, 1.5 and 4.5 Hz will be tested as well. For the estimation window and Wiener filter lengths 1 and 2 s, as well as, 2 and 4 s will be tested, as was the case for the P waves. The first security gap is defined by the standard deviation of the error between initial and manual reference pick (2.2 s). The other three security gaps were determined with the schemes of Table 2.1. The reference set was picked with all generated parameter sets and the best set with the smallest picking error was determined. This first test led to high picking errors between reference and automatic picks. One reason was that the S phases do not always arrive at the same time on both horizontal components, due to shear wave splitting. Because the manual reference pick was set only on one of the horizontal components, the automatic pick was correct in respect to the wave forms but still produced larger errors in cases where the reference pick was set on the other component. Therefore, the setup of the parameter was calculated only with those components where the manual reference pick was set and the horizontal components were rotated. As mentioned above, with OBS data it is not possible to rotate the components based on hypocentre locations to the direction of the incoming wave, because the horizontal components are not aligned to the North or East directions. However, the software package *Seismic handler* is capable of calculating the azimuth of the maximum polarization for two components in a certain time window and rotating the components to get an optimum separation of components. In the range of 10 s to the theoretical S phase arrival the program estimated the azimuth and the components were rotated by that value. This led to smaller differences between automatic and manual S picks. An example of an automatically picked S phase onset is shown in Figure 4.1. For the preliminary test no calibration of the weighting scheme was carried out because the data set is too small for reliable results. The location of the events was processed with equally weighted S phase arrivals and the standard deviations between the hypocentre locations of the hand picked to the fully automatically picked datasets were calculated. The values are about 3.5 km for latitude, about 1 km for longitude and about 4 km for depth for 12 events inside the network that show very good Wadati plots for the manually picked onsets. The fully automatically picked phase arrivals show good Wadati diagrams as well for those events, one example is presented in Figure 4.2. For high quality events it was possible to gain good results to detect S phase onsets with MPX, even with parameters that were not adapted optimally (initial pick, weighting scheme). These results appear to be promising that it is possible to detect S phases arrivals with MPX for the whole data set as well and a complete reference data set was prepared to determine the MPX parameter properly.

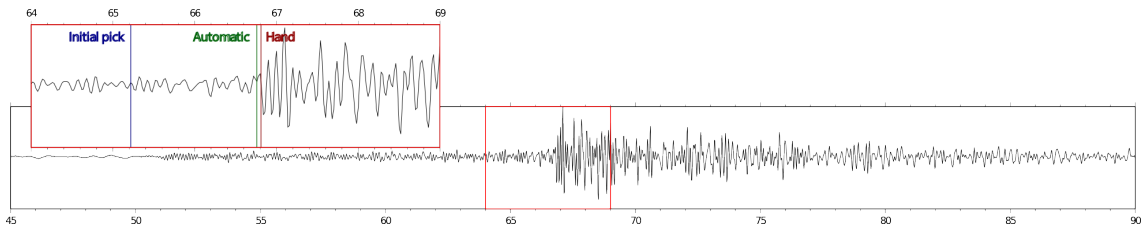

Figure 4.1.: Example of an automatically detected S wave onset with MPX on a horizontal component of station OB02. The green line marks the automatic pick while red is the hand picked reference pick. In blue is the initial pick which the picking algorithm requires as a first guide. It was calculated based on the automatic P wave onset and a 1D velocity model. The event occurred on 4 November 2010, 11:50:30.3 h, 34.5035°S and 73.7096°W at about 35 km depth (see red star in map in Figure 4.2). Starting time of record is 11:50:04.0 h.

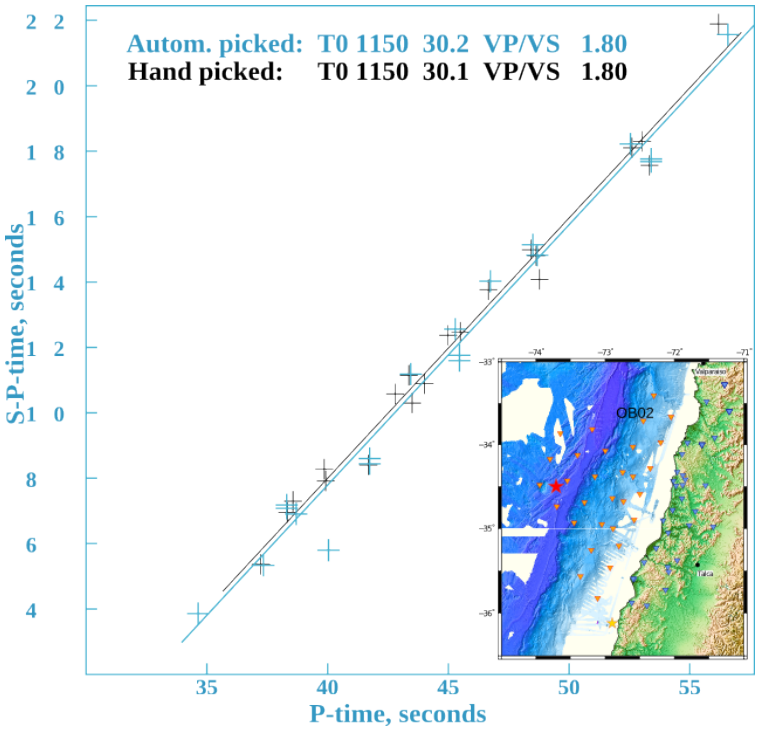

Figure 4.2.: Overlay of Wadati plots of hand picked (black) and fully automatically picked (blue) P and S wave onsets. Small map: The red star marks the epicenter of the selected earthquake shown in this Figure and in Figure 4.1). The yellow star is the epicentre of the main shock.

4.2. Initial pick

At first, the calculation of the theoretical S wave arrival was improved in order to generate an initial pick as close to the real phase arrival as possible. Therefore, the vp/vs value was determined from the Wadati plots of the reference data set which gave a value of 1.67. For reference, a value of 1.7 was tested as well but this did not lead to smaller differences between initial pick and phase arrival. The deviations between initial pick and reference pick were rather large and the initial pick was about 4 s too early as can be seen in Figure 4.3a. Figure 4.3b shows the corresponding differences between reference picks and automatic picks. MPX does detect most of the S phase arrivals correctly but an influence of the early initial picks is obvious as MPX detects a lot of S phases at about -5 s. However, even as most of the initial picks were misplaced by several seconds, most of the automatically picked phases were placed near the reference pick which shows that MPX is capable of detecting the S phase arrivals. In order to decrease the difference between initial and reference pick another velocity model was chosen for the calculation in *onset*. The model of *Arroyo et al.* (2010) is a minimum 1D model for the combined offshore and onshore domain of the study area. Therefore, a profile of the 2D velocity model generated for the location procedure of this study (see Chapter 3), through the submarine forearc, was used. Now, the initial picks show a deviation of 0.5 s $\pm$ 2.4 s to the reference picks.

4.3. Parameter setup

A reference data set, consisting of 20 events inside the network per location quality class A, B and C, i.e. 60 events with 554 reference picks on rotated horizontal components, was generated. According to the manual the reference set should consist of 500 to 1000 reference picks. After determining the standard deviation between initial and reference pick the value for the first MPX security gap was set. The procedure to determine the best parameter set of security gaps, frequency threshold and filter window lengths was the same as for the P wave arrivals. The first security gap was determined by the standard deviation of the difference from initial pick to reference pick. The determination of the other three security gaps followed the approaches described by Table 2.1. The estimation window lengths and Wiener filter length were set to 1 and 2 s as well as 2 and 4 s. The lower frequency threshold had a range of 1.5 to 4.5 Hz. In addition, the first security gap was set to 3 s to test any effects. In total 140 parameter sets were tested (Tab. D.1) and their absolute picking error plotted as box plots (Fig. D.1). Parameter set 7 showed the lowest

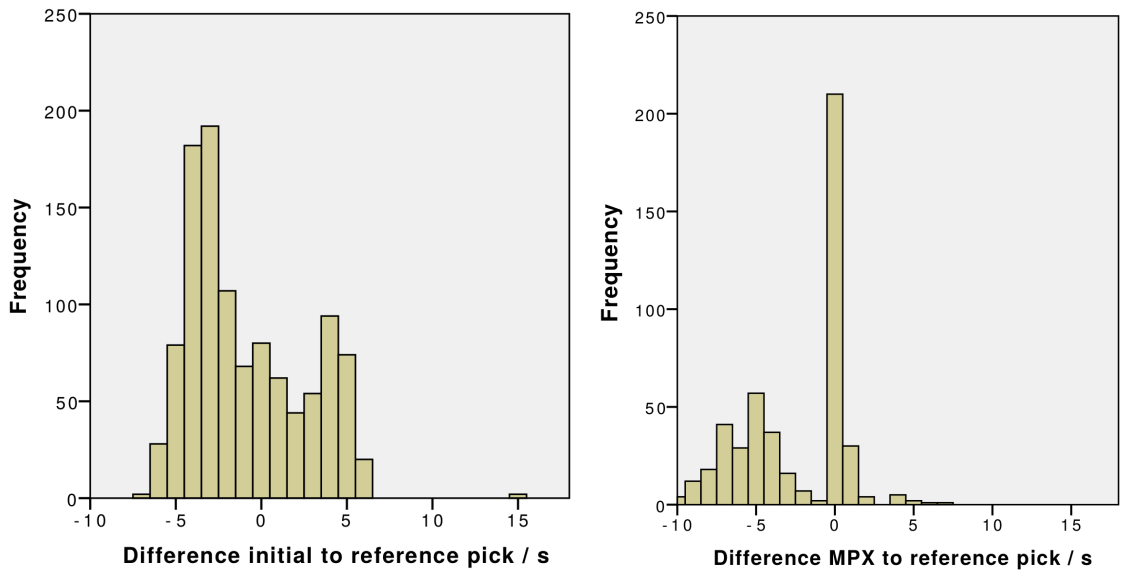

(a) (b)

Figure 4.3.: Histograms of differences between initial to reference pick (a), and automatic to reference pick (b).

absolute errors with 0.01 s, 0.05 s and 0.13 s for the 25th, 50th and 75th percentiles and will be applied in the production run. The final picking parameters for the S phase arrival determination are:

Security gaps:	2.40 s / 1.20 s / 0.58 s / 0.04 s
Estimation window lengths:	2 s
Wiener filter lengths:	4 s
Frequency threshold:	4.5 s

With only 187 automatic picks out of 554 reference picks, not enough picks were detected for the calibration of the quality assessment and the reference data set was extended with 888 additional picks from 58 events.

4.4. Calibration of weighting scheme

The reference set for the calibration of the weighting scheme consisted of 1442 S phase arrivals. However, only 460 arrivals could be detected by MPX and the calibration was performed with a little less than the 500 to 600 reference picks

suggested by the manual. Again, a variety of error boundaries and number of classes were tested. The best are shown in Table 4.1. Because the the configurations did not resolve all weighting classes properly, for example in class 1 of *TW2* (see page 26) in scheme B (Fig. 4.4), a merging of classes was tested. For schemes D and F only two classes were generated of the reference set by combining weights 0 and 1 as a new class 0 and classes 2 and 3 formed a new class 1. For schemes G and H classes 2 and 3 of the reference set were merged to one class while 0 and 1 remained two separated classes. Cross tabulations and the standard deviation of the picking errors

Table 4.1.: Tested weighting schemes with picking error boundaries (ε), amount of quality classes and upgraded, downgraded and correctly classified qualities.

Scheme	ε_1 **s**	ε_2 **s**	ε_3 **s**	**Classes**	**Correct** %	**Downgraded** %	**Upgraded** %
B	0.02	0.08	0.26	4	48.9	23.6	25.3
D	0.08	–	–	2	54.4	20.3	25.3
F	0.1	–	–	2	75.5	11.3	18.3
G	0.02	0.08	–	3	53.0	26.8	20.2
H	0.08	0.26	–	3	58.0	17.0	25.0

ε_{pick} inside the assigned classes were determined. In all cases the standard deviations were high above the picking boundaries. This is mainly because of a few outliers as can be seen in Figure 4.6, where a histogram of the picking errors for class 0 determined from scheme B is plotted. All picking errors but one with more than 3 s are below 0.5 s. Therefore, the quartiles were preferred over the standard deviation to determine if the picking errors fall inside the picking boundaries because they are less sensitive to outliers. However, this is only the case for scheme F (Tabs. 4.1 and 4.2 and Fig. 4.5). This scheme divides the data set in only two classes. Thus, when neglecting class 1 as unsuitable for the location process because of too high picking errors, there will only be S picks with one assigned weight. To generate a subset of higher quality picks the weighting classification was approached in a different way by combining the highest quality classes of two schemes. Scheme B showed the lowest 75th percentile and a low standard deviation and, therefore, class 0 of scheme B (0B) was considered to be the new best class 0 and the new class 1 was generated from class 0 of scheme F (0F):

$$\text{Weight } 0 = 0\text{B}$$
$$\text{Weight } 1 = 0\text{F} - 0\text{B}.$$

This solution results in two quality classes with high qualities for the S phase arrivals.

			MPX				Total
			0	1	2	3	
TW2	0	Count	80	27	19	11	137
		% within TW2	58,4%	19,7%	13,9%	8,0%	100,0%
		% of Total	17,4%	5,9%	4,1%	2,4%	29,8%
	1	Count	31	41	30	25	127
		% within TW2	24,4%	32,3%	23,6%	19,7%	100,0%
		% of Total	6,7%	8,9%	6,5%	5,4%	27,6%
	2	Count	22	18	43	14	97
		% within TW2	22,7%	18,6%	44,3%	14,4%	100,0%
		% of Total	4,8%	3,9%	9,3%	3,0%	21,1%
	3	Count	6	14	18	61	99
		% within TW2	6,1%	14,1%	18,2%	61,6%	100,0%
		% of Total	1,3%	3,0%	3,9%	13,3%	21,5%
Total		Count	139	100	110	111	460
		% within TW2	30,2%	21,7%	23,9%	24,1%	100,0%
		% of Total	30,2%	21,7%	23,9%	24,1%	100,0%

Figure 4.4.: Cross tabulation of automatically assigned MPX weights and *TrueWeight2* for weighting scheme B. Ideally, the entries on the diagonal would be 100 %. Grey: upgraded qualities, blue: downgraded qualities.

			MPX		Total
			0	1	
TW2	0	Count	205	84	289
		% within TW2	70,9%	29,1%	100,0%
		% of Total	44,6%	18,3%	62,8%
	1	Count	52	119	171
		% within TW2	30,4%	69,6%	100,0%
		% of Total	11,3%	25,9%	37,2%
Total		Count	257	203	460
		% within TW2	55,9%	44,1%	100,0%
		% of Total	55,9%	44,1%	100,0%

Figure 4.5.: Cross tabulation of automatically assigned MPX weights and *TrueWeight2* for weighting scheme F. Ideally, the entries on the diagonal would be 100 %. Grey: upgraded qualities, blue: downgraded qualities.

Table 4.2.: Mean, standard deviation, and 75th percentile of the picking errors and amount of detected picks per weighting class for the different tested weighting schemes. The percentile was calculated with the absolute error.

Scheme	Weight	75th percentile s	Mean s	Standard deviation s	Picks
B	0	0,05	-0,016	0,325	139
	1	0,09	0,002	0,281	100
	2	0,14	-0,087	0,645	110
	3	0,87	-0,515	1,700	111
D	0	0,08	-0,039	0,395	241
	1	0,45	-0,271	1,289	219
F	0	0,09	-0,043	0,397	257
	1	0,47	-0,285	1,333	203
G	0	0,06	-0,012	0,321	144
	1	0,11	-0,039	0,418	159
	2	0,57	-0,389	1,497	157
H	0	0,18	-0,149	0,946	175
	1	0,15	-0,145	0,806	152
	2	0,14	-0,155	1,074	133

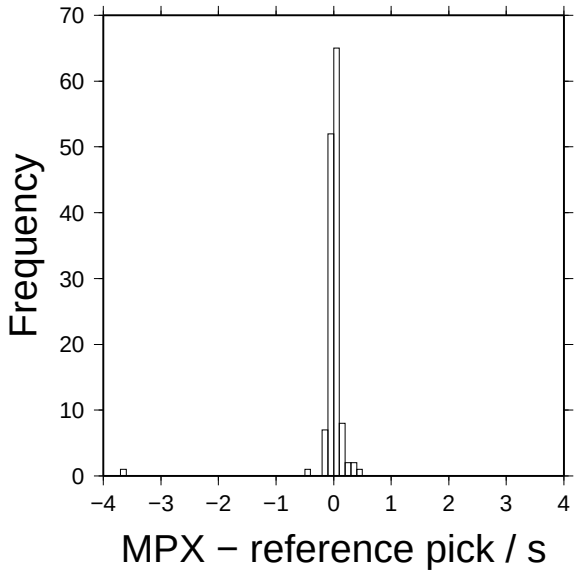

Figure 4.6.: Histogram of MPX picking errors for class 0 of scheme B.

For the location procedure only the best pick of both components is used. If picks on both components show the same weighting class, the pick with the least time residual after a location run with *HYP* (see Chapter 2.2.4) is used. The hand picked reference data set and the automatically picked events were located and the differences between the hypocentres were compared. For 99 events with a gap smaller than 180 degrees the 75th percentiles of the absolute differences between latitudes and longitudes were below 4 km (Tab. 4.3). This is a reasonable result and comparable to the differences between the reference data set and automatic data set for the adaption of the P wave picker for the OBS data set (Tab. 2.3). The differences between the depth are, with about 7 km, a little higher, but, as S phases have a great effect on the determination of hypocentre depth, small differences between the picked S phase arrivals can result in a greater depth deviation. However, with 25th and 50th percentiles of 0.7 and 2.2 km the results for the depths differences between both data sets are still reasonable.

Table 4.3.: Absolute errors of the hypocentre locations between manually and automatically picked reference data set. Only those events that show a gap of smaller than 180 degrees are taken into account.

Percentile %	**Latitude km**	**Longitude km**	**Depth km**
25	0.44	0.44	0.74
50	1.54	1.10	2.24
75	3.49	3.80	7.36

Dietrich Lange determined automated S phase arrivals for the land stations from March to September 2010 for his study and provided S phases for the land stations data set for the time span of this study (September to December 2010) as well using the S phase picker of *Diehl et al.* (2009). This algorithm combines three commonly used phase detection and picking methods: a STA/LTA detector and a S phase detector on unrotated components, and a predictive AR-AIC picking algorithm on rotated as well as unrotated components.

In total 9020 S phase arrival were detected for the 1043 best located events (see Chapter 3); 3485 on OBSs and 5535 on land stations.

4.5. Hypocentre determination including S phase arrivals

To determine the hypocentre locations for the event data including S phase arrivals, NLL was applied again. S wave velocity models were calculated from the P wave velocity models with a vp/vs ratio of 1.67 determined from the reference data set. Ten sequential runs were performed with NLL to minimize the cumulative standard deviations of the station corrections. The station corrections do not converge as clearly as those for the P wave velocity model (Fig 3.6b) but they cluster around a single value (Fig. 4.7b). The standard deviations of the station corrections for the included S phase arrivals are slightly higher than those for P phase arrivals only. But since the S wave velocity models were generated with a constant vp/vs value for the entire network, this is expected. That a constant vp/vs ratio does not reflect the conditions very well can be seen in Figure 4.7a, where a map with the station corrections is presented. For the land stations the station corrections are almost all negative while they are almost all positive for the OBSs. Thus the S wave velocities in the offshore domain are too fast while they are too slow onshore.

The hypocentre locations were categorised into five quality classes the same way as the hypocentres determined from P phase arrivals only (see Section 3.3). In total, 1034 of 1037 events could be located and 894 were categorised as “good” or better (Tab. 4.4). Including the S phase arrivals improved the hypocentre locations and the amount of events classified as “excellent” was more than doubled. On the other hand about 140 events that were classified as ”good“ or better before were now downgraded into lower quality classes. In Chapter 7.1 the differences between hypocentre locations with and without S phase arrivals is discussed in more detail.

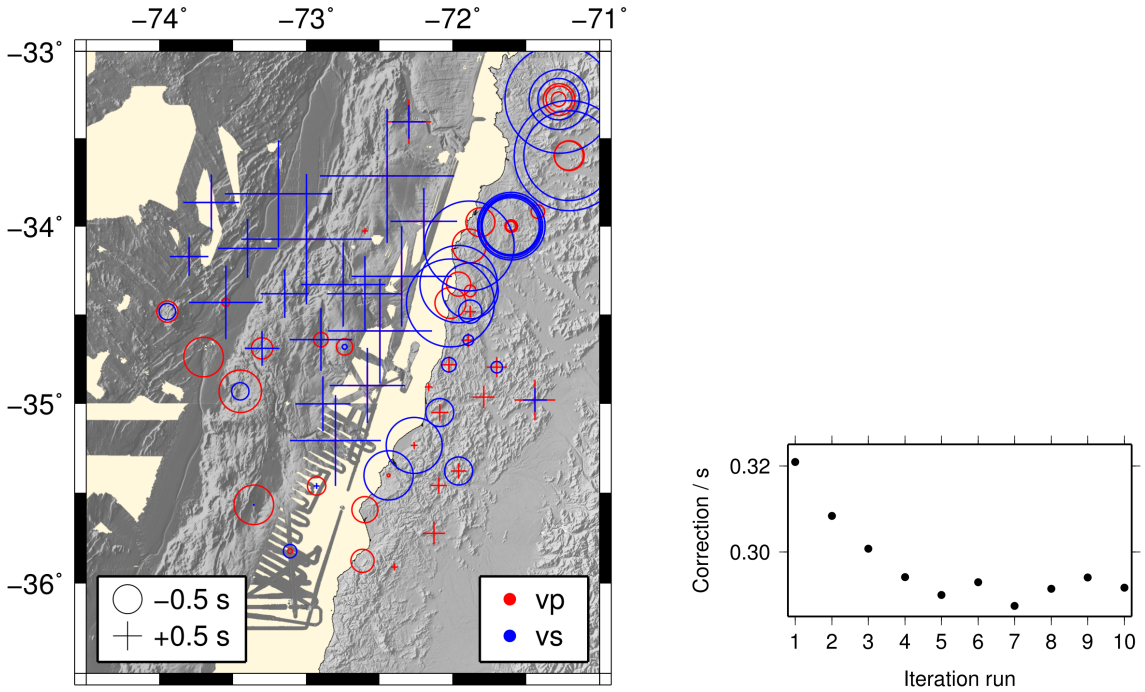

(a) (b)

Figure 4.7.: Station corrections for the network after including S phase arrivals. (a) Cumulative station corrections for each station after 10 iterations. Red = Station corrections corresponding to P wave velocity model. Blue = Station corrections corresponding to S wave velocity model. (b) Mean standard deviations over all stations per iteration.

Table 4.4.: Quality classes for earthquake locations (after *Husen and Smith* (2004)). "Distance" is the difference between the maximum likelihood and the expectation hypocentre location. "Average error" is the mean of the three axes of the 68 % error ellipsoid determined by NLL. Numbers in brackets in the last column are the amount of classified events after locating with P wave onsets only.

Class	**RMS** s	**Distance** km	**Average error** km	**Number of events**
A – excellent	< 0.5	< 0.5	< 2	348 (145)
B – very good	< 0.5	< 0.5	≥ 2	177 (370)
C – good	< 0.5	0.5 - 2	< 5	369 (528)
D – ambiguous E – poor	}			140

5. Moment magnitude and focal mechanisms

In this chapter the theoretical background on magnitude and focal mechanism determination is discussed. As one aim of this study is an automated approach for the analysis of the aftershock data set, the applied methods and routines work in an automatic mode.

5.1. Moment magnitude

There are several scales and methods to describe the size and strength of an earthquake, such as local magnitude, body wave magnitude, surface wave magnitude or moment magnitude. While the local, body wave and surface wave magnitudes are calculated from amplitudes of certain wave types the moment magnitude is directly connected to a source process: the seismic moment. The seismic moment M_0 is described by the average slip D over the fault area S:

$$M_0 = \mu DS, \tag{5.1}$$

where μ is the shear modulus (*Kanamori*, 1977). The seismic moment can be determined through field observations where the slip on the surface S can be observed and the distribution of aftershocks can deliver fault area D. Another way how to determine the seismic moment is with the source spectra. This will be described in the next section. An advantage of the moment magnitude scale is that it does not saturate like the scales obtained from amplitudes. For those magnitudes the measurement of the amplitude is frequency-dependent at about 1.0, 1.2 and 0.05 Hz for M_L, m_b and M_S (*Lay and Wallace*, 1995). If the frequency where the magnitude is determined lies above the corner frequency, i.e. not on the flat part but on the slope of the spectra, the correct magnitude cannot be resolved and the scale saturates. Figure 5.1 shows spectra for events with various sizes and their relationship to the frequencies at which M_S and m_b are detected. Large earthquakes occur over large fault lengths and therefore produce waves with long periods (low frequencies)

and shorter flat levels of the spectra. However, saturation will not be a problem in this study because the aftershocks six month after the main shock are expected to have magnitudes below the saturated magnitude values (M_S is fully saturated at approximately 8.0 and m_b at about 6.0).

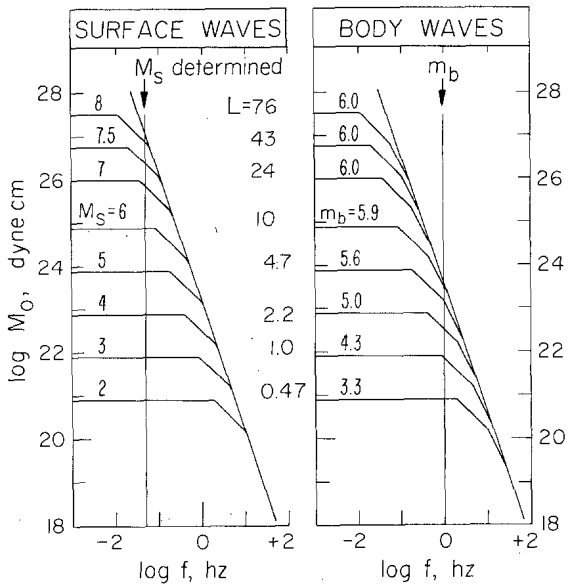

Figure 5.1.: Spectra for earthquakes with different magnitudes and the frequencies at which M_S and m_b are detected: 0.05 and 1 Hz (*Geller*, 1976).

Because it is directly connected to a source parameter and it does not saturate, the moment magnitude is considered to be the best measure of the size and energy release of an earthquake (*Lay and Wallace*, 1995; *Stein and Wysession*, 2009; *Ottemöller and Havskov*, 2003). *Ottemöller and Havskov* (2003) developed an automated routine that determines the moment magnitude from the displacement source spectra. In their study they show, that this routine is suitable to determine the moment magnitudes in local networks in a range from -1 to 8. The application of this routine to the OBS and land station data sets will be described after the next paragraph.

In this paragraph the determination of the seismic moment from the source spectra will briefly be discussed. It follows mainly the explanations of *Stein and Wysession* (2009). The source time function describes the earthquake's source signal and is the time derivative of the seismic moment function which describes the faulting process in terms of rigidity of the material μ and the history of the slip $D(t)$ and fault area $S(t)$:

$$M(t) = \mu D(t) S(t). \tag{5.2}$$

At each point of a fault that is ruptured by an earthquake seismic waves are radiated. Because the fault does not fail at once but rupture propagates along the fault with a certain velocity, the seismic waves radiated from the end of a rupture area will arrive later at a receiver than those waves radiated at the beginning of the fault. This results in a ramp function for the history of the slip with a rise time T_D (Fig. 5.2). The source time function can be described as a convolution of the rupture time T_R

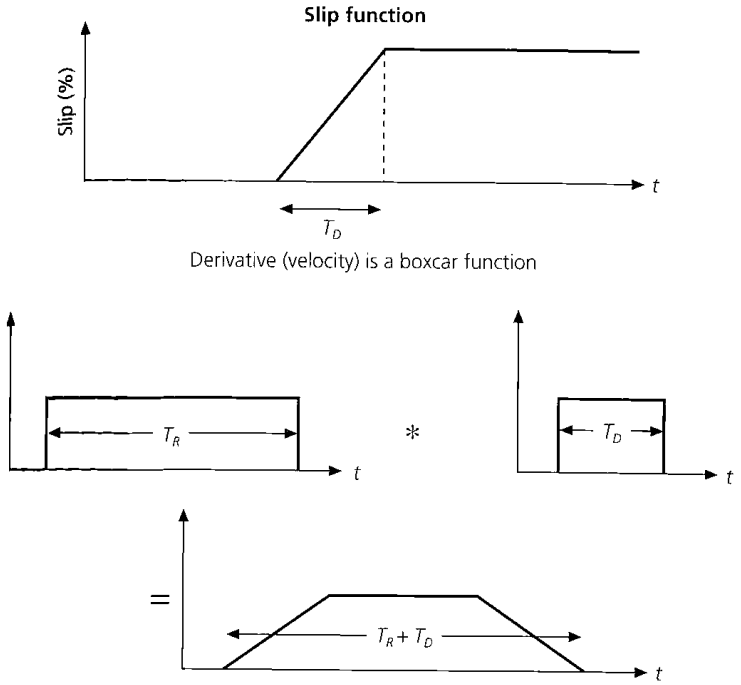

Figure 5.2.: The derivative of a ramp time history of the slip (top) is a boxcar. Convolution with the boxcar function of the rupture time (center) leads to a trapezoidal source time function (bottom) (*Stein and Wysession*, 2009). Copyright by 2003 by S. Stein and M. Wysession.

and the derivative of the slip history. As both are boxcar functions, a convolution leads to a trapezoidal source time function. The area under this function is the seismic moment M_0. Then, the spectral amplitude $A(\omega)$ of the source signal is:

$$|A(\omega)| = M_0 \left| \frac{\sin(\omega T_R/2)}{\omega T_R/2} \right| \left| \frac{\sin(\omega T_D/2)}{\omega T_D/2} \right|, \tag{5.3}$$

where the latter two terms are the results of the Fourier transform of both of the boxcar functions. The function for the spectral amplitude can be solved by approximating the sinc function ($\mathrm{sinc}\ x = (\sin x)/x$) as 1 for $x < 1$ and $1/x$ for $x > 1$. Then, the plot of the source spectra consists of three areas divided by the corner

frequencies $2/T_R$ and $2/T_D$ (Fig. 5.3). The approximation with a single corner frequency that is the intersection of the first and the third spectrum segments is also common. The flat segment that extends to zero frequency determines the seismic moment M_0.

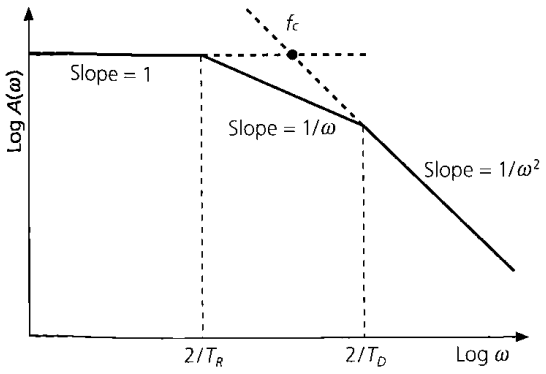

Figure 5.3.: Theoretical source spectrum of an event. From the flat part of the spectrum M_0 can be determined. For a detailed explanation see text. (*Stein and Wysession*, 2009). Copyright by 2003 by S. Stein and M. Wysession.

The calculation of the seismic moment M_0 from the source spectrum in *SEISAN*, a seismic analysis system (*Havskov and Ottemöller*, 1999), is based on a model of *Brune* (1970) and various assumptions about geometrical spreading and anelastic attenuation of the seismic waves:

$$M_0 = 4\pi \frac{\rho \; vp^3 \; 10^{OM}}{G(r,h) \; KK} \; , \tag{5.4}$$

where ρ is the density, vp is the P wave velocity OM is the logarithm of the spectral level, $G(r,h)$ is the hypocentral distance determined from distance and depth, and KK is a factor to correct for the free surface effect and radiation pattern. The derivation of this equation is described in detail in the *SEISAN* manual (*Ottemöller et al.*, 2011). In order to obtain the moment magnitude in *SEISAN*, a run with the implemented location routine *HYP* is necessary because some of the spectral parameter are distance dependent. But since *HYP* just uses a 1D model the recalculated hypocentres would be of much lower qualities than the ones determined with the 3D model. Therefore, the spectral parameter were calculated using *autosig* implemented in *SEISAN* and the seismic moment as well as the moment magnitude were calculated based on the same equations as in *SEISAN* (Eq. 5.4 and 5.5) but with the hypocentre and station–event distances determined in NLL. The moment magnitude M_w is calculated for every station from the seismic moment M_0 as

follows:

$$M_w = \frac{2}{3} \log M_0 - 6.06 \tag{5.5}$$

for a seismic moment given in Nm (*Kanamori*, 1977). In order to get the moment magnitude for the event the median of the magnitudes obtained per station is calculated. Afterwards, the seismic moment corresponding to this moment magnitude is calculated based on Equation 5.5. The seismic moment and moment magnitude were determined for 1037 events in the quality classes A, B, and C.

In this study only the broadband seismometers from the OBS network and the land stations were used for the determination of the moment magnitude because in general short-period stations do not result in reliable results for events with low frequencies. The short-period stations of the OBS network are equipped with 4.5 Hz seismometers, and thus, only events with corner frequencies above this frequency, i.e. events with small magnitudes, will give reliable results. Of the five broadband stations available in the offshore domain (OB03, OB09, OB11, OB15 and OB27), two showed clipped amplitudes for the whole deployment time span (OB03 and OB15) and one did not have data on the vertical component (OB27). Those stations were not used for the magnitude determination. Only picks that had a less than 1 s time-residual in the location process were considered. Phase arrivals that were picked on the hydrophone were transferred to the vertical component of the seismometer.

To test the reliability of the determined moment magnitudes a local magnitude calculation was tested but the automatic *SEISAN* routine was not able pick any amplitudes. However, in the study of *Lange et al.* (2012a) local magnitudes with the land station data set were calculated until the end of September 2010. Because there is a time overlap of about 10 days four events are available in both data sets. They show comparable results with two events resulting in the same value for the magnitude an the other two with deviations of 0.1. The moment magnitudes of the OBS were compared to those of the land stations in order to determine any constant deviation but no dependency could be detected.

5.2. Fault orientations and focal mechanisms

The descriptions in this section mainly follows the explanations of *Lay and Wallace* (1995) and *Stein and Wysession* (2009). The orientation of a fault can be determined by the polarity of the first-motion of the P wave arrivals with the help of stereographic projections. The first-motions of P wave arrivals are compressional or dilatational and are dependent on the pattern of radiated seismic waves which

varies with the station-event azimuth. The radiation patterns for isotropic media can be approximated by two force couples with opposite directions called douple couple (Fig. 5.4). One force couple is aligned along the fault while the other is aligned along an auxiliary plane perpendicular to the fault plane. The corresponding radiated pattern for P waves has four lobes. Two lobes are compressional and two lobes are dilatational. Thus, to get the fault orientation of an event, the nodal planes are determined by evaluating first-motions. Therefore, a small sphere around the source, the focal sphere, is imagined where the ray path of a P wave leaving the source can be described by the azimuth and the take-off angle (Fig. 5.5). In a stereographic projection the first motions of the P waves, upward for compression and downward for dilatation, are transferred from the lower focal hemisphere to an equatorial plane. In cases where the rays intersect the upper focal hemisphere they are projected back to the lower focal hemisphere. The intersections of the fault plane and the auxiliary plane with the focal sphere projected onto the equatorial plane are curves that divide regions with compressional motions from those with dilatational motions. Different fault types produce different equatorial projections, or focal mechanisms (Fig. 5.6). The discrimination between fault plane and auxiliary plane in a focal mechanism is ambiguous because slip along the auxiliary plane would produce the same focal mechanism as slip along the fault plane. To decide which of the nodal planes is the actual fault plane, additional observations, like faults outcropping to the surface or aftershock distributions, have to be taken into account.

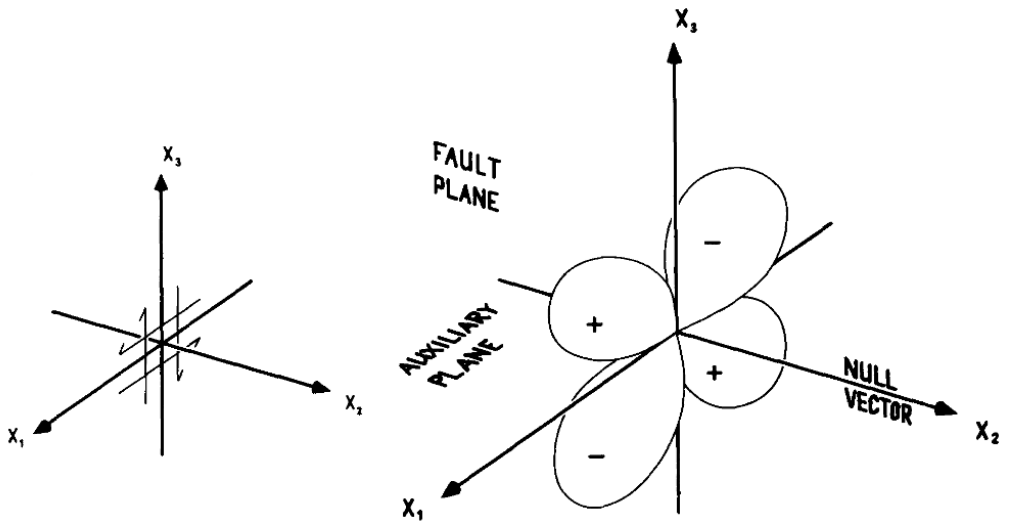

Figure 5.4.: Left: Double couple forces. Right: Radiation pattern of a P wave for a douple couple source consisting of four symmetrical lobes, two compressional and two dilatational (*Pearce*, 1977).

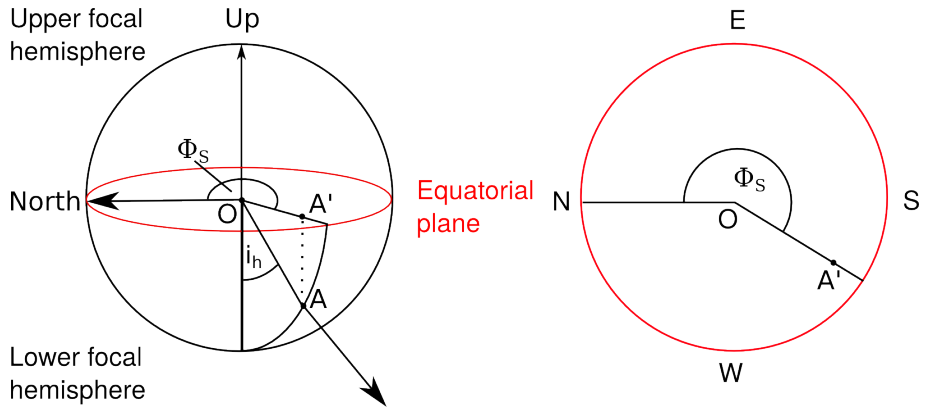

Figure 5.5.: From focal sphere to stereographic projection. *Left*: Focal sphere around the source (O). The ray path cuts the focal sphere at point A with an azimuth Φ_S and an angle of incidence i_h. *Right*: Projection of point A to A' onto the equatorial plane (after *Lay and Wallace* (1995)).

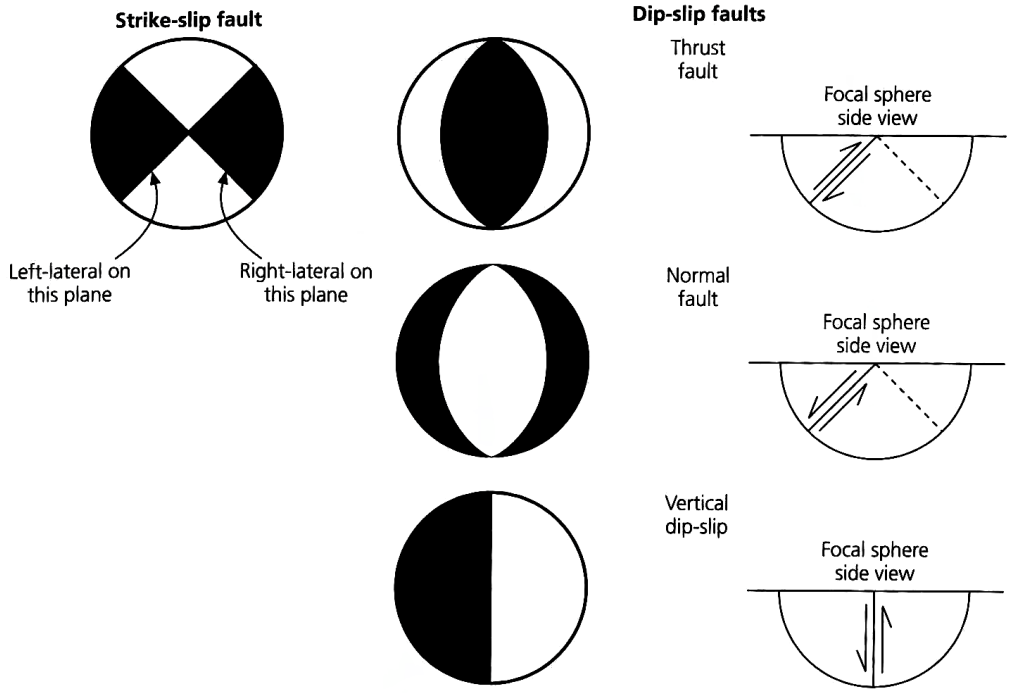

Figure 5.6.: Basis fault geometries and focal mechanisms. Black = compressional first-motions (*Stein and Wysession* (2009)). Copyright by 2003 by S. Stein and M. Wysession.

With the common approach that faulting occurs on planes 45° from the maximum and minimum compressive stresses the stress orientations can be obtained from focal mechanisms. The maximum compressive stress axis (P) and the minimum compressive stress axis (T) are located on a plane through both of the poles of the fault plane auxiliary plane, half-way between the nodal planes.

The focal mechanisms in this study were determined with *FPFIT* of *Reasenberg and Oppenheimer* (1985). The program calculates the double couple fault plane solution that best fits the observed first-motion polarities of an event. The best fit is obtained by comparing double couple source models to the observed polarities with a misfit function F, where $F = 0$ means a perfect fit and $F = 1$ a perfect misfit. The model that minimizes F then gives the fault plane solution. For the calculation only events with a minimum of 12 observed polarities from the best P wave onset (i.e. weighted as 0) are considered. Polarities determined on the hydrophone component were neglected as well, as the polarisation for some of the hydrophones was ambiguous. The program calculates several quantities that allow to estimate the quality of the solution:

- The misfit factor F (0 for perfect fit, 1 for perfect misfit).
- The station distribution ratio (SDR) ranges between 0 and 1 and quantifies the amount of polarities located near the nodal planes. Solutions that are based on a high number of polarities near nodal planes (<0.5) are less robust.
- The maximum half-width of 90% confidence rage of strike, dip and rake.

Solutions with a maximum half-width of 90% confidence $\geq 10°$ and a SDR ≤ 0.5 were neglected as well as solutions that did not converge. In addition, events that showed multiple solutions were not considered. This gave 32 fault plane solutions that were categorized into three quality classes based on the misfit factor F as follows:

Class A:	$F < 0.025$	(8 solutions)
Class B:	$0.025 \leq F \leq 0.1$	(11 solutions)
Class C:	$0.1 < F \leq 0.5$	(13 solutions)

The results of the obtained fault plane solutions are described in Section 7.3.

6. Splay fault acitivity revealed by aftershocks of the 2010 Mw 8.8 Maule earthquake, central Chile

The analysis of hypocenter locations derived by the P wave arrivals revealed a seismically active splay fault in the submarine forearc of central Chile. This feature was discussed in a paper published in Geology (Lieser, K., Grevemeyer, I., Lange, D., Flueh, E., Tilmann, F., Contreras-Reyes, E., 2014. Splay fault activity revealed by aftershocks of the 2010 Mw 8.8 Maule earthquake, central Chile. Geology 42, 823–826, doi:10.1130/G35848.1) that is included in this chapter in the original journal style. The publication has its own page numbers, refers to its own figure as well as table numbers and contains its own reference list. The related supplementary material can be found in Appendix E of this thesis. The supplementary material covers a brief describtion of the application and adaption of MPX, theoretical background of the Coulomb wedge theory that was applied in the paper to evaluate the mechanical state of the forearc, and a figure presenting a possible second active splay fault at the northern network boundary. Enlarged figures of the paper can be found in Appendix E (Figures E.1,E.2 and E.3).

Geology, published online on 29 July 2014 as doi:10.1130/G35848.1

Splay fault activity revealed by aftershocks of the 2010 M_W 8.8 Maule earthquake, central Chile

Kathrin Lieser[1], Ingo Grevemeyer[1], Dietrich Lange[1], Ernst Flueh[1], Frederik Tilmann[2,3], and Eduardo Contreras-Reyes[4]
[1]GEOMAR Helmholtz Centre for Ocean Research Kiel, 24148 Kiel, Germany
[2]GFZ German Research Centre for Geosciences Potsdam, 14473 Potsdam, Germany
[3]Free University Berlin, 14195 Berlin, Germany
[4]Departamento de Geofísica, Facultad de Ciencias Físicas y Matemáticas, Universidad de Chile, 8370449 Santiago, Chile

ABSTRACT

Splay faults, large thrust faults emerging from the plate boundary to the seafloor in subduction zones, are considered to enhance tsunami generation by transferring slip from the very shallow dip of the megathrust onto steeper faults, thus increasing vertical displacement of the seafloor. These structures are predominantly found offshore, and are therefore difficult to detect in seismicity studies, as most seismometer stations are located onshore. The M_w (moment magnitude) 8.8 Maule earthquake on 27 February 2010 affected ~500 km of the central Chilean margin. In response to this event, a network of 30 ocean-bottom seismometers was deployed for a 3 month period north of the main shock where the highest coseismic slip rates were detected, and combined with land station data providing onshore as well as offshore coverage of the northern part of the rupture area. The aftershock seismicity in the northern part of the survey area reveals, for the first time, a well-resolved seismically active splay fault in the submarine forearc. Application of critical taper theory analysis suggests that in the northernmost part of the rupture zone, coseismic slip likely propagated along the splay fault and not the subduction thrust fault, while in the southern part it propagated along the subduction thrust fault and not the splay fault. The possibility of splay faults being activated in some segments of the rupture zone but not others should be considered when modeling slip distributions.

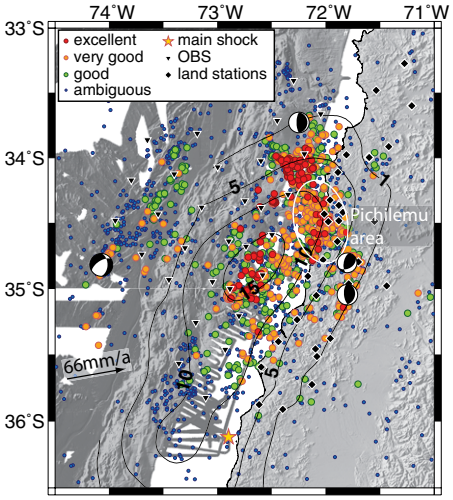

Figure 1. All aftershocks of the 2010 M_w 8.8 Maule earthquake, central Chile, recorded by the amphibious network (color coded by quality class). Black contour lines indicate coseismic slip (Moreno et al., 2012). Focal mechanisms were extracted from the global Centroid Moment Tensor catalog (Dziewonski et al., 1981; Ekström et al., 2012) for events during deployment time span and are shown at their relocated hypocenters. White ellipse marks the Pichilemu area. Convergence rate is from Angermann et al. (1999). OBS—ocean-bottom seismometer.

INTRODUCTION AND BACKGROUND

Thrust faults rising from plate interfaces in subduction zones to the seafloor are referred to as splay faults or megasplay faults (Moore et al., 2007; Melnick et al., 2012). They are considered to play a significant role in tsunami generation by enhancing vertical surface displacement and bringing it closer to the coast (e.g., Wendt et al., 2009), and may limit rupture propagation of great earthquakes (e.g., Melnick et al., 2012). Splay faults have been detected several times on reflection seismic profiles, e.g., in Chile and Japan (Geersen et al., 2011; Moore et al., 2007). In Sumatra, ocean-bottom seismometer (OBS) deployments in the aftermath of the 2004 Sumatra-Andaman megathrust earthquake have shown shallow forearc seismic activity, which has been associated with splay faults. However, seismicity distribution was diffuse and did not define a clear fault plane (Araki et al., 2006; Sibuet et al., 2007). Also in Sumatra, a deep-rooted master splay fault branching off at 50 km depth was postulated based on relocated global earthquakes (Waldhauser et al., 2012), and extrapolation of seismic reflection data. However, the inferred fault is not outlined directly by the seismicity. Observing seismicity associated with splay faults is challenging because they are located offshore, usually at the landward edges of accretionary prisms. Most of the local networks are installed onshore, so offshore seismicity and its relation to splay faulting are not well constrained and little is known about along strike variation of splay fault activity.

On 27 February 2010, the Chilean margin near Maule was struck by a megathrust event (moment magnitude M_w 8.8) followed by a destructive tsunami. In this paper we analyze the aftershocks of that megathrust event by combining OBS and land station data, and demonstrate active splay faulting in the submarine forearc off central Chile and along-strike variation of splay fault activation.

The Constitutión-Concepción segment in central Chile was considered to be a mature seismic gap showing little seismic activity on the megathrust since the last great earthquake in 1835. On 27 February 2010, this segment ruptured in the M_w 8.8 Maule earthquake, nucleating near 36°S and affecting a 500-km-long area of the margin. Coseismic slip, with as much as 16 m slip in the main patch north of the hypocenter, released most of the accumulated strain since the 1835 Darwin earthquake, therefore closing a known seismic gap (Moreno et al., 2012). After the main shock, a tsunami as high as 14 m hit the coast and caused enormous destruction (Vargas et al., 2011). Aftershocks of the M_w 8.8 Maule earthquake occurred along an ~500-km-long portion of the central Chilean margin; most of them were offshore (Lange et al., 2012; Rietbrock et al., 2012).

The Maule event triggered intense activity in the upper plate, particularly near Pichilemu, at ~34.5°S (Figs. 1 and 2) north of the main shock along a northwest-striking fault (e.g., Ryder et al., 2012; Farías et al., 2011); the two largest events (~M_w 7) occurred on 11 March 2010 and showed normal faulting focal mechanisms (see Fig. DR2 in the GSA Data Repository[1]).

The frontal accretionary prism near the trench (outer wedge) in the Maule region is ~40 km wide and is made of poorly consolidated sediments (Moscoso et al., 2011; Contreras-Reyes et al., 2010). It is limited by a backstop from an inner wedge, which consists of continental framework rock or continental crust made of paleo–accretionary complexes (Contreras-Reyes et al., 2010). Seismological constraints show that the updip limit of aftershock seismicity of the Maule event corresponds to the tran-

[1]GSA Data Repository item 2014296, Figure DR1 (station configuration), Figure DR2 (gCMT focal mechanisms), Figure DR3 (aftershock cluster at northern boundary), automatic P-wave picking and event localization, and critical Coulomb wedge theory, is available online at www.geosociety.org/pubs/ft2014.htm, or on request from editing@geosociety.org or Documents Secretary, GSA, P.O. Box 9140, Boulder, CO 80301, USA.

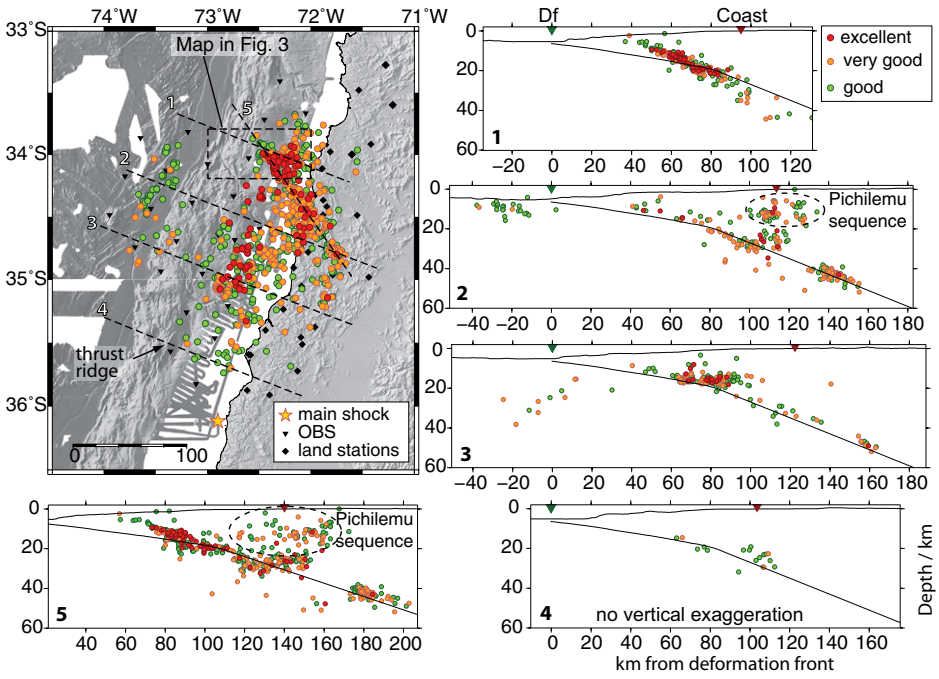

Figure 2. Map and profiles 1–5 showing aftershocks of the 2010 M_w 8.8 Maule earthquake, central Chile, with qualities good or better, and located within the network. Dashed lines in map indicate location of profiles perpendicular to the trench, as well as location of Figure 3A. Swath width of profiles is 20 km. Green and red triangles mark projected locations of the deformation front (df) and the coast, respectively. OBS—ocean-bottom seismometer. Plate boundary from refraction seismic measurements of Moscoso et al. (2011) (above ~20 km depth) and Slab1.0 model of Hayes et al. (2012) (below ~20 km depth).

sition between the frontal accretionary prism (outer wedge) and continental crust (inner wedge) (Moscoso et al., 2011; Lange et al., 2012), where splay faulting can occur (Collot et al. 2008). Because the inner wedge is significantly stronger than the outer wedge, seismic velocities should increase landward.

DATA AND PROCESSING

We deployed a local network of 30 OBSs for a 3 month period between 20 September and 25 December 2010, with a station spacing of ~40 km in the northern part of the rupture zone where the highest slip rates occurred. In addition, 33 temporary land stations from the late phase of the International Maule Aftershock Deployment (Beck et al., 2014) were included in the analysis, leading to an amphibious network that provides an excellent coverage of the northern part of the rupture plane offshore as well as onshore (Fig. DR1).

The picking of P-wave onsets was performed with an automated P-wave picking engine (MPX by Aldersons, 2004) and led to 67,454 P-wave onsets. After hypocenter localization with NonLinLoc (Lomax, 2011) with a 2.5-dimensional velocity model based on refraction seismic profiles (Moscoso et al., 2011) and a local earthquake study (Kraft, 2011; Dannowski et al., 2013), the events were classified into five quality categories using the scheme of Husen and Smith (2004) (Table DR2 in the Data Repository). In total, 3751 events were located and 1043 events were classified as good or better. Further details of the automated picking, event location, and velocity model are provided in the Data Repository.

RESULTS

Locations of all aftershocks divided into quality classes are displayed in Figure 1. The forearc seismicity is separated from outer rise seismicity by a zone nearly devoid of seismicity corresponding to the frontal accretionary prism. Aftershocks in the outer rise are aligned along fractures reaching to the seafloor (Fig. 1; see Fig. DR1 for bathymetry). Focal mechanisms provided by the global Centroid Moment Tensor catalog (Dziewonski et al., 1981; Ekström et al., 2012) for the entire aftershock sequence (Fig. DR2) show exclusively normal faulting events in the outer rise, indicating extension in the oceanic plate. In Figure 1, we present relocated global Centroid Moment Tensor catalog (gCMT) focal mechanisms during the deployment period where mechanisms in the forearc region are related to thrust events on the plate interface.

Figure 2 shows profiles cutting the network perpendicular to the trench where only events within the network are considered. The northernmost profile (profile 1) reveals a 50-km-long linear structure extending from the subducting plate to the seafloor, indicating postseismic activity in the upper plate, that we interpret as a splay fault. No further seismicity is detectable along the plate interface trenchward of the intersection of the splay fault and the subducting plate, indicating aseismic behavior of the plate interface for distances of <60 km to the deformation front. Figure 3A provides an enlarged view on the bathymetry in the splay fault region, where a prominent thrust ridge spatially coincides with the outcrop of the splay fault. The profile in Figure 3B includes the P-wave velocity distribution, based on the seismic refraction model of Moscoso et al. (2011), showing that the fault begins to branch off of the main fault at ~20 km depth, ~67 km from the deformation front, with an angle of 7°–8°. This region is characterized by a landward increase of seismic velocities indicating the transition from outer to inner wedge. An analysis of origin times of the splay fault events shows no time dependence, as they are evenly distributed over the three month deployment time span.

Profile 2 (Fig. 2) crosses the Pichilemu area, which has prominent crustal seismicity below the coastal region. Another clear feature in this profile is the seismic gap along the plate

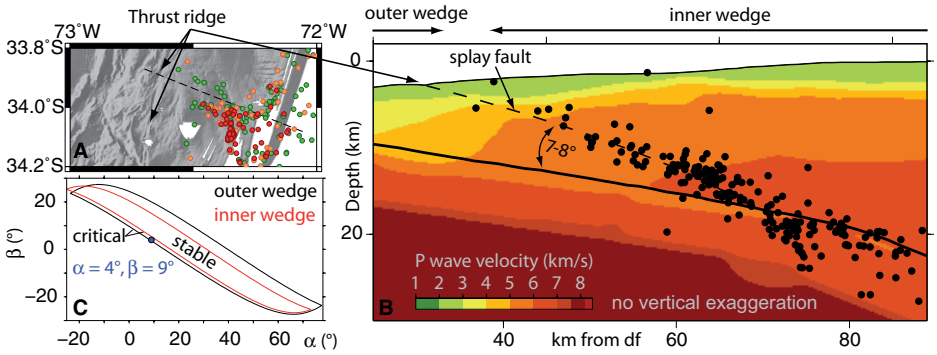

Figure 3. A: Bathymetry in the splay fault region. B: Profile 1 of Figure 2. P-wave velocity model is from Moscoso et al. (2011). Locations of outer and inner wedge are estimated from landward-increasing velocities; df—deformation front. C: Stability diagram for outer and inner wedge in the northern deployment area; α—surface slope, β—slab dip. Blue dot marks the taper corresponding to the splay fault region. For more information, see the Data Repository (see footnote 1).

interface at ~35–40 km depth (also observed by Lange et al., 2012; Rietbrock et al., 2012). This gap might be related to the intersection of the continental Moho and the plate interface, observed by receiver function analysis at 38 km depth (Dannowski et al., 2013).

Profile 5 is aligned parallel to the Pichilemu sequence, revealing its distinct onset at ~95 km profile length. In contrast, profile 3 contains no increased seismicity in the upper continental crust and the seismic gap is not as distinct as in profile 2. This is consistent with the results of Lange et al. (2012), wherein the seismic cluster below the gap was observed as not truly continuous, but as several subclusters elongated parallel to the trench.

In the southernmost profile (profile 4), the seismicity is exclusively related to the plate interface with a reduced number of events compared to the northern profiles. From profiles 2–4 in Figure 2, the updip limit of aftershocks along the plate interface can be identified at a distance ~40 km landward from the deformation front.

DISCUSSION

Our analysis of local aftershock data of the Maule event from a dense amphibious seismometer network revealed a well-resolved splay fault at the transition from outer to inner wedge in the submarine forearc of the central Chilean subduction zone. In map view the seismicity in the splay appears to form a continuous northwest-southeast–oriented lineament with the events in the Pichilemu area. However, profile 5 in Figure 2 along the strike direction of the large aftershocks demonstrates that the splay fault and Pichilemu seismicity form two clearly identifiable separate groups, with the onset of the crustal Pichilemu sequence at ~120 km distance to the deformation front, which is ~30 km downdip of where the splay fault branches off the main fault. The two groups show distinct focal mechanisms; thrust subparallel to the trench for the splay fault area, and extensional faulting oblique to the trench for the Pichilemu group (Fig. DR2).

Margin-parallel thrust ridges can be identified in the bathymetry almost throughout the network (see Fig. DR1). Based on reflection seismic data, Geersen et al. (2011) interpreted the thrust ridge crossing profile 4 in Figure 2 as connected with a splay fault; the branching off of the main fault is unclear because their seismic reflection lines do not resolve the plate boundary. However, active splay fault seismicity is only observed in the northern part of the survey area, indicating that the splay fault along the margin is only partly activated. Wang and Hu (2006) proposed, with the dynamic Coulomb theory, that the outer wedge, which overlies the velocity-strengthening part of the subduction fault, switches between stable and critical states during earthquake cycles and that coseismically activated splay faults will become more stable after an earthquake when the outer wedge becomes more stable due to relaxation. Rosenau et al. (2009) also suggested that reactivation of splay faults can act as a relaxation mechanism for coseismic compression. Therefore, the absence of a seismically active splay fault in the southern part of the deployment area suggests a stable wedge, whereas reactivation of a splay fault in the northern part implies that the wedge is in a critical state. This corresponds with an analysis of the mechanical properties of the Maule earthquake area (Cubas et al., 2013), which also implies that a large part of the wedge about north of profile 2 is critical while it is mostly stable south of it. Based on Cubas et al.'s (2013) parameters, we calculated a stability diagram for the outer and inner wedge (Fig. 3C; Fig. DR6) according to the critical Coulomb wedge theory, which simplifies wedges as homogeneous with constant parameters for internal density, friction coefficient, fluid pressure conditions, and effective basal friction coefficient (Dahlen, 1990; Davis et al., 1983). For the splay fault area, the wedge reaches a critical state and the location of the taper along the envelope suggests that the wedge is prone to fail by thrusting (Dahlen, 1984). The critical wedge in combination with the lack of any seismic activity along the plate interface updip of the splay fault indicates not only postseismic activity, but also coseismic activity along the splay thrust fault. Therefore, we suggest that the preexisting splay fault in the submarine forearc was favored over the plate boundary during the main shock and did not continue along the subduction thrust fault in the northern deployment area.

The splay fault is located north of the coseismic slip maximum in a region of large coseismic slip gradient (Fig. 1) and thus may have acted as a barrier limiting the along-strike extent of the rupture zone. Tsunami runups are poorly correlated with the coseismic slip distribution; for example, on average, they are as high at the coast opposite the inferred splay fault at 34°S as they are opposite the main slip patch just north of 35°S, in spite of much smaller displacement values (Fritz et al., 2011). Whereas interpreting tsunami runups is notoriously difficult due to the strong effects of shallow topography, a reason for this observation might be that the steeper dip of the splay fault has enhanced the local tsunami size.

At the northernmost boundary of the seismic network, a small cluster of aftershocks can be identified (72.3°W, 33.3°S; Fig. 1; Fig. DR3), which appear to rise from the plate interface to shallower depths, possibly suggesting another splay fault. Origin times show that the cluster is highly time dependent. However, because these events occurred outside of the network, the depth resolution is reduced and it is not certain whether the events follow the interface or a possible (splay) fault. The stability diagram (Fig. DR6) shows that the taper for that area is near the critical envelopes, suggesting thrust faulting.

The updip limit of aftershocks correlates with the thrust ridges (Fig. 2; Fig. DR1). However, the interpretation of this simple observation varies along strike. In the northern part of the survey area the updip limit along the plate interface is not related to where rupture terminated as it propagated along the splay fault. In contrast, in the southern part, where no hint of a splay fault was found in our data, rupture appears to have propagated along the plate interface.

CONCLUSIONS

Aftershocks of the 2010 Maule event observed on an amphibious seismic network reveal a seismically active 50-km-long splay fault in the submarine forearc of central Chile. The plate interface trenchward of the branching point shows no seismic activity during the deployment period. From this observation we consider it likely that slip in this part of the rupture zone transferred onto a splay fault. Critical taper theory suggests that this part of the wedge is at the edge of instability in a compressive stress state. Rupture of future great megathrust earthquakes in that area may propagate along the splay fault again or may reactivate other splay faults when the outer wedge enters the critical state, increasing vertical displacements due to the steeper dip of the splay fault compared to the plate interface, and therefore potentially increasing the amplitude of a tsunami wave.

Between 34.5°S and 36°S, the updip limit of the aftershock seismicity is clearly identified ~40 km landward from the deformation front. As ruptures can propagate along splay faults, the updip limit, as seen in seismicity distribution maps, is not necessarily related to events along the plate boundary but instead to splay faulting in the overriding plate.

Although margin-parallel thrust ridges can be observed almost throughout the network, postseismic splay faulting occurred only for a small fraction, indicating that the splay fault was only partly activated. Thus, when modeling slip distributions it should be considered that slip does not necessarily propagate along the entire extent of a splay fault inferred from bathymetry or reflection seismic data.

The location of the splay fault coincides with large slip gradients at the northern termination of the rupture zone and may have limited northward rupture propagation of the Maule 2010 main shock.

ACKNOWLEDGMENTS

Marine efforts were funded by the German government through grant 03G0212A. Data analysis was funded by German Science Foundation (DFG) grant GR1964/14-1. This study is part of the Maule Earthquake: Integration of Seismic Cycle Observations and Structural Investigations (MARISCOS) project.

We thank the crew of the RV *SONNE* for their great support. The land station network was deployed by GeoForschungsZentrum Potsdam (GFZ) and is archived under FDSN network code ZE (2010-2011) at the GEOFON (GeoForschungsNetz) data center. Figures were generated with Generic Mapping Tools (GMT; Wessel and Smith, 1998). We thank the editors R. Holdsworth and A. Barth and three reviewers for constructive comments.

REFERENCES CITED

Aldersons, F., 2004, Toward a three-dimensional crustal structure of the Dead Sea region from local earthquake tomography [Ph.D. thesis]: Tel Aviv, Israel, Tel Aviv University, 123 p.

Angermann, D., Klotz, J., and Reigber, C., 1999, Space-geodetic estimation of the Nazca–South America Euler vector: Earth and Planetary Science Letters, v. 171, p. 329–334, doi:10.1016/S0012-821X(99)00173-9.

Araki, E., Shinohara, M., Obana, K., Yamada, T., Kaneda, Y., Kanazawa, T., and Suyehiro, K., 2006, Aftershock distribution of the 26 December 2004 Sumatra-Andaman earthquake from ocean bottom seismographic observation: Earth, Planets, and Space, v. 58, p. 113–119.

Beck, S., Rietbrock, A., Tilmann, F., Barrientos, S., Meltzer, A., Oncken, O., Bataille, K., Roecker, S., Vilotte, J.-P., and Russo, R.M., 2014, Advancing subduction zone science with international collaboration and open data: Eos (Transactions, American Geophysical Union), v. 95, p. 193–194, doi:10.1002/2014EO230001.

Collot, J.-Y., Agudelo, W., Ribodetti, A., and Marcaillou, B., 2008, Origin of a crustal splay fault and its relation to the seismogenic zone and underplating at the erosional north Ecuador-south Colombia oceanic margin: Journal of Geophysical Research, v. 113, B12102, doi:10.1029/2008JB005691.

Contreras-Reyes, E., Flueh, E.R., and Grevemeyer, I., 2010, Tectonic control on sediment accretion and subduction off south central Chile: Implications for coseismic rupture processes of the 1960 and 2010 megathrust earthquakes: Tectonics, v. 29, TC6018, doi:10.1029/2010TC002734.

Cubas, N., Avouac, J.-P., Souloumiac, P., and Leroy, Y., 2013, Megathrust friction determined from mechanical analysis of the forearc in the Maule earthquake area: Earth and Planetary Science Letters, v. 381, p. 92–103, doi:10.1016/j.epsl.2013.07.037.

Dahlen, F.A., 1984, Noncohesive critical Coulomb wedges: An exact solution: Journal of Geophysical Research, v. 89, no. B12, p. 10125–10133, doi:10.1029/JB089iB12p10125.

Dahlen, F.A., 1990, Critical taper model of fold-and-thrust belts and accretionary wedges: Annual Review of Earth and Planetary Sciences, v. 18, p. 55–99, doi:10.1146/annurev.ea.18.050190.000415.

Dannowski, A., Grevemeyer, I., Kraft, H., Arroyo, I., and Thorwart, M., 2013, Crustal thickness and mantle wedge structure from receiver functions in the Chilean Maule region at 35° S: Tectonophysics, v. 592, p. 159–164, doi:10.1016/j.tecto.2013.02.015.

Davis, D.M., Suppe, J., and Dahlen, F.A., 1983, Mechanics of fold-and-thrust belts and accretionary wedges: Journal of Geophysical Research, v. 88, p. 1153–1172, doi:10.1029/JB088iB02p01153.

Dziewonski, A.M., Chou, T.-A., and Woodhouse, J.H., 1981, Determination of earthquake source parameters from waveform data for studies of global and regional seismicity: Journal of Geophysical Research, v. 86, p. 2825–2852, doi:10.1029/JB086iB04p02825.

Ekström, G., Nettles, M., and Dziewonski, A.M., 2012, The global CMT project 2004–2010: Centroid-moment tensors for 13,017 earthquakes: Physics of the Earth and Planetary Interiors, v. 200–201, p. 1–9, doi:10.1016/j.pepi.2012.04.002.

Farías, M., Comte, D., Roecker, S., Carrizo, D., and Pardo, M., 2011, Crustal extensional faulting triggered by the 2010 Chilean earthquake: The Pichilemu seismic sequence: Tectonics, v. 30, TC6010, doi:10.1029/2011TC002888.

Fritz, H.M., et al., 2011, Field survey of the 27 February 2010 Chile tsunami: Pure and Applied Geophysics, v. 168, p. 1989–2010, doi:10.1007/s00024-011-0283-5.

Geersen, J., Behrmann, J.H., Völker, D., Krastel, S., Ranero, C.R., Diaz-Naveas, J., and Weinrebe, W., 2011, Active tectonics of the South Chilean marine fore arc (35° S–40° S): Tectonics, v. 30, TC3006, doi:10.1029/2010TC002777.

Hayes, G.P., Wald, D.J., and Johnson, R.L., 2012, Slab1.0: A three-dimensional model of global subduction zone geometries: Journal of Geophysical Research, v. 117, B01302, doi:10.1029/2011JB008524.

Husen, S., and Smith, R., 2004, Probabilistic earthquake relocation in three-dimensional velocity models for the Yellowstone National Park region, Wyoming: Seismological Society of America Bulletin, v. 94, p. 880–896, doi:10.1785/0120030170.

Kraft, H.A., 2011, Lokalbebenanalyse am aktiven Kontinentalrand Südamerikas zwischen 34°S und 36°S [M.S. thesis]: Kiel, IFM-GEOMAR and Christian-Albrechts-University Kiel, 79 p.

Lange, D., et al., 2012, Aftershock seismicity of the 27 February 2010 Mw 8.8 Maule earthquake rupture zone: Earth and Planetary Science Letters, v. 317–318, p. 413–425, doi:10.1016/j.epsl.2011.11.034.

Lomax, A., 2011, NonLinLoc Version 6.00: Probabilistic, non-linear, global-search earthquake location in 3D media: NonLinLoc, http://alomax.free.fr/nlloc/index.html.

Melnick, D., Moreno, M., Motagh, M., Cisternas, M., and Wesson, R.L., 2012, Splay fault slip during the M_w 8.8 2010 Maule Chile earthquake: Geology, v. 40, p. 251–254, doi:10.1130/G32712.1.

Moore, G.F., Bangs, N.L., Taira, A., Kuramoto, S., Pangborn, E., and Tobin, H.J., 2007, Three-dimensional splay fault geometry and implications for tsunami generation: Science, v. 318, p. 1128–1131, doi:10.1126/science.1147195.

Moreno, M., et al., 2012, Toward understanding tectonic control on the M_w 8.8 2010 Maule Chile earthquake: Earth and Planetary Science Letters, v. 321–322, p. 152–165, doi:10.1016/j.epsl.2012.01.006.

Moscoso, E., Grevemeyer, I., Contreras-Reyes, E., Flueh, E.R., Dzierma, Y., Rabbel, W., and Thorwart, M., 2011, Revealing the deep structure and rupture plane of the 2010 Maule, Chile earthquake (Mw = 8.8) using wide angle seismic data: Earth and Planetary Science Letters, v. 307, p. 147–155, doi:10.1016/j.epsl.2011.04.025.

Rietbrock, A., Ryder, I., Hayes, G., Haberland, C., Comte, D., Roecker, S., and Lyon-Caen, H., 2012, Aftershock seismicity of the 2010 Maule Mw=8.8, Chile, earthquake: Correlation between co-seismic slip models and aftershock distribution?: Geophysical Research Letters, v. 39, L08310, doi:10.1029/2012GL051308.

Rosenau, M., Lohrmann, J., and Oncken, O., 2009, Shocks in a box: An analogue model of subduction earthquake cycles with application to seismotectonic forearc evolution: Journal of Geophysical Research, v. 114, B01409, doi:10.1029/2008JB005665.

Ryder, I., Rietbrock, A., Kelson, K., Bürgmann, R., Floyd, M., Socquet, A., Vigny, C., and Carrizo, D., 2012, Large extensional aftershocks in the continental forearc triggered by the 2010 Maule earthquake, Chile: Geophysical Journal International, v. 188, p. 879–890, doi:10.1111/j.1365-246X.2011.05321.x.

Sibuet, J.-C., et al., 2007, 2004 great Sumatra-Andaman earthquake: Co-seismic and post-seismic motions in northern Sumatra: Earth and Planetary Science Letters, v. 263, p. 88–103, doi:10.1016/j.epsl.2007.09.005.

Vargas, G., Farías, M., Carretier, S., Tassara, A., Baize, S., and Melnick, D., 2011, Coastal uplift and tsunami effects associated to the 2010 Mw8.8 Maule earthquake in Central Chile: Andean Geology, v. 38, p. 219–238, doi:10.5027/andgeoV38n1-a12.

Waldhauser, F., Schaff, D.P., Diehl, T., and Engdahl, E.R., 2012, Splay faults imaged by the fluid-driven aftershocks of the 2004 M_w 9.2 Sumatra-Andaman earthquake: Geology, v. 40, p. 243–246, doi:10.1130/G32420.1.

Wang, K., and Hu, Y., 2006, Accretion prisms in subduction earthquake cycles: The theory of dynamic Coulomb wedge: Journal of Geophysical Research, v. 111, B06410, doi:10.1029/2005JB004094.

Wendt, J., Oglesby, D.D., and Geist, E.L., 2009, Tsunamis and splay fault dynamics: Geophysical Research Letters, v. 36, L15303, doi:10.1029/2009GL038295.

Wessel, P., and Smith, W.H., 1998, New, improved version of generic mapping tools released: Eos (Transactions, American Geophysical Union), v. 79, p. 579, doi:10.1029/98EO00426.

Manuscript received 7 May 2014
Revised manuscript received 2 July 2014
Manuscript accepted 3 July 2014

Printed in USA

7. Results

The seismicity distribution with the main focus on forearc seismic activity was described in the Geology paper, in Chapter 6. Therefore, the first section of this chapter on seismicity distribution focuses on the seismic activity in the outer rise and the differences between hypocentre locations derived from P and S phase arrivals combined and locations from P phase arrivals alone. Afterwards, the results of the magnitude and seismic moment as well as focal mechanism determinations are presented. The last section of this chapter analyses the data set deployed in 2008 prior to the Maule earthquake.

7.1. Seismicity distribution

The main features of the seismic activity, already described in the paper (*Lieser et al.*, 2014), are: (1) the forearc seismicity separated from outer rise seismicity by a zone nearly devoid of seismicity corresponding to the frontal accretionary prism, (2) splay fault activity in the northern part of the network, (3) the alignment of aftershocks in the outer rise along fractures reaching to the sea floor, (4) a seismic gap along the plate interface at about 35–40 km depth (also observed by *Lange et al.* (2012a) and *Rietbrock et al.* (2012)), (5) and the crustal seismicity below the coastal region near Pichilemu, and (6) the updip limit of aftershocks along the plate interface identified at a distance about 40 km landward from the deformation front.

Figure 7.1 shows the seismicity distribution of the detected aftershocks colour coded by quality class. In addition to Figure 2 of the paper, the 100°C boundary from *Grevemeyer et al.* (2005) is included as well as a subset of events classified as "ambiguous", and events that were located outside of the network. The location of the 100°C line correlates well with the updip limit of aftershocks about 40 km trenchward of the deformation front, indicating that one factor limiting the seismicity updip may be the transition from stable sliding clays to stronger clays at about 100–150°C. This process usually takes place in depth of 5–15 km that correlates as well with the depths of the updip limit in the data.

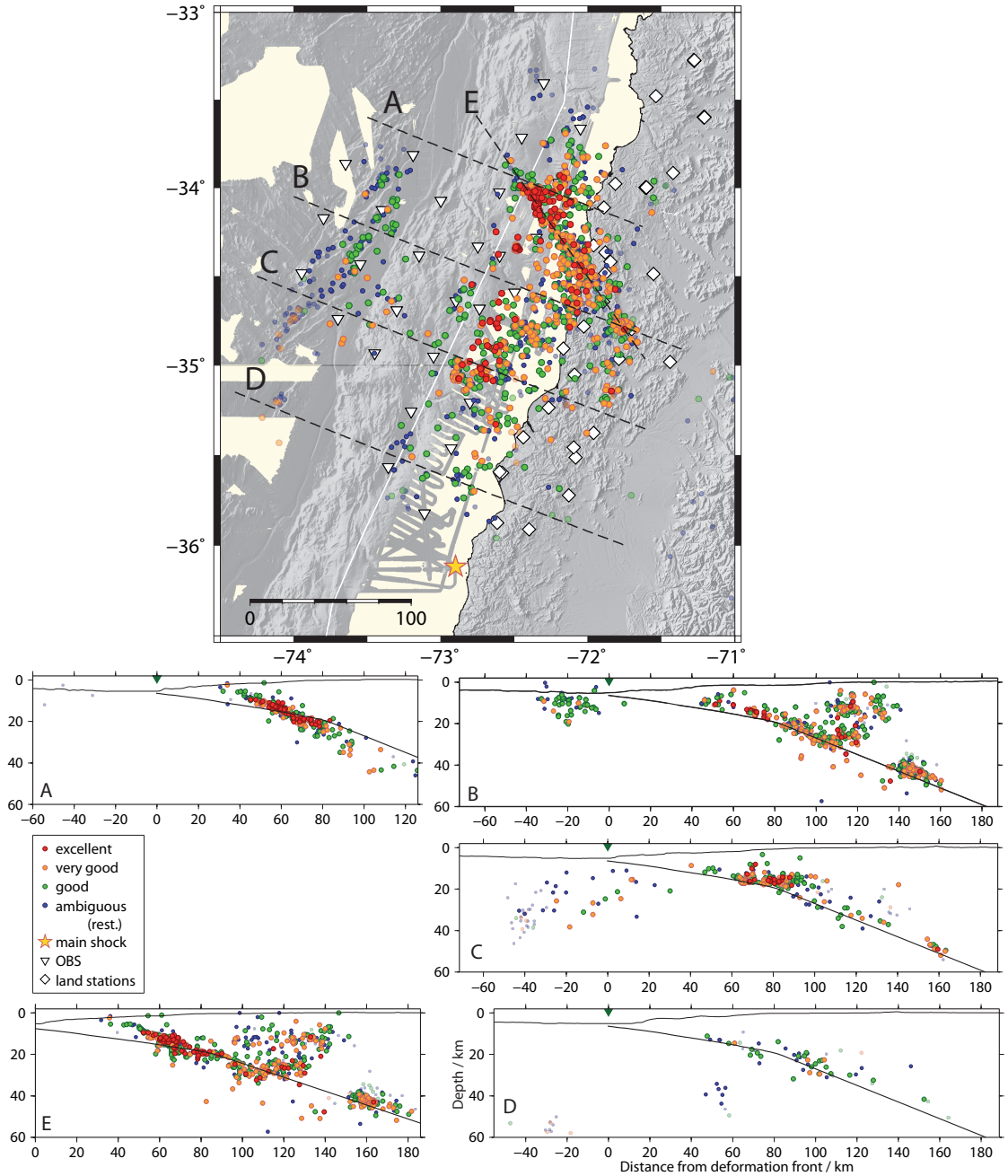

Figure 7.1.: Seismicity distribution derived from P phase arrivals. The white line in the map marks the 100°C boundary (from *Grevemeyer et al.* (2005)). The transparent events show a gap of greater than 180° while the opaque ones are events within the network (gap $< 180°$). Events classified as "ambiguous" are restricted to a maximum average error ellipsoid half-axis of 8 km. Swath widths for profiles A,C and D: 20 km; swath widths for profiles B and E: 30 km. No vertical exaggeration in cross-sections.

Aftershocks in the outer rise are aligned along fractures reaching to the sea floor (Fig. 7.1). As the largest location errors are usually related to depth and not the location of the epicentre, it is worthwhile to consider not only events with good location qualities but also lower qualities. In Figure 3.7, showing a map and cross section with events of all location qualities, the alignment of outer rise earthquakes along discrete fractures that correlate with trench-parallel bathymetric structures becomes more pronounced. Hypocentre locations of the outer rise events appear to increase in depth to the South as can be seen in cross sections B, C and D of Figure 7.1. In cross section B they are restricted to the upper about 15 km while further south, in section C, the hypocentre depths reach to about 50 km and in section D to even 60 km depth. Further, in cross section C the outer rise events seem to be aligned along two landward dipping bands. Hypocenter locations in the outer rise in 50 or 60 km depths are highly unlikely because they would be located in a region of the upper mantle where the material is not strong enough to build up strain that is released in an earthquake. The hypocentre locations below 40 km depth in sections C and D are located outside the network what strongly decreases the resolution, especially in depth. However, the hypocentre locations from events within the network reach depths to about 40 km in section C. This is still very deep for outer rise events. In order to better constrain the hypocentre depths, the arrival times of the S and P phases of events located in the near vicinity of a station are subtracted. Ideally, the events would be located directly beneath a station for this procedure. Because P waves travel faster than S waves the difference between P and S phase travel times increases with increasing distance from the hypocentre. There are three stations in the outer rise where events are located in the near proximity, OB09, OB13 and OB14 (see Fig. 7.1 and 7.2). Because the horizontal components of OB15 show poor data quality, the S-P time for the event located near that station cannot be determined. The S-P times show that the events below OB13 are located deeper than below OB09, whereas events below OB14 show approximately the same S-P times than OB09. However, OB14 is located in a greater distance from the trench than OB09 and OB15. The determined hypocentres of those events are located in about 30 km depth, but they are not well constrained as either the event is classified as “ambiguous” or the gap is bigger than 180°, both strongly affecting hypocentre depth determination. Therefore, the events below OB14 are likely to be located in lower depth than determined in the location process. However, when comparing S-P times from OB09 and OB13, there is an indication that events below OB13, more to the South, are located in greater depth than below OB09. With various assumptions on the velocity, the hypocentre depth could be determined from S-P times. But as this depth would only be constrained by a single time and a velocity assumption, the determined hypocentres by NLL are more reliable. Cross section D shows a cluster of seismicity in the descending slab, about 40 to 60 km landward to the trench, in about 40 km depth. The cluster consists of events classified as “ambiguous”, or of events of higher quality class but with gaps greater

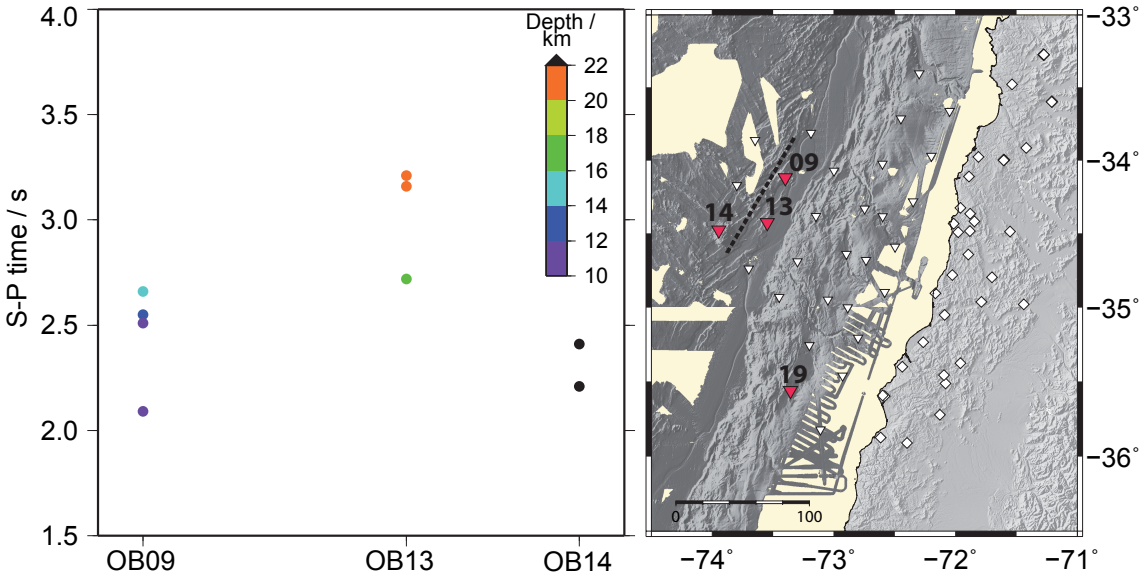

Figure 7.2.: S-P times for three stations in the outer rise. Stations positions are projected along the dashed profile through the outer rise. Hypocenter depths from NLL. For S-P results regarding OB19 see text. Triangles are OBS locations and diamonds land station locations.

than 180°, and therefore is not well constrained in depth. The S-P times determined for three events near OB19, two located along the plate boundary and one located in the deeper cluster, are all within the same time range with 3.72 s for the cluster event and 3.61 s and 3.67 s for the plate boundary events. The S-P time for the cluster event is a little bit higher but it is also located a bit farther away from the station. Therefore, the three events are probably located in the same depth either in the deeper cluster or along the plate boundary. The events near OB13 show similar S-P times but are located in greater depth than where the plate boundary is assumed below OB19. However, the sediments below OB19 are significantly thicker in the forearc than in the outer rise, increasing P and S wave travel times. Therefore, the "deeper" cluster may more likely be located along the plate boundary.

Figure 7.3 shows the seismicity distribution after the hypocentre determination including S wave onsets compared to the seismicity distribution derived by P phase arrivals only. In general, the hypocentre distribution did not change much. But, the amount of events classified as "excellent" increased significantly, especially in the Pichilemu cluster. The structures within the cluster are now sharper with additional S phase arrivals. In the splay fault area, hypocentre locations were improved: the events aligned above the splay fault are now located closer to the fault (cross section A). However, there is also a considerate amount of events that is downgraded into quality classes lower than "good" after including S phase arrivals, especially in the

outer rise. Along with this, the deep outer rise events in cross section C are now located in even greater depth. This is most likely an effect of the hypocentre determination process assuming that the vp/vs-ratio is constant over the entire survey area. With a better constrained vp/vs-ratio distribution the hypocentre determination including S phase arrivals could be improved.

7.2. Moment magnitudes and seismic moment release

In Figure 7.4 the magnitude distribution in map view and on cross sections cutting through the network are presented. The magnitudes show a homogeneous distribution vertically as well as horizontally. Larger or smaller events are not confined to the outer rise or forearc, nor to shallow or large depths. This can also be seen in Figure 7.5, where a histogram and the depth distribution of the magnitudes are presented. The smallest magnitude that could be detected was 1.9. Especially offshore where only two stations were available for the magnitude determination, smaller events may have originated too far away from a station to have been detected. The largest event that took place during the deployment time span had a magnitude of 4.6. It is located at the northern network boundary in the submarine forearc at about 24 km depth at the plate boundary (33.75° S, 72.30° E). Most events have a moment magnitude of about 2.5.

The relation between frequency of occurrence and size was described by *Gutenberg and Richter* (1941) for a given time period in a given region with the equation:

$$\log N = A - bM, \tag{7.1}$$

where N is the number of events, A and b are constants, and the magnitude M varies in a fixed range. A gives the maximum expected earthquake when considering a time period of a year and the b-value being 1. The higher the b-value, the higher is the amount of smaller events compared to larger events. In seismically active regions it is usually close to 1. If the b-value deviates much from the expected range it can be an indication that the magnitude catalogue of the survey area is incomplete or the magnitude calculation contains errors. The b-value in this study (about 1.5) is higher than expected because b-values of other studies in Chile are considerably lower (*Barrientos*, 1981; *Sobiesiak*, 2000). However, *Barrientos et al.* (2004) found a b-value of 1.4 in a study of crustal seismicity in central Chile for earthquakes between 1986 and 2001.

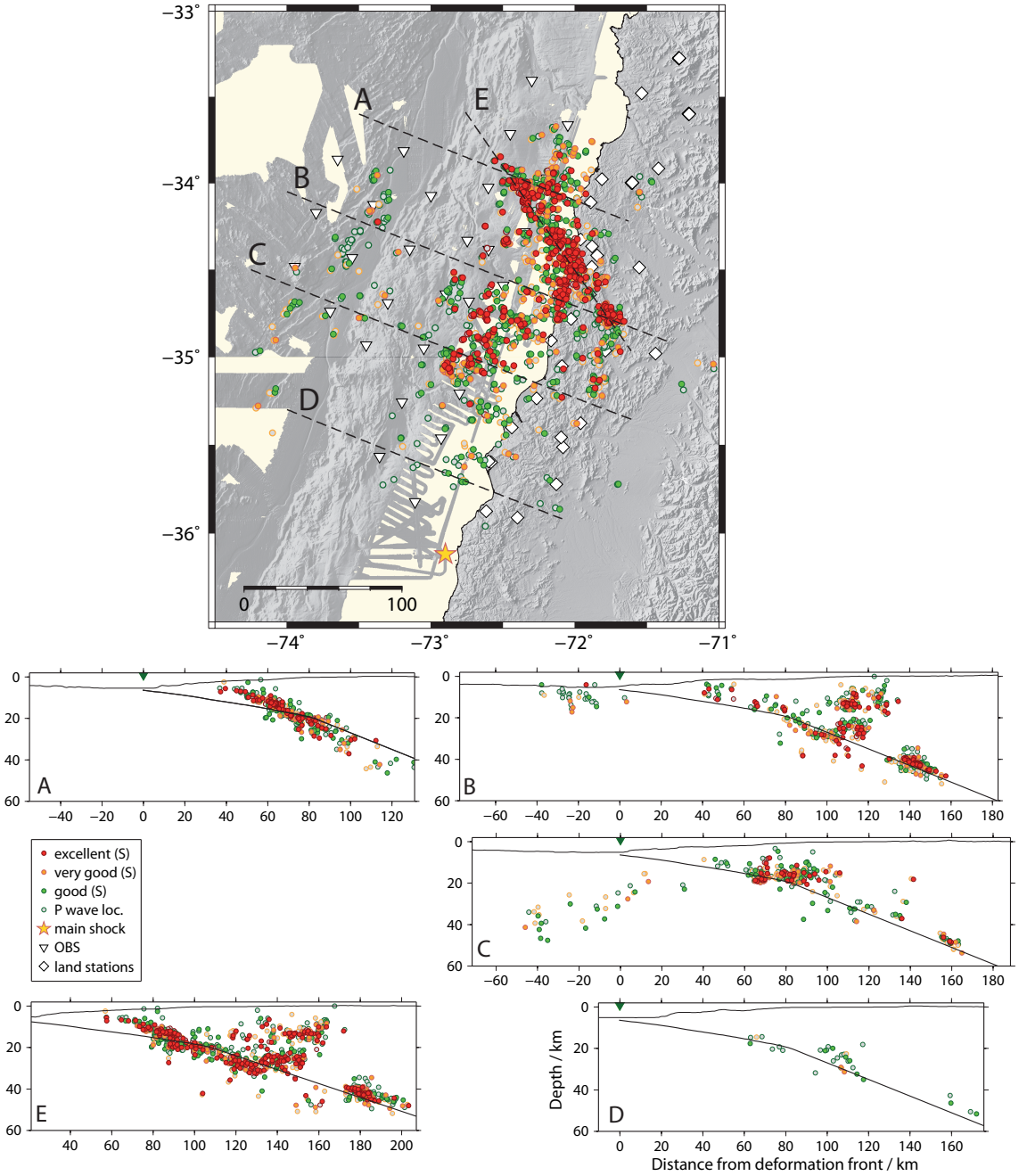

Figure 7.3.: Hypocenter locations including S phase arrivals (coloured) compared to locations derived by P phase arrivals only (grey). No vertical exaggeration in cross-sections. Green triangle marks the deformation front

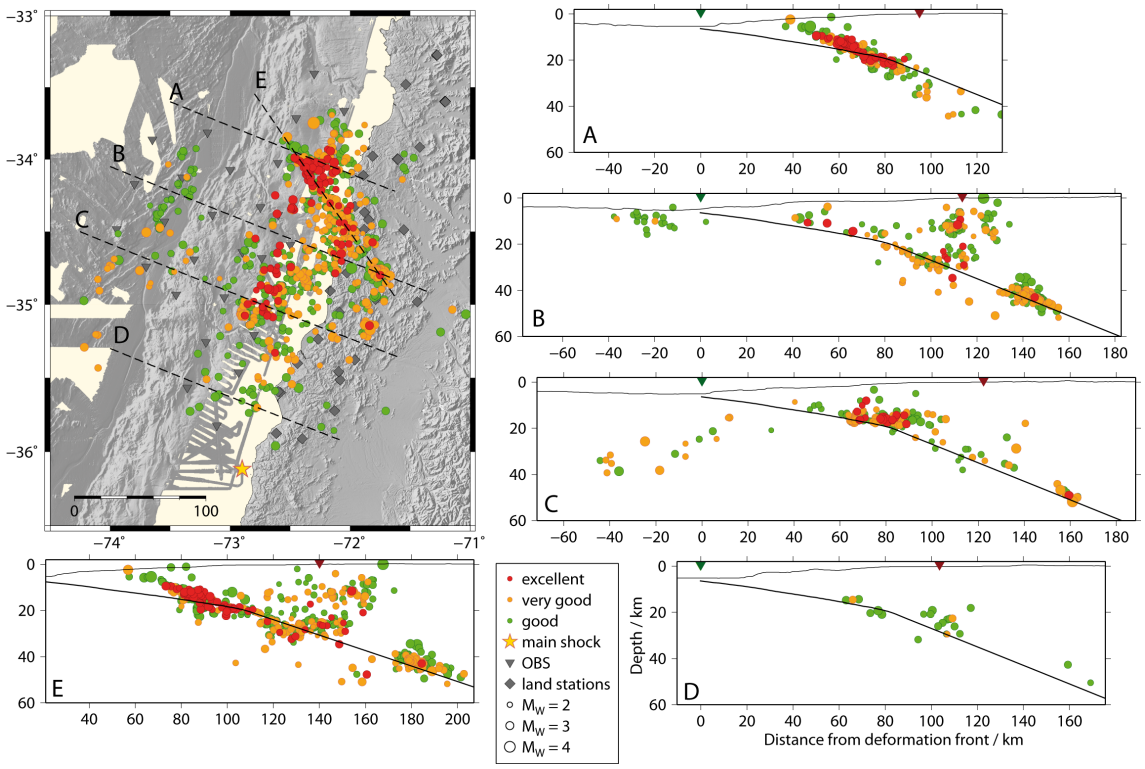

Figure 7.4.: Moment magnitude distribution for events with quality classes "excellent" to "good". The green triangles in the cross sections mark the deformation front while the red triangles mark the location of the coast.

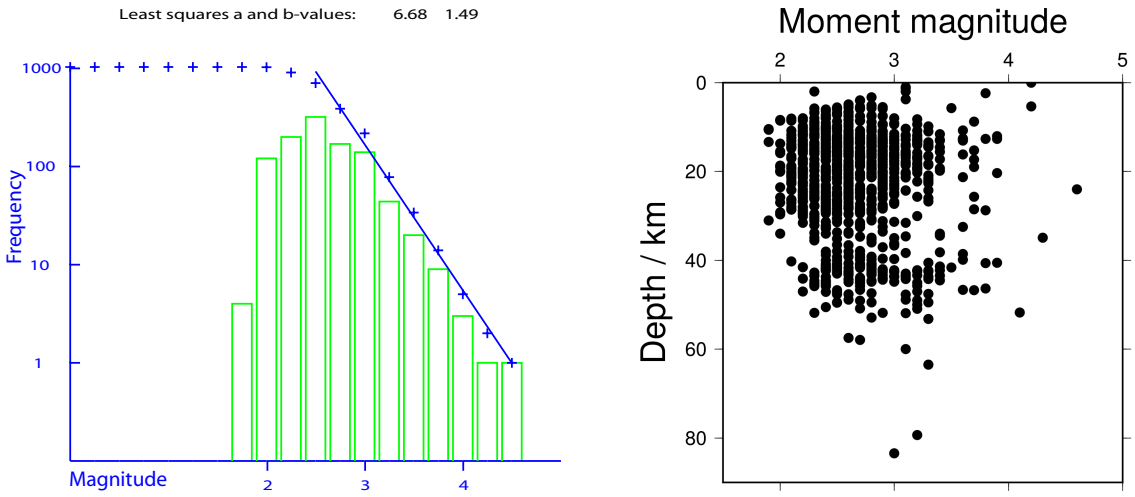

Figure 7.5.: (a): Histogram of magnitudes from the program *bvalue* implemented in SEISAN for the calculation of the b-value. The crosses mark the cumulated amount of events. The blue line is calculated with the Gutenberg-Richter relation (Eq. 7.1). (b): Magnitude–depth distribution.

The lower bound of seismic energy radiated by an earthquake can be described as:

$$E_0 = \frac{\Delta\sigma}{2\mu} M_0, \tag{7.2}$$

where M_0 is the seismic moment, $\Delta\sigma$ is the stress drop and μ is the shear modulus (*Stein and Wysession*, 2009). The ratio of $\Delta\sigma/\mu$, or the strain release, of earthquakes is roughly constant and the radiated energy is proportional to the seismic moment. With an average stress drop of 50 bar and $\mu = 5 \times 10^{11}$dyn/cm for events in the crust or upper mantle this ratio is $\approx 10^{-4}$ (also in SI system) (*Stein and Wysession*, 2009). In order to estimate areas with the highest seismic energy released, the survey area was divided into 10x10 km squares and the released seismic moment within the squares was summed up for the deployment time span. Figure 7.6 shows a map of the survey area and the gridded seismic moment release. There are three areas with a high seismic moment release, and therefore energy release: (1) one is located at about 34° S in the submarine forearc where an active splay fault could be detected (see Chapter 6). (2) Another patch of high seismic moment release is related to a cluster of seismic activity at about 40-50 km depth along the plate boundary (see Fig. 7.4, cross section B) at about 34.8° S and 71.75° W. This cluster is separated by an aseismic part of the plate boundary from the seismic activity updip. Both areas of high seismic energy release are seismically highly active as can be seen in Figure 7.7a where the amount of events per grid cell is plotted. A time-dependent

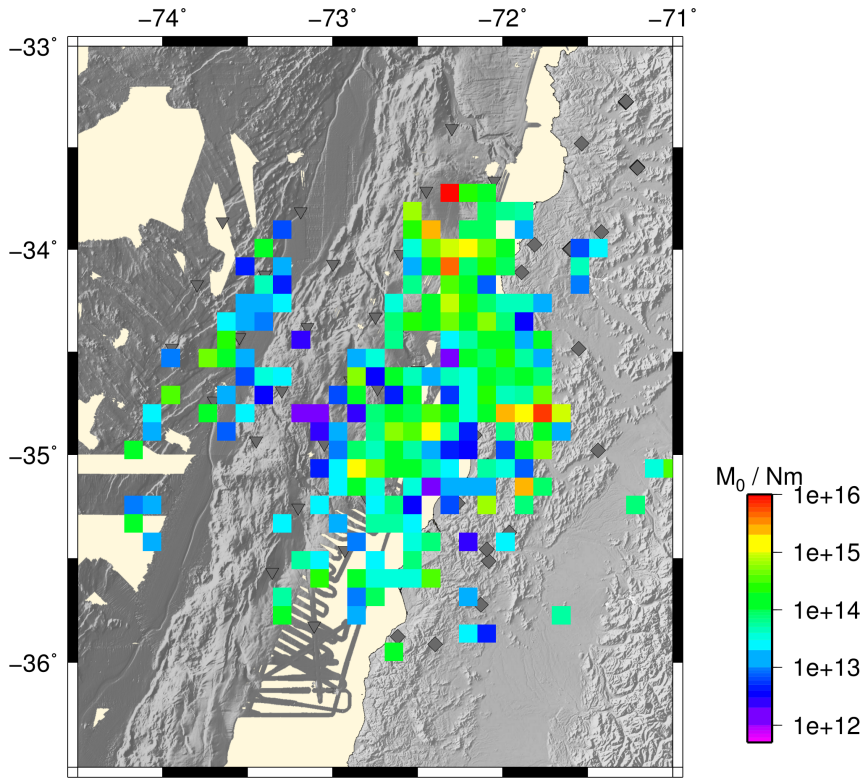

Figure 7.6.: Cumulative seismic moment in 10x10 km grid cells. Triangles are OBS locations, diamonds land station locations.

plot of the events (Fig. 7.7b) shows that the seismicity in the highly active areas is distributed continuously over time and they are active over the whole deployment time. However, at around the 8 October 2010, a patch of events between 10 and 15 km depth occurred in the splay fault area. (3) The grid cell with the highest seismic moment release is located at the most northern boundary of the network and contains the earthquake with the highest moment magnitude of 4.6. Because the seismic moment is a logarithmic value few large events release much more energy than many smaller events.

7.3. Focal mechanisms

Di Stefano et al. (2006) showed that high-quality weighted polarities picked by MPX are suitable for focal mechanism determination and can have a higher confidence than bulletin data (*Di Stefano et al.*, 2002). The focal mechanisms determined in this study show a rough partitioning by subduction zone area. The outer rise is

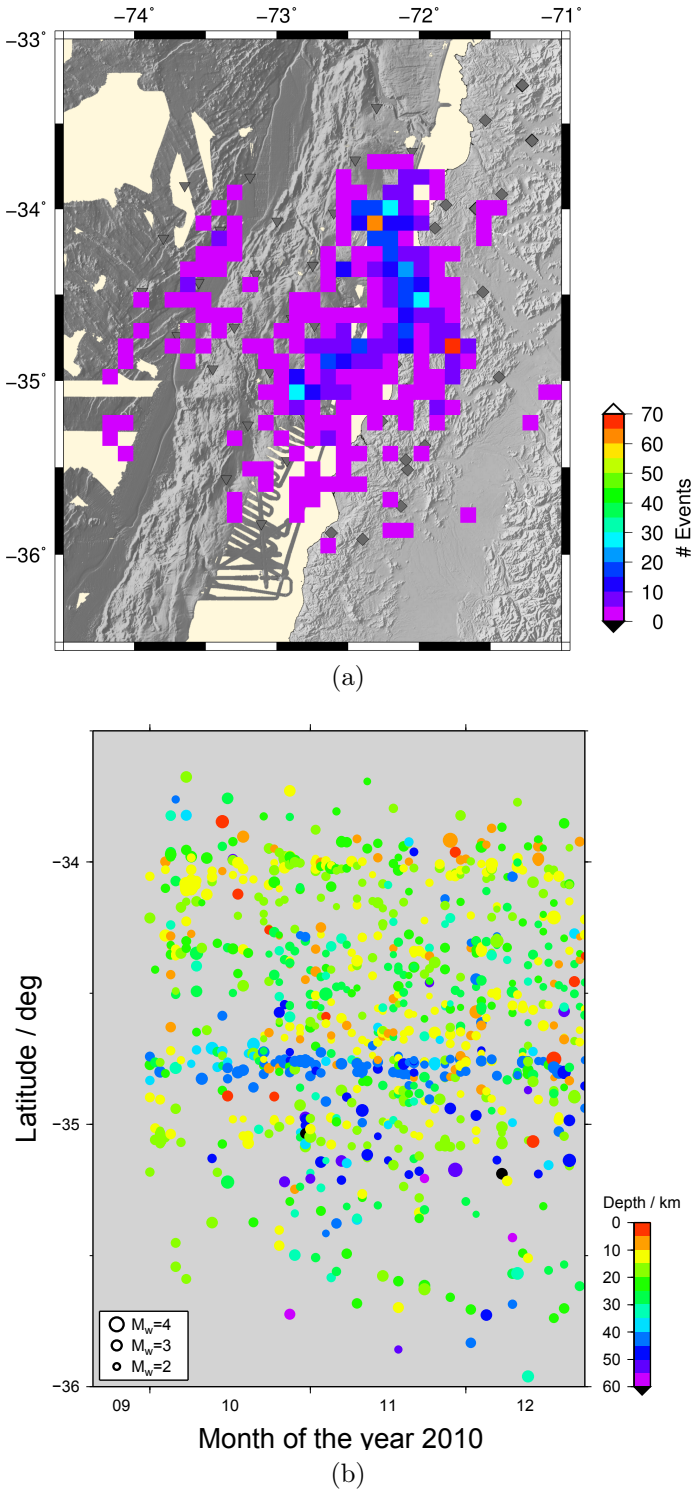

Figure 7.7.: (a): Number of events per grid cell. (b): Time distribution of events along latitude.

dominated by normal faulting while the forearc mainly shows thrust faulting and some strike-slip as well as normal faults (Fig. 7.8). Relocated focal mechanisms from the global Centroid Moment Tensor catalogue (gCMT) (*Dziewonski et al.*, 1981; *Ekström et al.*, 2012) show the same pattern as well (Fig. 1 of Chapter 6, Fig. E.1); where mechanisms in the forearc are related to thrust events on the plate interface. The focal mechanisms of the gCMT catalogue for the entire aftershock sequence show exclusively normal faulting events in the outer rise, indicating extension in the oceanic plate (see Figure DR1 of supplementary material to Chapter 6). The orientation of the P axes are mostly aligned in about an E-W direction (Fig. 7.9), indicating that the stress regime is governed by the subducting slab. Relocated thrust events from the gCMT catalogue show the same pattern in a study of *Agurto et al.* (2012). Events in the vicinity of the Pichilemu cluster and events located deeper than about 40 km form an exception. Here, the directions of the maximum stress axes are aligned roughly parallel to the trench. The minimum compressive stress axes scatter in orientation and do not favour a clear direction (Fig. 7.10). In the forearc the plunge of the P and T axes are in accordance for what is expected, with steep dipping T axes and shallower dipping P axes opposite to the dip of the subducting plate (e.g. *Dahlen*, 1984; *Wang and Hu*, 2006; *Hardebeck*, 2012). In contrast, in the outer rise the P axes dip steeper than the T axes.

7.4. Before the Maule earthquake

In order to compare the seismicity distribution of the 2008 data set to the 2010 data set, the manually picked phase arrivals, determined by Ivonne Aden-Arroyo and Helene Kraft, are located with the same procedure as the 2010 data set. The velocity model was extended until 150 km depth because the land stations cover a wider area and therefore events along the slab in greater depth could be recorded. After the hypocentre determination with 10 sequential runs, in order to determine the station corrections, the events were categorised into the same quality classes with the same parameter settings as valid for the 2010 aftershocks (see Table 7.1).

The seismicity distribution presented in Figure 7.11 reveals higher slab activity compared to the activity before the Maule event. The locations for the cross sections cutting through the 2008 network are the same as for the 2010 network to allow a better comparison between both data sets. The updip limit of seismicity along the plate interface is located about 70 km landwards from the trench. In the area between the updip limit and outer rise, i.e. the frontal accretionary prism, there is only scarce seismicity. The outer rise events show the same pattern as in 2010, with increasing hypocentre depths to the South. The small event cluster at about

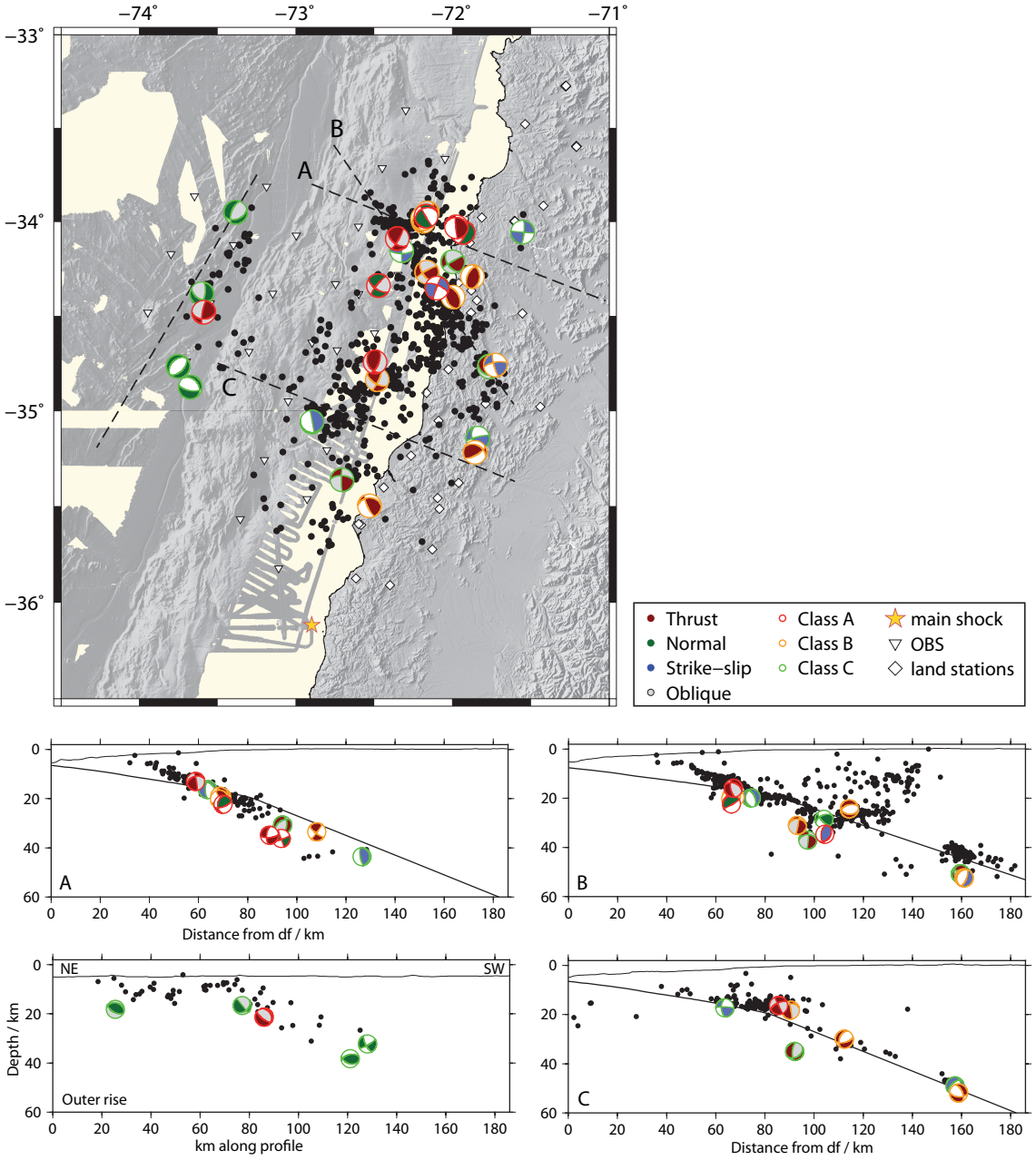

Figure 7.8.: Map and cross sections of focal mechanisms colour coded by quality class of mechanisms (see Section 5.2) for earthquakes with a gap smaller than 180°. Black are events of classes A, B and C with a gap smaller than 180°. Mechanisms in map view are lower hemisphere projections. Mechanisms in cross sections are projected onto the profile planes. df = deformation front. No vertical exaggeration in cross-sections.

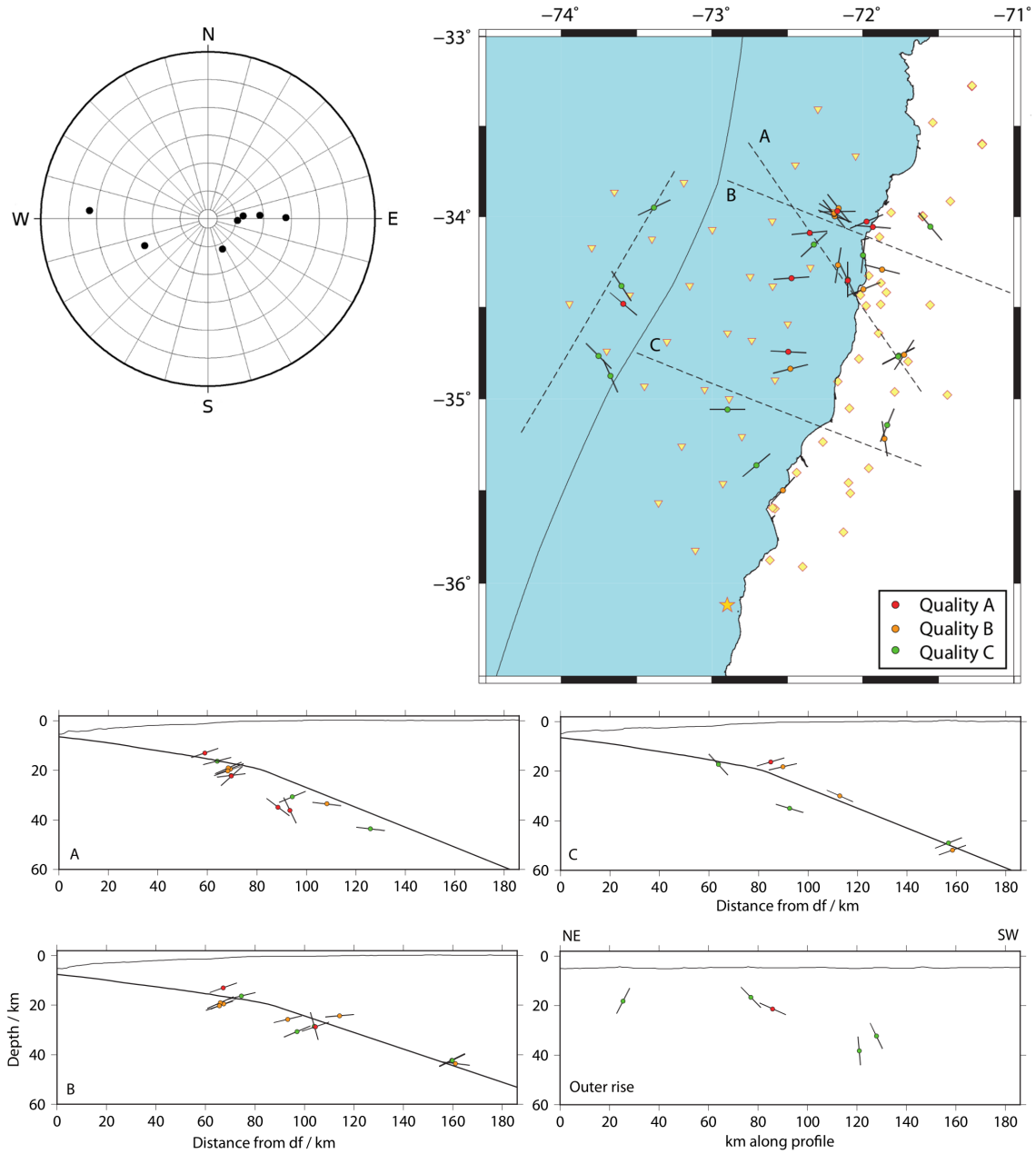

Figure 7.9.: Azimuth and plunge of maximum compressive stress axes (P). Map: colour coded by quality class of focal mechanisms. Plunges were rotated into the cross-section plane. df = deformation front, yellow star = location of Maule main shock, yellow triangles and diamonds = OBS and land station locations, respectively. Polar projection: only axes from focal mechanisms of class A, excluding outer rise events. No vertical exaggeration in cross-sections.

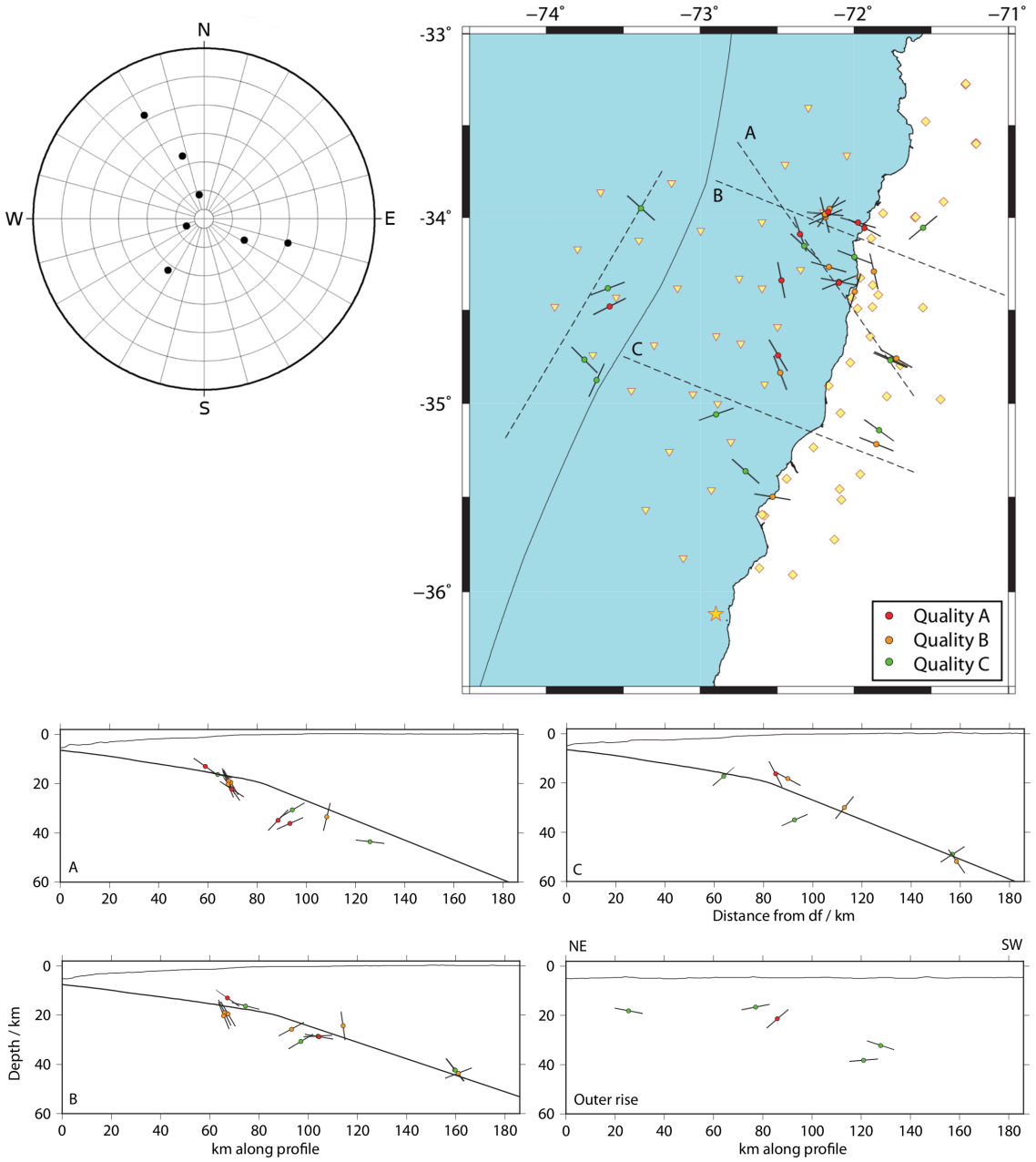

Figure 7.10.: Azimuth and plunge of minimum compressive stress axes (T). Map: colour coded by quality class of focal mechanisms. Plunges were rotated into the cross-section plane. df = deformation front, yellow star = location of Maule main shock, yellow triangles and diamonds = OBS and land station locations, respectively. Polar projection: only axes from focal mechanisms of class A, excluding outer rise events. No vertical exaggeration in cross-sections.

Table 7.1.: Quality classes for earthquake locations (after *Husen and Smith* (2004)). "Distance" is the difference between the maximum likelihood and the expectation hypocentre location. "Average error" is the mean of the three axes of the 68 % error ellipsoid determined by NLL.

Class	**RMS** s	**Distance** km	**Average error** km	**Number of events**
A – excellent	< 0.5	< 0.5	< 2	248
B – very good	< 0.5	< 0.5	≥ 2	565
C – good	< 0.5	0.5 - 2	< 5	231
D – ambiguous	< 0.5	≥ 0.5*	–	756
E – poor	> 0.5	–	–	3
* Except class C				

50–60 km depth along the plate boundary is visible in this data set, too. However, there is no distinct seismic gap along the plate boundary updip of the cluster, as is the case for the Maule aftershocks. There is some crustal seismicity below the volcanoes in the northern part of the survey area. In cross section A, the deeper seismicity does not follow the plate boundary but descends steeper into the mantle. The reason likely is, that this profile is located outside of the 2008 network and, therefore, shows lower hypocentre location resolution.

In order to evaluate the earthquake sizes for the 2008 data set, local magnitudes were determined from amplitudes, manually picked by I. Aden-Arroyo and H. Kraft, with *HYPOCENTER 3.2* (*Lienert and Havskov*, 1995). Therefore, the hypocentre locations determined with NLL and the velocity model of this study were used and kept fixed, in order to prevent *HYPOCENTER 3.2* from recalculating new event locations. The b-value of this data set of 2.5 is in the order of values usually assigned to earthquake swarms (Fig. 7.12). This may be an indication that the data set is incomplete or the amplitude readings are biased, for example due to incorrect response corrections. The magnitude-depth distributions (Fig. 7.12) for both studies cannot be compared directly due to the different magnitude scales. *Lange et al.* (2012a) compared moment magnitude to local magnitude for the 2010 land station data set and found that the relation of moment magnitude to local magnitude is about 2/3 for local magnitudes smaller than about 3 while for larger local magnitudes the relation is about 1. Although the 2008 network shows a higher amount of events with a magnitude above 3 as the 2010 network this does not necessarily mean that the events in 2008 were stronger in general. The 2008 network covered a wider range, especially to the East, and more of the deeper slab events could be detected due to the network configuration. The magnitudes are homogeneously distributed vertically as well as laterally over the different subduction zone segments (Fig. F.1).

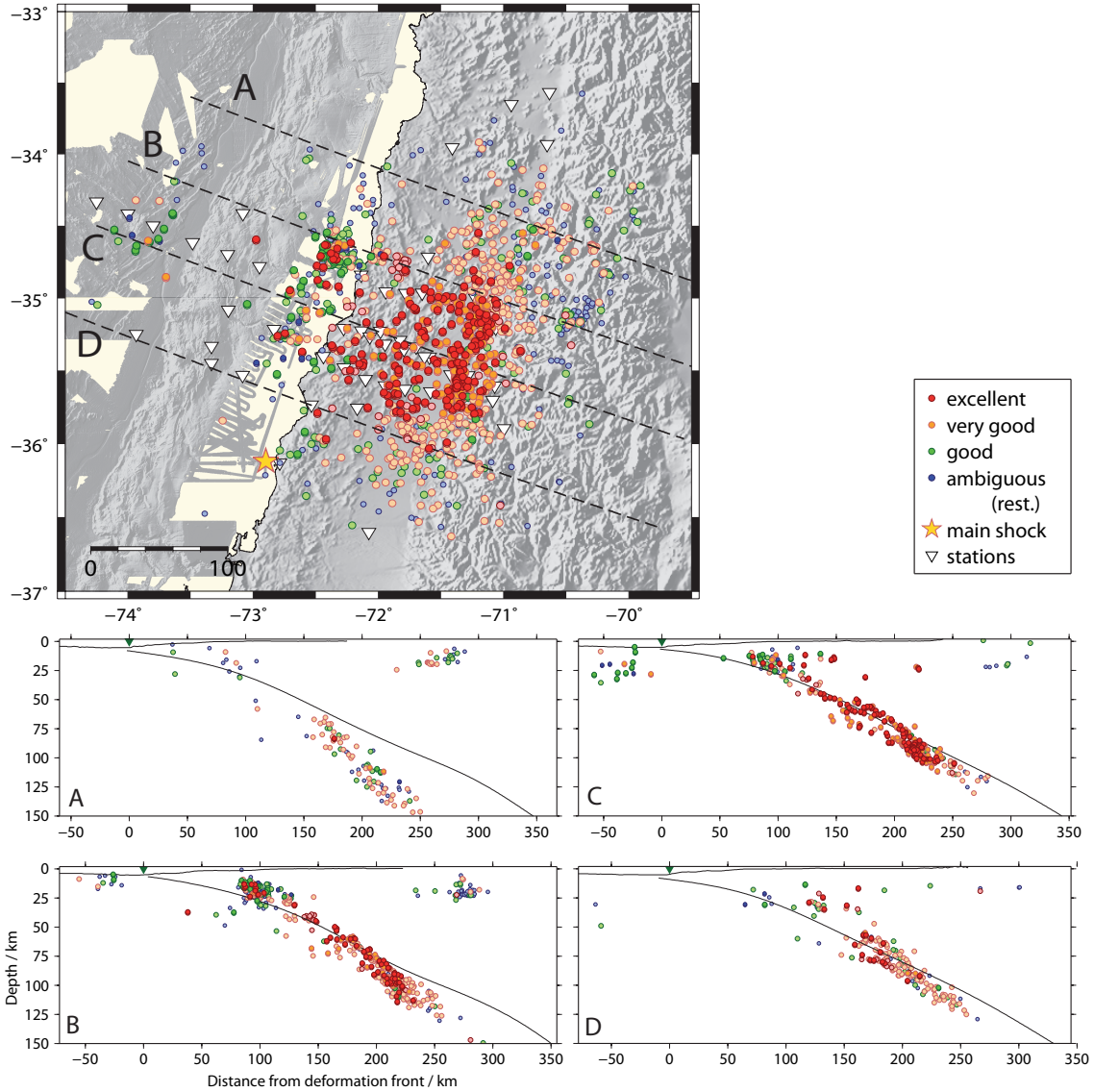

Figure 7.11.: Seismicity distribution from 2008. The transparent events show a gap of greater than 180° while the opaque ones are events within the network (gap $< 180°$). Events classified as "ambiguous" are restricted to a maximum average error ellipsoid half-axis of 8 km. Slab = Slab1.0 from *Hayes et al.* (2012). No vertical exaggeration in cross-sections.

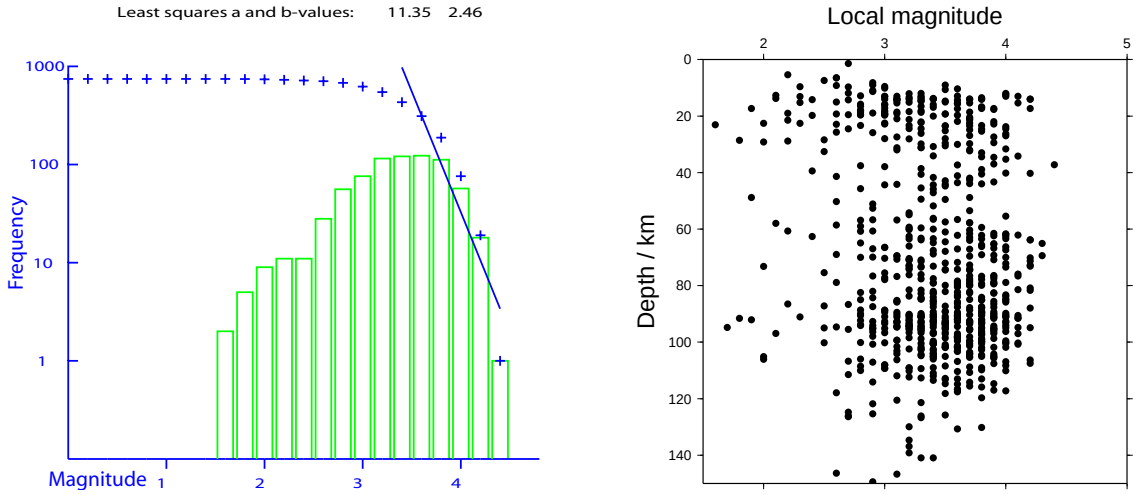

Figure 7.12.: (a): Histogram of magnitudes from the program *bvalue* implemented in SEISAN for the calculation of the b-value. The crosses mark the cumulated amount of events. The blue line is calculated with the Gutenberg-Richter relation (Eq. 7.1). (b): Magnitude–depth distribution.

Focal mechanisms and stress orientations are determined the same way as for the 2010 seismic network (see Section 5.2). For the 2008 data there are about a third of the number of solutions available than for the 2010 network, but the total amount of highest quality solutions is comparable (Tab. 7.2). The focal mechanism solutions

Table 7.2.: Amount of focal mechanisms derived from the 2008 network divided by quality class. In brackets are the counts from the 2010 network.

Class	**# of solutions**
A	7 (8)
B	1 (11)
C	1 (13)
Total	9 (32)

from the 2008 network show a heterogenic distribution of strike-slip, normal as well as thrust faults (Fig. 7.13) in the forearc no dominant fault type is obvious. For the outer rise there are no focal mechanism solutions available from the data of this network. Only one event is registered in the gCMT catalogue for the deployment

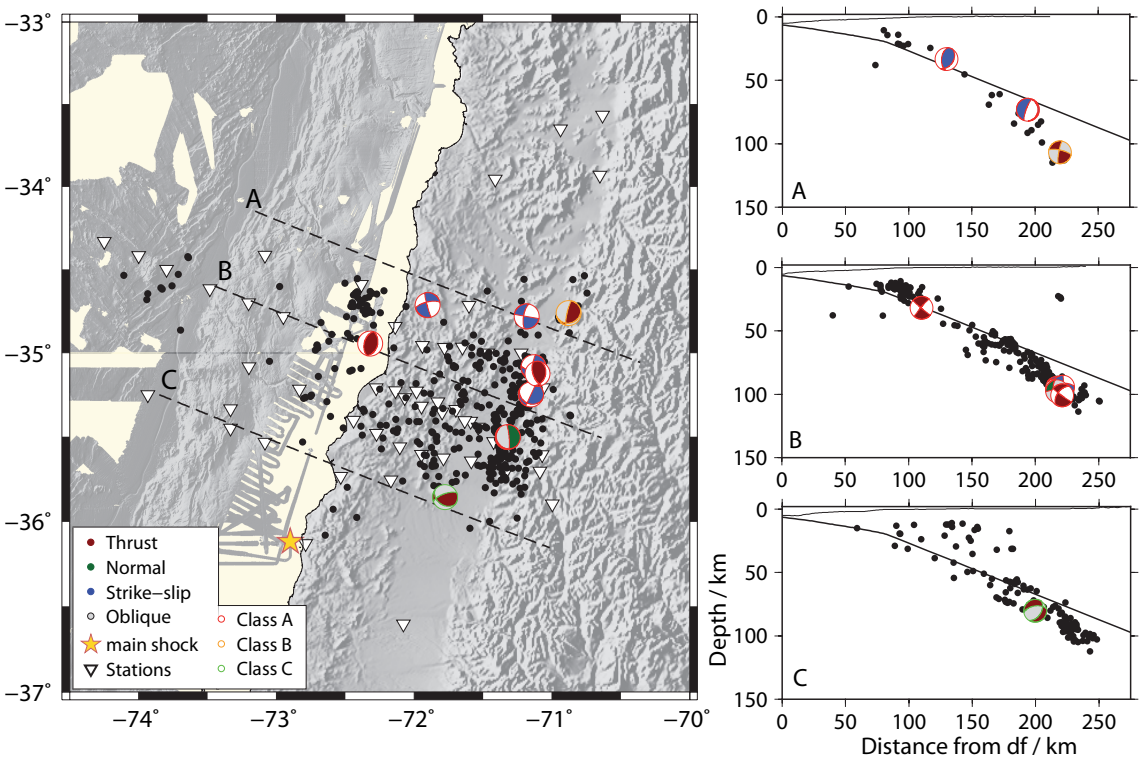

Figure 7.13.: Map and cross sections of focal mechanisms colour coded by quality class of mechanisms (see Section 5.2) for earthquakes with a gap smaller than 180° in the 2008 seismic network. Black are events of classes A, B and C with a gap smaller than 180°. Mechanisms in map view are lower hemisphere projections. Mechanisms in cross sections are projected onto the profile planes. df = deformation front.

period of this network, showing a thrust faulting mechanism at the eastern boundary of the network in a depth where the subducting slab is located. The majority of P axes is oriented perpendicular to the trench and dip either almost parallel to the subducting slab or at a shallow angle opposite to the direction of the subducting slab (Fig. 7.14). The majority of T axes dip almost perpendicular to the subducting slab (Fig. 7.15). P axes parallel to the subducting slab imply downdip compression along the plate interface. However, this would be expected either in depth greater than 300 km (*Isacks and Molnar*, 1969; *Brudzinski and Chen*, 2005) or after a megathrust event (*Astiz and Kanamori*, 1986).

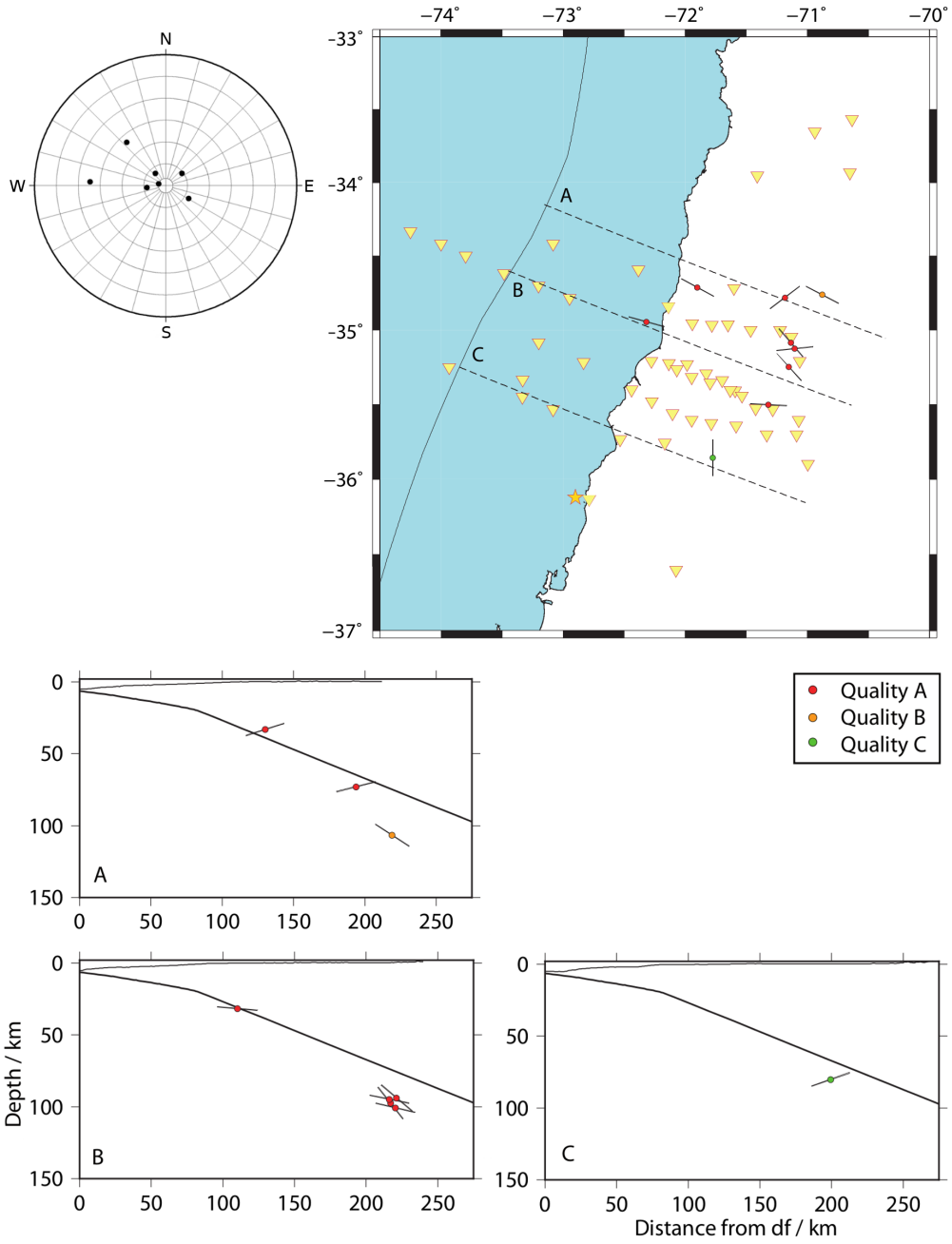

Figure 7.14.: Azimuth and Plunge of maximum compressive stress axes (P) from the 2008 seismic network. Map: colour coded by quality class of focal mechanisms. Plunges are rotated into the cross-section planes. df = deformation front, yellow star = location of Maule main shock, yellow triangles = OBS and land station locations. Polar projection: only axes from focal mechanisms of class A.

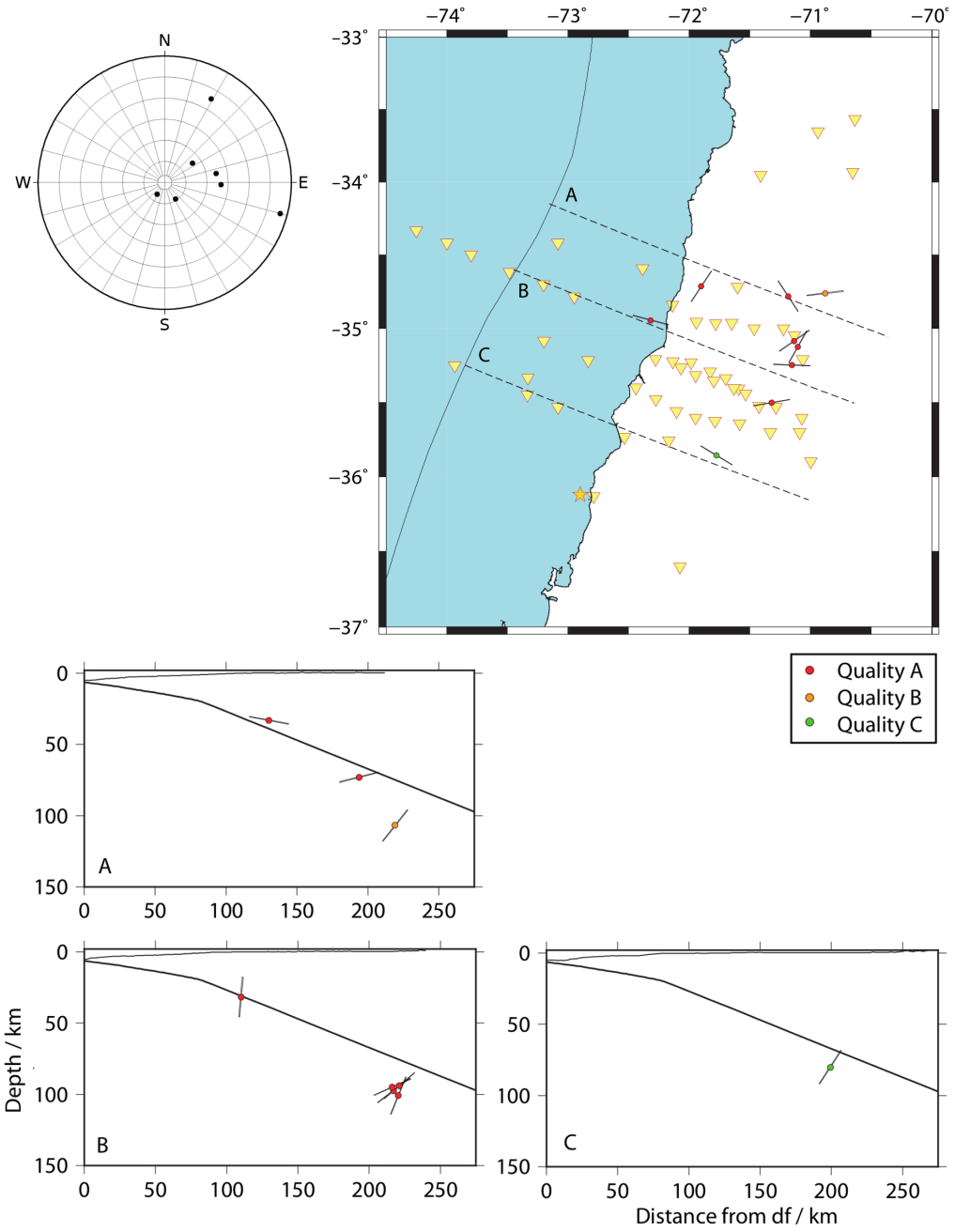

Figure 7.15.: Azimuth and Plunge of minimum compressive stress axes (T) from the 2008 seismic network. Map: colour coded by quality class of focal mechanisms. Plunges are rotated into the cross section planes. df = deformation front, yellow star = location of Maule main shock, yellow triangles = OBS and land station locations. Polar projection: only axes from focal mechanisms of class A.

8. Discussion

The first part of this chapter discusses the results obtained in the previous chapter and compares the distribution of seismic activity and stress orientations before and after the Maule event. The last section of this chapter addresses the application of the automatic picking routines and the quality of their results. A detailed discussion on splay fault activity in the submarine forearc can be found in Chapter 6.

8.1. Distribution of seismic activity

When the OBS seismic network was deployed, six month after the Maule main shock in 2010, the amount of daily occurring aftershocks had decreased considerably by then because the frequency of aftershocks decays roughly by the reciprocal of time after the main shock (*Omori*, 1895). However, the Maule area was considered to be a mature seismic gap showing no events larger than magnitude five since the last megathrust event in 1985 and therefore, it is unlikely that the amount of detected events in 2010 are not related to the main shock but to background seismicity. Both networks, from 2008 and 2010, recorded about the same amount of well located events (i.e. classes A, B and C). But, the stations from the 2008 network recorded 1044 events in about 3 month (5.7 events per day) while the stations of the 2010 network registered 1043 in 6 month (11 events per day). Thus, about 2 times more well determined events were located after the main shock in 2010 compared to 2008. Considering events with qualities of at least D, about even 3 times the events were recorded in the 2010 network (2730 events, or 28.7 events per day) compared to 2008 (1800 events, or 9.7 events per day). Therefore, it can be concluded that the seismic activity recorded in the 2010 network is still affected by the Maule main shock.

Studies show that aftershocks usually occur in areas with low coseismic slip of the main shock. In the area of highest coseismic slip usually only small events occur (*Das and Henry*, 2003). Magnitudes are distributed homogeneously over the network (Fig. 7.4) and no clear distinction between smaller events in regions of large coseismic slip and larger events in the regions of small coseismic slip can be ob-

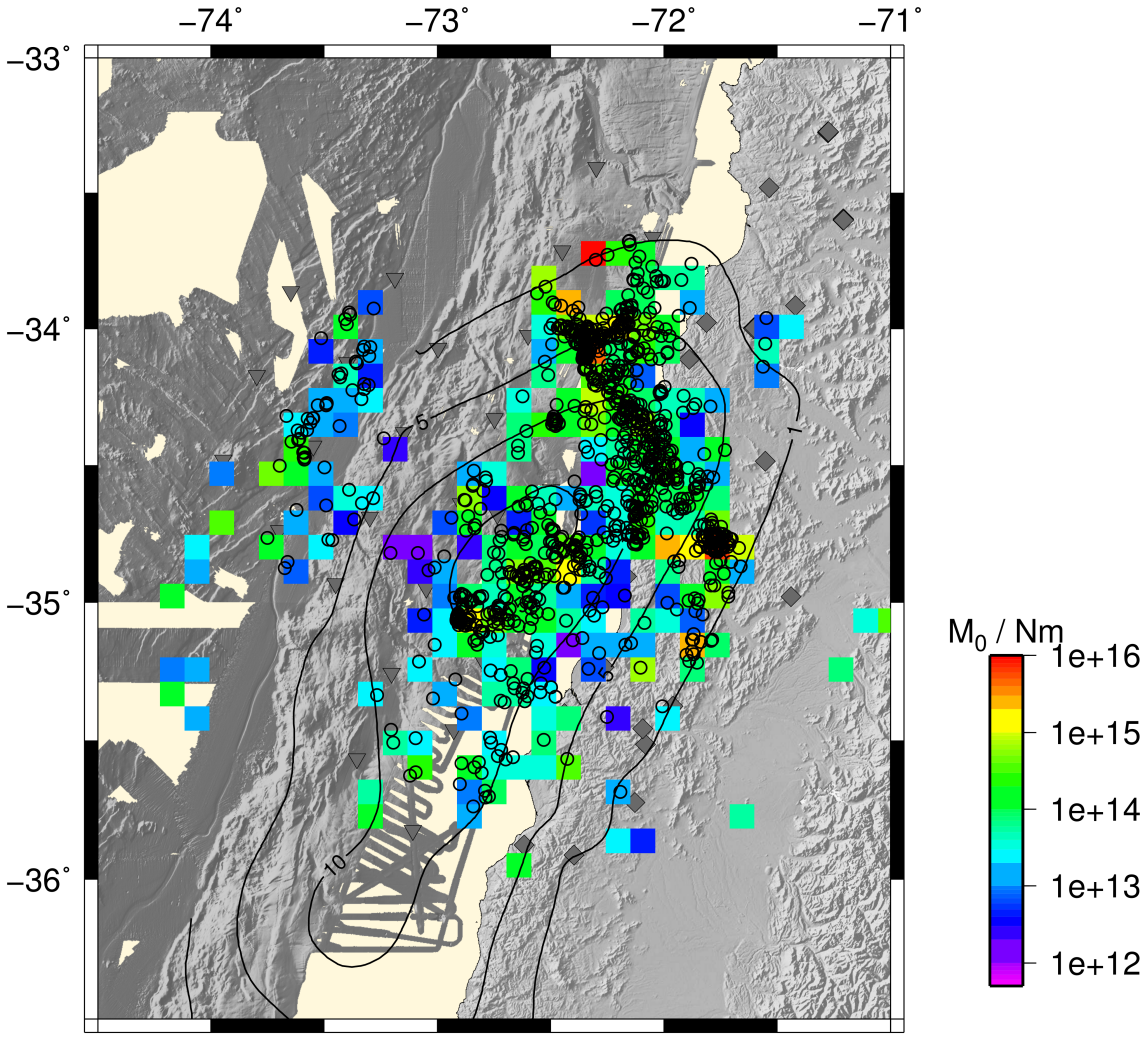

Figure 8.1.: Aftershock distribution, cumulative seismic moment release and coseismic slip. Black circles are events with quality classes A-C.Triangles are OBS locations and diamonds land station locations.

tained. Figure 8.1 shows the aftershock distribution of well determined events of this study and the cumulative seismic moment release with respect to the coseismic slip derived by *Moreno et al.* (2012). Areas with high aftershock seismicity and high seismic moment release are indeed located in areas where the coseismic slip was low. However, in the area with the highest coseismic slip of above 15 m, the seismic activity is actually increased with respect to the directly surrounding areas (cf. Fig. 7.7a). Other studies of the Maule aftershocks show seismicity in the area of largest slip as well (*Lange et al.*, 2012a; *Rietbrock et al.*, 2012), but those are mainly events with magnitudes smaller than four (*Agurto et al.*, 2012). In the afterslip analysis of *Agurto et al.* (2012) large thrust faulting events occur in regions of moderate coseismic slip while in the area of high coseismic slip no major seismicity is observed. This is in accordance with the findings of *Das and Henry* (2003), that usually the smaller aftershocks occur in high-slip regions. An explanation why this typical aftershock distribution is not obtained in the data of this study is that only events six month after the main shock are observed. As the highest magnitude registered in this seismic network is Mw 4.6, all recorded events can be considered as smaller aftershocks of the Maule earthquake.

A striking feature between the distributions of seismic activity before and after the Maule event is the sudden decrease of slab seismicity below about 50 km depth after the Maule event (Fig. 8.2). Although the intermediate-depth slab events detected in the 2008 network lie outside of the 2010 network boundaries, some seismic activity in the slab should have been detected by the 2010 network. Even if this would have been locations of low qualities like, for example, in the northernmost cross section of the 2008 network (Fig. 8.2, cross section A). Here, the events from 2008 do not follow the slab model but are located a couple of kilometres deeper than expected, caused by poor resolution outside of the network. The horizontal extend of the location search grid in the hypocentre determination was the same for both the data sets, thus, the absence of slab seismicity cannot be explained by errors related to the search grid of the location procedure. The smallest events recorded in about 100 km depth in the 2008 network have a local magnitude of $Ml < 2$ and events with comparable small magnitudes should have been detected in the 2010 network. Therefore, events with magnitudes too small to be recorded in the network after the Maule event do not seem to be a reason for the absence of slab seismicity. Although other studies on aftershocks of the Maule event observed sparse intermediate-depth events, the amount of those events in this study is substantially lower (*Lange et al.*, 2012a; *Rietbrock et al.*, 2012; *Agurto et al.*, 2012) and it seems that this study underestimates slab seismicity in intermediate depth. An explanation may be that the high forearc seismicity masked the slab seismicity in such a way that it could not be detected by the STA/LTA network trigger. Even though this may be the case for the aftershock set in this study, the slab seismicity from 2008 still is considerably higher compared to the recorded seismic events from the studies

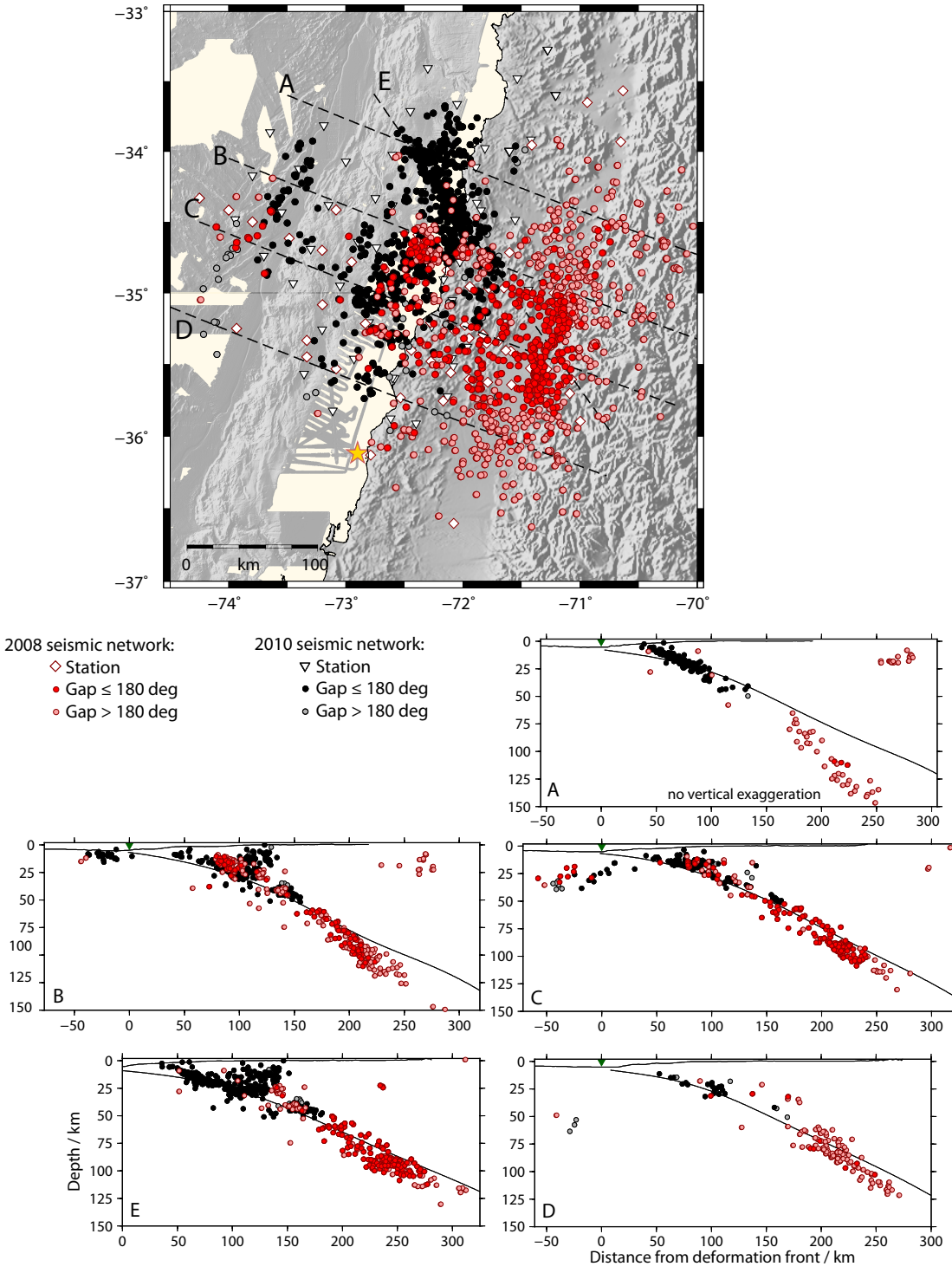

Figure 8.2.: Comparison between the seismic distributions derived from the seismic networks of 2008 and 2010, with quality classes A-C. Events within the network (gap$<$ 180°) are displayed in opaque colours.

of *Lange et al.* (2012a); *Rietbrock et al.* (2012) and *Agurto et al.* (2012). A similar pattern was observed after the 2004 Sumatra-Andaman earthquake (*Engdahl et al.*, 2007) and the amount of large intermediate-depths events decreased for a couple of years after the 1964 Alaska and the 1985 Valparaíso earthquakes (*Astiz et al.*, 1988). In general, fewer aftershocks occur for intermediate-depths events than for shallow or deep earthquakes (*Frohlich*, 1987), probably caused by fluid migration and loss (*Hacker et al.*, 2003). A decrease in slab pull at intermediate-depths may also have reduced seismic activity along the slab after the main shock. The orientations of the stress axes of this study support downdip compression rather than downdip extension. However, only few focal mechanisms were available and previous studies observed tension in the subducting slab before 2010 (*Cahill and Isacks*, 1992; *Pardo et al.*, 2002; *Brudzinski and Chen*, 2005; *Anderson et al.*, 2007).

In 2008, the updip limit of the seismogenic zone was located about 70 km landward from the deformation front (Fig. 8.2, cross section B) while the aftershock distribution of the Maule earthquake extends about 30 km further along the subduction thrust until about 40 km landward from the trench. The distinct seismic gap at the downdip limit in about 40 to 50 km depth in the aftershock distribution is also observed in tomographic studies as a high velocity anomaly (*Arroyo et al.*, 2010; *Hicks et al.*, 2014). This structure is interpreted as up to 15 km thick dense bodies of ultramafic peridotite, perhaps relic blocks of mantle that could have influenced the crustal seismicity in the Pichilemu area (*Hicks et al.*, 2014). Prior to the Maule event, some clustered seismicity can be found in the seismic gap of 2010 (Fig. 8.2, cross sections B and E). The well determined events appear to form a lineated structure, probably on top of the relic mantle body. This seismic cluster stops where the crustal seismicity of Pichilemu begins in 2010 (Fig. 8.2, cross sections B and E) supporting the suggestion that the ultramafic body affected the crustal aftershock seismicity.

8.2. Focal mechanisms and stress orientations

The focal mechanisms from the aftershock data of the dense amphibious seismic network show a rough partitioning by subduction zone segment with mainly normal faults in the outer rise and thrust faulting in the forearc as can also be seen in mechanisms of the gCMT catalogue and additional fault plane solutions from studies of *Lange et al.* (2012a); *Rietbrock et al.* (2012) and *Agurto et al.* (2012). Focal mechanisms of the gCMT catalogue are aligned predominantly trench-parallel and in more agreement with the orientation of the subducting slab than the focal mechanisms of the 2010 data set. Their orientations scatter from the trench parallel direction.

Table 8.1.: Plunge of P and T axes from the 2008 and 2010 seismic networks from focal mechanism solutions of the highest quality class A, excluding events in the outer rise.

Axis	**Plunge 2008 deg**	**Plunge 2010 deg**
P	14	26
T	37	34

However, the gCMT catalogue comprises of events with magnitudes larger than 5 and focal mechanisms were obtained by moment tensor inversion and therefore are better constrained than the focal mechanisms of this study determined from first motion polarities. Because the focal mechanisms of the 2008 data set show a rather chaotic pattern and with no available fault plane solutions in the outer rise at all, a comparison of both data sets, before and after the Maule event, is difficult. To increase the amount of fault plane solutions the gCMT catalogue was searched for events during both deployment time spans. For the first deployment time in 2008 there was only one event available as the area was considered to be a mature seismic gap and the amount of events with a sufficient magnitude to determine moment tensor inversions is scarce. In spite of the low number of well determined fault plane solutions, a stress tensor inversion was attempted for the 2008 and 2010 data set of this study. But the inversion failed as the angular fit was about 60 to 70° with standard deviation of above 50°. On the basis of the assumption that events occur on randomly oriented faults, averaged directions of the P and T axes are good indicators of the general orientations of the maximum compressive stress axes σ_1 and least compressive stress axes σ_3, respectively (*Wang et al.*, 2004). Therefore, to determine possible stress rotations between 2008 and 2010, the median of the P and T axes were determined and compared (Tab. 8.1). The P axes dip by 12 degrees steeper after the Maule event while the plunge of the T axes is almost equal. *Hardebeck* (2012) studied stress rotations before and after megathrust events and determined the stress tensor from gCMT catalogue data before (since 1976) and in a six month period after the 2010 Maule, 2011 Tohoku and 2004 Sumatra events and concluded that the stress axes plunged shallower before the Maule event and steeper afterwards. However, her study showed, that both, P and T axes, plunge steeper than 45° after the Maule event. In contrast, in this study, the P and T axes plunge at a considerably lower angle and the T-axes did only rotate by three degrees. *Hardebeck* (2012) compared the stress tensors of a larger area than affected by the Maule rupture, including the generally more seismic active regions north of the previous seismic gap and at the Arauco peninsula. Because the axes of the 2008 network are mainly derived from focal mechanisms from events in greater depth

than the 2010 events, a direct comparison of stress rotations from both networks is not possible.

There are no focal mechanisms available along the splay fault in 2008 as well as 2010. However, at the foot of the splay fault thrust mechanisms can be observed. The study of *Agurto et al.* (2012) based on relocated focal mechanisms of the gCMT catalogue as well as fault plane solutions from regional moment tensors shows exclusive thrust faulting in the splay fault area.

In the outer rise no focal mechanisms are available before the Maule event due to poor station coverage in this area. In the gCMT catalogue only four outer rise events are available between 33°S and 36°S since the beginning of the catalogue in 1976 and the Maule event in 2010 (Fig. 8.3). None of which are located in the area opposite to the peak coseismic slip of the Maule earthquake (cf. Fig. 8.1) while after the Maule event, increased shallow extensional outer rise events can be observed in this area. This is in accordance with the stress concentrator model of *Mueller et al.* (1996) that predicts that either no large outer rise event will occur before or after a megathrust event. *Mueller et al.* (1996) consider normal faulting events caused by bending related stress distributions as the standard state in the outer rise. The rarer thrust faulting events on the other hand are caused by elevated compressional stresses due to local resistances to subduction, like buoyant bathymetric features or interplate asperities. Therefore, the absence of thrust faults in the outer rise after the Maule event indicates that there are no elevated compressional stresses in the downgoing slab offshore Maule. However, north of the survey area, a large thrust event (Mw 7.1) ruptured in the outer rise at about 33°S four years before the 1985 Valparaíso (Mw 7.8) earthquake. Here, the accumulation of compressional stresses is caused by the subduction of the Juan-Fernandez-Ridge at about 33°S (*Clouard et al.*, 2007). The increased amount of extensional events in the outer rise after the Maule event can be explained by the transfer of slab pull to the outer rise activating discrete trench-parallel faults. The outer rise events occur opposite to the maximum coseismic slip where the underthrusting motion is largest, and therefore, the slab pull highest.

S-P wave arrival times show that events in the outer rise tend to nucleate in greater depths in the southern part of the survey area than in the northern part. The events used for S-P time calculations are located in depths that are still consistent with shallow extensional outer rise events. But, stations used for the determination of S-P times did not cover the deepest events further to the south. Bending models explain the tensional stresses in the upper part and compressional stresses in the lower part of the subducted lithosphere (e.g. *Stauder*, 1968a,b; *Seno and Yamanaka*, 1996). The transition between tensional to compressional regions is thought to be located in a depth were the 450°C isotherm is expected (*Seno and*

Yamanaka, 1996) while the deep compressional outer rise events usually occur in regions cooler than 600°C (*McKenzie et al.*, 2005). For central Chile these isotherms would be in about 20 to 25 km depth and 25 to 30 km depth, respectively (*Seno and Yamanaka*, 1996; *Contreras-Reyes et al.*, 2008). Seismic distributions from both deployment time spans show a similar pattern of two linear landward dipping structures (Fig. 8.2, cross section C) reaching down to about 35 km depth at the southern network boundaries. Because those deep features are recorded in two separate seismic networks with different station configurations it is unlikely that they are solely caused by boundary effects in the hypocentre determination process. The deepest events are located in a region where thrust faulting events would be expected. However, focal mechanisms suggest extensional faulting (Fig. 7.8). Events in the gCMT catalogue show extensional faulting mechanisms as well but they are constricted to the upper 20 km of the oceanic plate (Fig. 8.3). Between 32.5°S and 33°S a Mw 7.0 extensional event ruptured the outer rise close to the Juan-Fernandez Ridge in 2001 triggering a series of aftershocks that reached down to 30 to 40 km depth (*Fromm et al.*, 2006; *Clouard et al.*, 2007) as well. The main shock was caused by a combination of bending and slab pull forces (*Clouard et al.*, 2007). *Fromm et al.* (2006) speculates that the outer rise event could have broken the whole effective thickness of the lithosphere and the aftershocks are distributed along a conjugate normal fault system extending into the lithospheric mantle. Other studies on outer rise faulting offshore central Chile show that plate bending resulted in deep fractures cutting into the oceanic mantle and supporting plate hydration (*Grevemeyer et al.*, 2005; *Ranero et al.*, 2005; *Contreras-Reyes et al.*, 2007, 2008). Thus, slab pull and plate bending after the Maule event probably contributed to extending normal faults, already reaching into the oceanic mantle, into greater depths. However, to better constrain the hypocentre depths at the southern network boundaries, further studies from a seismic network with better coverage of this part of the outer rise are needed.

8.3. Automatic phase detection

In total, 83,610 automatically picked P wave onsets (46,397 on OBS and 37,213 on land stations) were detected by MPX and applied to the hypocentre location process. To asses the reliability of these automatic phase onsets, the results of the picking parameter and weighting scheme calibration determinations are compared to other studies that applied MPX (Tab. 8.2). For OBS and land station data, the parameters are in good accordance with the other studies. Hit rate, efficiency as well as picking errors fall well into the ranges of the other studies. When comparing the hit rate of the weighting scheme to the other studies it is important to keep in mind that *Di Stefano et al.* (2006) and *Diehl et al.* (2009) generated their data

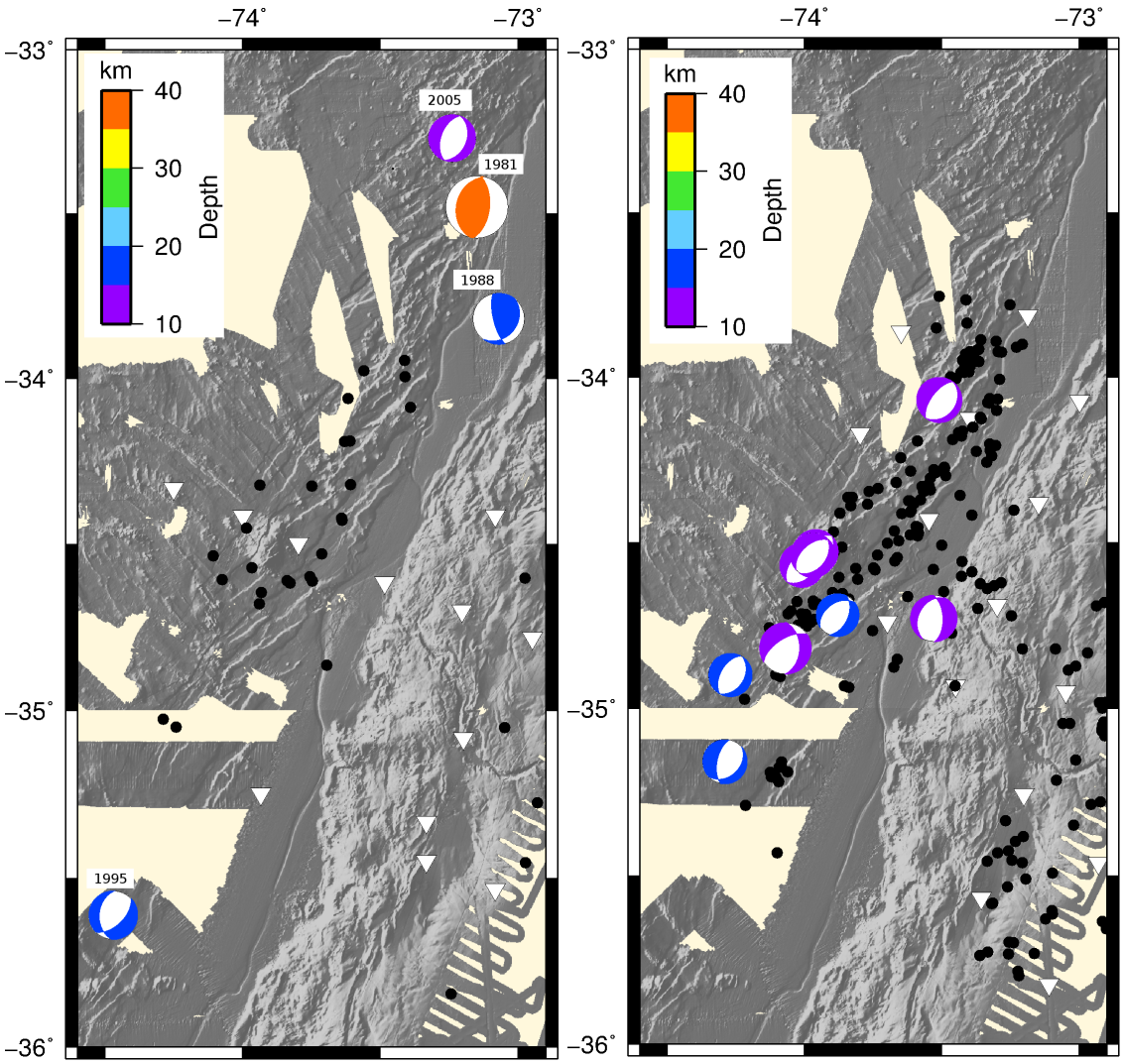

(a) 01.01.1976 to 26.02.2010

(b) 27.02.2010 to 24.12.2010

Figure 8.3.: Focal mechanisms of the gCMT catalogue in the outer rise before and after the Maule earthquake. Black dots are events with quality classes A-D from the local networks, where D was restricted to locations with a maximum average error ellipsoid half-axis of 8 km. Size of beach balls is proportional to magnitude of event. White triangles are OBS locations. (a) Focal mechanisms since the beginning of the gCMT catalogue in 1976 to 26.02.2010. Magnitudes are between Mw 5.4 and Mw 5.8, except the event of 1981 (Mw 7.1) (b) Mechanisms between 27.02.2010 (day of Maule main shock) and 24.12.2010 (end of deployment time of the amphibious seismic network). Magnitudes are between Mw 4.9 and Mw 5.9.

sets for tomography studies and, therefore, needed data with the highest accuracy. As a consequence their final weighting schemes downgrade the pick qualities by a large extend in order to avoid upgrading of low quality picks to high qualities. However, the amount of upgraded picks for the OBS and land station data set is only slightly higher than the amount of qualities in the study of *Di Stefano et al.* (2006). The majority of qualities were assigned correctly and less than one third of the picks have been downgraded in the calibration procedure. For tomographic studies the weighting scheme probably should be repeated with a better reference data set, preferably from events of location quality A, in order to decrease the amount of upgraded picks. However, the weighting scheme provided good results, as can be seen in Tables 8.2 and 2.7. The means and standard deviations of the distances between the hypocentres of the reference data set to the automatically picked events are in general below 2.8 and 4.6 km, respectively. The land station locations show very low standard deviations of even below 1.6 km. Only the mean and standard deviations of the hypocentre depths from the OBS network are a little higher but this is due to one large outlier of about 70 km distance to the reference hypocentre depth. The median and 25th and 75th percentiles, that are far less sensitive to outliers, are substantially lower. About 75% of the distances in depth between reference and automatic data set are below 3.1 km and 25% of the automatically determined hypocentre depths do not differ at all from the reference depths (Tab. 2.7). Therefore, the automatic picking routine does produce reliable results for both OBS and land station networks.

The performance of the MDA, that connects the signal-describing predictors to the manually set pick weights, is strongly dependent on the data set (*Diehl and Kissling*, 2008). As mentioned in Section 1.4, OBS data usually is affected by a higher amount of noise than land station data. However, the weighting scheme of the OBS data set is adjusted slightly better to the manual weights as a higher percentage of picks was assigned to the correct quality class and less picks were upgraded into higher qualities. Nevertheless, as mentioned above, the location errors between the automatically determined hypocentres and the reference data set are still lower for the land station network.

The data set of 2008 gives a good opportunity to compare the results from a data set where phase arrivals are determined automatically to a data set with manually picked phase onsets. The manually picked data set consists of far less poor quality hypocentre locations. But this is expected because the automatic picking routine tries to determine a pick around every initial pick, regardless whether those are related to an actual phase arrival or to noise etc, and the location procedure is supposed to find those. Also the autopicker cannot distinguish between two different earthquakes on the same seismogram trace while a human picker is most likely able to assign the phase onsets to the specific events. Thus, events for which most of

Table 8.2.: A comparison of MPX performance between this study and previous studies. *Hitrate* is the percentage of phase arrivals found by MPX with respect to the manual reference data set. *Efficiency* is the percentage of located events based on automatic picks to located events of manual reference data set (e.g. 80% means that 8 events based on automatic picks could be located out of 10 events of the manual reference set). *Picking error* is the error boundaries that were assigned to the different pick qualities in the weighting scheme calibration. *Weighting scheme* compares the automatically assigned MPX weights to the reference weights, where *Upgraded* means that picks are automatically assigned to higher pick qualities (e.g. from 2 to 0). LS = Land stations.

	This study		**Previous studies**			
	OBS	**LS**				
Hitrate / %	80.0	80.0	75.0 [1]	78.0 [2]	92.7 [3]	
Efficiency / %	82.0	100.0	89.0 [5]	99.1 [3]		
Picking error / s	0.06/0.12/0.18		0.10/0.20/0.40/0.80 [2] 0.04/0.08/0.14 [3] 0.05/0.10/0.20/0.40 [4]			
Weighting scheme:			[2]	[3]	[4]	[5]
Correct / %	57.1	56.2	46.2	66.8	36.2	63.0
Upgraded / %	12.5	13.7	11.3	7.7	4.0	–
Downgraded/ %	30.4	30.1	40.3	25.0	60.0	–
Location error:			[1]			
Latitude / km	1.6 ± 2.6	0.3 ± 0.7	0.3 ± 4.6			
Longitude / km	2.8 ± 4.6	0.4 ± 1.6	1.3 ± 3.7			
Depth / km	5.4 ± 13.8	1.4 ± 1.5	2.6 ± 5.1			

[1] *Lange et al.* (2012a)
[2] *Di Stefano et al.* (2006)
[3] *Aldersons* (2004)
[4] *Diehl et al.* (2009)
[5] *Valoroso et al.* (2009)

the phase arrivals are related to noise or originate from different earthquakes, the location quality decreases. However, the high amount of low quality locations is not a sign that data from an autopicker is generally of low quality but rather that the location procedure with NLL does work as a quality control and reliably eliminates poor quality picks and events. From about 80,000 automatically detected P wave onsets, about 20% were weighted out by NLL in the hypocentre determination process. Divided by network, about 72% of the OBS picks and about 90% of the land station data were used in the final NLL location run. This reflects as well the higher noise level in OBS data.

For the more complex process of S phase detection, MPX was applied to the OBS data set as well because most S wave pickers involve the rotation of the horizontal components. For OBS data it is not possible to directly rotate the components into the direction of the incoming wave determined by hypocentre location as the horizontal components are oriented randomly and not along East or North. For the land station data, the picker of *Diehl et al.* (2009) was applied by Dietrich Lange. Both picking approaches were tested on reference data sets. The hitrate of the land station S picker was about 50% while the hitrate for the OBS data set was about 33%. The mean difference between manually picked and automatically determined phase onsets for the OBS data set is 0.06 s with a standard deviation of 0.41 s. This is slightly higher than the average picking uncertainty of 0.23 s in the study of *Diehl et al.* (2009). However, this may be caused by large outliers as 75% of the differences of the OBS data set are below 0.26 s and are comparable to the uncertainties of *Diehl et al.* (2009). The median for the OBS picking errors is 0.08 s and the 25th percentile is 0.02 s. Thus, the S phase arrivals from the OBS data are well determined and of comparable quality to the land station data (Fig. G.1).

From 9020 detected S phase arrivals of the best 1043 located events (i.e. location quality classes A to C) about 95% have not been weighted out by NLL in the hypocentre determination hence about 88% of the OBS S phase arrivals and 99% of the land station data were used. One reason why less OBS picks were used compared to land station picks is, again, the higher noise level in OBS data. However, the main reason likely is that both data sets were analysed with a different phase picker. The approach to not only determine the P phase arrivals with MPX but also the S phase arrivals as well yielded in few well determined S phase picks of good qualities. The additional S phases improved the hypocentre locations and the amount of excellent events increased significantly. Especially the structures within the Pichilemu clusters are resolved more clearly. However, in total, less events were classified as "good" or better compared to the events determined by P wave onsets solely. Thus, for the interpretation of the results, hypocentres determined from both P phases only as well as P and S phases should be considered: the P phase hypocentres for a more general view and the P+S hypocentres for a more detailed view on localised structures.

Although the qualities of the automatically determined S phases are good, the hitrate is rather low. To increase hitrate the S phase picker by *Diehl et al.* (2009) could be modified in such way that the rotation of the horizontal components into the direction of the incoming wave based on the hypocentre location is skipped. In its current application the picker calculates rotation angles based on both, hypocentre locations and maximum energy, and skips events if both rotation angles differ too much. *Baillard et al.* (2014) recently developed another promising S phase picker that is based on kurtosis and was tested on OBS data. The median picking error was -0.09 s and the hit rate was as high as 77%. However, the picker detected almost twice as many S phase arrivals as a human picker in a reference data set. Thus, the picker probably detects some poor S phases as well, or noise. By now, the MPX engine is extended to process data on three-components and to pick S phase arrivals as well and could be tested on OBS data.

9. Conclusions

The Mw 8.8 Maule earthquake on 27 February 2010, affected an about 500 km long segment of the central Chilean margin between 34°S and 38.5°S that was considered to be a mature seismic gap. In response to this event, a network of 30 ocean-bottom seismometers was deployed for a three-month period north of the main shock where the highest co-seismic slip rates were detected, and combined with land station data providing a good coverage of the northern part of the rupture area onshore as well as offshore.

In this study aftershocks of the Mw 8.8 Maule earthquake from 2010 were analysed from the amphibious seismic network in order to gain information about the rupture zone, stress distributions, and faulting in the forearc after a megathrust event. Two years prior to the Maule event the German Collaborative Research Center SFB 574 "Volatiles and Fluids in Subduction Zones" operated an amphibious seismic network in the same area. Both data sets gave a great opportunity to compare seismicity and stress distributions before and after a megathrust event and to study the evolution of a subduction zone within the seismic cycle of a megathrust event.

The aim of this study was to answer the following questions:

- *Is it possible to automatically detect P and S phase arrivals of the Maule aftershocks on ocean-bottom seismometers and accomplish reliable hypocentre locations from those automatic picks? How is the quality of the determined phase arrivals compared to the automatically picked onsets from land station data? Is the quality of the automatically determined picks from the OBS data sufficient to extend the automated approach in such way that also magnitudes and focal mechanisms can be obtained automatically as well?*

  The approach to automatically detect S and P phase arrivals on OBS data yielded in well determined picks from that successfully well resolved hypocentre locations could be determined. Only the hit rate of the S phase picking was a little low. From the P phase picks and polarities magnitudes and fault plane solutions could be calculated. The focal mechanisms did scatter but so did the fault plane solutions of the manually picked data set from 2008 where the

mechanisms do not show a clear distribution by subduction zone segments.

Automatic picking engines produce picks with high consistency. However, human pickers still do have advantages. They can better tell apart spikes from actual phase onsets and if several earthquakes occurred in a short time span, a human picker is able to assign the phase onsets to the different events while in an automated approach the events would probably be classified as one poorly located earthquake. Thus, automatic phase arrival determination yields to well resolved picks but probably to less locatable events. For big data sets, e.g. catalogue data of several years or aftershock networks, this may not be a problem. However, if necessary, the amount of well determined events could be increased by manually evaluating and adopting the phase onsets of events categorised in lower quality classes. Together with a strong location algorithm that is capable of identifying and weighting down noise and mispicks, like NLL, the approach of this study to automatically determine phase onsets on OBS data leads to fast and reliable results.

- *How did the seismicity and magnitude distributions change after the Maule megathrust event? Did the stress field change within the seismic cycle?*

  Two local amphibious seismic networks with good coverage of the rupture plane of the Maule event, on- as well as offshore, provided the opportunity to compare seismicity, magnitude, and stress distributions before and after a large subduction event. The most profound features are: (1) a sharp reduction in intraslab seismic activity after the Maule earthquake, probably caused by a decrease of slab pull in intermediate-depth after the Maule earthquake, (2) a sharp increase in seismic activity at the slab interface above 50 km depth, where large parts of the rupture zone were mainly aseismic prior to the Maule earthquake. Further, the aftershock seismicity shows a broader depth distribution above 50 km depth, shifting the updip limit of the seismogenic zone about 30 km closer to the trench, and (3) an active seismic cluster in the 2008 data while in 2010 there is a seismic gap in about 40 to 50 km depth along the plate boundary. This lineated feature probably is related to a relic mantle body that is considered to have caused the seismic gap along the plate boundary.

  The seismic activity after the Maule event is not distributed in the typical aftershock pattern where larger events occur preferentially in regions of low coseismic slip while the region of smaller slip shows events with smaller magnitudes. The magnitudes are distributed homogeneously in both seismic networks. As the highest magnitude of an aftershock is Mw 4.6 in the 2010 seismic network it is likely that the events recorded during the deployment time span, starting six month after the main shock, are the smaller aftershocks of the

Maule main shock. This is supported by the findings of other studies of Maule aftershocks recorded earlier in 2010 that do confirm the typical distribution of aftershocks (*Agurto et al.*, 2012).

A comparison of stress changes in the subducting plate due to the Maule event is difficult because of two reasons. (1) The focal mechanism determination did not lead to reliable results, especially the fault plane solutions before the megathrust event are distributed heterogeneously. (2) The obtained stress orientations are located in different parts of the subduction zone. Before the Maule main shock, fault plane solutions are available for events below about 50 km depth while before, mainly focal mechanisms in the forearc are available. For the outer rise, fault plane solutions could be obtained only after the Maule earthquake. However, seismicity occurring in the outer rise indicate that after the Maule event, tensional stresses induced by slab pull increased in the outer rise. Before the Maule event only few events occurred in this area while the amount of normal faulting earthquakes, probably in large depths, increased substantially afterwards.

- *Are there any hints whether active splay faulting occurred in the wake of the Maule event and if so what triggered or promoted the splay fault reactivation?*

  Aftershocks of the 2010 Maule event reveal a well resolved seismically active 50 km long splay fault in the submarine forearc of central Chile. In previous studies in Sumatra shallow forearc seismicity detected in seismic networks was associated with splay faults (*Araki et al.*, 2006; *Sibuet et al.*, 2007; *Waldhauser et al.*, 2012). However, seismicity distributions were diffuse and did not define a clear fault plane other than the splay fault revealed in this study. The plate interface trenchward of the branching-point shows no seismic activity during the deployment period. From this observation it is likely that slip in this part of the rupture zone transferred onto a splay fault. Critical taper theory suggests that this part of the wedge is at the edge of instability in a compressive stress state. Rupture of future great megathrust earthquakes in that area may propagate along the splay fault again or may reactivate other splay faults when the outer wedge enters the critical state, increasing vertical displacements due to the steeper dip of the splay fault compared to the plate interface, and therefore, potentially increasing the amplitude of a tsunami wave. The possibility of splay faults being activated in some segments of the rupture zone but not others should be considered when modelling slip distributions. Between 34.5°S and 36°S the updip limit of the aftershock seismicity is clearly identified about 40 km landwards from the deformation front. As ruptures can propagate along splay faults, the updip limit, as seen in seismicity distribution maps, is not necessarily related to events along the plate boundary but instead to splay

faulting in the overriding plate. Although margin-parallel thrust ridges can be observed almost throughout the entire network post-seismic splay faulting occurred only for a small fraction indicating that the splay fault was only partly activated. Thus, when modelling slip distributions it should be considered that slip does not necessarily propagate along the whole extend of a splay fault inferred from bathymetry or reflection seismic data. The location of the splay fault coincides with large slip gradients at the northern termination of the rupture zone and may have limited northward rupture propagation of the Maule 2010 main shock.

Bibliography

Agurto, H., A. Rietbrock, I. Ryder, and M. Miller (2012), Seismic-afterslip characterization of the 2010 MW 8.8 Maule, Chile, earthquake based on moment tensor inversion, *Geophysical Research Letters*, *39*(20), L20,303, doi:10.1029/2012GL053434.

Aldersons, F. (2004), Toward a three-dimensional crustal structure of the Dead Sea region from local earthquake tomography, Ph.D. thesis, Tel-Aviv University, 130 pages.

Aldersons, F. (2005), *MannekenPix 1.7 User Guide*, http://faldersons.net/Software/MPX/MannekenPix.html.

Allen, R. (1978), Automatic earthquake recognition and timing from single traces, *Bulletin of the Seismological Society of America*, *68*(5), 1521–1532.

Allen, R. (1982), Automatic phase pickers: their present use and future prospects, *Bulletin of the Seismological Society of America*, *72*(6B), S225–S242.

Anderson, M., P. Alvarado, G. Zandt, and S. Beck (2007), Geometry and brittle deformation of the subducting nazca plate, central chile and argentina, *Geophysical Journal International*, *171*, 419–434, doi:10.1111/j.1365-246X.2007.03483.x.

Angermann, D., J. Klotz, and C. Reigber (1999), Space-geodetic estimation of the nazca-south american euler vector, *171*, 329–334, doi:10.1016/S0012-821X(99)00173-9.

Araki, E., M. Shinohara, K. Obana, T. Yamada, Y. Kaneda, T. Kanazawa, and K. Suyehiro (2006), Aftershock distribution of the 26 December 2004 Sumatra-Andaman earthquake from ocean bottom seismographic observation, *Earth, Planets, and Space*, *58*(2), 113–119.

Arroyo, I., I. Grevemeyer, E. Flueh, H. Kraft, D. Comte, M. Thorwart, Y. Dzierma, M. Lefeldt, and W. Rabbel (2010), Velocity structure and seismotectonics prior

to the 2010 chile earthquake (mw 8.8) in the maule region from an amphibious seismological network, in *Abtract G33A-0813*, presented at 2010 Fall Meeting, AGU, San Francisco, Calif., 13-17 Dec.

Aster, R., B. Beaudoin, J. Hole, M. Fouch, J. Fowler, and D. James (2005), IRIS Seismology Program marks 20 years of discovery, *Eos, Transactions American Geophysical Union*, *86*(17), 171–172, doi:10.1029/2005EO170002.

Astiz, L., and H. Kanamori (1986), Interplate coupling and temporal variation of mechanisms of intermediate-depth earthquakes in Chile, *Bulletin of the Seismological Society of America*, *76*(6), 1614–1622.

Astiz, L., T. Lay, and H. Kanamori (1988), Large intermediate-depth earthquakes and the subduction process, *Physics of the Earth and Planetary Interiors*, *53*(1-2), 80 – 166, doi:10.1016/0031-9201(88)90138-0.

Baer, M., and U. Kradolfer (1987), An automatic phase picker for local and teleseismic events, *Bulletin of the Seismological Society of America*, *77*(4), 1437–1445.

Baillard, C., W. C. Crawford, V. Ballu, C. Hibert, and A. Mangeney (2014), An Automatic Kurtosis-Based P- and S-Phase Picker Designed for Local Seismic Networks, *Bulletin of the Seismological Society of America*, *104*(1), 394–409, doi: 10.1785/0120120347.

Barrientos, S. (1981), Regionalizacion sismica de Chile, Master's thesis, Universidad de Chile.

Barrientos, S., E. Vera, P. Alvarado, and T. Monfret (2004), Crustal seismicity in central chile, *Journal of South American Earth Sciences*, *16*(8), 759 – 768, doi: 10.1016/j.jsames.2003.12.001.

Bremond d'Ars, J., C. Jaupart, and R. S. J. Sparks (1995), Distribution of volcanoes in active margins, *Journal of Geophysical Research*, *100*(B10), 20,421–20,432, doi: 10.1029/95JB02153.

Brudzinski, M. R., and W.-P. Chen (2005), Earthquakes and strain in subhorizontal slabs, *Journal of Geophysical Research*, *110*(B8), 08,303, doi:10.1029/2004JB003470.

Brune, J. N. (1970), Tectonic stress and the spectra of seismic shear waves from earthquakes, *Journal of Geophysical Research*, *75*(26), 4997–5009, doi:10.1029/JB075i026p04997.

Cahill, T., and B. L. Isacks (1992), Seismicity and shape of the subducted Nazca Plate, *Journal of Geophysical Research*, *97*(B12), 17,503–17,529, doi: 10.1029/92JB00493.

Campos, J., D. Hatzfeld, R. Madariaga, G. Lopez, E. Kausel, A. Zollo, G. Iannacone, R. Fromm, S. Barrientos, and H. Lyon-Caen (2002), A seismological study of the 1835 seismic gap in south-central chile, *Physics of the Earth and Planetary Interiors*, *132*(1–3), 177–195, doi:10.1016/S0031-9201(02)00051-1.

Christensen, D. H., and L. J. Ruff (1988), Seismic coupling and outer rise earthquakes, *Journal of Geophysical Research: Solid Earth*, *93*(B11), 13,421–13,444, doi:10.1029/JB093iB11p13421.

Clift, P., and P. Vannucchi (2004), Controls on tectonic accretion versus erosion in subduction zones: Implications for the origin and recycling of the continental crust, *Reviews of Geophysics*, *42*(2), RG2001, doi:10.1029/2003RG000127.

Clouard, V., J. Campos, A. Lemoine, A. Perez, and E. Kausel (2007), Outer rise stress changes related to the subduction of the Juan Fernandez Ridge, central Chile, *Journal of Geophysical Research*, *112*(B5), B05,305, doi:10.1029/2005JB003999.

Collings, R., D. Lange, A. Rietbrock, F. Tilmann, D. Natawidjaja, B. Suwargadi, M. Miller, and J. Saul (2012), Structure and seismogenic properties of the Mentawai segment of the Sumatra subduction zone revealed by local earthquake traveltime tomography, *Journal of Geophysical Research*, *117*(B1), B01,312,, doi: 10.1029/2011JB008469.

Collins, J. A., F. L. Vernon, J. A. Orcutt, R. A. Stephen, K. R. Peal, F. B. Wooding, F. N. Spiess, and J. A. Hildebrand (2001), Broadband seismology in the oceans: lessons from the Ocean Seismic Network Pilot Experiment, *Geophysical Research Letters*, *28*(1), 49–52, doi:10.1029/2000GL011638.

Collot, J.-Y., W. Agudelo, A. Ribodetti, and B. Marcaillou (2008), Origin of a crustal splay fault and its relation to the seismogenic zone and underplating at the erosional north Ecuador–south Colombia oceanic margin, *Journal of Geophysical Research*, *113*(B12102), doi:10.1029/2008JB005691.

Contreras-Reyes, E., I. Grevemeyer, E. R. Flueh, M. Scherwath, and M. Heesemann (2007), Alteration of the subducting oceanic lithosphere at the southern central Chile trench–outer rise, *Geochemistry, Geophysics, Geosystems*, *8*(7), 1–19, doi: 10.1029/2007GC001632.

Contreras-Reyes, E., I. Grevemeyer, E. R. Flueh, and C. Reichert (2008), Upper lithospheric structure of the subduction zone offshore of southern Arauco peninsula, Chile, at 38°S, *Journal of Geophysical Research*, *113*(B7), B07,303, doi: 10.1029/2007JB005569.

Contreras-Reyes, E., E. R. Flueh, and I. Grevemeyer (2010), Tectonic control on sediment accretion and subduction off south central Chile: Implications for coseismic rupture processes of the 1960 and 2010 megathrust earthquakes, *Tectonics*, *29*(6), doi:10.1029/2010TC002734.

Dahlen, F. A. (1984), Noncohesive critical Coulomb wedges: An exact solution, *Journal of Geophysical Research*, *89*(B12), 10,125–10,133, doi:10.1029/JB089iB12p10125.

Dannowski, A., I. Grevemeyer, H. Kraft, I. Arroyo, and M. Thorwart (2013), Crustal thickness and mantle wedge structure from receiver functions in the Chilean Maule region at 35° S, *Tectonophysics*, *592*, 159–164, doi:10.1016/j.tecto.2013.02.015.

Das, S., and C. Henry (2003), Spatial relation between main earthquake slip and its aftershock distribution, *Reviews of Geophysics*, *41*(3), 3–1 – 3–16, doi:10.1029/2002RG000119.

Delouis, B., J.-M. Nocquet, and M. Vallée (2010), Slip distribution of the February 27, 2010 Mw = 8.8 Maule Earthquake, central Chile, from static and high-rate GPS, InSAR, and broadband teleseismic data, *Geophysical Research Letters*, *37*(17), L17,305, doi:10.1029/2010GL043899.

Dessa, J.-X., F. Klingelhoefer, D. Graindorge, C. André, H. Permana, M.-A. Gutscher, A. Chauhan, S. C. Singh, and the SUMATRA-OBS Scientific Team (2009), Megathrust earthquakes can nucleate in the forearc mantle: Evidence from the 2004 Sumatra event, *Geology*, *37*(7), 659–662, doi:10.1130/G25653A.1.

Di Stefano, R., A. Amato, F. Aldersons, and E. Kissling (2002), Automatic repicking and re-weighting of first arrival times from the Italian Seismic Network waveforms database, in *AGU Fall Meeting Abstracts*.

Di Stefano, R., F. Aldersons, E. Kissling, P. Baccheschi, C. Chiarabba, and D. Giardini (2006), Automatic seismic phase picking and consistent observation error assessment: application to the Italian seismicity, *Geophysical Journal International*, *165*, 121–134, doi:10.1111/j.1365-246X.2005.02799.x.

Diehl, T., and E. Kissling (2008), Users Guide for MPX Picking System, in *3-*

D seismic velocity models of the alpine crust from local earthquake tomography, chap. Appendix D, T. Diehl, PhD thesis.

Diehl, T., E. Kissling, S. Husen, and F. Aldersons (2009), Consistent phase picking for regional tomography models: application to the greater Alpine region, *Geophysical Journal International*, *176*(2), 542–554, doi:10.1111/j.1365-246X.2008.03985.x.

Diehl, T., N. Deichmann, E. Kissling, and S. Husen (2009), Automatic S-wave picker for local earthquake tomography, *Bulletin of the Seismological Society of America*, *99*(3), 1906–1920, doi:{10.1785/0120080019}.

Dziewonski, A. M., T.-A. Chou, and J. H. Woodhouse (1981), Determination of earthquake source parameters from waveform data for studies of global and regional seismicity, *Journal of Geophysical Research*, *86*(B4), 2825–2852, doi:10.1029/JB086iB04p02825.

Ekström, G., M. Nettles, and A. Dziewonski (2012), The global cmt project 2004–2010: Centroid-moment tensors for 13,017 earthquakes, *Physics of the Earth and Planetary Interiors*, *200 – 201*(0), 1 – 9, doi:10.1016/j.pepi.2012.04.002.

Engdahl, E. R., A. Villaseñor, H. R. DeShon, and C. H. Thurber (2007), Teleseismic Relocation and Assessment of Seismicity (1918-2005) in the Region of the 2004 Mw 9.0 Sumatra-Andaman and 2005 Mw 8.6 Nias Island Great Earthquakes, *Bulletin of the Seismological Society of America*, *97*(1A), S43–S61, doi:10.1785/0120050614.

Farías, M., D. Comte, S. Roecker, D. Carrizo, and M. Pardo (2011), Crustal extensional faulting triggered by the 2010 Chilean earthquake: The Pichilemu Seismic Sequence, *Tectonics*, *30*(6), doi:10.1029/2011TC002888.

Fischer, R. (1936), The use of multiple measurements in taxonomic problems, *Annals of Eugenics*, *7*, 179–188.

Fischer, R. (1938), The statistical utilization of multiple measurements, *Annals of Eugenics*, *8*, 376–386.

Frohlich, C. (1987), Aftershocks and temporal clustering of deep earthquakes, *Journal of Geophysical Research: Solid Earth*, *92*(B13), 13,944–13,956, doi:10.1029/JB092iB13p13944.

Fromm, R., P. Alvarado, S. Beck, and G. Zandt (2006), The April 9, 2001 Juan

Fernández Ridge (Mw 6.7) Tensional Outer-Rise Earthquake and its Aftershock Sequence, *Journal of Seismology*, *10*(2), 163–170, doi:10.1007/s10950-006-9013-3.

Fujiwara, T., S. Kodaira, T. No, Y. Kaiho, N. Takahashi, and Y. Kaneda (2011), The 2011 Tohoku-Oki Earthquake: Displacement Reaching the Trench Axis, *Science*, *334*(6060), 1240, doi:10.1126/science.1211554.

Geersen, J., J. H. Behrmann, D. Völker, S. Krastel, C. R. Ranero, J. Diaz-Naveas, and W. Weinrebe (2011), Active tectonics of the South Chilean marine fore arc (35°S–40°S), *Tectonics*, *30*(3), TC3006, doi:10.1029/2010TC002777.

Geller, R. J. (1976), Scaling relations for earthquake source parameters and magnitudes, *Bulletin of the Seismological Society of America*, *66*(5), 1501–1523.

Gill, J. B. (1981), *Orogenic andesites and plate tectonics*, vol. 390, Springer-Verlag Berlin.

Grevemeyer, I., N. Kaul, J. L. Diaz-Naveas, H. W. Villinger, C. R. Ranero, and C. Reichert (2005), Heat flow and bending-related faulting at subduction trenches: Case studies offshore of nicaragua and central chile, *Earth and Planetary Science Letters*, *236*(1–2), 238 – 248, doi:10.1016/j.epsl.2005.04.048.

Gutenberg, B., and C. F. Richter (1941), Seismicity of the Earth, *Geological Society of America Special Papers*, *34*, 1–126, doi:10.1130/SPE34-p1.

Hacker, B. R., S. M. Peacock, G. A. Abers, and S. D. Holloway (2003), Subduction factory 2. Are intermediate-depth earthquakes in subducting slabs linked to metamorphic dehydration reactions?, *Journal of Geophysical Research*, *108*(B1), doi:10.1029/2001JB001129.

Hardebeck, J. L. (2012), Coseismic and postseismic stress rotations due to great subduction zone earthquakes, *Geophysical Research Letters*, *39*(21), 21,313, doi:10.1029/2012GL053438.

Havskov, J., and L. Ottemöller (1999), SeisAn Earthquake Analysis Software, *Seismological Research Letters*, *70*(5), 532–534, doi:10.1785/gssrl.70.5.532.

Hayes, G. P., D. J. Wald, and R. L. Johnson (2012), Slab1. 0: A three-dimensional model of global subduction zone geometries, *Journal of Geophysical Research: Solid Earth (1978–2012)*, *117*(B1), doi:10.1029/2011JB008524.

Hicks, S. P., A. Rietbrock, I. M. Ryder, C.-S. Lee, and M. Miller (2014), Anatomy

of a megathrust: The 2010 m8.8 maule, chile earthquake rupture zone imaged using seismic tomography, *Earth and Planetary Science Letters*, *405*, 142 – 155, doi:http://dx.doi.org/10.1016/j.epsl.2014.08.028.

Husen, S., and R. B. Smith (2004), Probabilistic earthquake relocation in three-dimensional velocity models for the Yellowstone National Park region, Wyoming, *Bulletin of the Seismological Society of America*, *94*(3), 880–896, doi:10.1785/0120030170.

Hyndman, R. D., M. Yamano, and D. A. Oleskevich (1997), The seismogenic zone of subduction thrust faults, *Island Arc*, *6*(3), 244–260, doi:10.1111/j.1440-1738.1997.tb00175.x.

Isacks, B., and P. Molnar (1969), Mantle earthquake mechanisms and the sinking of the lithosphere, *Nature*, *223*(5211), 1121–1124, doi:10.1038/2231121a0.

Kanamori, H. (1977), The energy release in great earthquakes, *Journal of Geophysical Research*, *82*(20), 2981–2987, doi:10.1029/JB082i020p02981.

Kraft, H. A. (2011), Lokalbebenanalyse am aktiven Kontinentalrand Südamerikas zwischen 34°S and 36°S, Master's thesis, IFM-GEOMAR and Christian-Albrechts-University Kiel.

Kuo-Chen, H., F. T. Wu, and S. W. Roecker (2012), Three-dimensional P velocity structures of the lithosphere beneath Taiwan from the analysis of TAIGER and related seismic data sets, *Journal of Geophysical Research*, *117*(B6), B06,306, doi:10.1029/2011JB009108.

Küperkoch, L., T. Meier, J. Lee, W. Friederich, and E. W. Group (2010), Automated determination of P-phase arrival times at regional and local distances using higher order statistics, *Geophysical Journal International*, *181*(2), 1159–1170, doi:10.1111/j.1365-246X.2010.04570.x.

Küperkoch, L., T. Meier, and T. Diehl (2012), *New Manual of Seismological Observatory Practice 2 (NMSOP-2)*, chap. 16 (Automated Event and Phase Identification), Deutsches GeoForschungsZentrum GFZ, Potsdam, doi:10.2312/GFZ.NMSOP-2_ch16.

Lange, D., F. Tilmann, S. E. Barrientos, E. Contreras-Reyes, P. Methe, M. Moreno, B. Heit, H. Agurto, P. Bernard, J.-P. Vilotte, and S. Beck (2012a), Aftershock seismicity of the 27 February 2010 Mw 8.8 Maule earthquake rupture zone, *Earth and Planetary Science Letters*, *317*, 413–425, doi:10.1016/j.epsl.2011.11.034.

Lange, D., F. J. Tilmann, K. Lieser, I. Grevemeyer, S. E. Barrientos, and T. Diehl (2012b), Local Earthquake Tomography of the Northern Part of the 27 February 2010 Maule Earthquake with the Extensional Aftershock Cluster of Pichilemu, Abstract T43E-2726 presented at 2012 Fall Meeting, AGU, San Francisco, Calif., 3-7 Dec.

Lay, T., and T. C. Wallace (1995), *Modern global seismology*, Academic press.

Lay, T., C. J. Ammon, H. Kanamori, K. D. Koper, O. Sufri, and A. R. Hutko (2010), Teleseismic inversion for rupture process of the 27 February 2010 Chile (Mw 8.8) earthquake, *Geophysical Research Letters*, *37*(13), L13,301, doi:10.1029/2010GL043379.

Lay, T., C. J. Ammon, H. Kanamori, L. Xue, and M. J. Kim (2011), Possible large near-trench slip during the 2011 Mw 9.0 off the Pacific coast of Tohoku Earthquake, *Earth, Planets and Space*, *63*(7), 687–692, doi:10.5047/eps.2011.05.033.

Li, S., M. Moreno, M. Rosenau, D. Melnick, and O. Oncken (2014), Splay fault triggering by great subduction earthquakes inferred from finite element models, *Geophysical Research Letters*, *41*(2), 385–391, doi:10.1002/2013GL058598.

Lienert, B., and J. Havskov (1995), A computer program for locating earthquakes both locally and globally, *Seismological Research Letters*, *66*, 26–36, doi:10.1785/gssrl.66.5.26.

Lieser, K., I. Grevemeyer, D. Lange, E. Flueh, F. Tilmann, and E. Contreras-Reyes (2014), Splay fault activity revealed by aftershocks of the 2010 Mw 8.8 Maule earthquake, central Chile, *Geology*, *42*(9), 823–826, doi:10.1130/G35848.1.

Lomax, A., J. Virieux, P. Volant, and C. Berge-Thierry (2000), Probabilistic Earthquake Location in 3D and Layered Models, in *Advances in Seismic Event Location*, *Modern Approaches in Geophysics*, vol. 18, edited by Thurber, CliffordH. and Rabinowitz, Nitzan, pp. 101–134, Springer, doi:10.1007/978-94-015-9536-0_5.

Lomax, A., A. Michelini, and A. Curtis (2009), Earthquake Location, Direct, Global-Search Methods, in *Encyclopedia of Complexity and Systems Science*, edited by R. A. Meyers, pp. 2449–2473, Springer, doi:10.1007/978-0-387-30440-3_150.

McKenzie, D., J. Jackson, and K. Priestley (2005), Thermal structure of oceanic and continental lithosphere, *Earth and Planetary Science Letters*, *233*(3–4), 337 – 349, doi:10.1016/j.epsl.2005.02.005.

Melnick, D., M. Moreno, M. Motagh, M. Cisternas, and R. L. Wesson (2012a), Splay fault slip during the Mw 8.8 2010 Maule Chile earthquake, *Geology*, *40*(3), 251–254, doi:10.1130/G32712.1.

Melnick, D., M. Moreno, M. Cisternas, and A. Tassara (2012b), Darwin seismic gap closed by the 2010 Maule earthquake, *Andean geology*, *39*, 558–563, doi:10.5027/andgeoV39n3-a11.

Mittag, H.-J. (2011), Kenngrößen univariater empirischer Verteilungen, in *Statistik*, pp. 49–63, Springer Berlin Heidelberg, doi:10.1007/978-3-642-17846-7_5.

Moore, G. F., N. L. Bangs, A. Taira, S. Kuramoto, E. Pangborn, and H. J. Tobin (2007), Three-Dimensional Splay Fault Geometry and Implications for Tsunami Generation, *Science*, *318*(5853), 1128–1131, doi:10.1126/science.1147195.

Moreno, M., D. Melnick, M. Rosenau, J. Baez, J. Klotz, O. Oncken, A. Tassara, J. Chen, K. Bataille, M. Bevis, et al. (2012), Toward understanding tectonic control on the Mw 8.8 2010 Maule Chile earthquake, *Earth and Planetary Science Letters*, *321*, 152–165, doi:10.1016/j.epsl.2012.01.006.

Moscoso, E., I. Grevemeyer, E. Contreras-Reyes, E. R. Flueh, Y. Dzierma, W. Rabbel, and M. Thorwart (2011), Revealing the deep structure and rupture plane of the 2010 Maule, Chile earthquake (Mw= 8.8) using wide angle seismic data, *Earth and Planetary Science Letters*, *307*(1), 147–155, doi:10.1016/j.epsl.2011.04.025.

Mueller, S., W. Spence, and G. L. Choy (1996), Inelastic models of lithospheric stress-11. Implications for outer-rise seismicity and dynamics, *Geophysical Journal International*, *125*(1), 54–72, doi:10.1111/j.1365-246X.1996.tb06534.x.

Müller, R. D., W. R. Roest, J.-Y. Royer, L. M. Gahagan, and J. G. Sclater (1997), Digital isochrons of the world's ocean floor, *Journal of Geophysical Research*, *102*(B2), 3211–3214, doi:10.1029/96JB01781.

National Geophysical Data Center, NOAA (2015), Significant Earthquake Database, doi:10.7289/V5TD9V7K, visited on 30. Jan 2015.

Oleskevich, D. A., R. D. Hyndman, and K. Wang (1999), The updip and downdip limits to great subduction earthquakes: Thermal and structural models of Cascadia, south Alaska, SW Japan, and Chile, *Journal of Geophysical Research*, *104*(B7), 14,965–14,991, doi:10.1029/1999JB900060.

Omori, F. (1895), On the after-shocks of earthquakes.

Ottemöller, L., and J. Havskov (2003), Moment magnitude determination for local and regional earthquakes based on source spectra, *Bulletin of the Seismological Society of America*, *93*(1), 203–214, doi:10.1785/0120010220.

Ottemöller, L., P. Voss, and J. Havskov (2011), *SEISAN Earthquake Analysis Software for Windows, Solaris, Linux and MACOSX*.

Pardo, M., D. Comte, and T. Monfret (2002), Seismotectonic and stress distribution in the central chile subduction zone, *Journal of South American Earth Sciences*, *15*(1), 11 – 22, doi:10.1016/S0895-9811(02)00003-2.

Pearce, R. G. (1977), Fault plane solutions using relative amplitudes of P and pP, *Geophysical Journal International*, *50*(2), 381–394, doi:10.1111/j.1365-246X.1977.tb04179.x.

Pesicek, J. D., E. R. Engdahl, C. H. Thurber, H. R. DeShon, and D. Lange (2012), Mantle subducting slab structure in the region of the 2010 M8.8 Maule earthquake (30–40°S), Chile, *Geophysical Journal International*, *191*(1), 317–324, doi:10.1111/j.1365-246X.2012.05624.x.

Ranero, C. R., J. Phipps Morgan, K. McIntosh, and C. Reichert (2003), Bending-related faulting and mantle serpentinization at the Middle America trench, *Nature*, *425*(6956), 367–373, doi:10.1038/nature01961.

Ranero, C. R., A. Villaseñor, J. Phipps Morgan, and W. Weinrebe (2005), Relationship between bend-faulting at trenches and intermediate-depth seismicity, *Geochemistry, Geophysics, Geosystems*, *6*(12), 1–25, doi:10.1029/2005GC000997.

Ranero, C. R., R. von Huene, W. Weinrebe, and C. Reichert (2006), Tectonic processes along the chilean convergent margin, in *The Andes*, Springer-Verlag Berlin Heidelberg, doi:10.1007/978-3-540-48684-8_5.

Reasenberg, P. A., and D. Oppenheimer (1985), *FPFIT, FPPLOT and FPPAGE: Fortran computer programs for calculating and displaying earthquake fault-plane solutions*, U.S. Geological Survey Open-File Report 85-739.

Richter, C. (1955), Foreshocks and aftershocks, *Div. of Mines Bulletin*, *171*.

Rietbrock, A., I. Ryder, G. Hayes, C. Haberland, D. Comte, S. Roecker, and H. Lyon-Caen (2012), Aftershock seismicity of the 2010 Maule Mw= 8.8, Chile, earthquake:

Correlation between co-seismic slip models and aftershock distribution?, *Geophysical Research Letters*, *39*(8), doi:10.1029/2012GL051308.

Ryder, I., A. Rietbrock, K. Kelson, R. Bürgmann, M. Floyd, A. Socquet, C. Vigny, and D. Carrizo (2012), Large extensional aftershocks in the continental forearc triggered by the 2010 Maule earthquake, Chile, *Geophysical Journal International*, *188*(3), 879–890, doi:10.1111/j.1365-246X.2011.05321.x.

Schweitzer, J. (2004), *onset*, ftp://ftp.norsar.no/pub/outgoing/johannes/onset/.

Seno, T., and Y. Yamanaka (1996), *Double Seismic Zones, Compressional Deep Trench-Outer Rise Events, and Superplumes*, pp. 347–355, American Geophysical Union, doi:10.1029/GM096p0347.

Sibuet, J.-C., C. Rangin, X. Le Pichon, S. Singh, A. Cattaneo, D. Graindorge, F. Klingelhoefer, J.-Y. Lin, J. Malod, T. Maury, et al. (2007), 26th December 2004 great Sumatra–Andaman earthquake: co-seismic and post-seismic motions in northern Sumatra, *Earth and Planetary Science Letters*, *263*(1), 88–103, doi:10.1016/j.epsl.2007.09.005.

Simoes, M., J. P. Avouac, R. Cattin, and P. Henry (2004), The Sumatra subduction zone: A case for a locked fault zone extending into the mantle, *Journal of Geophysical Research*, *109*(B10), B10,402, doi:10.1029/2003JB002958.

Sobiesiak, M. M. (2000), Fault plane structure of the Antofagasta, Chile Earthquake of 1995, *Geophysical Research Letters*, *27*(4), 577–580, doi:10.1029/1999GL010498.

Stauder, W. (1968a), Mechanism of the Rat Island earthquake sequence of February 4, 1965, with relation to island arcs and sea-floor spreading, *Journal of Geophysical Research*, *73*(12), 3847–3858, doi:10.1029/JB073i012p03847.

Stauder, W. (1968b), Tensional character of earthquake foci beneath the Aleutian Trench with relation to sea-floor spreading, *Journal of Geophysical Research*, *73*(24), 7693–7701, doi:10.1029/JB073i024p07693.

Stein, S., and M. Wysession (2009), *An introduction to seismology, earthquakes, and earth structure*, John Wiley & Sons.

Stern, R. J. (2002), Subduction zones, *Reviews of geophysics*, *40*(4), 3–1–3–38, doi:10.1029/2001RG000108.

Syracuse, E. M., and G. A. Abers (2006), Global compilation of variations in slab depth beneath arc volcanoes and implications, *Geochemistry, Geophysics, Geosystems*, *7*(5), 1–18, doi:10.1029/2005GC001045.

Tarantola, A., and B. Valette (1982), Inverse problems - Quest for information, *Journal of Geophysics*, *50*, 159–170.

Tilmann, F. J., T. J. Craig, I. Grevemeyer, B. Suwargadi, H. Kopp, and E. Flueh (2010), The updip seismic/aseismic transition of the Sumatra megathrust illuminated by aftershocks of the 2004 Aceh-Andaman and 2005 Nias events, *Geophysical Journal International*, *181*(3), 1261–1274, doi:10.1111/j.1365-246X.2010.04597.x.

Valoroso, L., L. Improta, L. Chiaraluce, R. D. Stefano, L. Ferranti, A. Govoni, and C. Chiarabba (2009), Active faults and induced seismicity in the Val d'Agri area (Southern Apennines, Italy), *Geophysical Journal International*, *178*, 488–502, doi:10.1111/j.1365-246X.2009.04166.x.

Vargas, G., M. Farias, S. Carretier, A. Tassara, S. Baize, and D. Melnick (2011), Coastal uplift and tsunami effects associated to the 2010 Mw8. 8 Maule earthquake in Central Chile, *Andean Geology*, *38*(1), 219–238, doi:10.5027/andgeoV38n1-a12.

Vietor, T., and H. Echtler (2006), Episodic neogene southward growth of the andean subduction orogen between 30°s and 40°s – plate motions, mantle flow, climate, and upper-plate structure, in *The Andes*, Springer-Verlag Berlin Heidelberg, doi:10.1007/978-3-540-48684-8_18.

Vigny, C., A. Socquet, S. Peyrat, J.-C. Ruegg, M. Métois, R. Madariaga, S. Morvan, M. Lancieri, R. Lacassin, J. Campos, D. Carrizo, M. Bejar-Pizarro, S. Barrientos, R. Armijo, C. Aranda, M.-C. Valderas-Bermejo, I. Ortega, F. Bondoux, S. Baize, H. Lyon-Caen, A. Pavez, J. P. Vilotte, M. Bevis, B. Brooks, R. Smalley, H. Parra, J.-C. Baez, M. Blanco, S. Cimbaro, and E. Kendrick (2011), The 2010 Mw 8.8 Maule Megathrust Earthquake of Central Chile, Monitored by GPS, *Science*, *332*(6036), 1417–1421, doi:10.1126/science.1204132.

Wagner, L. S., S. Beck, and G. Zandt (2005), Upper mantle structure in the south central chilean subduction zone (30°to 36°s), *Journal of Geophysical Research*, *110*, B01,308, doi:10.1029/2004JB003238.

Waldhauser, F., D. P. Schaff, T. Diehl, and E. R. Engdahl (2012), Splay faults imaged by fluid-driven aftershocks of the 2004 Mw 9.2 Sumatra-Andaman earthquake, *Geology*, *40*(3), 243–246, doi:10.1130/G32420.1.

Wang, K., and Y. Hu (2006), Accretionary prisms in subduction earthquake cycles: The theory of dynamic Coulomb wedge, *Journal of Geophysical Research*, *111*(B6), B06,410, doi:10.1029/2005JB004094.

Wang, K., I. Wada, and Y. Ishikawa (2004), Stresses in the subducting slab beneath southwest Japan and relation with plate geometry, tectonic forces, slab dehydration, and damaging earthquakes, journal = Journal of Geophysical Research, *109*(B8), B08,304, doi:10.1029/2003JB002888.

Wendt, J., D. D. Oglesby, and E. L. Geist (2009), Tsunamis and splay fault dynamics, *Geophysical Research Letters*, *36*(15), L15,303, doi:10.1029/2009GL038295.

A. Introduction

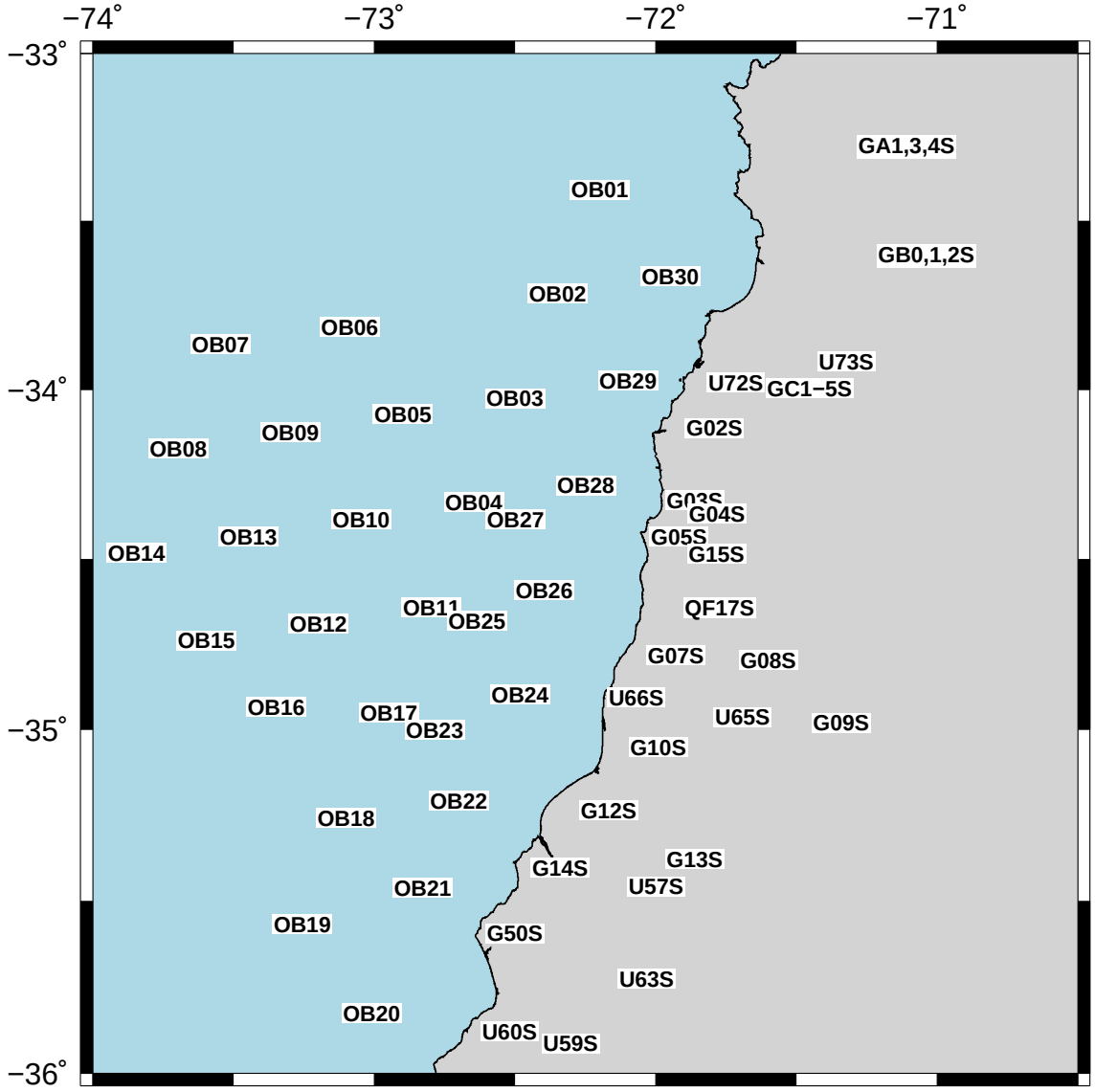

Figure A.1.: Network configuration including station names.

B. Automated picking of P waves

B.1. MPX command files

```
.************  Command File for MannekenPix (V.1.7.9 June 2004)  **************
.                                                                              .
.      All lines starting with '.' are ignored. Do not delete blank lines.     .
.      '|' marks the column of the last authorized character.                  .
.      It is recommended to perform a backup of the original command file.     .
.                                                                              .
................................................................................
.                                                                              |
. 1) Title and Input - Output                                                  |
.    ------------------------                                                  |
.                                                                              |
.       Title for output                                                       |
MPX 1.7.9 - HA - Test -
.                                                                              |
.       Input file containing the list of seismograms to pick                  |
Mpx.Liste_OBS
.                                                                              |
.       Output log file (No log file if blank)                                 |
Mpx_R_OBS.Log
.                                                                              |
.       Output summary file: RECOMMENDED (No summary file if blank)            |
Mpx_R_OBS.Sum
.                                                                              |
.       Output unpicked list of seismograms (No unpicked list if blank)        |
Mpx_R_OBS.Unp
.                                                                              |
.       Output error log (No error log if blank)                               |
Mpx_R_OBS.Err
.                                                                              |
.       Output export file (No export file if blank)                           |
Mpx_R_OBS.Exp
.                                                                              |
.       Velest cnv file (No cnv if blank)                                      |
Mpx_R_OBS.Cnv
.                                                                              |
.       Write Reference to cnv if available and no Auto-P found (Y = 1, N = 0) |
                0
.                                                                              |
.       Write Auto-P to Sac file ( Y = 1 ,  N = 0 )                            |
                0
.                                                                              |
................................................................................
.                                                                              |
. 2) Basic Options   ( Pick seismogram = 1 ;  Do not pick seismogram = 0 )     |
.    -------------                                                             |
.                                                                              |
.    Routine value exists        Routine value is missing                      |
             1                           1
.                                                                              |
.    Reference value exists      Reference value is missing                    |
             1                           1
.                                                                              |
.    Predicted value exists      Routine and Predicted missing (1 not valid)   |
             1                           0
.                                                                              |
................................................................................
.                                                                              |
. 3) Event Selection           ( Y = 1 ,  N = 0 )                              |
.    ---------------                                                           |
.                                                                              |
.    Network select (Use All = 0, Keep some = 1, Exclude some = -1) N Networks  |
             0                                                          2
.                                                                              |
.    Networks, Max.5 ( Maximum 8 Characters, comma separated. )                |
IL,JD
.                                                                              |
.    Station select (Use All = 0, Keep some = 1, Exclude some = -1)    N Sta   |
             0                                                          3
.                                                                              |
.    Stations, Max.15 ( Maximum 4 Characters, comma separated. )               |
BAD,BAD2,WORS
.                                                                              |
.    Component selection         Use   V    N-S    W-E                        |
             0                         1     0      0
.                                                                              |
.    Magnitude bandpass          Mag Min                  Mag Max              |
             0                     -5.0                     10.0
.                                                                              |
.    Distance selection          Distance min (km)   Distance max (km)        |
             0                          0.0               500.0
.                                                                              |
.    Sampling rate selection     N SR     SR1    SR2    SR3    SR4    SR5     |
             0                    2      50.    100.
.                                                                              |
................................................................................
.                                                                              |
. 4) Picking Parameters                                                        |
.    ------------------                                                        |
.                                                                              |
.    Picking Mode ( 1 = Highest Accuracy , 2 = Highest Hit Rate )              |
           1
.                                                                              |
.    Try to Despike ( Y = 1 ,  N = 0 )                                         |
           0
.                                                                              |
.    Wiener Filter Noise window (sec)     Wiener Filter Signal window (sec)    |
                  2.0                                 2.0
.                                                                              |
.    Wiener Filter Picked noise safety gaps     (4 values, sec)                |
                  0.7   0.35   0.18  0.090
.                                                                              |
.    Wiener Filter Picked signal safety gaps    (4 values, sec)                |
                  0.7   0.35   0.18  0.09
.                                                                              |
.    Wiener Filter Predicted noise safety gaps  (4 values, sec)                |
                  0.7   0.35   0.18   0.09
.                                                                              |
.    Wiener Filter Predicted signal safety gaps (4 values, sec)                |
                  0.7   0.35   0.18   0.09
.                                                                              |
.    Wiener Filter length (sec)                                                |
              4.0
.                                                                              |
.    Lower threshold (Hz) for maximum of signal amplitude spectrum             |
                           0.5
.                                                                              |
................................................................................
.                                                                              |
. 5) Weighting Scheme (Fischer's linear discriminant coefficients)             |
.    ----------------                                                          |
.                                                                              |
.    Number of classes  ( N <= 5 )                                             |
              4
.                                                                              |
.    Constant   ( <= 5, class 1 to N )  > MP1.6.2 DEAD SEA HIGHEST ACCURACY <  |
-13.650 -14.739 -16.388 -16.981
.                                                                              |
.    WFStoN     ( <= 5, class 1 to N )                                         |
0.293   0.344   0.383   0.360
.                                                                              |
.    GDStoN     ( <= 5, class 1 to N )                                         |
-0.726  -0.786  -0.738  -0.873
.                                                                              |
.    GDAmpRatio ( <= 5, class 1 to N )                                         |
0.750   0.831   0.805   0.907
.                                                                              |
.    SigFmaxRa  ( <= 5, class 1 to N )                                         |
0.241   0.232   0.217   0.205
.                                                                              |
.    DFAmpMax   ( <= 5, class 1 to N )                                         |
0.001   0.062   0.040   -0.008
.                                                                              |
.    CFRatio    ( <= 5, class 1 to N )                                         |
0.195   -0.140  -0.203  -0.024
.                                                                              |
.    PcAbove    ( <= 5, class 1 to N )                                         |
-0.108  -0.033  0.349   0.784
.                                                                              |
.    PcBelow    ( <= 5, class 1 to N )                                         |
0.142   0.153   0.197   0.238
.                                                                              |
.    CFNoiDev   ( <= 5, class 1 to N )                                         |
2.922   3.585   3.730   3.783
.                                                                              |
................................................................................
.                                                                              |
. 6) Application of WF                                                         |
.    -----------------                                                         |
.                                                                              |
.    Filtering ( Unfiltered = 0 ,  Filtered = 1 ,  Filtered + Unfiltered = 2 ) |
         1
.                                                                              |
................................................................................
.                                                                              |
. 7) MP Modes                  ( Y = 1 ,  N = 0 )                              |
.    --------                                                                  |
.                                                                              |
.    Full Batch                                                                |
         0
.                                                                              |
.******************  End of Command File for MannekenPix  *********************
```

Figure B.1.: Final MannekenPix command file (MannekenPix.cmd) for OBS network.

```
.*************  Command File for MannekenPix (V.1.7.9 June 2004)  **************
.                                                                               .
.      All lines starting with '.' are ignored. Do not delete blank lines.      .
.      '|' marks the column of the last authorized character.                   .
.      It is recommended to perform a backup of the original command file.      .
.                                                                               .
.................................................................................
.                                                                               |
. 1) Title and Input - Output                                                   |
.    ------------------------                                                   |
.                                                                               |
.       Title for output                                                        |
MPX 1.7.9 - HA - Test -
.                                                                               |
.       Input file containing the list of seismograms to pick                   |
Mpx.Liste_LAND
.                                                                               |
.       Output log file (No log file if blank)                                  |
MpxR_LAND.Log
.                                                                               |
.       Output summary file: RECOMMENDED (No summary file if blank)             |
MpxR_LAND.Sum
.                                                                               |
.       Output unpicked list of seismograms (No unpicked list if blank)         |
MpxR_LAND.Unp
.                                                                               |
.       Output error log (No error log if blank)                                |
MpxR_LAND.Err
.                                                                               |
.       Output export file (No export file if blank)                            |
MpxR_LAND.Exp
.                                                                               |
.       Velest cnv file (No cnv if blank)                                       |
MpxR_LAND.Cnv
.                                                                               |
.       Write Reference to cnv if available and no Auto-P found (Y = 1, N = 0) |
                0
.                                                                               |
.       Write Auto-P to Sac file ( Y = 1 ,  N = 0 )                             |
                0
.                                                                               |
.................................................................................
.                                                                               |
. 2) Basic Options   ( Pick seismogram = 1 ;  Do not pick seismogram = 0 )      |
.    -------------                                                              |
.                                                                               |
.    Routine value exists        Routine value is missing                       |
            1                           1
.                                                                               |
.    Reference value exists      Reference value is missing                     |
            1                           1
.                                                                               |
.    Predicted value exists      Routine and Predicted missing (1 not valid)    |
            1                           0
.                                                                               |
.................................................................................
.                                                                               |
. 3) Event Selection           ( Y = 1 ,  N = 0 )                               |
.    ---------------                                                            |
.                                                                               |
.    Network select (Use All = 0, Keep some = 1, Exclude some = -1) N Networks   |
            0                                                           2
.                                                                               |
.    Networks, Max.5 ( Maximum 8 Characters, comma separated. )                 |
IL,JD
.                                                                               |
.    Station select (Use All = 0, Keep some = 1, Exclude some = -1)    N Sta    |
            0                                                           3
.                                                                               |
.    Stations, Max.15 ( Maximum 4 Characters, comma separated. )                |
BAD,BAD2,WORS
.                                                                               |
.    Component selection         Use   V    N-S    W-E                         |
            0                          1     0      0
.                                                                               |
.    Magnitude bandpass          Mag Min                   Mag Max             |
            0                     -5.0                      10.0
.                                                                               |
.    Distance selection          Distance min (km)   Distance max (km)         |
            0                         0.0               500.0
.                                                                               |
.    Sampling rate selection     N SR     SR1    SR2    SR3    SR4    SR5      |
            0                     2      50.    100.
.                                                                               |
.................................................................................
.                                                                               |
. 4) Picking Parameters                                                         |
.    ------------------                                                         |
.                                                                               |
.    Picking Mode ( 1 = Highest Accuracy , 2 = Highest Hit Rate )               |
           1
.                                                                               |
.    Try to Despike ( Y = 1 ,  N = 0 )                                          |
           0
.                                                                               |
.    Wiener Filter Noise window (sec)     Wiener Filter Signal window (sec)     |
                    2.0                                 2.0
.                                                                               |
.    Wiener Filter Picked noise safety gaps     (4 values, sec)                 |
                    0.4   0.2   0.10  0.05
.                                                                               |
.    Wiener Filter Picked signal safety gaps    (4 values, sec)                 |
                    0.4   0.2   0.10  0.05
.                                                                               |
.    Wiener Filter Predicted noise safety gaps  (4 values, sec)                 |
                    0.4   0.2   0.10   0.05
.                                                                               |
.    Wiener Filter Predicted signal safety gaps (4 values, sec)                 |
                    0.4   0.2   0.10   0.05
.                                                                               |
.    Wiener Filter length (sec)                                                 |
               4.0
.                                                                               |
.    Lower threshold (Hz) for maximum of signal amplitude spectrum              |
                               1.0
.                                                                               |
.................................................................................
.                                                                               |
. 5) Weighting Scheme (Fischer linear discriminant coefficients)             |
.    ----------------                                                           |
.                                                                               |
.    Number of classes  ( N <= 5 )                                              |
              4
.                                                                               |
.    Constant   ( <= 5, class 1 to N )  > MP1.6.2 DEAD SEA HIGHEST ACCURACY <   |
-11.050 -9.828  -10.965 -9.274
.                                                                               |
.    WFStoN     ( <= 5, class 1 to N )                                          |
0.241   0.258   0.250   0.192
.                                                                               |
.    GDStoN     ( <= 5, class 1 to N )                                          |
-0.379  -0.315  -0.402  -0.403
.                                                                               |
.    GDAmpRatio ( <= 5, class 1 to N )                                          |
0.236   0.169   0.287   0.303
.                                                                               |
.    SigFmaxRa  ( <= 5, class 1 to N )                                          |
0.215   0.195   0.200   0.198
.                                                                               |
.    DFAmpMax   ( <= 5, class 1 to N )                                          |
-0.027  -0.014  -0.032  0.006
.                                                                               |
.    CFRatio    ( <= 5, class 1 to N )                                          |
0.039   -0.151  -0.197  -0.106
.                                                                               |
.    PcAbove    ( <= 5, class 1 to N )                                          |
-0.305  -0.547  -0.383  0.158
.                                                                               |
.    PcBelow    ( <= 5, class 1 to N )                                          |
0.069   0.095   0.129   0.116
.                                                                               |
.    CFNoiDev   ( <= 5, class 1 to N )                                          |
1.482   2.236   2.163   2.276
.                                                                               |
.................................................................................
.                                                                               |
. 6) Application of WF                                                          |
.    -----------------                                                          |
.                                                                               |
.    Filtering ( Unfiltered = 0 ,  Filtered = 1 ,  Filtered + Unfiltered = 2 ) |
          1
.                                                                               |
.................................................................................
.                                                                               |
. 7) MP Modes                  ( Y = 1 ,  N = 0 )                               |
.    --------                                                                   |
.                                                                               |
.    Full Batch                                                                 |
           0
.                                                                               |
.******************  End of Command File for MannekenPix  ********************
```

Figure B.2.: Final MannekenPix command file (MannekenPix.cmd) for land station network.

B.2. Picking parameter (OBS)

Table B.1.: Set up for all evaluated 93 MPX parameter sets.

Parameter	Gaps				Estimation windows	Wiener filter	Threshold
	s				s	s	Hz
1	0.55	0.28	0.14	0.07	1.0	2.0	0.5
2	0.55	0.38	0.21	0.04	2.0	4.0	0.5
3	0.55	0.38	0.21	0.04	1.0	2.0	0.75
4	0.55	0.38	0.21	0.04	1.0	2.0	0.5
5	0.55	0.28	0.14	0.07	2.0	4.0	0.5
6	0.55	0.28	0.14	0.07	1.0	2.0	0.75
7	0.55	0.28	0.14	0.07	1.0	2.0	1.5
8	0.55	0.38	0.21	0.04	1.0	2.0	1.5
9	1.0	0.68	0.32	0.04	1.0	2.0	1.5
10	1.0	0.68	0.32	0.04	1.0	2.0	0.75
11	1.0	0.68	0.32	0.04	1.0	2.0	0.5
12	1.0	0.70	0.39	0.08	1.0	2.0	0.75
13	1.0	0.70	0.39	0.08	2.0	4.0	0.75
14	1.0	0.70	0.39	0.08	2.0	4.0	1.5
15	1.0	0.70	0.39	0.08	1.0	2.0	0.5
16	1.0	0.70	0.39	0.08	1.0	2.0	1.5
17	0.55	0.28	0.14	0.07	2.0	4.0	1.5
18	0.55	0.38	0.21	0.04	2.0	4.0	1.5
19	1.0	0.68	0.36	0.04	2.0	4.0	1.5
20	1.0	0.68	0.36	0.04	2.0	4.0	0.5
21	1.0	0.7	0.39	0.08	1.0	2.0	1.5
22	1.0	0.7	0.39	0.08	2.0	4.0	0.5
23	2.5	1.25	0.64	0.04	2.0	4.0	0.5
24	2.5	1.25	0.64	0.04	2.0	4.0	1.5
25	2.5	1.25	0.64	0.04	1.0	2.0	0.5
26	2.5	1.25	0.64	0.04	1.0	2.0	1.5
27	2.5	1.68	0.87	0.05	1.0	2.0	0.5
28	2.5	1.68	0.87	0.05	1.0	2.0	1.5
29	2.5	1.68	0.87	0.05	2.0	4.0	0.5
30	2.5	1.68	0.87	0.05	2.0	4.0	1.5
31	2.5	1.25	1.03	0.08	2.0	4.0	1.5
32	2.5	1.25	1.03	0.08	2.0	4.0	0.5
33	2.5	1.25	1.03	0.08	1.0	2.0	0.5
34	2.5	1.25	1.03	0.08	1.0	2.0	1.5
35	2.5	1.7	0.89	0.08	2.0	4.0	1.5
36	2.5	1.7	0.89	0.08	2.0	4.0	0.5
37	2.5	1.7	0.89	0.08	1.0	2.0	0.5
38	2.5	1.7	0.89	0.08	1.0	2.0	1.5
39	1.5	0.75	0.4	0.03	2.0	4.0	0.5
40	1.5	0.75	0.45	0.03	2.0	4.0	0.5
41	1.5	0.7	0.4	0.03	2.0	4.0	0.5
42	1.5	0.8	0.4	0.03	2.0	4.0	0.5
43	2.0	0.8	0.4	0.030	2.0	4.0	0.5
44	2.0	1.0	0.4	0.03	2.0	4.0	0.5
45	2.0	1.0	0.7	0.03	2.0	4.0	0.5

Table B.1 (Continued): Set up for all evaluated 93 MPX parameter sets.

Parameter	**Gaps**				**Estimation windows**	**Wiener filter**	**Threshold**
	s				**s**	**s**	**Hz**
46	2.0	1.0	0.7	0.04	2.0	4.0	0.5
47	2.0	1.0	0.5	0.040	2.0	4.0	0.5
48	2.0	1.0	0.5	0.04	2.0	4.0	1.5
49	2.5	1.25	1.0	0.04	2.0	4.0	0.5
50	2.5	1.25	0.8	0.04	2.0	4.0	0.5
51	1.5	0.75	0.4	0.04	2.0	4.0	0.5
52	1.5	0.75	0.4	0.04	2.0	4.0	1.5
53	1.5	0.75	0.5	0.04	2.0	4.0	0.5
54	1.5	0.75	0.5	0.04	2.0	4.0	1.5
55	2.0	0.75	0.5	0.04	2.0	4.0	0.5
56	1.5	1.0	0.5	0.04	2.0	4.0	0.5
57	1.5	0.9	0.5	0.04	2.0	4.0	0.5
58	1.5	0.9	0.4	0.04	2.0	4.0	0.5
59	1.5	0.9	0.6	0.04	2.0	4.0	0.5
60	1.5	0.8	0.5	0.04	2.0	4.0	0.5
61	1.5	0.8	0.4	0.04	2.0	4.0	0.5
62	1.5	0.8	0.6	0.04	2.0	4.0	0.5
63	1.6	0.8	0.5	0.04	2.0	4.0	0.5
64	1.7	0.8	0.5	0.04	2.0	4.0	0.5
65	1.6	0.9	0.5	0.04	2.0	4.0	0.5
66	1.7	0.8	0.5	0.03	2.0	4.0	0.5
67	1.6	0.8	0.5	0.03	2.0	4.0	0.5
68	1.6	0.9	0.5	0.03	2.0	4.0	0.5
69	1.4	0.75	0.5	0.04	2.0	4.0	0.5
70	1.4	0.7	0.5	0.04	2.0	4.0	0.5
71	1.5	0.75	0.5	0.03	2.0	4.0	0.5
72	1.5	0.85	0.5	0.04	2.0	4.0	0.5
73	1.7	0.85	0.5	0.04	2.0	4.0	0.5
74	1.8	0.9	0.5	0.04	2.0	4.0	0.5
75	1.8	0.9	0.6	0.04	2.0	4.0	0.5
76	1.5	0.9375	0.5	0.04	2.0	4.0	0.5
77	1.875	0.9375	0.5	0.04	2.0	4.0	0.5
78	1.5	0.75	0.5	0.04	2.0	4.0	1.0
79	1.5	0.75	0.5	0.04	1.0	2.0	0.5
80	2.0	1.0	0.75	0.04	2.0	4.0	0.5
81	1.5	0.75	0.5	0.08	2.0	4.0	0.5
82	2.0	1.0	0.75	0.08	2.0	4.0	0.5
83	1.5	0.75	0.4	0.08	2.0	4.0	0.5
84	1.5	0.75	0.5	0.06	2.0	4.0	0.5
85	1.5	0.75	0.4	0.06	2.0	4.0	0.5
86	2.0	0.8	0.4	0.08	2.0	4.0	0.5
87	2.0	1.0	0.7	0.08	2.0	4.0	0.5
88	2.0	0.8	0.4	0.06	2.0	4.0	0.5
89	2.0	1.0	0.7	0.06	2.0	4.0	0.5
90	1.5	0.75	0.45	0.03	2.0	4.0	0.5
91	0.7	0.35	0.21	0.07	2.0	4.0	1.5
92	0.7	0.35	0.18	0.09	2.0	4.0	1.5
93	0.7	0.35	0.18	0.09	2.0	4.0	0.5

Box plots (OBS)

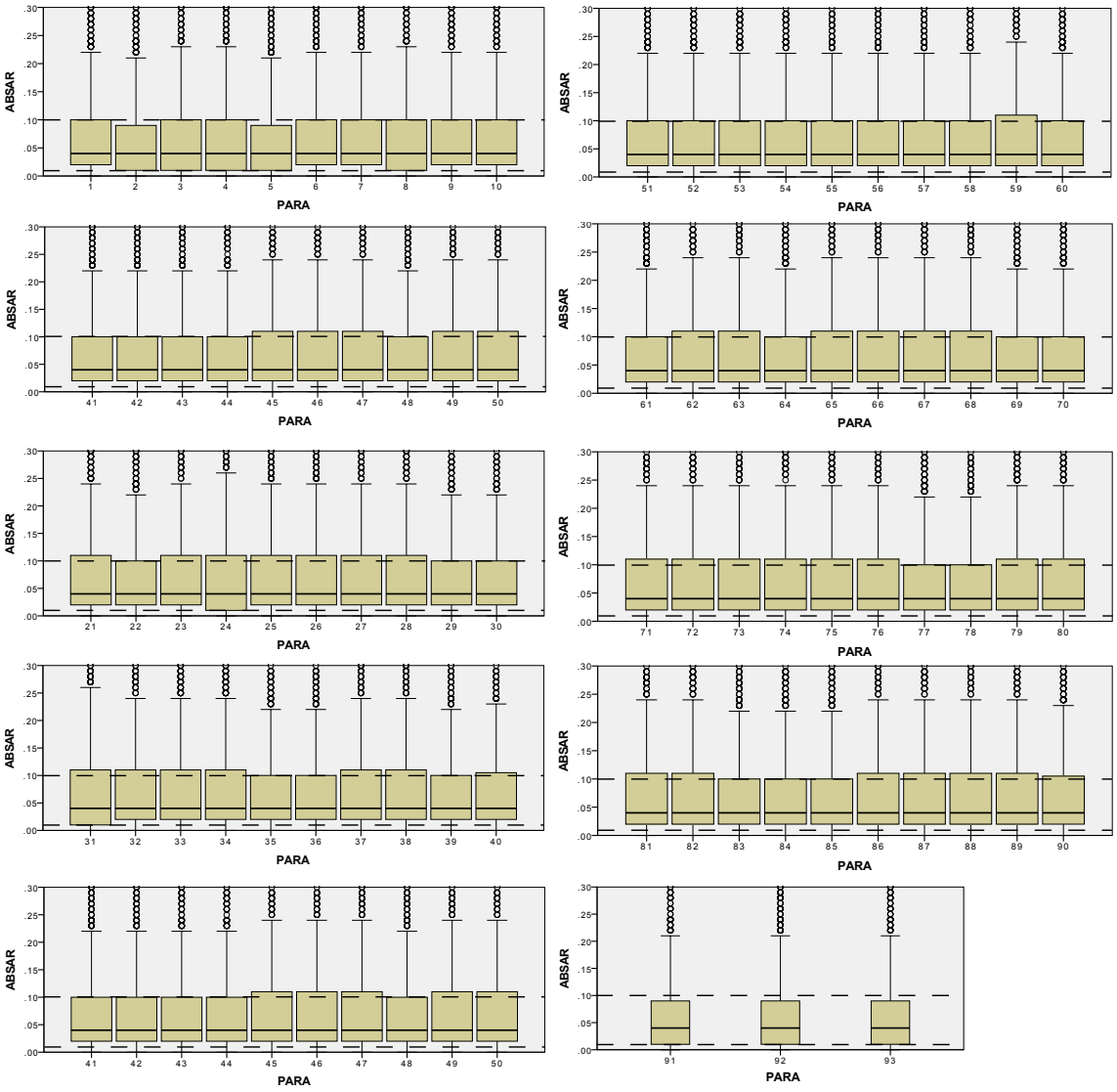

Figure B.3.: Box plots showing the scattering of absolute difference between manual reference picks and automatic picks (ABSAR). Outliers are calculated as shown in chapter 2.2.1 and are depicted as small circles. For a better comparison 0.01 s and 0.1 s are marked as dashed lines.

Parameter statistics (OBS)

Table B.2.: Statistics of the difference between reference and automatic picks. N=Amount of automatically picked phases. Parameters with the best boxplots are highlighted in yellow. (see Tab. B.1).

Parameter	Mean	Standard deviation	Picked phases	
	s	s	N	%
17	-0,0074	0,20964	1981	74
5	-0,0084	0,21365	2011	75
92	-0,0098	0,22569	2099	79
18	-0,0078	0,22638	1983	74
93	-0,0101	0,22726	2128	80
2	-0,0079	0,23129	2013	75
91	-0,0060	0,23602	2096	79
14	-0,0044	0,24226	2153	81
13	-0,0069	0,24542	2193	82
22	-0,0070	0,24554	2199	82
19	-0,0025	0,26511	2140	80
20	-0,0060	0,27140	2186	82
83	-0,0109	0,28032	2238	84
61	-0,0055	0,29118	2243	84
85	-0,0080	0,29227	2235	84
52	-0,0028	0,29246	2184	82
70	-0,0043	0,29303	2243	84
51	-0,0054	0,29411	2240	84
39	-0,0050	0,29443	2244	84
48	0,0054	0,29703	2190	82
47	0,0008	0,29991	2252	84
62	-0,0069	0,30195	2248	84
42	-0,0013	0,30697	2252	84
63	-0,0058	0,30742	2250	84
76	-0,0010	0,31034	2252	84
73	-0,0005	0,31037	2255	84
64	-0,0041	0,31064	2253	84
41	-0,0064	0,31107	2246	84
71	-0,0064	0,31135	2260	85
58	-0,0080	0,31147	2246	84
7	-0,0014	0,31338	1974	74
67	-0,0052	0,31380	2253	84
60	-0,0080	0,31410	2254	84
66	-0,0030	0,31430	2259	85
30	0,0066	0,31449	2225	83
6	-0,0007	0,31517	1996	75
77	0,0025	0,31642	2265	85
1	0,0000	0,31656	2001	75
69	-0,0019	0,31763	2248	84
56	-0,0027	0,31784	2237	84
54	-0,0011	0,31907	2197	82
8	-0,0032	0,31929	1969	74
45	0,0015	0,31995	2280	85
35	0,0105	0,32085	2234	84
88	-0,0027	0,32229	2265	85
72	-0,0023	0,32231	2249	84
46	0,0010	0,32275	2282	85

Parameter	Mean	Standard deviation	Picked phases	
	s	s	N	%
44	-0,0034	0,32283	2261	85
74	0,0035	0,32318	2265	85
84	-0,0060	0,32376	2260	85
78	-0,0042	0,32450	2232	84
75	0,0006	0,32468	2258	85
86	-0,0048	0,32478	2269	85
53	-0,0060	0,32564	2258	85
55	0,0010	0,32633	2260	85
57	0,0002	0,32672	2258	85
81	-0,0052	0,32714	2260	85
43	0,0000	0,32791	2268	85
3	-0,0058	0,32827	1992	75
89	0,0038	0,32832	2288	86
65	0,0005	0,32897	2255	84
4	-0,0049	0,32952	1998	75
40	0,0017	0,33048	2256	84
90	0,0017	0,33048	2256	84
29	-0,0013	0,33077	2299	86
31	0,0065	0,33469	2241	84
59	-0,0008	0,33562	2259	85
80	0,0026	0,33688	2286	86
68	0,0002	0,33717	2261	85
87	0,0054	0,33760	2295	86
24	-0,0009	0,33977	2216	83
82	0,0031	0,34047	2299	86
36	0,0010	0,34175	2307	86
50	-0,0045	0,34729	2311	87
23	-0,0095	0,35160	2286	86
28	0,0070	0,35365	2132	80
38	0,0019	0,35430	2148	80
16	-0,0047	0,35446	2116	79
21	-0,0047	0,35446	2116	79
34	-0,0034	0,35554	2125	80
9	-0,0073	0,35664	2122	79
79	-0,0080	0,35993	2176	81
12	-0,0073	0,36038	2149	80
32	-0,0049	0,36121	2318	87
15	-0,0069	0,36149	2155	81
49	-0,0025	0,36343	2316	87
10	-0,0099	0,36397	2151	81
11	-0,0106	0,36677	2158	81
37	-0,0060	0,36826	2226	83
27	-0,0026	0,37429	2208	83
26	0,0061	0,37951	2160	81
33	-0,0095	0,38473	2206	83
25	-0,0003	0,39905	2231	84

B.3. Calibration of weighting scheme

Cross tabulations for OBS data

			MPX			Total
			0	1	2	
TW2	0	Count	448	161	42	651
		% within TW2	68,8%	24,7%	6,5%	100,0%
		% of Total	36,7%	13,2%	3,4%	53,4%
	1	Count	85	190	83	358
		% within TW2	23,7%	53,1%	23,2%	100,0%
		% of Total	7,0%	15,6%	6,8%	29,3%
	2	Count	26	69	116	211
		% within TW2	12,3%	32,7%	55,0%	100,0%
		% of Total	2,1%	5,7%	9,5%	17,3%
Total		Count	559	420	241	1220
		% within TW2	45,8%	34,4%	19,8%	100,0%
		% of Total	45,8%	34,4%	19,8%	100,0%

(a) Cross tabulation of MPX weights and *TrueWeight2*

MPX	Mean / s	Std. Deviation / s
0	-,0245	,06110
1	-,0332	,10260
2	-,0182	,19121

(b) Standard deviations

Figure B.4.: Weighting scheme O: (a) Cross tabulation of automatically asigned MPX weights and *TrueWeight2*. Ideally, the entries on the diagonal would be 100 %. (b) Standard deviations between automatically and manually picked phases within every MPX assigned weight. The standard deviations should fall within the error boundaries (see Table 2.2). In this case, the standard deviation of class 0 lies above the boundary.

			MPX			Total
			0	1	2	
TW2	0	Count	452	155	44	651
		% within TW2	69,4%	23,8%	6,8%	100,0%
		% of Total	37,0%	12,7%	3,6%	53,4%
	1	Count	83	172	84	339
		% within TW2	24,5%	50,7%	24,8%	100,0%
		% of Total	6,8%	14,1%	6,9%	27,8%
	2	Count	27	77	126	230
		% within TW2	11,7%	33,5%	54,8%	100,0%
		% of Total	2,2%	6,3%	10,3%	18,9%
Total		Count	562	404	254	1220
		% within TW2	46,1%	33,1%	20,8%	100,0%
		% of Total	46,1%	33,1%	20,8%	100,0%

(a) Cross tabulation of MPX weights and *TrueWeight2*

MPX	Mean / s	Std. Deviation / s
0	-,0245	,06096
1	-,0313	,10136
2	-,0224	,18911

(b) Standard deviations

Figure B.5.: Weighting scheme O1: (a) Cross tabulation of automatically asigned MPX weights and *TrueWeight2*. Ideally, the entries on the diagonal would be 100 %. (b) Standard deviations between automatically and manually picked phases within every MPX assigned weight. The standard deviations should fall within the error boundaries (see Table 2.2). In this case, the standard deviation of class 0 lies above the boundary.

			MPX			Total
			0	1	2	
TW2	0	Count	467	169	48	684
		% within TW2	68,3%	24,7%	7,0%	100,0%
		% of Total	38,3%	13,9%	3,9%	56,1%
	1	Count	59	163	71	293
		% within TW2	20,1%	55,6%	24,2%	100,0%
		% of Total	4,8%	13,4%	5,8%	24,0%
	2	Count	29	87	127	243
		% within TW2	11,9%	35,8%	52,3%	100,0%
		% of Total	2,4%	7,1%	10,4%	19,9%
Total		Count	555	419	246	1220
		% within TW2	45,5%	34,3%	20,2%	100,0%
		% of Total	45,5%	34,3%	20,2%	100,0%

(a) Cross tabulation of MPX weights and *TrueWeight2*

MPX	Mean / s	Std. Deviation / s
0	-,0263	,05554
1	-,0282	,10677
2	-,0231	,18977

(b) Standard deviations

Figure B.6.: Weighting scheme O2: (a) Cross tabulation of automatically asigned MPX weights and *TrueWeight2*. Ideally, the entries on the diagonal would be 100 %. (b) Standard deviations between automatically and manually picked phases within every MPX assigned weight. The standard deviations should fall within the error boundaries (see Table 2.2). In this case, the standard deviations lie inside the boundaries.

			MPX				Total
			0	1	2	3	
TW2	0	Count	430	160	25	36	651
		% within TW2	66,1%	24,6%	3,8%	5,5%	100,0%
		% of Total	35,2%	13,1%	2,0%	3,0%	53,4%
	1	Count	68	103	59	51	281
		% within TW2	24,2%	36,7%	21,0%	18,1%	100,0%
		% of Total	5,6%	8,4%	4,8%	4,2%	23,0%
	2	Count	8	30	41	35	114
		% within TW2	7,0%	26,3%	36,0%	30,7%	100,0%
		% of Total	,7%	2,5%	3,4%	2,9%	9,3%
	3	Count	22	36	35	81	174
		% within TW2	12,6%	20,7%	20,1%	46,6%	100,0%
		% of Total	1,8%	3,0%	2,9%	6,6%	14,3%
Total		Count	528	329	160	203	1220
		% within TW2	43,3%	27,0%	13,1%	16,6%	100,0%
		% of Total	43,3%	27,0%	13,1%	16,6%	100,0%

(a) Cross tabulation of MPX weights and *TrueWeight2*

MPX	Mean / s	Std. Deviation / s
0	-,0274	,05604
1	-,0060	,10250
2	-,0727	,11341
3	-,0183	,19516

(b) Standard deviations

Figure B.7.: Weighting scheme P: (a) Cross tabulation of automatically asigned MPX weights and *TrueWeight2*. Ideally, the entries on the diagonal would be 100 %. (b) Standard deviations between automatically and manually picked phases within every MPX assigned weight. The standard deviations should fall within the error boundaries (see Table 2.2). In this case, the standard deviations of class 0 and 1 lie above the boundary.

			MPX				Total
			0	1	2	3	
TW2	0	Count	405	160	50	36	651
		% within TW2	62,2%	24,6%	7,7%	5,5%	100,0%
		% of Total	33,2%	13,1%	4,1%	3,0%	53,4%
	1	Count	44	85	30	41	200
		% within TW2	22,0%	42,5%	15,0%	20,5%	100,0%
		% of Total	3,6%	7,0%	2,5%	3,4%	16,4%
	2	Count	26	49	71	49	195
		% within TW2	13,3%	25,1%	36,4%	25,1%	100,0%
		% of Total	2,1%	4,0%	5,8%	4,0%	16,0%
	3	Count	18	37	29	90	174
		% within TW2	10,3%	21,3%	16,7%	51,7%	100,0%
		% of Total	1,5%	3,0%	2,4%	7,4%	14,3%
Total		Count	493	331	180	216	1220
		% within TW2	40,4%	27,1%	14,8%	17,7%	100,0%
		% of Total	40,4%	27,1%	14,8%	17,7%	100,0%

(a) Cross tabulation of MPX weights and *TrueWeight2*

MPX	Mean / s	Std. Deviation / s
0	-,0286	,05520
1	-,0003	,10383
2	-,0735	,08898
3	-,0203	,19579

(b) Standard deviations

Figure B.8.: Weighting scheme P1: (a) Cross tabulation of automatically asigned MPX weights and *TrueWeight2*. Ideally, the entries on the diagonal would be 100 %. (b) Standard deviations between automatically and manually picked phases within every MPX assigned weight. The standard deviations should fall within the error boundaries (see Table 2.2). In this case, the standard deviations of class 0 and 1 lie above the boundary.

Test localisation of reference data set (OBS)

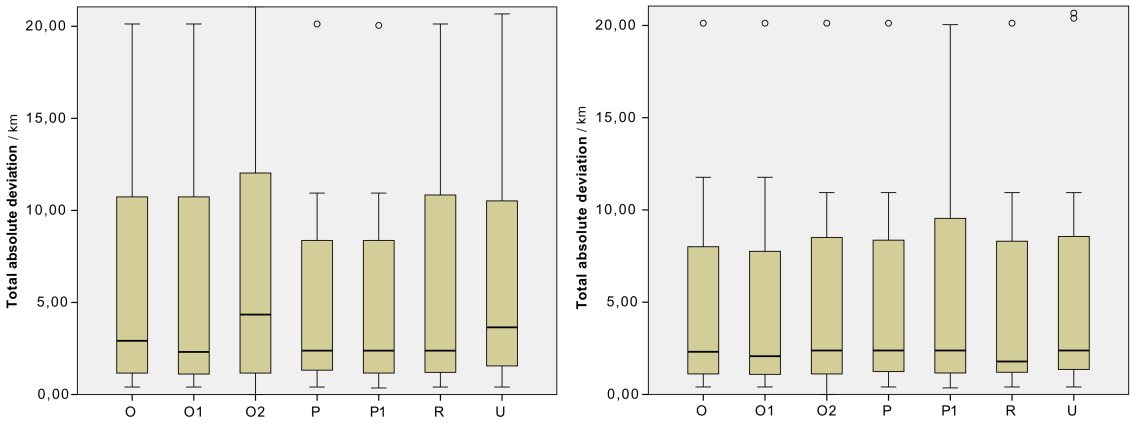

Figure B.9.: Box plots of absolute total deviation between locations of reference hypocenters and calculated hypocenters. (a) Box plots of all located events as stated in Table B.3. (b) Box plots of 23 events located by all schemes to compare the results on the same data base.

Table B.3.: Located events per weighting scheme. The reference data set consisted of 33 events inside the network.

Scheme	**O**	**O1**	**O2**	**P**	**P1**	**R**	**U**
No. of located events	26	25	26	25	25	27	27

Cross tabulations for land station data

			MPX			Total
			0	1	2	
TW2	0	Count	265	82	19	366
		% within TW2	72,4%	22,4%	5,2%	100,0%
		% of Total	34,1%	10,6%	2,4%	47,1%
	1	Count	36	136	84	256
		% within TW2	14,1%	53,1%	32,8%	100,0%
		% of Total	4,6%	17,5%	10,8%	32,9%
	2	Count	17	44	94	155
		% within TW2	11,0%	28,4%	60,6%	100,0%
		% of Total	2,2%	5,7%	12,1%	19,9%
Total		Count	318	262	197	777
		% within TW2	40,9%	33,7%	25,4%	100,0%
		% of Total	40,9%	33,7%	25,4%	100,0%

(a) Cross tabulation of MPX weights and *TrueWeight2*

MPX	Mean / s	Std. Deviation / s
0	-,0240	,03436
1	-,0236	,08479
2	,0590	,13498

(b) Standard deviations

Figure B.10.: Weighting scheme O: (a) Cross tabulation of automatically asigned MPX weights and *TrueWeight2*. Ideally, the entries on the diagonal would be 100 %. (b) Standard deviations between automatically and manually picked phases within every MPX assigned weight. The standard deviations should fall within the error boundaries (see Table 2.6). In this case, the standard deviations lie inside the boundaries.

			MPX			Total
			0	1	2	
TW2	0	Count	268	98	16	382
		% within TW2	70,2%	25,7%	4,2%	100,0%
		% of Total	34,5%	12,6%	2,1%	49,2%
	1	Count	23	121	67	211
		% within TW2	10,9%	57,3%	31,8%	100,0%
		% of Total	3,0%	15,6%	8,6%	27,2%
	2	Count	18	60	106	184
		% within TW2	9,8%	32,6%	57,6%	100,0%
		% of Total	2,3%	7,7%	13,6%	23,7%
Total		Count	309	279	189	777
		% within TW2	39,8%	35,9%	24,3%	100,0%
		% of Total	39,8%	35,9%	24,3%	100,0%

(a) Cross tabulation of MPX weights and *TrueWeight2*

MPX	Mean / s	Std. Deviation / s
0	-,0239	,03411
1	-,0195	,08400
2	,0566	,13964

(b) Standard deviations

Figure B.11.: Weighting scheme O1: (a) Cross tabulation of automatically asigned MPX weights and *TrueWeight2*. Ideally, the entries on the diagonal would be 100 %. (b) Standard deviations between automatically and manually picked phases within every MPX assigned weight. The standard deviations should fall within the error boundaries (see Table 2.6). In this case, the standard deviations lie inside the boundaries.

			MPX			Total
			0	1	2	
TW2	0	Count	268	98	16	382
		% within TW2	70,2%	25,7%	4,2%	100,0%
		% of Total	34,5%	12,6%	2,1%	49,2%
	1	Count	24	125	62	211
		% within TW2	11,4%	59,2%	29,4%	100,0%
		% of Total	3,1%	16,1%	8,0%	27,2%
	2	Count	24	63	97	184
		% within TW2	13,0%	34,2%	52,7%	100,0%
		% of Total	3,1%	8,1%	12,5%	23,7%
Total		Count	316	286	175	777
		% within TW2	40,7%	36,8%	22,5%	100,0%
		% of Total	40,7%	36,8%	22,5%	100,0%

(a) Cross tabulation of MPX weights and *TrueWeight2*

MPX	Mean / s	Std. Deviation / s
0	-,0273	,03657
1	-,0093	,09246
2	,0520	,13701

(b) Standard deviations

Figure B.12.: Weighting scheme O2: (a) Cross tabulation of automatically asigned MPX weights and *TrueWeight2*. Ideally, the entries on the diagonal would be 100 %. (b) Standard deviations between automatically and manually picked phases within every MPX assigned weight. The standard deviations should fall within the error boundaries (see Table 2.6). In this case, the standard deviations lie inside the boundaries.

			MPX				Total
			0	1	2	3	
TW2	0	Count	253	79	26	8	366
		% within TW2	69,1%	21,6%	7,1%	2,2%	100,0%
		% of Total	32,6%	10,2%	3,3%	1,0%	47,1%
	1	Count	27	93	45	39	204
		% within TW2	13,2%	45,6%	22,1%	19,1%	100,0%
		% of Total	3,5%	12,0%	5,8%	5,0%	26,3%
	2	Count	2	26	28	33	89
		% within TW2	2,2%	29,2%	31,5%	37,1%	100,0%
		% of Total	,3%	3,3%	3,6%	4,2%	11,5%
	3	Count	13	34	17	54	118
		% within TW2	11,0%	28,8%	14,4%	45,8%	100,0%
		% of Total	1,7%	4,4%	2,2%	6,9%	15,2%
Total		Count	295	232	116	134	777
		% within TW2	38,0%	29,9%	14,9%	17,2%	100,0%
		% of Total	38,0%	29,9%	14,9%	17,2%	100,0%

(a) Cross tabulation of MPX weights and *TrueWeight2*

MPX	Mean / s	Std. Deviation / s
0	-,0236	,03187
1	-,0012	,09866
2	-,0388	,08217
3	,0722	,13776

(b) Standard deviations

Figure B.13.: Weighting scheme P: (a) Cross tabulation of automatically asigned MPX weights and *TrueWeight2*. Ideally, the entries on the diagonal would be 100 %. (b) Standard deviations between automatically and manually picked phases within every MPX assigned weight. The standard deviations should fall within the error boundaries (see Table 2.6). In this case, the standard deviations lie inside the boundaries.

			MPX				Total
			0	1	2	3	
TW2	0	Count	246	65	34	7	352
		% within TW2	69,9%	18,5%	9,7%	2,0%	100,0%
		% of Total	31,7%	8,4%	4,4%	,9%	45,3%
	1	Count	33	78	43	39	193
		% within TW2	17,1%	40,4%	22,3%	20,2%	100,0%
		% of Total	4,2%	10,0%	5,5%	5,0%	24,8%
	2	Count	6	28	30	38	102
		% within TW2	5,9%	27,5%	29,4%	37,3%	100,0%
		% of Total	,8%	3,6%	3,9%	4,9%	13,1%
	3	Count	14	30	25	61	130
		% within TW2	10,8%	23,1%	19,2%	46,9%	100,0%
		% of Total	1,8%	3,9%	3,2%	7,9%	16,7%
Total		Count	299	201	132	145	777
		% within TW2	38,5%	25,9%	17,0%	18,7%	100,0%
		% of Total	38,5%	25,9%	17,0%	18,7%	100,0%

(a) Cross tabulation of MPX weights and *TrueWeight2*

MPX	Mean / s	Std. Deviation / s
0	-,0258	,02446
1	,0102	,10116
2	-,0464	,07954
3	,0681	,13646

(b) Standard deviations

Figure B.14.: Weighting scheme P1: (a) Cross tabulation of automatically asigned MPX weights and *TrueWeight2*. Ideally, the entries on the diagonal would be 100 %. (b) Standard deviations between automatically and manually picked phases within every MPX assigned weight. The standard deviations should fall within the error boundaries (see Table 2.6). In this case, the standard deviations of class 1 lie above the boundary.

			MPX				Total
			0	1	2	3	
TW2	0	Count	252	83	15	16	366
		% within TW2	68,9%	22,7%	4,1%	4,4%	100,0%
		% of Total	32,4%	10,7%	1,9%	2,1%	47,1%
	1	Count	27	101	43	33	204
		% within TW2	13,2%	49,5%	21,1%	16,2%	100,0%
		% of Total	3,5%	13,0%	5,5%	4,2%	26,3%
	2	Count	10	27	36	16	89
		% within TW2	11,2%	30,3%	40,4%	18,0%	100,0%
		% of Total	1,3%	3,5%	4,6%	2,1%	11,5%
	3	Count	14	28	36	40	118
		% within TW2	11,9%	23,7%	30,5%	33,9%	100,0%
		% of Total	1,8%	3,6%	4,6%	5,1%	15,2%
Total		Count	303	239	130	105	777
		% within TW2	39,0%	30,8%	16,7%	13,5%	100,0%
		% of Total	39,0%	30,8%	16,7%	13,5%	100,0%

(a) Cross tabulation of MPX weights and *TrueWeight2*

MPX	Mean / s	Std. Deviation / s
0	-,0268	,03611
1	-,0107	,08801
2	,0123	,13368
3	,0714	,12145

(b) Standard deviations

Figure B.15.: Weighting scheme U: (a) Cross tabulation of automatically asigned MPX weights and *TrueWeight2*. Ideally, the entries on the diagonal would be 100 %. (b) Standard deviations between automatically and manually picked phases within every MPX assigned weight. The standard deviations should fall within the error boundaries (see Table 2.6). In this case, the standard deviations lie inside the boundaries.

Test localisation of reference data set (LS)

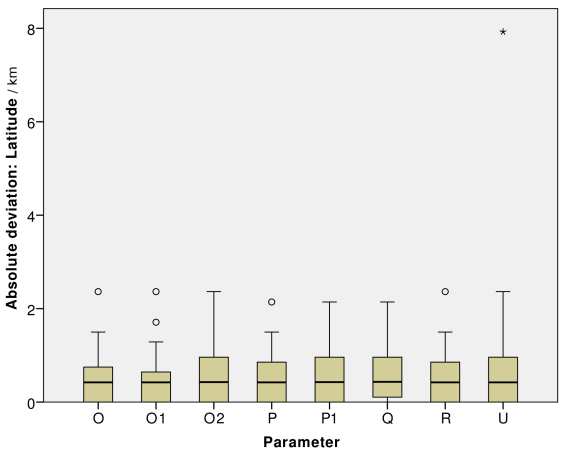

(a) Latitude / km

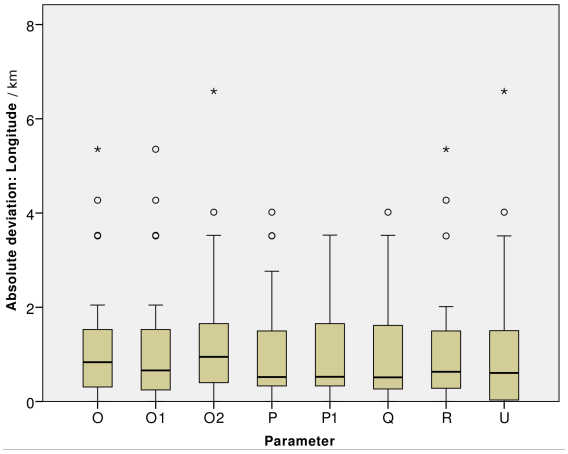

(b) Longitude / km

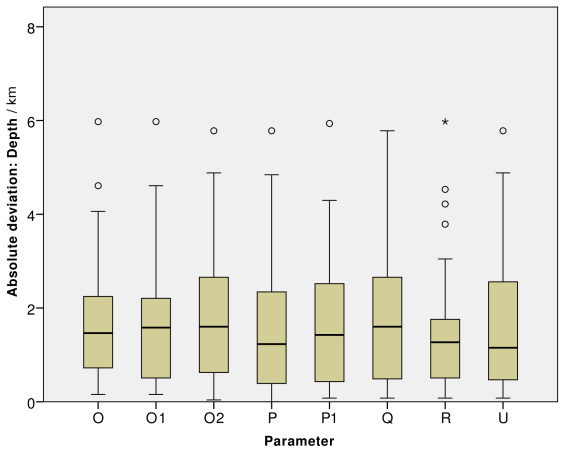

(c) Depth / km

Figure B.16.: Box plots of absolute deviation of latitude, longitude and depth between locations of reference hypocenters and calculated hypocenters.

C. Hypocentre determination

C.1. 1D P wave velocity model

Table C.1.: 1D P wave velocity model derived by *Arroyo et al.* (2010) from an OBS and land station data study from 2008 in the Maule area.

Depth **km**	$\mathbf{v_p}$ **km/s**
-1.0	5.00
2.5	5.50
5.0	5.80
10.0	6.20
15.0	6.50
20.0	6.70
25.0	7.02
35.0	7.36
45.0	7.69
60.0	7.96
75.0	7.96
90.0	7.96
105.0	8.20
125.0	8.30
150.0	8.50

D. Picking of S phases

D.1. Picking parameter

Table D.1.: Parameter sets for the set up of MPX parameter for S phase arrival detection. The parameter set number correspond to the increases in frequency threshold (0.5 Hz steps).

Parameter	**Gaps**				**Estimation windows**	**Wiener filter**	**Threshold**
	s				**s**	**s**	**Hz**
1 - 7	2.4	1.20	0.58	0.04	2.0	4.0	1.5 - 4.5
8 - 14	2.4	1.20	0.58	0.04	1.0	2.0	1.5 - 4.5
15 - 21	2.4	1.20	0.56	0.08	2.0	4.0	1.5 - 4.5
22 - 28	2.4	1.20	0.56	0.08	1.0	2.0	1.5 - 4.5
29 - 35	2.4	1.61	0.82	0.04	2.0	4.0	1.5 - 4.5
36 - 42	2.4	1.61	0.82	0.04	1.0	2.0	1.5 - 4.5
43 - 49	2.4	1.63	0.86	0.08	2.0	4.0	1.5 - 4.5
50 - 56	2.4	1.63	0.86	0.08	1.0	2.0	1.5 - 4.5
57 - 63	2.4	1.20	0.60	0.30	2.0	4.0	1.5 - 4.5
64 - 70	2.4	1.20	0.60	0.30	1.0	2.0	1.5 - 4.5
71 - 77	3.0	1.50	0.73	0.04	2.0	4.0	1.5 - 4.5
78 - 84	3.0	1.50	0.73	0.04	1.0	2.0	1.5 - 4.5
85 - 91	3.0	1.50	0.71	0.08	2.0	4.0	1.5 - 4.5
92 - 98	3.0	1.50	0.71	0.08	1.0	2.0	1.5 - 4.5
99 - 105	3.0	2.01	1.02	0.04	2.0	4.0	1.5 - 4.5
106 - 112	3.0	2.01	1.02	0.04	1.0	2.0	1.5 - 4.5
113 - 119	3.0	2.03	1.06	0.08	2.0	4.0	1.5 - 4.5
120 - 126	3.0	2.03	1.06	0.08	1.0	2.0	1.5 - 4.5
127 - 133	3.0	1.50	0.75	0.38	2.0	4.0	1.5 - 4.5
134 - 140	3.0	1.50	0.75	0.38	1.0	2.0	1.5 - 4.5

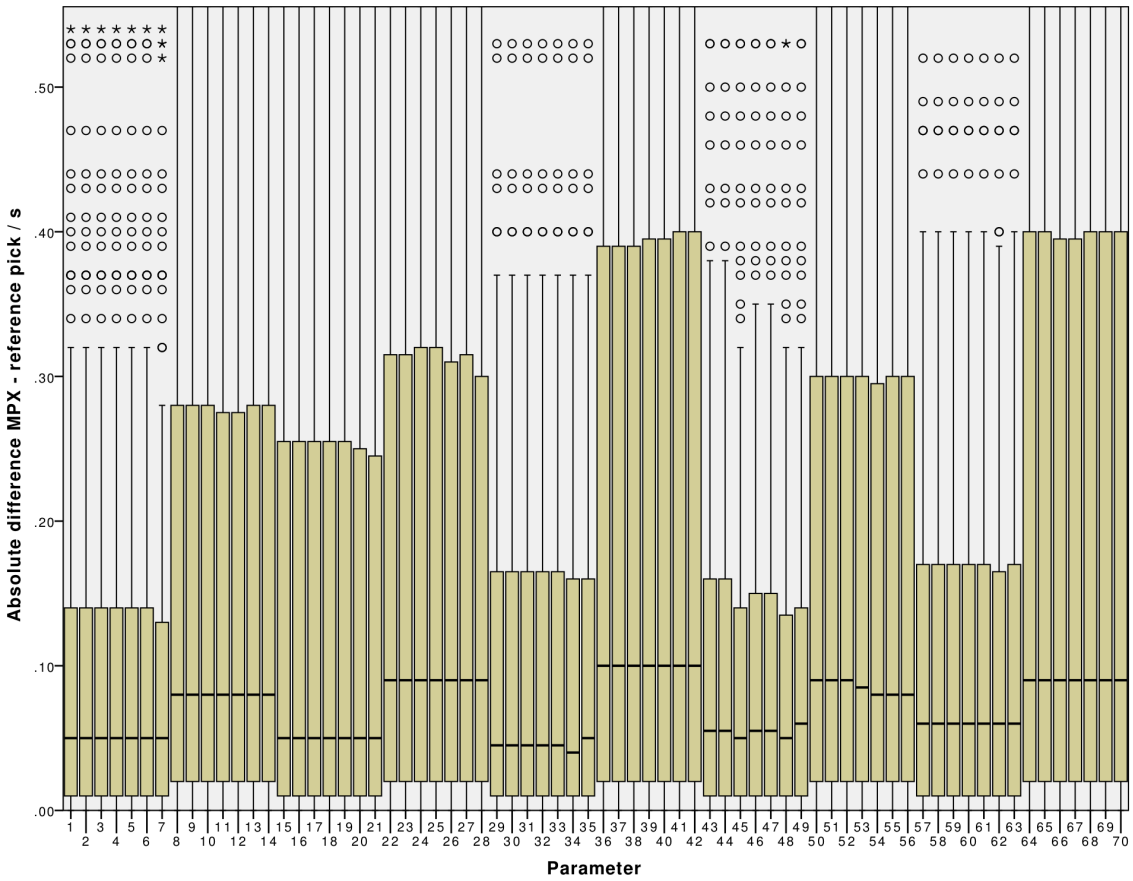

(a) Parameter set 1 to 70

Figure D.1.: Box plots showing the scattering of absolute difference between manual reference picks and automatic picks. Outliers are calculated as shown in Chapter 2.2.1 and are depicted as small circles.

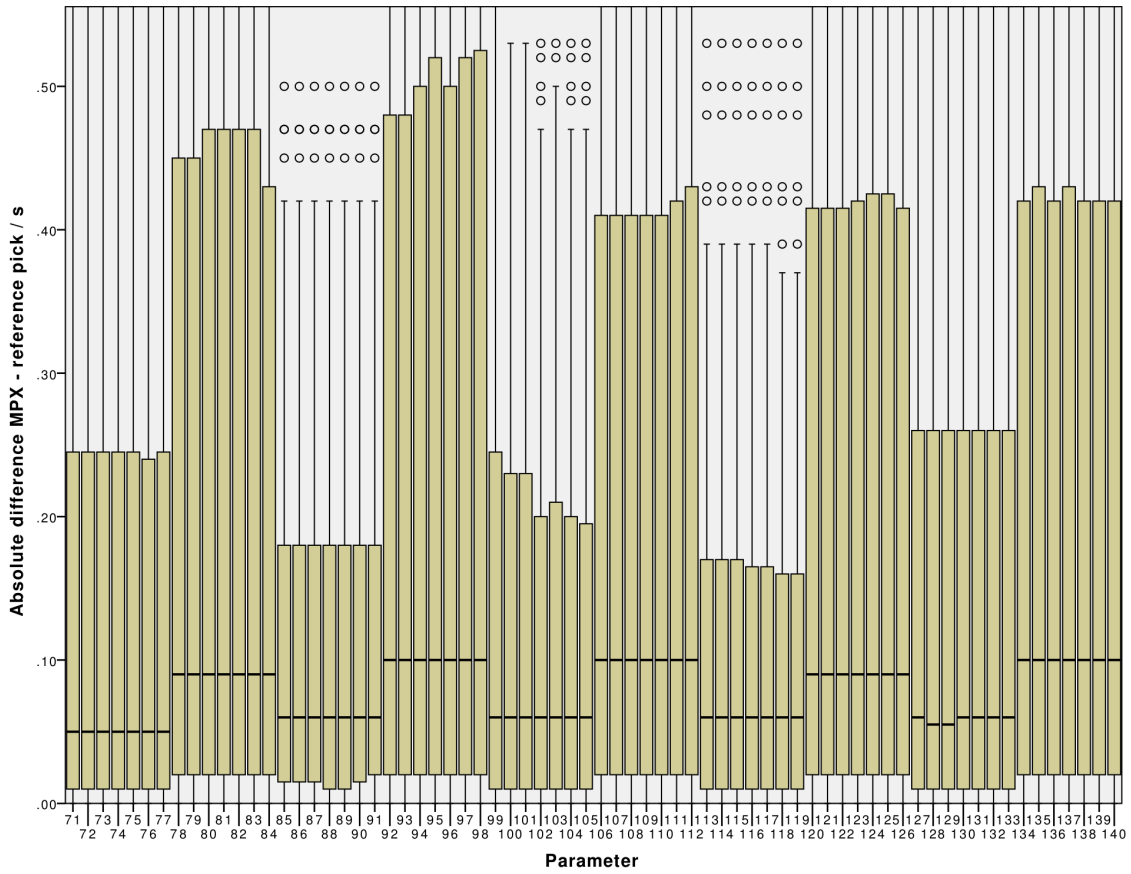

(b) Parameter set 71 to 140

Figure D.1.: (Continued) Box plots showing the scattering of absolute difference between manual reference picks and automatic picks. Outliers are calculated as shown in Chapter 2.2.1 and are depicted as small circles.

D.2. Cross tabulations

			MPX		
			0	1	Total
TW2	0	Count	147	116	263
		% within TW2	55,9%	44,1%	100,0%
		% of Total	32,0%	25,3%	57,3%
	1	Count	93	103	196
		% within TW2	47,4%	52,6%	100,0%
		% of Total	20,3%	22,4%	42,7%
Total		Count	240	219	459
		% within TW2	52,3%	47,7%	100,0%
		% of Total	52,3%	47,7%	100,0%

Figure D.2.: Cross tabulation of automatically asigned MPX weights and *TrueWeight2* for weighting scheme D. Ideally, the entries on the diagonal would be 100 %.

			MPX			Total
			0	1	2	
TW2	0	Count	82	41	14	137
		% within TW2	59,9%	29,9%	10,2%	100,0%
		% of Total	17,8%	8,9%	3,0%	29,8%
	1	Count	32	57	38	127
		% within TW2	25,2%	44,9%	29,9%	100,0%
		% of Total	7,0%	12,4%	8,3%	27,6%
	2	Count	30	61	105	196
		% within TW2	15,3%	31,1%	53,6%	100,0%
		% of Total	6,5%	13,3%	22,8%	42,6%
Total		Count	144	159	157	460
		% within TW2	31,3%	34,6%	34,1%	100,0%
		% of Total	31,3%	34,6%	34,1%	100,0%

Figure D.3.: Cross tabulation of automatically asigned MPX weights and *TrueWeight2* for weighting scheme G. Ideally, the entries on the diagonal would be 100 %.

			MPX			Total
			0	1	2	
TW2	0	Count	124	59	30	213
		% within TW2	58,2%	27,7%	14,1%	100,0%
		% of Total	27,0%	12,8%	6,5%	46,3%
	1	Count	36	66	26	128
		% within TW2	28,1%	51,6%	20,3%	100,0%
		% of Total	7,8%	14,3%	5,7%	27,8%
	2	Count	15	27	77	119
		% within TW2	12,6%	22,7%	64,7%	100,0%
		% of Total	3,3%	5,9%	16,7%	25,9%
Total		Count	175	152	133	460
		% within TW2	38,0%	33,0%	28,9%	100,0%
		% of Total	38,0%	33,0%	28,9%	100,0%

Figure D.4.: Cross tabulation of automatically asigned MPX weights and *TrueWeight2* for weighting scheme H. Ideally, the entries on the diagonal would be 100 %.

E. Supplementary material to Chapter 6

In the first part of this chapter the figures of the paper are included in an enlarged version. Afterwards, the supplementary material to the published Geology paper presented in Chapter 6 is included in its original style published in the Geology Data Respository and contains its own page and figure numbers.

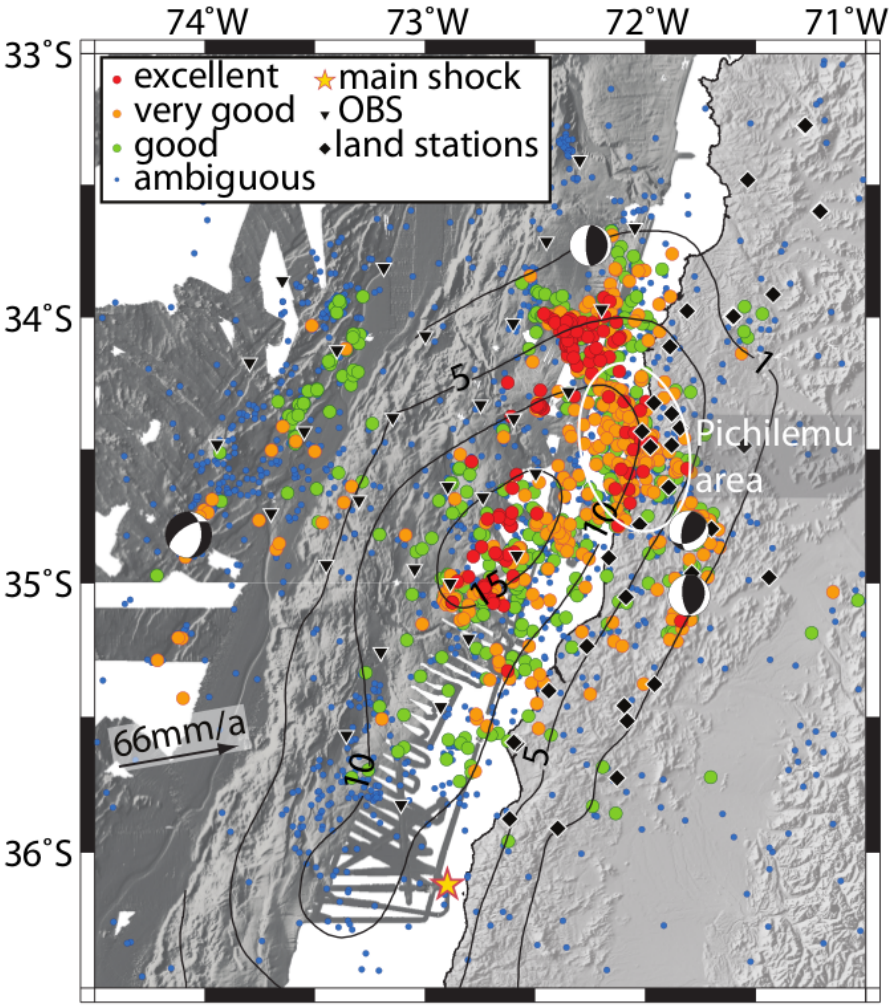

Figure E.1.: Figure 1 of paper: All aftershocks of the 2010 Mw 8.8 Maule earthquake, central Chile, recorded by amphibious network (color coded by quality class). Black contour lines indicate coseismic slip (Moreno et al., 2012). Focal mechanisms were extracted from the global Centroid Moment Tensor catalog (Dziewonski et al., 1981; Ekström et al., 2012) for events during deployment time span and are shown at their relocated hypocenters. White ellipse marks the Pichilemu area. Convergence rate is from Angermann et al. (1999). OBS–ocean-bottom seismometer.

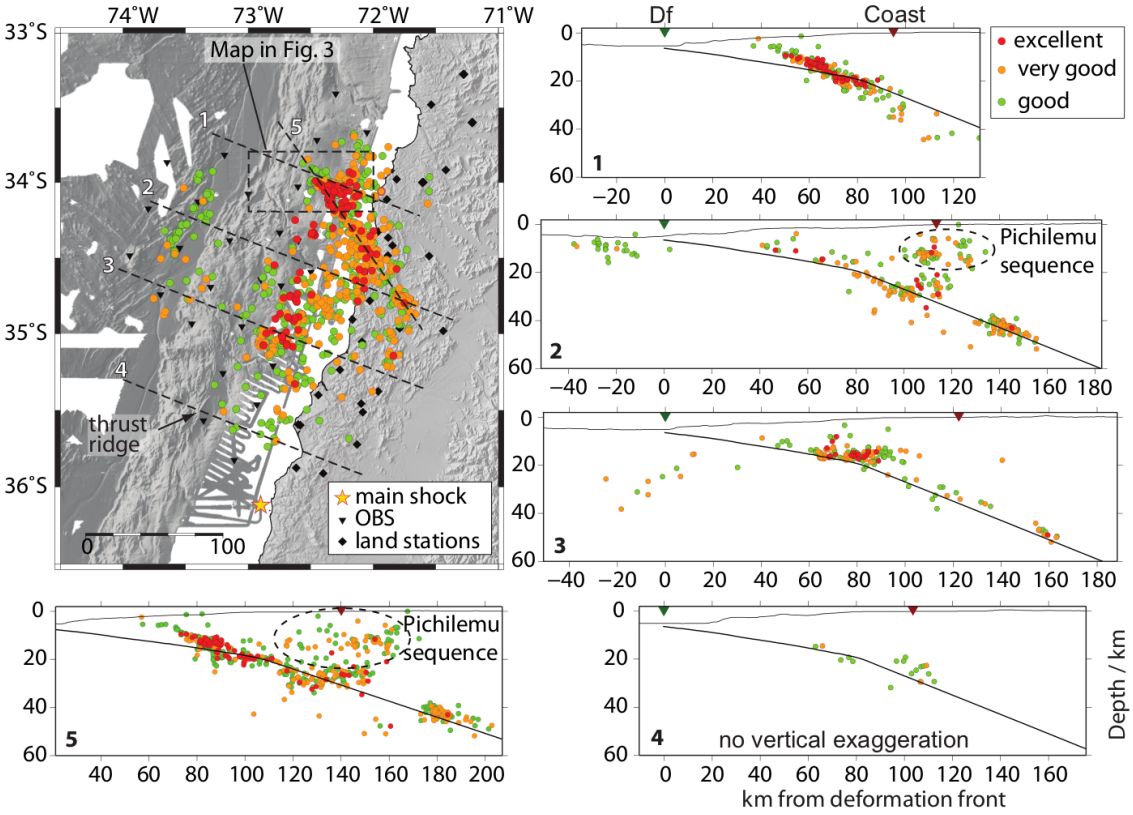

Figure E.2.: Figure 2 of paper: Map and profiles 1-5 showing aftershocks of the 2010 Mw 8.8 Maule earthquake, central Chile, with qualities good or better, and located within the network. Dashed lines in map indicate location of profiles perpendicular to the trench, as well as location of Figure 3A. Swath width of profiles is 20 km. Green and red triangles mark projected locations of the deformation front (df) and the coast, respectively. OBS-ocean-bottom seismometer. Plate boundary from refraction seismic measurements of Moscoso et al. (2011) (above 20 km depth) and Slab1.0 model of Hayes et al. (2012) (below 20 km depth).

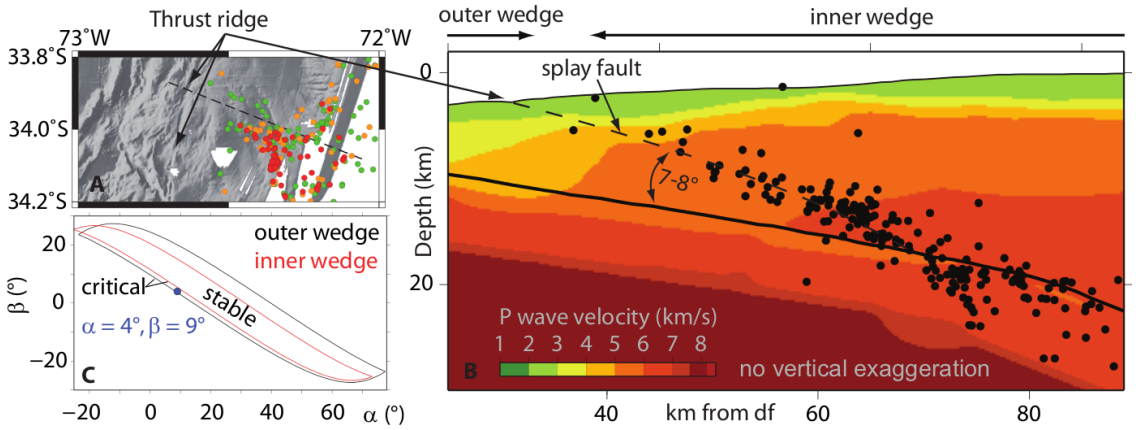

Figure E.3.: Figure 3 of paper: A: Bathymetry in the splay fault region. B: Profile 1 of Figure 2. P-wave velocity model is from Moscoso et al. (2011). Locations of outer and inner wedge are estimated from landward-increasing velocities; df–deformation front. C: Stability diagram for outer and inner wedge in the northern deployment area; α–surface slope, β–slab dip. Blue dot marks the taper corresponding to the splay fault region. For more information, see the Data Repository.

GSA DATA REPOSITORY 2014296

Supplementary material

Splay fault activity revealed by aftershocks of the 2010 Mw=8.8 Maule earthquake, Central Chile

Lieser, K., Grevemeyer, I., Lange, D., Flüh, E., Tilmann, F.,
and Contreras-Reyes, E.

Contents

1 FIGURES

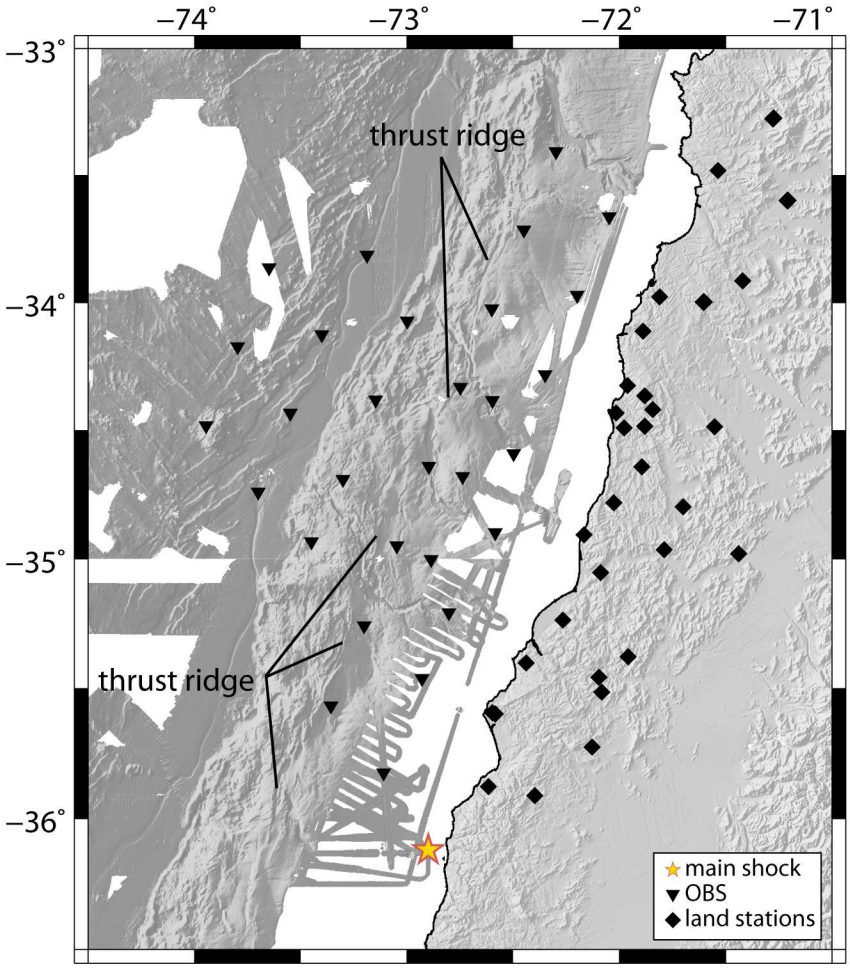

Figure DR1: Map of station configuration.

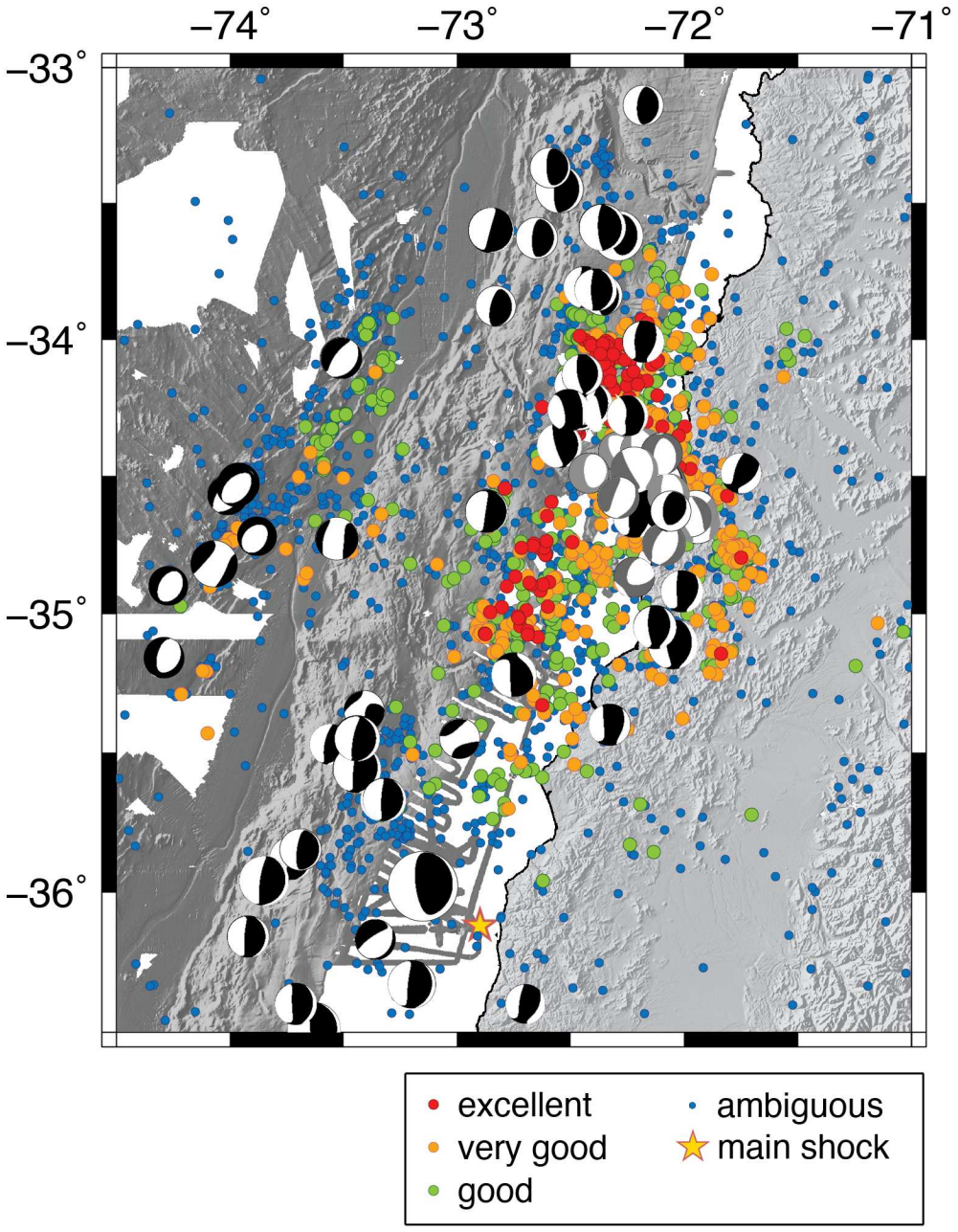

Figure DR2: Map with aftershocks of the Maule event from September to December 2010 from the local amphibious network and focal mechanisms with hypocenters from the gCMT catalog (Dziewonski et al., 1981; Ekström et al., 2012) from February to December 2010 . Events with extensive focal mechanisms of the Pichilemu cluster are shown in gray. Size of focal mechanisms is relative to magnitude.

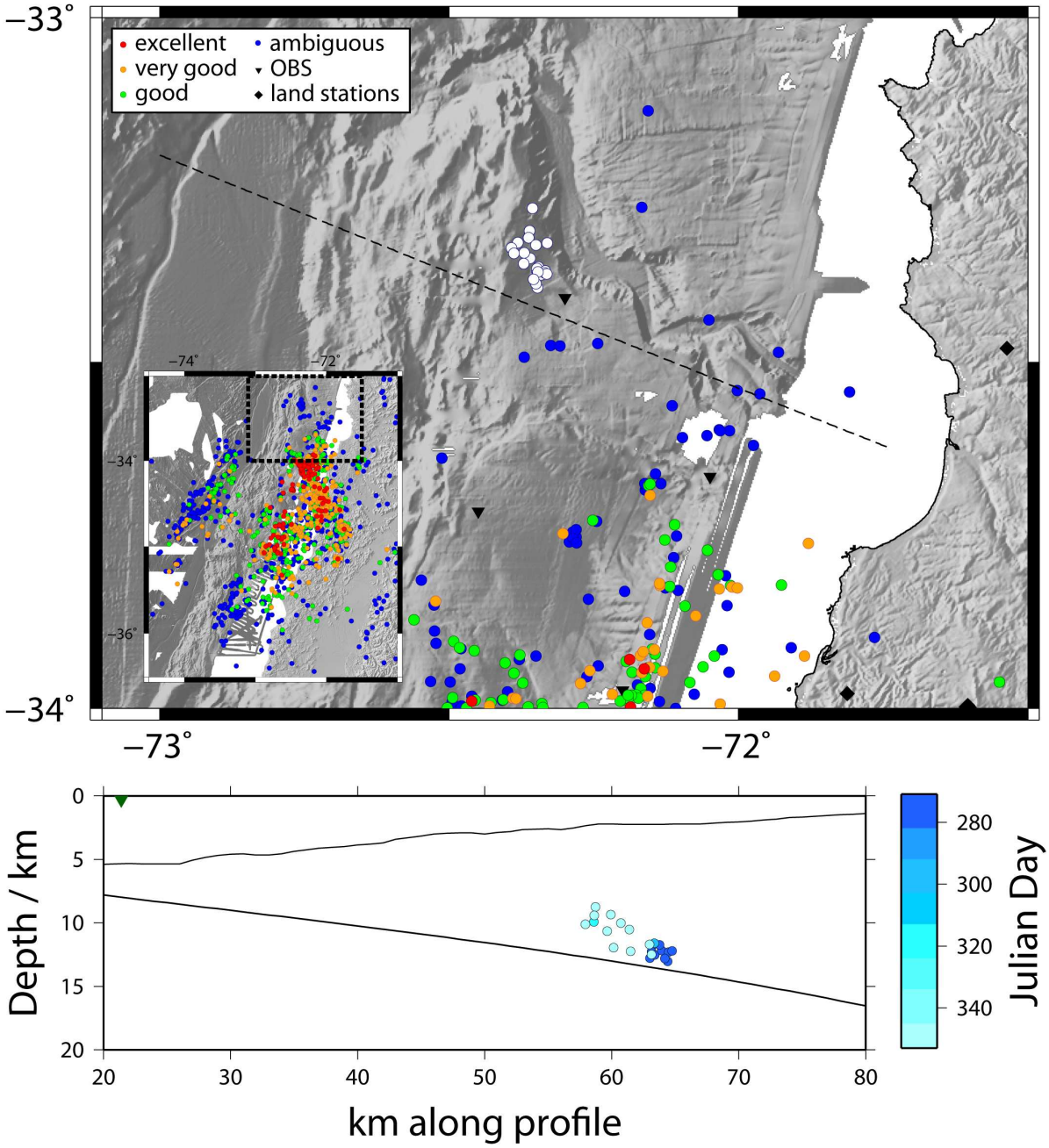

Figure DR3: Cluster, highlighted in white, at the northern boundary of the survey area and projected onto a cross-section perpendicular to the trench. Quality class "ambiguous" was restricted to the maximum average error within the cluster of 23 km (see Table DR2). Cluster events in the cross-section are color coded by origin time showing two episodes of faulting with a first set of events nucleating within two days at the end of September and a second one originating within three days at the end of December (October 1., 2010 = 274 Julian day; November 1., 2010 = 305 Julian day; December 1. ,2010 = 335 Julian day). Plate boundary by Slab1.0 model (Hayes et al., 2012).

2 AUTOMATIC P WAVE PICKING AND EVENT LOCATION

Event detection was carried out with a STA/LTA trigger and a coincidence criterion leading to 4,592 events. The picking of P wave onsets was performed with the automatic P wave picking engine MPX by Aldersons (2004), whose parameters have to be tuned to the data set. At first, the program requires an initial pick time near the P wave onset, usually an existing manual pick or a calculated onset based on catalog locations and a chosen velocity model. Since neither exists, the traces of each station per event were analyzed again by the STA/LTA trigger with adapted parameters in order to get the initial pick. Trigger parameters were optimized to obtain as many P wave onsets as possible but also as little noise, spikes, and S wave onsets as possible. Most of the initial picks not related to a P wave onset are not recognized by MPX. However, multiple picked onsets in a single seismogram occur and have been evaluated before event location as follows: the event is located with HYPOCENTER 3.2 (Lienert and Havskov, 1995) which calculates the residual for every onset. The one with the least residual is considered to be the correct pick. Stations where only a single pick was made but did not detect the correct onset will be automatically weighted down in the final event location. Trigger and MPX picking parameter were optimized for both OBS and land station network separately and tested on a reference data set consisting of 44 events. The 75% percentile of the absolute difference between manual and automatic picks for the OBS network was 0.09 s and for the land station network 0.08 s (Table DR1). MPX is also able to classify

the quality of an onset which will have an effect on event location since onsets with lower qualities will be weighted down. In order to adapt this classification scheme a reference data set was picked both automatically as well as manually followed by a hypocenter determination. For the final scheme the 75% percentiles were in the range of 2.3 - 5 km for deviations in longitude, latitude and depth for the OBS network. Deviations for the land stations showed 75% percentiles with values in the range of about 0.5 - 2 km in all three directions. 67,454 P wave onsets could be identified by MPX in its final setting.

The event localization was performed by NonLinLoc (Lomax, 2011), a probabilistic, global-search earthquake location software. Since 1-D velocity models provided either good results for the onshore or the offshore domain but only poor results for the whole survey area, a 2.5-D model was generated. Results from a seismic refraction and wide-angle profile crossing the network (Moscoso et al., 2011) defined the offshore domain and coastal region while constraints from a local earthquake study between 34°S and 36°S (Kraft, 2011; Dannowski et al., 2013) defined the domain onshore (DR4). The upper part of the subducting slab until about 20 km depth was constrained by the results of the seismic refraction and wide-angle profile and due to decreasing depth resolution of the refraction seismic data below 20 km depth the slab was defined by the Slab1.0 model of Hayes et al. (2012) for larger depths. By stretching this 2-D model along the geometry of the trench a 2.5-D model was set up. NonLinLoc determines a maximum likelihood hypocenter based on the probability density function (PDF) calculated for each event. From the PDF scatter samples a 3-D 68% confidence error ellipsoid and an expected hypocenter are estimated. Based on those parameters the located events were classified into five quality categories (see Table DR2, after Husen and Smith, 2004). Several sequential location runs were performed to determine station corrections, which were set to the average residuals at each station in the previous run. In total 3,751 of the triggered events could be located and 1,043 events were classified as “good” or better.

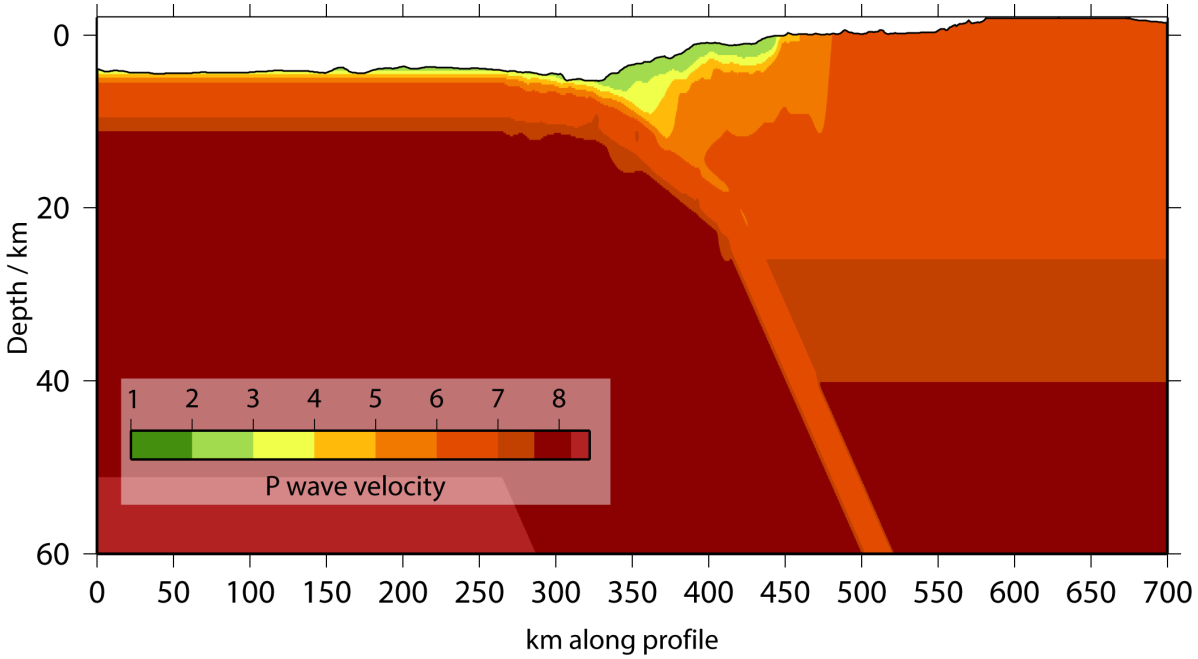

Figure DR4: Upper 60 km of velocity model used for event location derived by seismic refraction and wide-angle profile crossing the network (Moscoso et al., 2011) and a local earthquake study (Kraft, 2011; Dannowski et al., 2013).

ADDITIONAL REFERENCES

Lienert, B.R., and Havskov, J., 1995, A computer program for locating earthquakes both locally and globally: Seismological Research Letters, v. 66, no. 5, p. 26–36, doi:10.1785/gssrl.66.5.26.

TABLE DR1. DEVIATIONS BETWEEN MANUALLY AND AUTOMATICALLY PICKED DATA SETS

Percentiles	Picking time	Hypocenter location		
		Latitude	Longitude	Depth
	(s)	(km)		
OBS				
25%	0.01	0.18	0.40	0.00
50%	0.04	0.36	0.75	0.63
75%	0.09	2.28	4.89	3.09
Land stations				
25%	0.01	0.00	0.28	0.58
50%	0.03	0.42	0.69	1.29
75%	0.08	0.85	1.51	2.03

Table DR1: Deviations in picking time and hypocenter location between manually and automatically picked data sets.

TABLE DR2. QUALITY CLASSES FOR EARTHQUAKE LOCATIONS

Class	RMS	Distance	Average error	Number of events
	(s)	(km)	(km)	
A – excellent	< 0.5	< 0.5	< 2	145
B – very good	< 0.5	< 0.5	≥ 2	370
C – good	< 0.5	0.5 – 2	< 5	528
D – ambiguous	< 0.5	≥ 0.5*	-	1689
E – poor †	> 0.5	-	-	1019

* Except class C

† Not displayed in figures.

Table DR2: Quality classes for earthquake locations (after Husen and Smith, 2004). "Distance" is the difference between the maximum likelihood and the expectation hypocenter location and "Average error" is the mean of the three axes of the 68% error ellipsoid from NonLinLoc.

3 CRITICAL COULOMB WEDGE THEORY

The critical Coulomb wedge theory considers accretionary wedges as similar to wedges of soil or snow generated by a bulldozer and was successfully applied to convergent margins (e.g. Wang and Hu, 2006; Cubas et al., 2013). We will briefly describe the main equations and refer the reader to Dahlen (1990) and Davis et al. (1983) for further reading.

For a critical wedge the following equation is valid:

$$\alpha + \beta = \Psi_B - \Psi_0 \tag{3.1}$$

where Ψ_B is the angle between the maximum principal stress σ_1 and basal slope, Ψ_0 is the angle between surface slope and σ_1, α and β describe the angles between the horizontal and surface slope and the base of the wedge, respectively (Fig. DR5).

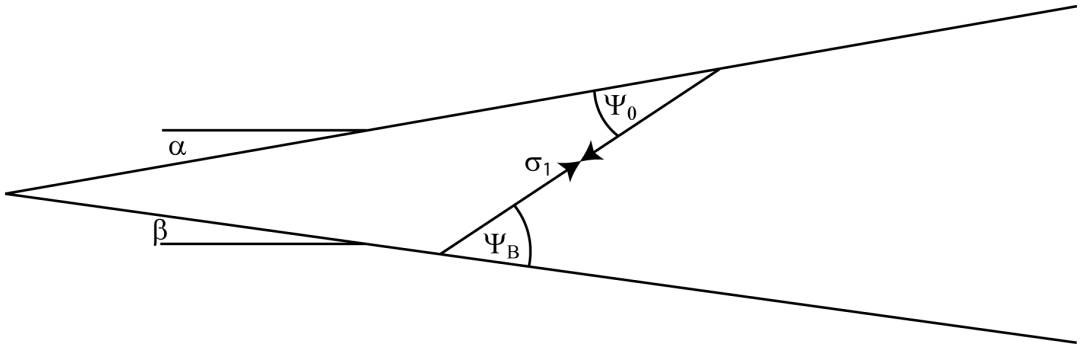

Figure DR5: Sketch of a wedge with the angles α, β, Ψ_B and Ψ_0.

The angles $\Psi_{B,0}$ are:

$$\Psi_B = \frac{1}{2}\arcsin\left(\frac{\sin\phi_b^{'}}{\sin_{int}}\right) - \frac{1}{2}\phi_b^{'} \tag{3.2}$$

and

$$\Psi_B = \frac{1}{2}\arcsin\left(\frac{\sin\alpha^{'}}{\sin_{int}}\right) - \frac{1}{2}\alpha^{'} \tag{3.3}$$

where

$$\tan\phi_b^{'} = \left(\frac{1-\lambda_b}{1-\lambda}\right)\tan\phi_b = \frac{\tan\Phi_b^{EFF}}{1-\lambda} \tag{3.4}$$

with $\tan\phi_b^{EFF} = (1-\lambda_b\tan\phi_b)$ (Cubas et al., 2013) and

$$\alpha^{'} = \arctan\left[\left(\frac{1-\rho_w/\rho}{1-\lambda}\right)\tan\alpha\right], \tag{3.5}$$

where λ is the pore pressure ratio and ρ is the density of water and of rock, respectively. The angles ϕ_{int} and ϕ_b are internal and basal friction angles with $\mu_{int,b} = \tan\phi_{int,b}$. Values for ϕ_{int}, λ and ϕ_b^{EFF} for outer and inner wedge were taken from Cubas et al. (2013) and ρ was set to 3000 kg/m^3. Calculating β for a set of given α with equation 3.1 with different parameter for the inner and outer wedge leads to the critical envelopes in the stability diagram in Figure DR6. Inside the envelopes the wedge is in a stable state whereas outside it is in an unstable state and along the branches of the envelope in a critical state and at the verge of failure.

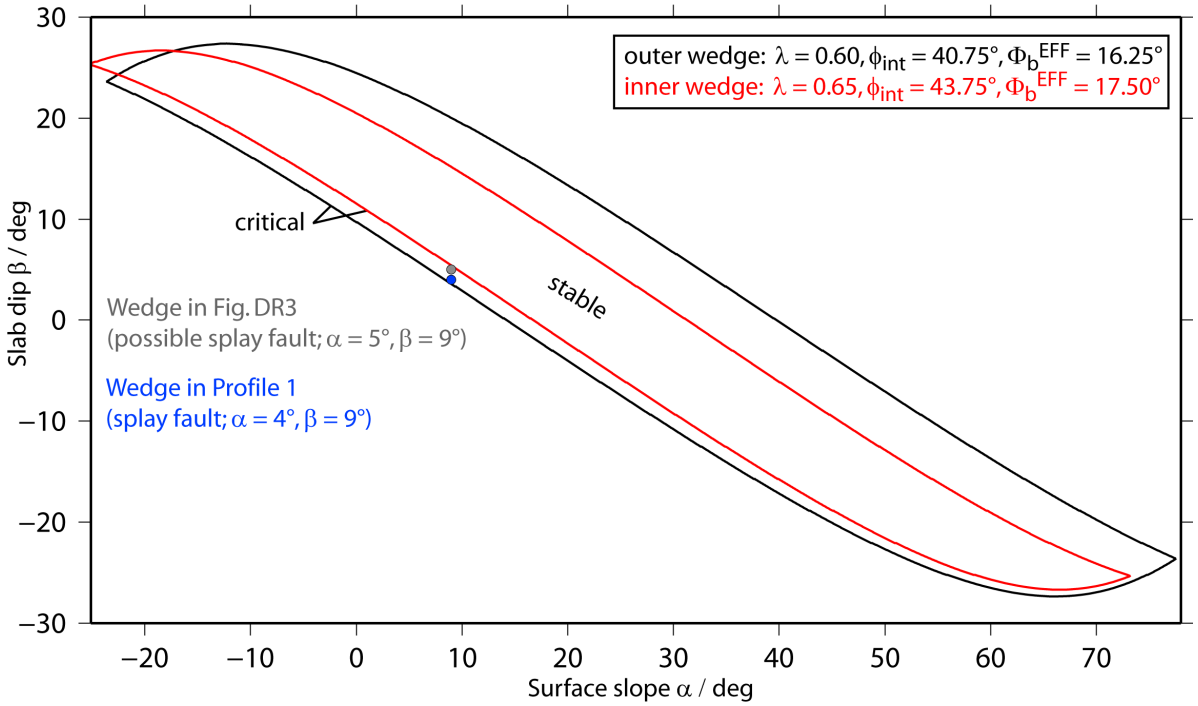

Figure DR6: Stability diagram for the outer and inner wedge in the northern deployment area. The blue dot marks the taper corresponding to the splay fault region and the grey dot marks the taper for where the cluster at the northern boundary of the deployment area is located. Parameter for outer and inner wedge according to Cubas et al. (2013).

F. Results

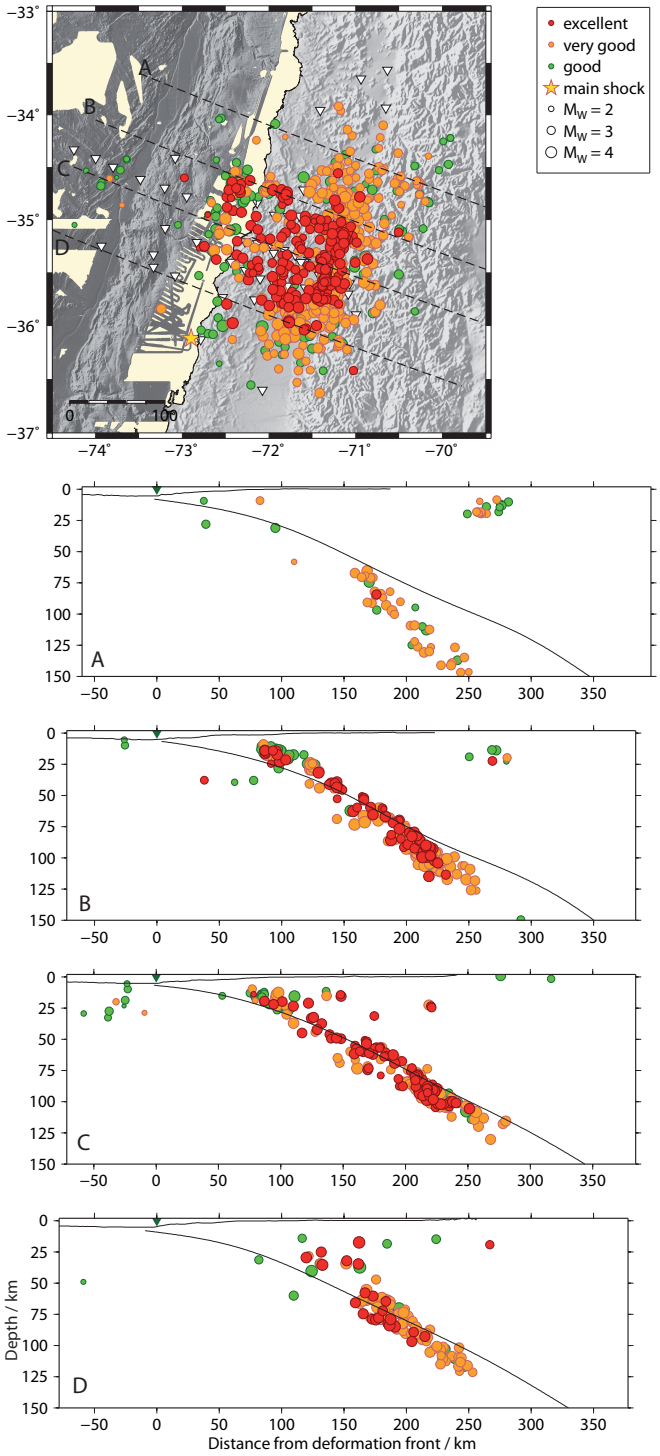

Figure F.1.: Local magnitude distribution for events with quality classes “excellent” to “good” for the 2008 data set. Triangles are OBS locations, diamonds land station locations.

G. Discussion

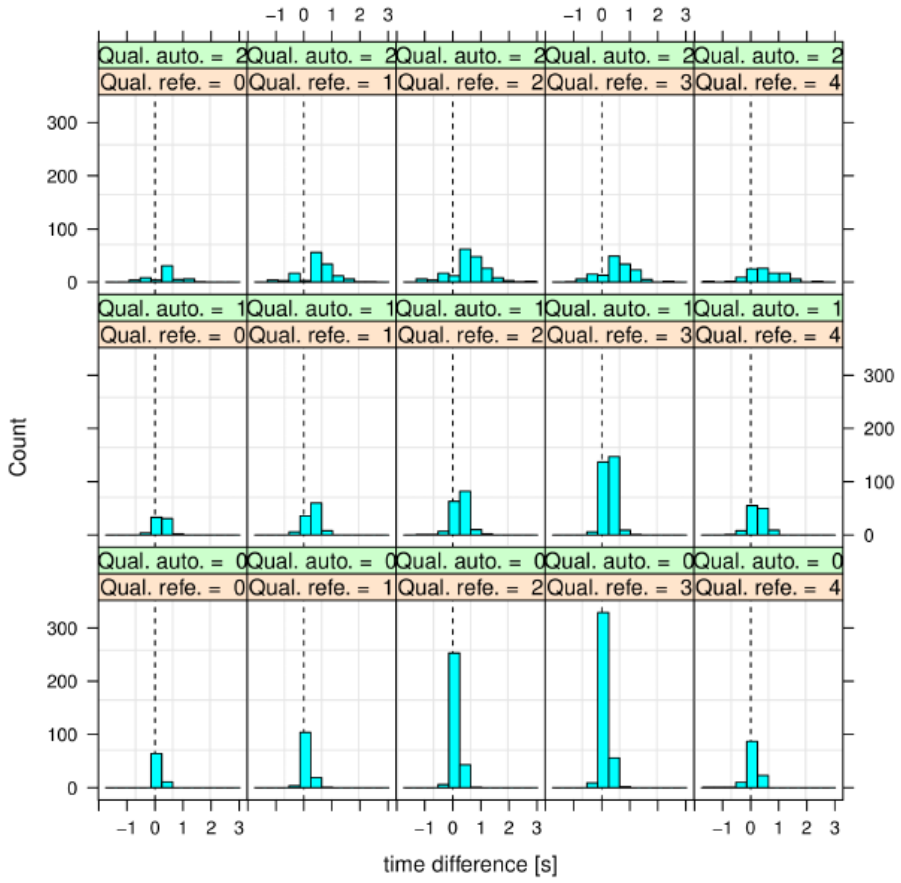

Figure G.1.: Picking errors for the S phase picker of *Diehl et al.* (2009) for the land station data (*Lange et al.*, 2012b).

Acknowledgements

Ingo, vielen Dank dass Du mir die Stelle im Projekt angeboten und somit diese Arbeit erst ermöglicht hast. Danke vielmals für die umfassende Betreuung, Unterstützung und fachlichen Rat in den vergangenen Jahren!

Herr Rabbel, Sie haben mich schon durch das Diplom begleitet, vielen Dank, dass Sie sich auch dazu bereit erklärt haben, das zweite Gutachten zu übernehmen.

Dietrich, vielen lieben Dank, für Deine Unterstützung und dass Du Dir die Zeit genommen hast, Dich so gründlich durch meine Arbeit zu lesen!

Ein großes Dankeschön an die OBS-Fischer ohne die es die Daten für diese Arbeit nicht gegeben hätte: Ingo, Ernst, Wiebke, Stefan, Ivonne, Ingo, Anne-Dörte und natürlich an die tolle Crew der "alten" Sonne.

Alexey, thank you for lending me your big, fat screen that made thesis writing at home a lot more comfortable! And thank you so much for your support with the Barents Sea project!

Vielen Dank an die komplette Geodynamikabteilung für eine schöne Zeit am GEOMAR, besonders auf See.

Veit, vielen lieben Dank für Deine großartige Unterstützung, sei es Korrekturlesen, Kochen oder generell mich vom Wahnsinn abzuhalten. Ich freue mich auf die Zeiten, in denen keine Ozeane zwischen uns liegen.

This thesis was created with LaTeX.

Most of the figures were created with the Generic Mapping Tool (GMT) by Paul Wessel and Walter H. F. Smith.

Hiermit erkläre ich, dass ich die vorliegende Doktorarbeit selbständig - abgesehen von der Beratung durch den Betreuer - und ohne Zuhilfenahme unerlaubter Hilfsmittel erstellt habe. Weder diese noch eine ähnliche Arbeit wurde an einer anderen Abteilung oder Hochschule im Rahmen eines Prüfungsverfahrens vorgelegt, veröffentlicht oder zur Veröffentlichung vorgelegt. Ferner versichere ich, dass die Arbeit unter Einhaltung der Regeln guter wissenschaftlicher Praxis der Deutschen Forschungsgemeinschaft entstanden ist.

Kiel, den .....

Kathrin Lieser